Metallurgical Studies of Friction Stir Lap Welding

Shamzin Yazdanian

A thesis submitted to Auckland University of Technology in fulfilment of the requirements for the degree of Doctor of Philosophy (PhD)

2012

School of Engineering

Abstract

Friction stir welding (FSW) is a solid-state joining technique which can be used for joining not only traditionally weldable aluminium alloys but also high strength aluminium and other metallic alloys that are hard to weld using conventional fusion welding processes. During FSW a rotating tool consisting of a shoulder and a pin is first plunged into the joint line of two plates to be welded. Intensive heat is generated as the tool rotates and travels against the plates, causing the latter to be softened without gross melting. The softened material is then stirred and deposited at the back of pin as the tool traverses the joint line, hence making a joint. The process of conducting FSW in lap joint configuration is called friction stir lap welding (FSLW).

Mechanical strength of FSL welds under static loading is commonly determined using tensile shear testing and fracture strength (σ_{Lap}) corresponding to the maximum load in a test over the sample width is widely used the strength value. During FSLW of similar metallic alloys, a part of the original lapping interface between the plates is lifted up due to a specific material flow induced by the rotating threaded tool pin, taking a hook shape. Such a hook in a FSL welds often provides a favourable site for crack propagation under loading and thus adversely affects σ_{Lap}. Furthermore, FS heat causes local softening but grain refinement by dynamic recrystallisation contributes to hardening in stir zone. Thus strength is location dependent. In FSLW of dissimilar metallic alloys with large differences in melting temperatures, a metallurgical bond is established through the formation of interfacial intermetallics. However, as these intermetallic compounds are generally believed to be brittle with limited ductility, they are commonly viewed to adversely affect σ_{Lap}.

Currently, the nature (shape and continuity) of hooks in FSL welds of similar alloys have not been discussed well in literature. A detailed thermomechanical explanation on how FSLW parameters (rotation speed-ω and linear speed-v) affect the hook size (*h*), shape and continuity has not been given. The relative role and contribution of hooking (considering size, shape and continuity), FS softening, stress concentration and local ductility during tensile shear testing on σ_{Lap} have not been clearly described. Regarding FSLW of dissimilar metallic alloys with large differences in melting temperatures, how

exactly the microstructure in the interfacial region is related to fracture behaviour and thus σ_{Lap} is far from being fully understood.

Thus, the aim of the present research is to provide thermomechanical explanation on how ω and ν affects hook formation during FSLW; to understand how hooking, FS softening, stress concentration and local deformation mechanisms (under loading) relate to σ_{Lap} of Al and Mg FSL welds; and to reveal how the interface structure is affected by FS conditions and how the formation of interface structure affects σ_{Lap} of Al/Steel and Al/Ti FSL welds.

Experimentally, FSLW of age-hardened aluminium alloy (6060) and strain-hardened magnesium alloy (AZ31B), thus alloys with not only different strengthening mechanisms but also different crystallographic structures, were performed using a wide range of ω and ν, and using various pin lengths (L_{pin}). Temperature of stir zone (T_{SZ}) was monitored for some selected experiments. Hook size (h) and stir volume per unit length in the bottom stir zone ($A_{B\text{-}SZ}$) were measured to study how $A_{B\text{-}SZ}$ and T_{SZ} are related to h. Tensile shear testing of welded specimens were performed and the effect of loading geometry on local deformation was investigated using SEM/EBSD and by detailed fractographic observation. Finite element method (FEM) modelling was conducted to investigate the stress distribution and stress relaxation due to local deformation during tensile shear testing. Thus, how stress concentration/relaxation together with FS softening and hooking contributes to the final σ_{Lap} could be studied in detail. FSLW of Al 6060-T5 to mild steel and Al 6060-T5 to Ti6Al4V alloy were performed using various pin positioning distances, in relation to the bottom plate (either steel or Ti6Al4V). Aluminium plates were placed on top of steel or Ti6Al4V plates. T_{SZ} was also monitored in all experiments. In the specifically designed experiments, downforce of the tool (during FSLW) was monitored to indicate the contact condition between the pin and bottom plate (steel or Ti6Al4V). The thermal and pin positioning conditions were then related the microstructure formed in the interfacial region. The effect of the various interfacial microstructures on σ_{Lap} was studied using tensile shear testing and detailed fractographic examination.

For FSL welds of Al 6060-T5, it was found that low penetration required low v for a sufficient bonding. For sufficient penetration, (ω, v)-$A_{B\text{-}SZ}$-h relationships were presented. Measured data have suggested that the increase of $A_{B\text{-}SZ}$ as ω increases is the result of increase in T_{SZ} and thus the stir zone plasticity. A rapid increase in h to a maximum value (h_{Max}) when $A_{B\text{-}SZ}$ increased from a minimum value was identified. Evidence of shoulder flow limiting the h_{Max} will be shown and explained. When h tended to zero, despite of the existence of an un-welded lap and thus a high stress concentration, σ_{Lap} (422 N/mm) was very close to σ_{BoP} (fracture strength of butt joint geometry). This is due to local bending offered by the high ductility of the Al FCC structure thus reorientating to reduce considerably the stress concentration. It was found that when h < ~ 30% of the plate thickness (t_{Plate}), σ_{Lap} was not strongly affected by h. This surprising result has been explained by considering hook shape, hook discontinuity and FS softening that competes with hooking for the local deformation and fracture. When h > ~ 30% t_{Plate}, it started to invoke a significant effect on reducing σ_{Lap}, due to the increasingly larger reduction in load bearing area.

It will be demonstrated that FS flow and the subsequent tensile-shear mechanical behaviours of magnesium alloy AZ31B-H24 are significantly different from those of Al 6060-T5 alloy. For AZ31B-H24 alloy, FS zone was comparatively smaller and there was little discontinuity in each hook. It will be shown that due to lack of local sample rotation during tensile shear testing, as a result of low number of slip systems offered for plastic deformation by Mg alloy, high stress concentration of the lap joint geometry was maintained (during testing) causing failure with a significantly lower σ_{Lap} value (290 N/mm), when h tended to zero. Also for the same reason, unlike Al 6060-T5 welds, FS softening could not compete with hooking for local deformation and fracture. Thus hooking location was always the location of fracture. Results of numerical modelling and artificial hook testing experiments showed that stress distribution at hook region (during tensile shear testing) was considerably affected by the orientation of hooking. This explains that fracturing proceeds away from the hook, for negative hooking samples. Significant stress concentration caused by tensile shear loading enhanced the localised operation of twinning at the hook region, facilitating a fracture in brittle manner.

Finally, detailed evidence has suggested that the major factor determining σ_{Lap} of Al/Steel and Al/Ti FSL welds is the degree of contact between the bottom of the pin and surface of bottom plate (steel or to Ti6Al4V) during welding. Insufficient contact resulted in discontinuous intermetallic layer in the form of outbursts. This type of interface will be shown to resist loading poorly and thus low σ_{Lap} was obtained. When the pin was at a very short distance or just touching the bottom plate, a thin intermetallic layer formed at the interface. Further pin penetration into the bottom plate resulted in the formation of a mix interface region consisting of cut layers of the bottom plate material and irregular intermetallic layers. The mixed layer interface region corresponded to reasonable weld strength ($\sigma_{Lap}\approx$ 300 N/mm in Al/Steel FSLW and $\sigma_{Lap}\approx$ 340 N/mm in Al/Ti FSLW) consistent with data in literature. It will be demonstrated that a thin intermetallic layer formed under the condition of carefully positioning the pin very close or just touching the bottom plate (without severely penetrating) provided the most unfavourable crack propagation path. As a result, high strength joints with σ_{Lap}=435 N/mm in Al/Steel FSLW and σ_{Lap}=732 N/mm in Al/Ti FSLW was achieved.

Acknowledgement

I would like to express my sincere gratitude and deep appreciation to my principle supervisor, Professor Zhan Chen for his generous support, encouragement and leading me through this research work. His enthusiasm and strong interest on research have made a deep impression on me. Professor Guy Littlefair (secondary supervisor) is gratefully acknowledged for his valuable discussions. Dr Jenifer Wilkinson is gratefully thanked for help on SEM/EBSD. I would also like to thank Mark Masterton, Ross Reichardt, and Bradley Scott for their time and guidance during experiments.

My heartfelt appreciation goes to Nashmil, my wife, who stood by me through this venture, for her ongoing love, understanding and patience. I am indebted to Honia, my lovely daughter, whose ongoing smile has accompanied me through to the completion of this thesis.

Statement of Originality

I hereby declare that this submission is my own work and that, to the best of my knowledge and belief, it contains no material previously published or written by another person nor material which to a substantial extent has been accepted for the qualification of any other degree or diploma of a university or other institution of higher learning, except where due acknowledgement is made in the acknowledgements.

Name:

Date:

Table of Contents

List of Figures

List of Tables

Nomenclatures

Symbols	Meaning	Units
ω	Tool rotation speed	rpm
ν	Tool linear speed	mm/s
θ	Tool tilt angle: angle between vertical axis and toll axis	^{o}
λ	Welding pitch	mm/rev
$D_{shoulder}$	Diameter of tool Shoulder size	mm
D_{pin}	Diameter of tool pin size	mm
L_{pin}	Length of Pin tool	mm
L_{dis}	Distance between pin tip and bottom plate	mm
h	Hook size	mm
h_{Max}	Maximum hook size	mm
t_{efc}	effective load bearing thickness of the top plate	mm
σ_{Lap}	Fracture strength	N/mm
UTS	Ultimate tensile strength	MPa
σ_{BoP}	Fracture strength value of bead-on-plate samples	MPa
T_{SZ}	Temperature of stir zone	^{o}C
$T_{SZ\text{-}P}$	Peak temperature of stir zone	^{o}C

F_Z	Downward force applied to the tool pin	KN
E	Elastic Modulus	N/m^2
$A_{B\text{-}SZ}$	Flow volume in the bottom stir zone	Mm^2
t_{Plate}	Plate thickness	mm
HK	Hardness in Knoop scale	
HI	Heat index parameter	

1. Introduction and Literature Review

1.1 Friction Stir Lap Welding (FSLW): Background

Friction stir welding (FSW) is a solid state joining technique invented in 1991 by Wayne Thomas and associates at The Welding Institute in UK [1]. During FSW a non-consumable rotating tool is plunged into the joint line between the plates to be welded, and traverse along the joint line (as illustrated in Figure 1-1). The tool consists of two features, a shoulder and pin. The plates to be welded are clamped firmly onto a backing plate to prevent them being forced apart. Intensive contact frictional heat is generated between the rotating tool and the material of the workpieces. In addition heat is also generated by plastic deformation of the material. The generated heat results in softening of the material (without reaching the melting point) which then flows around the tool pin and deposits at the back of pin during welding. There are two sides with respect to the welding tool during FSW. The advancing side (AS) is the side where the tool rotational motion and traverse direction are in the same direction, and the retreating side (RS) is the side where the tool rotational motion is opposite to the traverse direction.

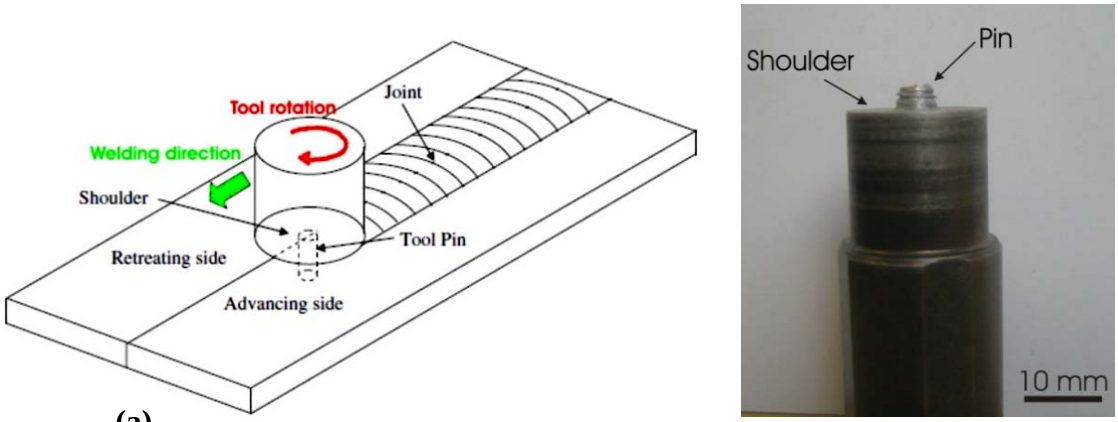

(a) **(b)**

Figure 1-1 (a) Schematic illustration of FSW process [2] and (b) an actual tool with treaded pin

As FSW is a solid-state joining process (material does not melt during the process), it is free from solidification-related defects associated with fusion welding such as solidification cracking and porosity. Also, this process requires less energy compared to conventional fusion welding techniques, hence lower heat input is transferred to the workpiece which reduces distortion. Compared to fusion welding techniques, FSW does not require shielding gas/flux, thus making it more environmentally friendly. Moreover, during FSW dynamic recrystallization will occur in the stir zone due to the significant frictional heating and intensive plastic deformation (induced by the rotating pin), which

results in the formation of fine and equiaxed recrystallized grains. The formation of a recrystallized fine grain microstructure in weld results in improved mechanical properties such as higher joint fracture strength and fatigue resistance.

Due to its many advantages, FSW has been the subject of numerous studies and has already been applied in many industries, including aerospace, automotive and shipbuilding industries [3, 4]. As an example, the difficulty of fusion welding of high-strength aerospace aluminum alloys, such as highly alloyed 2xxx and 7xxx series, has long inhibited the wide use of fusion welding for joining these alloys. Solidification cracking and porosity formation are typical problems of fusion welding of these aluminum alloys that can be overcome with FSW. Nowadays FSW is also being applied in butt welding of aluminium, magnesium, copper, steel and titanium alloys. High quality welds with superior mechanical performance (using optimum process conditions), compared to conventional fusion welding techniques have been widely recognised [2, 3].

In addition to butt joint configuration, the lap joint configuration is widely used in the joining of metallic structures. The process of conducting FSW in lap joint configuration is called friction stir lap welding (FSLW). Figure 1-2 schematically illustrates the FSLW process in which the top and bottom plates are joined together, forming a lap joint. For process control and joint integrity, a number of parameters and variables must be considered. Variables include the types of alloy plates to be welded, tool shoulder diameter ($D_{shoulder}$), tool pin diameter (D_{pin}), tool pin length (L_{pin}), tool tilt angle (θ), tool rotation velocity (ω) and tool forward velocity (v). Some of these parameters are illustrated in Figure 1-2.

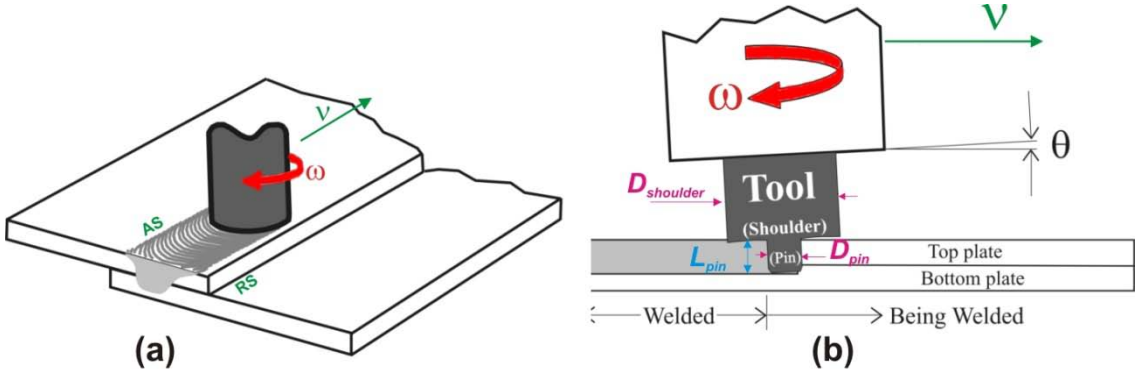

Figure 1-2 Schematic illustration: (a) FSLW process and (b) various FSLW parameters

Both wrought aluminium alloys and wrought magnesium alloys are known for their widespread use as structural materials in the transportation industry as they offer high strength-to-weight ratios, which reduce structure weight and hence fuel consumption. However the difficulties of joining these alloys using conventional fusion welding techniques prevents extensive use of these light alloys in lap joint configurations which are inevitably encountered in transportation industries. Therefore increasing interest has been devoted to development of FSLW (as solid-state joining process) of high strength aluminium alloys over the last decade in order to verify its potential to replace riveted lap joints in aircraft structures. Rivet holes are often preferential sites for crack nucleation due to fatigue and fretting and provide a path for propagation of multi-site damage [5]. Development of FSLW for welding similar materials of either aluminium or magnesium alloys could make FSLW the technology of choice as it may lead to lighter and more reliable structures at lower manufacturing costs [6, 7].

In industrial applications the need for joining dissimilar materials is often required to achieve a combination of properties of both materials. As an example, there is strong tendency for joining aluminium alloys to either titanium alloys or steels in the automotive/aerospace industries to reduce fuel consumption by weight savings. However physical mismatches such as differences in melting point, thermal expansion coefficients and thermal conductivity can make joining almost unpractical using conventional fusion welding techniques. Formation of thick brittle intermetallic layers (due to high heat input and liquation of aluminium) is known to deteriorate mechanical properties of the joints [4]. It is essential to develop more reliable joining procedures than those currently available for dissimilar material joints. Therefore development of FSLW as a solid-state joining process is of high importance from both scientific and industrial point of view.

Since its discovery, FSW has been studied extensively and many aspects of the process have been studied with a relatively wide range of materials and process conditions. Research associated with FSW has been reviewed by Mishra et al [3], Nandan et al [4] and Threadgill et al [2]. However, the current literature has mainly focused on butt joint geometry and FSLW has received significantly less attention. As will be shown later, the current literature on FSLW lacks systematic work addressing some of the fundamental issues relating to the structural integrity and final microstructure-property relationships of FSL welds (for either similar or dissimilar materials), which are the

major focuses of this thesis. Here we use a schematic, shown in Figure 1-3, to illustrate the key microstructural features (after FSLW) which affect the fracture behaviour of FSL welds, under static loading.

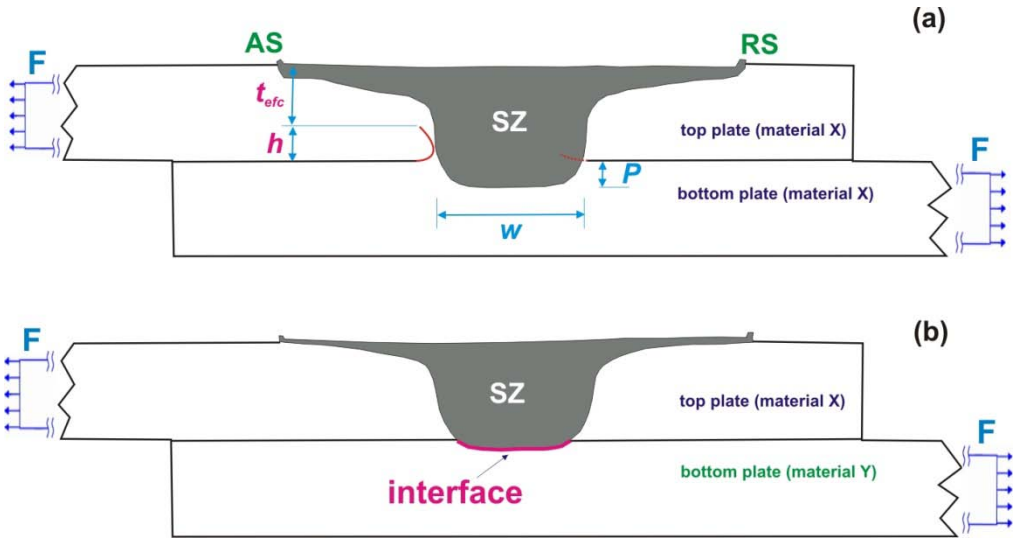

Figure 1-3 Schematic illustration: (a) a FSL weld of similar material, under static loading and (b) a FSL weld of dissimilar material, under static loading

In FSLW of similar materials (Figure 1-3a), the pin is sufficiently penetrated into the bottom plate and material mixing in stir zone creates the metallic bond between the top and bottom plates. In this case, the material flow (during FSLW) results in disruption of original lapping interfaces in SZ, and lift-up and re-orientation of lapping interfaces next to SZ (Figure 1-3a). However due to asymmetric material flow in advancing and retreating sides, during FSLW, the profile of the re-oriented lapping interface on advancing side is different from that on retreating side. On advancing side, the lapping interface usually folds upwards in a sharp angle along the SZ boundary, taking a hook shape and thus is commonly known as hook. While on the retreating side, the lapping interface is gently curved upward and penetrates into the SZ. Hooks can act as preferential crack initiation site and reduce the effective load bearing thickness of the top plate (indicated by t_{efc} in Figure 1-3a) under loading, thus negatively affecting the fracture strength of the joint. Furthermore FSLW-induced microstructural evolution in and around the SZ such as grain size distribution, variation of local strength and crystallographic orientation, width of stir zone (W), and depth of penetration into bottom plate (P) can also affect the fracture behaviour of a FSL weld. The above mentioned physical quantities depend not only on the on various FSLW process parameters such as ω, ν and tool design, but also on base material type and properties.

Therefore, how FSLW conditions affect the hook formation (on advancing side), and also how the final microstructure is related to fracture behaviour of welds, are fundamental questions regarding structural integrity of FSL welds (similar materials) which are investigated in this thesis.

When FSLW is conducted on two different materials with large differences in melting point, mechanisms of joint formation and also the prevailing parameters on structural integrity of the weld are different from those of FSLW of similar materials. Local mechanical interlocking and intermetallics formation at the interface (as indicated in Figure 1-3b) have been reported [8-10] as the mechanisms of joint formation in dissimilar materials FSL welds. Also when intermetallic layers are formed at the interface, they can be of various forms of intermetallic compounds depending on the type of materials being welded and thermomechanical conditions during FSLW. Therefore how the FSLW conditions affect the microstructure at the interface region of welds, and also how the final microstructure is related to the fracture behaviour of welds, are fundamental questions regarding structural integrity of FSL welds (dissimilar materials) which is investigated in this thesis.

Following the above brief introduction to FSLW, and prior to detailing the aspects of this thesis, a detailed literature review is presented; firstly on the relationship between process parameters (ω, ν) and hook formation, fracture behaviour and stress distribution during tensile shear testing of aluminium FSL welds, in section 1.2. Secondly, a detailed review of the effect of process parameters (ω, ν) on hook formation, role of hook orientation and deformation mechanism on fracture behaviour of magnesium FSL weld is provided in section 1.3. Thirdly, a detailed review on joint formation and the effect of interface microstructure on fracture behaviour of Al/Steels and Al/Ti FSL welds are given in section 1.4. Following the detailed literature reviews, the scope and sequence of this PhD research will be presented.

1.2 FSLW of Similar Materials: Aluminium Alloys

In this section, we will first briefly introduce wrought aluminium alloys. Then how material flow (during FSLW) and thermomechanical condition, affect the hook formation in aluminium FSL welds will be addressed. Lastly, current understanding on the role of important parameters affecting structural integrity and fracture strength of aluminium FSL welds will be given.

1.2.1 Wrought Aluminium Alloys

Wrought aluminium alloys are divided into eight categories based on the major alloying elements present. A standard system of alloy and temper designations for wrought aluminium alloys is presented in Table 1-1. For example, consider aluminium alloy 6060-T5 (which has been used in this PhD thesis). The first digit of designation, 6, signifies that this alloy belongs to 6xxx series in which magnesium and silicon are the two principal alloying elements. The T5 denotes that the alloy is artificially aged only [11].

Table 1-1 System of alloy and temper designations for wrought aluminium alloys [11]

First part (Indicates the main alloying elements)	**Second part** (Indicates the temper condition)
1xxx : With aluminum > 99.00%	**F (As-Fabricated) :** applies to products shaped by cold working or hot working with no special control over thermal conditions or strain hardening **O (Annealed)**: applies to wrought products that are annealed to obtain lowest strength. **H (Strain-Hardened)** : applies to products that have been strengthened by strain hardening H10 and H11: slightly strain hardened H23, H24, and H26: strain hardened and partially annealed **T (Solution Heat-Treated):** applies to alloys whose strength is stable within a few weeks of solution heat treatment. T4: solution heat treated T5: artificially aged only T6: solution heat treated and artificially aged T8: solution heat treated, cold worked, and artificially aged
2xxx : copper is the principal alloying element, though other elements, notably magnesium, may be specified	
3xxx : manganese is the principal alloying element	
4xxx : silicon is the principal alloying element	
5xxx : magnesium is the principal alloying element	
6xxx : magnesium and silicon are principal alloying elements	
7xxx : zinc is the principal alloying element, but other elements such as copper, magnesium, chromium, and zirconium may be specified	
8xxx : including tin and some lithium	

The elements added to aluminium alloys such as copper, magnesium, manganese and silicon have significant solid solubilities in aluminum at high temperatures. However the solubility limits decreases with decreasing temperature. This significant decrease in solubility limit is a fundamental characteristic that provides the basis for substantially increasing the hardness and strength of aluminum alloys [11]. Some aluminium alloys respond to thermal treatment based on the solubilities of added elements. Such alloys are described as heat treatable alloys. However some wrought alloys rely instead on

work hardening through mechanical operation. These alloys are described as non-heat treatable alloys.

Strengthening in non-heat-treatable alloys occurs from solid-solution formation, second-phase microstructural constituents, and strain hardening. Wrought alloys of this type are mainly those of the 3*xxx* and 5*xxx* groups, containing magnesium and manganese. Strengthening in heat treatable alloys includes a solution heat treatment to maximize solubility of added alloying elements, followed by rapid quenching to obtain a solid solution supersaturated with solute elements. Then artificial ageing is conducted which involves exposure at above room temperatures, so as to produce the transitional (metastable) forms of the equilibrium precipitates which remain coherent with the solid solution matrix. The presence of the transitional precipitates results in higher strength through obstruction and retardation of the movement of dislocations. However with further exposure at aging temperatures, the precipitate particles not only grow but also convert to the equilibrium phases, which generally are not coherent with the matrix. As a result the dislocations can bypass the particles by bowing into a roughly semicircular shape between them under the action of an applied shear stress. Therefore the material becomes softer and strength decreases. This phenomenon is commonly known as softening (over-aging) [11].

Aluminium alloy 6060-T5 (which is being studied in this PhD thesis), contains silicon and magnesium in the proportions required for formation of magnesium silicide (Mg_2Si), thus making them heat treatable. Therefore investigating FSLW of Al 6060-T5 is a representative study of FSLW of heat treatable aluminium alloys. Figure 1-4 shows a typical microstructure of aluminium 6060, particles are Fe_3SiAl_{12} (gray), distributed in the matrix of aluminium.

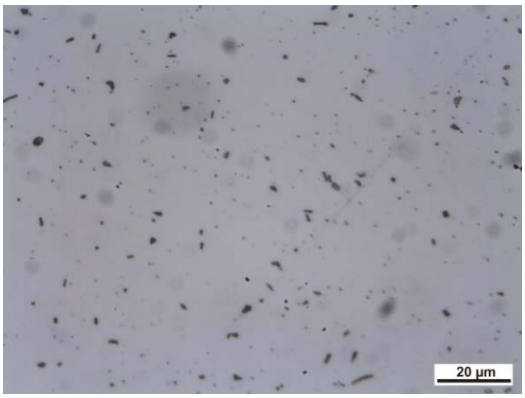

Figure 1-4 Microstructure of Al 6060 showing particles of Fe_3SiAl_{12} distributed in matrix of aluminium

1.2.2 Material Flow during FSLW and Hook Formation

It is well known that three major microstructural zones are formed in FSW of either aluminum or magnesium alloys [2, 4, 12, 13], as indicated in the Figure 1-5. These zones are stir zone (SZ), thermo-mechanically affected zone (TMAZ) and heat affected zone (HAZ). The stir zone is the region that is subjected to intense plastic deformation at high temperature, which results in recrystallized fine-grained microstructure, often with smaller grains than that found in the base material. Mechanisms such as discontinuous dynamic recrystallization and continuous dynamic recrystallization have been proposed for recrystallization of grains at SZ during FSW [2]. Thermo-mechanically affected zone forms on either sides of SZ. In this region, the amount of plastic deformation (strain induced by the rotating tool pin) and the heat from the process is not enough for complete dynamic recrystallization (in aluminium alloys only). Therefore distinct boundary exists between the recrystallized SZ and the significantly deformed and rotated grains of TMAZ zone. Beyond the TMAZ there is HAZ, which experiences a thermal cycle but no deformation during welding. For materials with the microstructure of thermally unstable (like the heat treatable aluminium alloys), grain growth and over-aging of precipitations are the common unfavourable phenomena that take place in that region [2].

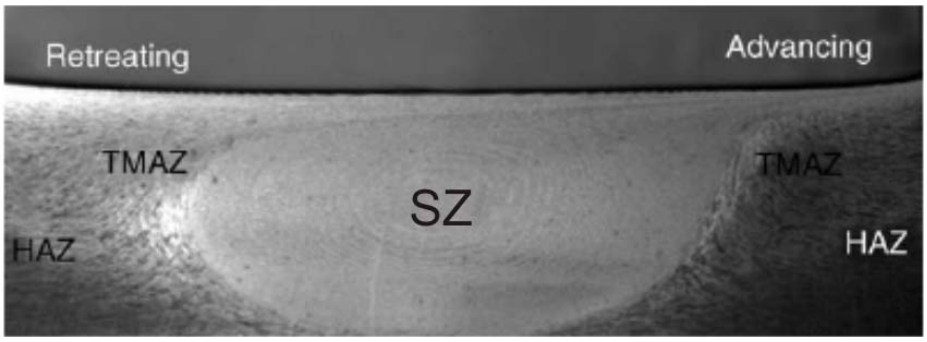

Figure 1-5 A micrograph showing various microstructural zones in a friction stir welded aluminium alloy 2024 (in butt joint configuration) [3]

During FSW, immediately next to the pin the plasticized material is driven downward by the rotating threads. Figure 1-6a shows an image of pin-workpiece couple obtained through sudden pin stopping action [14]. It can be seen that sheared flow layers exist around the pin threads (such as those indicated as L2, L3 in Figure 1-6a). These sheared layers are driven downward (also toward the advancing side) and detach at the back of pin as the pin rotates and moves ahead. Due to this downward material flow (induced by the rotating threads), the material originally located at the lower part of plate is pushed

upwards as well as outward. This can be better seen at the cross section of the weld (Figures 1-6b and 1-6c) illustrating that the material at the SZ boundary has been pushed upward by aforementioned upward material flow.

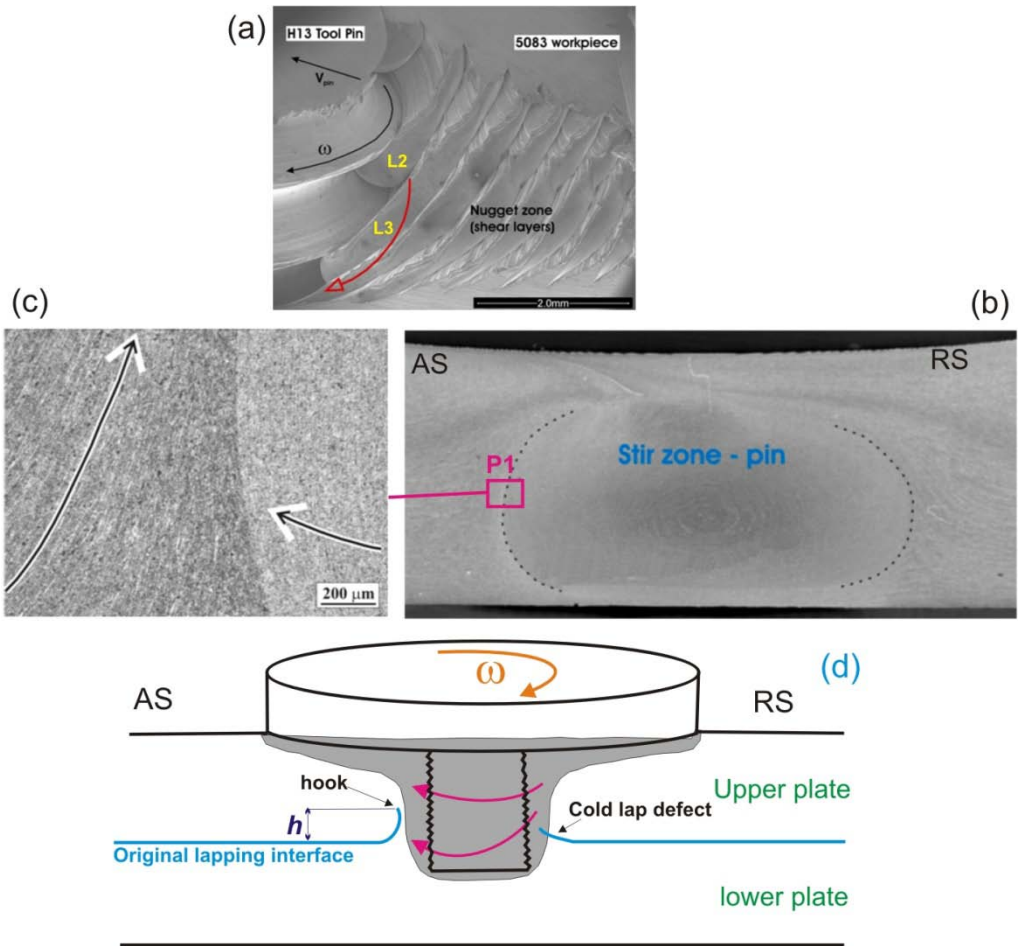

Figure 1-6 (a) SEM image of pin-workpiece couple obtained by the pin stop action showing the formation of sheared layer around pin driven downward [14], (b) cross section of weld [14], (c) higher magnification image of region P1 in Figure 1-6b [14] and (d) schematic illustration of material flow which results in formation of hooking during FSLW

In FSLW original lapping interfaces (which consist of original surface oxides of top and bottom plates) will be disrupted or redistributed due to that material flow during welding. In the stir zone, the original lapping interface is disrupted and may or may not disappear completely due to severe mechanical mixing induced by the rotating pin. However the original lapping interface is lifted up and re-oriented on TMAZ of both advancing and retreating sides, as shown schematically in Figure 1-6d. As described in section 1.1, due to asymmetrical material flow in advancing and retreating sides (during FSLW), the profile of the re-oriented lapping interface on advancing side is different from that on retreating side. On advancing side, the lapping interface usually folds upwards along the nugget boundary, taking a hook shape and thus is commonly referred

to as hook [2, 15]. While on the retreating side the lapping interface is gently curved upward and penetrates into the SZ, thus is referred to as cold lap defect [15] or straight crack [2]. It should be noted that in current literature, hook size (h) refers to the vertical distance of the hook [6, 7, 12, 15-17] as indicated in Figure 1-6b.

Figure 1-7 shows the macro and microstructure of a typical aluminum alloy FSL weld illustrating the redistribution of the original lapping interface along the hook on advancing side. EDS line scan across hooking clearly shows the presence of oxide along the hook, as seen in Figure 1-8 [18]. Due to the presence of oxide along the hook a complete metallurgical bond cannot be obtained (along the hook) and hence it can affect the mechanical performance of FSL welds under loading, which will be discussed further in section 1.2.4.

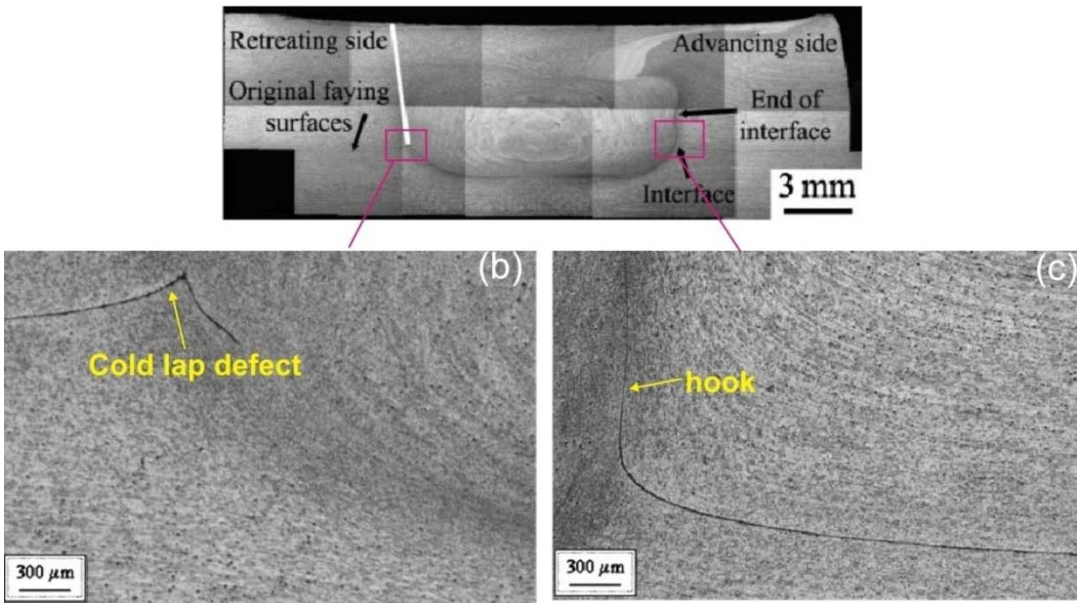

Figure 1-7 Microstructures of Al 5083 FSL weld made using ω =584 rpm and ν =120 mm/min: (a) macrograph (white line indicate the fracture path during tensile shear testing), (b) cold lap defect on retreating side and (c) hook on advancing side [18]

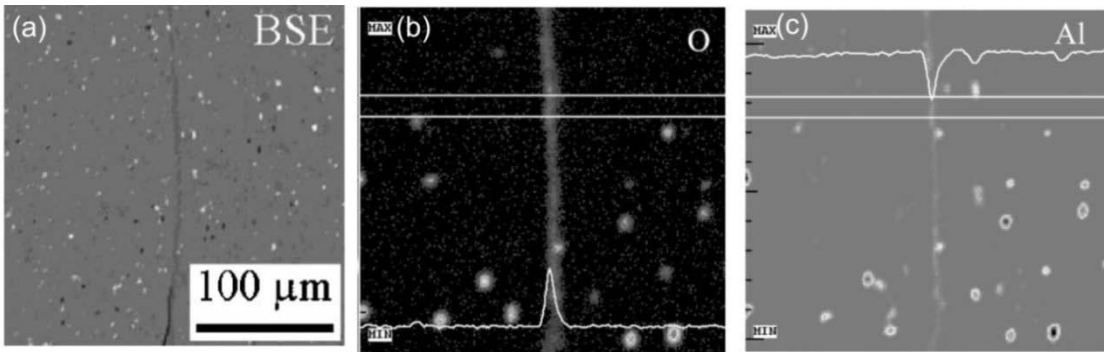

Figure 1-8 (a) SEM image showing hooking, (b) EDS scan line for oxygen, and (c) EDS scan line for aluminium [18]

1.2.3 Effect of Speeds (ω, ν) on hook size (*h*)

The use of higher ω or lower ν has been reported to result in a larger *h* [16, 19-22]. Figure 1-9 shows the macrographs for welds made using FSLW of Al 5052 to Al 6061with various ω and ν. It can be seen that the amount of pull-up of the bottom plate (5052) to the top plate (6061) increases with increasing ω (Figure 1-9 a-c) and decreasing *v* (Figure 1-9 d-f). Based on these metallographic observation Lee et al [22] has suggested that a higher ω or a lower ν results in a higher volume of vertical material transport thus lifting up more original lapping interfaces. In other words, the effect of vertical material transport and the resulted *h* was thought to be a pure mechanical effect although no precise material flow volume measurement and its relationship with *h* was investigated.

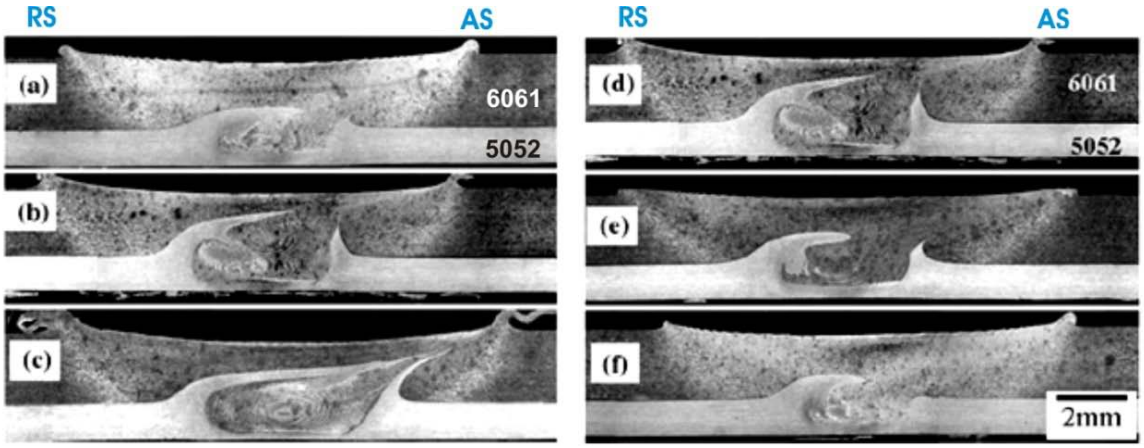

Figure 1-9 Macrographs of Al 6061 to Al 5052 FSL welds made using ν =267 mm/min and ω = (a) 1250 rpm, (b) 2500 rpm, and (c) 3600 rpm; and ω =1600 rpm and *v* = (d) 127 mm/min, (e) 267 mm/min, and (f) 507 mm/min [22]

Further to this mechanical effect, Dubourg et al [6] has pointed out the possible effect of increasing ω on increasing temperature and the plasticity of the SZ thus affecting the amount of up-lift and *h*. However this suggestion was not based on actual temperature measurement of SZ but instead, heat index (*HI*) parameter has been used to indicate the SZ temperature during FSLW. It should be pointed out that Arbegast et al [23] introduced the pseudo *HI* (ω^2/ν) to describe the FSW parameter dependence of temperature and they showed that in several aluminium alloys a general relationship between maximum SZ temperature (T) and FSW parameters (ω, ν) can be expressed by

$$\frac{T}{T_m} = K\left(\frac{\omega^2}{\nu .10^4}\right)^{\alpha} \qquad 1\text{-}1$$

where the exponent α was reported to range from 0.04 to 0.06, the constant K is between 0.65 and 0.75, and T_m is the melting point of alloy [3]. According to equation 1-1, either higher ω or lower *v* results in increasing *HI* and thus higher SZ temperatures during welding. However it worth noting that equation 1-1 was obtained using curve fitting of a number of experiments in which ω varied for constant ν values; and hence it was not validated through experimental observation in a wide range of ω and ν. Consequently in some other studies [24, 25] it has been reported that *HI* could not be used as a parameter to describe the SZ temperature. Therefore precise effect of SZ temperature on *h* cannot be understood using *HI* parameter. From the above discussion it is clear that a detailed thermomechanical explanation supported by corresponding experimental data has not been fully given in literature and a better understanding of how FSLW speeds (ω, ν) affects the *h* is required.

1.2.4 Parameters Affecting Fracture Strength of Aluminium FSL Welds

The mechanical performance of FSL welds under static loading is normally determined using tensile shear testing method [6, 7, 12, 15-18, 20-22, 26-29]. Schematic illustration of tensile shear testing is shown in Figure 1-10. Maximum failure load in a test divided by the width of the sample is defined as σ_{Lap}, which is commonly used. However due to the asymmetry in profile of hook (on advancing side) and cold lap defect (on retreating side), FSL welds can be loaded in two different ways, as shown in Figure 1-10. In advancing loading configuration, the advancing side of a lap weld on the upper plate is placed under loading while in retreating loading configuration, the retreating side of a lap joint on the upper plate is loaded. As the hook on advancing side is usually folds upwards in a sharp angle along the nugget boundary [2, 15, 16], therefore the hook profile is generally considered to have more detrimental effect on mechanical performance of FSL welds , compared to the cold lap defect on retreating side [16], and thus the advancing side loading is the only testing mode used in this study.

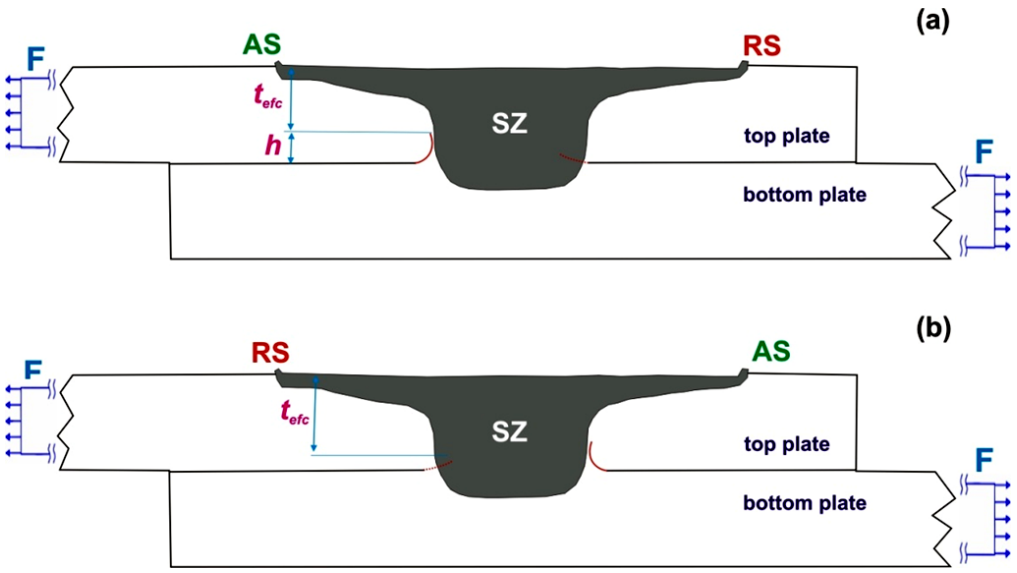

Figure 1-10 Schematic illustration of tensile shear testings: (a) advancing loading configuration and (b) retreating loading configuration

As described earlier, due to the presence of oxides along the hook a complete metallurgical bond cannot be obtained and thus failure in FSL welds has been found to occur along the hook [6, 15, 16] . In current literature hook size (h) refers to the vertical distance of the hook [6, 7, 12, 15-17], as shown in Figure 1-10. It is commonly accepted that the presence of hook reduces the effective load bearing thickness of the top plate (t_{efc}), as indicated in Figure 1-10, during tensile shear testing therefore increasing h known to result in decreasing σ_{Lap} [6, 7, 12, 15-17]

There have been a number of studies in recent literature on the mechanical properties of aluminium alloy FSL welds made using a relatively wide range of ω, ν. Brief descriptions of FSLW conditions (ω, ν and pin dimensions), maximum achieved σ_{Lap} and associated joint efficiency are given in Table 1-2. Joint efficiency is defined as maximum achievable load during tensile shear testing, divided by maximum achievable load during uniaxial tensile testing of base material (of the same sample width and thickness). The joint efficiency ratio indicates how the strength of weld is compared to the strength of base metal and thus the welds with high joint efficiency are more desirable. It can be seen that the maximum joint efficiency reported in literature is 86% which is for FSLW of heat treatable Al 2024-T3 to Al 7075-T6 alloys. However in the FSL weld with high value σ_{Lap} of 937 N/mm, the fracture did not initiated from the hook and instead failure location was in the top plate close to the edge of shoulder [16], meaning that failure occurred at the HAZ. Furthermore the obtained joint efficiency of

86% is similar to results of FSW butt joints in Al 2024-T3 with reported joint efficiency of 83% [30].

Table 1-2 Summary of the FSLW conditions with maximum σ_{Lap} achieved for aluminium welds (data collected from literature)

Ref.	Base materials	Welding speeds	Pin dimension (mm)	Maximum σ_{Lap} (N/mm)	Joint efficiency (%)
[15]	6111-T4 : 6111-T4 (1 mm- 1 mm)	ω =1500-2000 rpm v =190-380 mm/min	$D_{shoulder}$ = 12 $D_{pin=}$ 4 $L_{pin=}$ 1.4	200	67
[21]	5182 : 6022 (2 mm- 2.3 mm)	ω =1700-2100 rpm v =60-90 mm/min	$D_{shoulder}$ = 10.2 $D_{pin=}$ 4 $L_{pin=}$ 3.17	420	68
[22]	6061-T6 : 5052-H112 (2 mm- 1 mm)	ω=1250- 3600 rpm v=127-507 mm/min	-	240	-
[16]	2024-T3 :7075-T6 (2.3 mm- 2.3 mm)	ω =500-2000 rpm *v* =50-1000 mm/min	$D_{shoulder}$ = 19 $D_{pin=}$ 6.3	937	86
[20]	2198-T4 : 2198-T4 (3.2 mm- 3.2 mm)	ω =500-1000 rpm *v* =100 mm/min	$D_{shoulder}$ = 20 $D_{pin=}$ 6, 5.8, 6.6 $L_{pin=}$ 4.6, 4.9	570	-
[18]	5083-O : 5083-O (6 mm - 6 mm)	ω =584 rpm v=120-240 mm/min	-	-	-

Figure 1-11 shows a graph in which σ_{Lap} has been plotted against *h* (data reported by Cederqvist et al [16]) for FSL welds of Al 2024-T3 (top plate) to Al 7075-T6 (bottom plate). It can be seen that increasing *h* adversely affects the σ_{Lap} but this relationship is not linear. Also the large scatter of data in Figure 1-11 indicates that σ_{Lap} does not only depend on *h*, this is more evident for the welds with $h < 0.4$ mm. Although welds with small hook of $h = 0.2$ mm has been made but it is not understood how σ_{Lap} extrapolates if *h* tends to zero, which is the case of an ideal weld with no hook.

As explained in section 1.1.2, in the current literature the hook size has been defined as the vertical distance of the hook [6, 16, 18-22, 29], as shown in Figure 1-10. However this definition does not take into account the effect of shape, orientation and degree of continuity of the hook. In other words, hooks with different characteristics, but same size (*h*), have been considered to have the same effect on σ_{Lap}, which should not be correct and thus the details of hooking and quality of hook need to be further investigated.

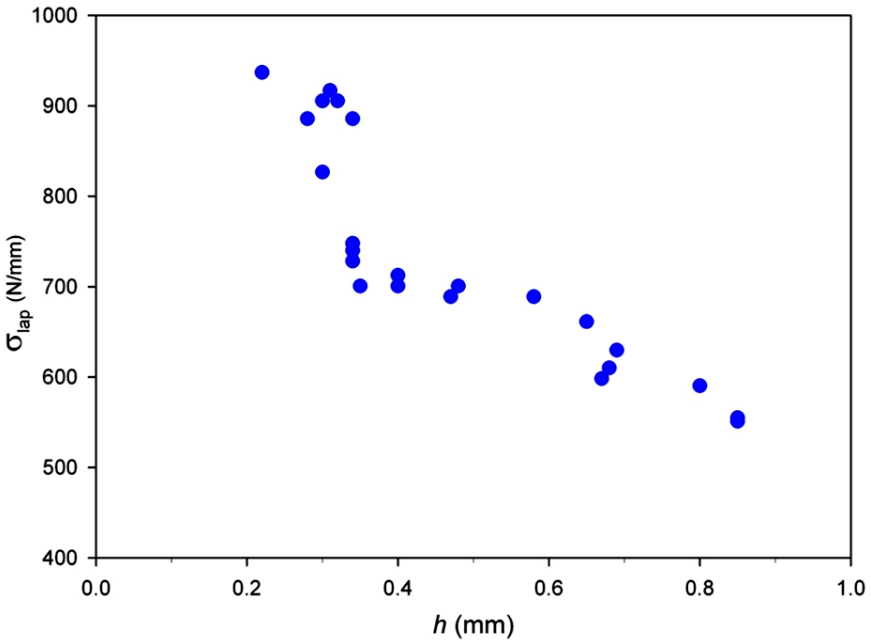

Figure 1-11σ_{Lap} as function of *h* for FSL welds of Al 2024-T3 to Al 7075-T6 (plotted based on data in Ref.[16])

While a hook is an important macro-feature of FSLW, significant heat generation during FSW also results in softening in various regions of the weld. Figure 1-12 shows a typical hardness distribution across the cross section of butt joint FSW of Al 6061-T6 (heat treatable alloy) using ω=2000 rpm and ν=100 mm/min [31]. Cross section of fractured specimen after testing is also shown. Although the entire weld region has lost its original hardness (softened), it can be seen that the fracture location matches the location of minimum hardness, which has became the weakest point. The softening phenomenon is known to be occurring due to dissolution and growth of the original nano-precipitates (which acts as strengthening mechanism as described in section 1.2.1) by the thermal cycles well above the normal precipitation hardening temperature [2, 32]. Therefore softening can also significantly affect σ_{Lap}. In current literature, the relative role of hooking and softening on fracture behaviour and σ_{Lap} of aluminium FSL welds has not been studied.

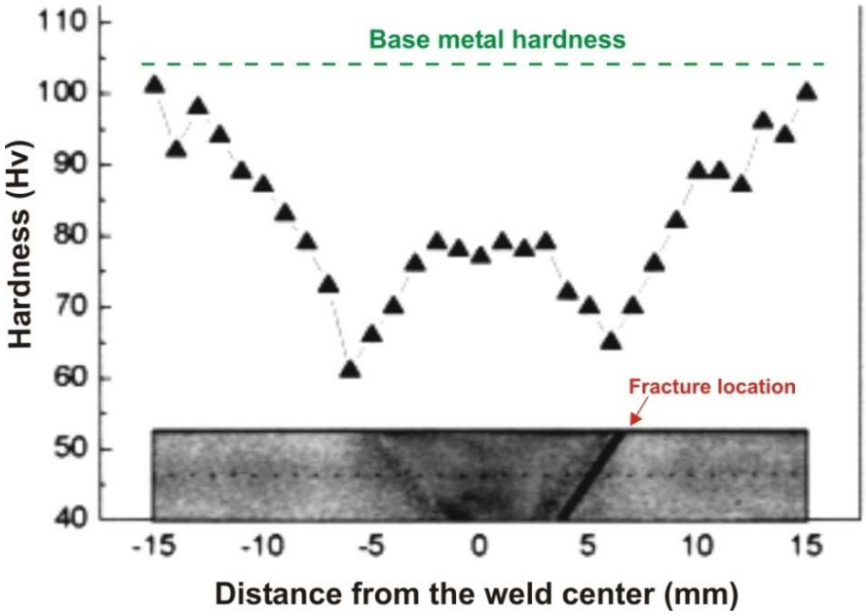

Figure 1-12 Representative Vicker's hardness values at various locations and matching macrographs of FSW Al 6061-T6 alloy, joined at ω =2000 rpm and ν =100 mm/min [31]

Although tensile shear testing is the most widely used testing method for the evaluation of the mechanical properties of FSL welds, little detail of the testing mechanic has been studied. Figure 1-13 shows a suggested stress distribution, which is frequently referred to in literature regarding FSLW to describe the state of stresses during tensile shear testing. According to this qualitative model, the tensile stress in the top and bottom plates progressively decreases from a maximum at the loaded end to zero at the unloaded end [6, 12, 16, 20] indicating a non-uniform stress distribution. Furthermore this qualitative model is based on an ideal lap joint with no lapping interface and hence does not consider the notch effect caused by presence of lapping interfaces such as a hook.

The model shown in Figure 1-13 appears to have been developed from studies reported on stress distribution in solder and adhesive lap joints (such as that shown in Figure 1-14) which have similar geometry to lap welds. For example Figure 1-14 shows a typical stress distribution results (obtained using finite element modelling) for an adhesive bonded lap joint, where the shear stress and peel stress are defined as stresses in x-axis and y-axis direction respectively. It should be noted that the peel stress is due to bending moments that takes place under lap shear loading [33-35]. Also Figure 1-14 indicates that stress concentrations occur close to the adhesive/adherend interface, at both ends of the joint. However the overall distribution and magnitude of stresses depends on number of parameters including thickness of adherents and adhesive, ratio

of adherent to adhesive elastic modulus and overlap length [33, 34, 36-38]. This discussion demonstrates that further numerical modelling of tensile shear loading for FSL welds (considering presence of hook) is required for a better understanding of stress distribution and subsequent fracture behaviour of FSL welds during testing.

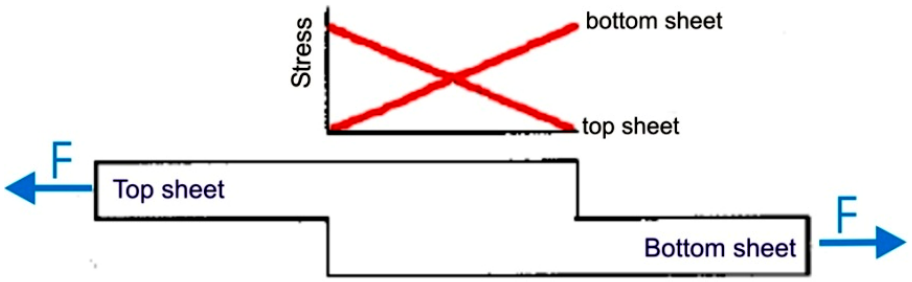

Figure 1-13 Schematic representation of stress distribution in an ideal lap joint with no sheet interfaces [16]

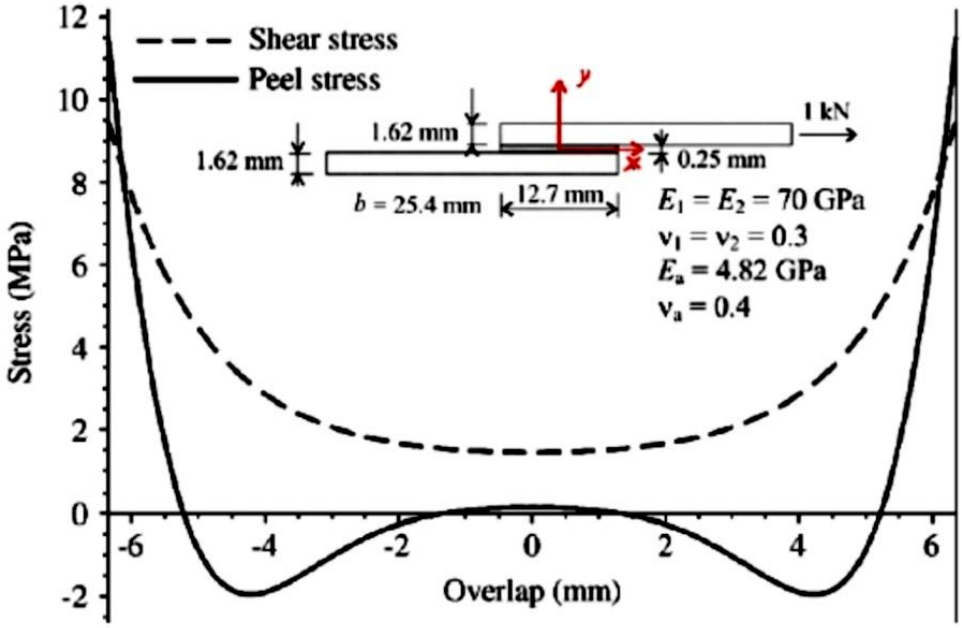

Figure 1-14 Shear and peel stress distributions for aluminium alloy adherents and epoxy adhesives (dimension of lap joint and mechanical properties of adhesive and adherent are also shown) [33]

1.3 FSLW of Similar Materials: Magnesium Alloys

In this section, a detailed review on the important microstructural features, local deformation mechanism and fracture strength of magnesium FSL welds is given. The microstructure of wrought magnesium alloy AZ31B-H24 is presented first, followed by a brief review on the effect of FSLW speeds (ω, ν) on hooking. Then the current understanding on FS parameters affecting structural integrity and fracture strength of AZ31 FSL welds is described. Finally, plastic deformation mechanisms and twin formation in magnesium alloys under static loading is presented. This last topic is important for understanding the mechanical behaviour of magnesium alloys joints during mechanical testing.

1.3.1 Microstructure of Wrought Magnesium Alloy AZ31B-H24

AZ31B-H24 is a widely used wrought magnesium alloy in which aluminium and zinc are principle alloying elements (3% Al and 1% Zn). This alloy is strain hardened and then partially annealed [11]. Figure 1-15 shows the typical microstructure of AZ31B-H24, consisting of both equiaxed and pancaked grains of various sizes. Also, a large number of deformation twins can be observed. These twins formed during hot rolling. The heterogeneity in the grain structure may originate from incomplete dynamic recrystallization during hot rolling and also post partial annealing [7, 13, 39-42].

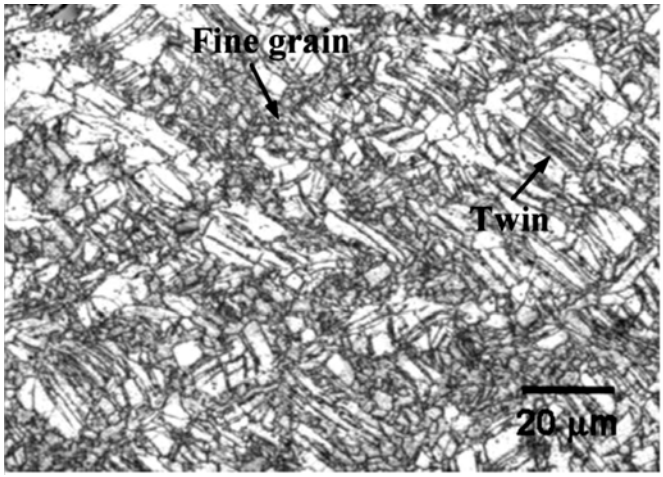

Figure 1-15 Typical microstructure of AZ31B-H24 showing heterogeneous fine grains and deformation twins [7]

1.3.2 Effect of Speeds (ω, ν) on hook size

The use of higher ω or lower ν values has been reported to result in a larger *h* in FSLW of magnesium alloys [7, 12, 17], similar to the general trend reported on the effect of (ω, ν) on *h* in FSLW of aluminium alloys (section 1.2.3). Therefore, as with FSLW of

aluminium alloys, it has been suggested [7] that higher ω or lower ν results in increasing the temperature and plasticity of the SZ, thus affecting the amount of up-lift and *h*. However this suggestion was not based on actual temperature measurement of SZ, but instead on heat index (*HI*) parameter, which was used to indicate the SZ temperature during FSLW.

In Figure 1-16, *h* values are plotted as a function of *HI* for AZ31 FSL welds [7] made using conventional cylindrical tool pins. It can be seen that when $HI < 300x10^2$, *h* increased significantly with the increase of *HI*, regardless of the tool pin used. However at $HI > 300x10^2$, *h* varied little as *HI* increased. As *HI* parameter was used to indicate the SZ temperature, Figure 1-16 suggest that SZ temperature has little influence on *h* when $HI > 300x10^2$; however the reason for this is not understood. As explained in section 1.2.3, *HI* parameter is not the true indicator of SZ temperature and thus the effect of SZ temperature on *h* in magnesium FSL welds may not be understood from the data available in literature such as that shown in figure 1-16. It is therefore apparent that the current literature lacks a detailed thermomechanical explanation supported by experimental data in order to obtain a better understanding of how process speeds (ω, ν) affects the hooking in FSLW.

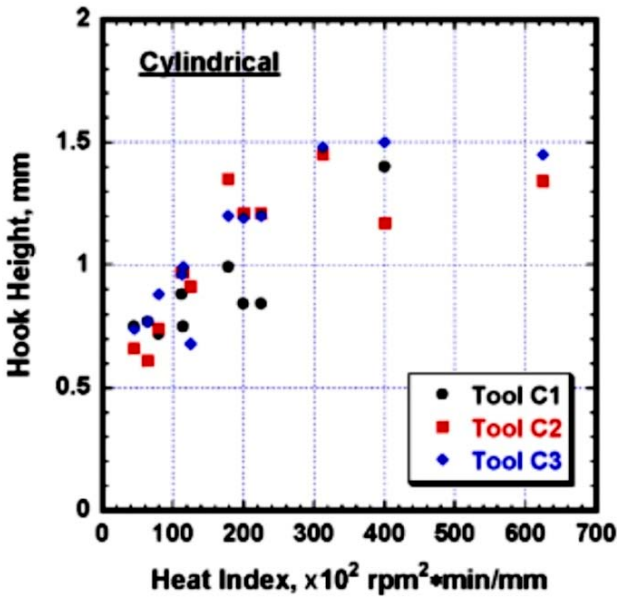

Figure 1-16 Hook size as function of *HI* for AZ31 FSL welds made using three cylindrical pin tools. For tool C1, $D_{shoulder}$ =12 mm & D_{pin} =5 mm. For tool C2, $D_{shoulder}$ =14mm & D_{pin} =5 mm. For tool C3, $D_{shoulder}$ =14 mm & D_{pin} =4mm [7]

Furthermore, as explained in section 1.2.2, the hook is a material flow related feature, affected by the pin induced material flow volume which causes up-lifting of the original

lapping interfaces. As the flow volume is affected by the material's behaviour during FSLW thus the hook characteristics can be affected by type of material used. However no comparison of hooking in different materials can be found in literature. Therefore it is not clear how the hook characteristics (size, shape and continuity) in magnesium alloys FSL welds differ from those in aluminium alloys FSL welds, if the same process parameters (ω, v) are used.

1.3.3 Parameters Affecting Fracture Strength of AZ31 FSL Welds

Recently there have been a number of studies on the fracture strength of AZ31B-H24 FSL welds. Brief descriptions of FSLW conditions, maximum achieved σ_{Lap} and associated joint efficiency are given in Table 1-3. Similarly to FSLW of aluminium alloys, *h* was found to be the major factor affecting σ_{Lap} and increasing *h* has been reported to decrease σ_{Lap} [7, 12, 17]. As explained in section 1.2.4, it is commonly accepted that the presence of hook reduces the effective thickness of the top plate and hence load bearing area of top plate, during tensile shear testing, resulting in lower σ_{Lap}. However, this is a simplest way of viewing the effect of *h* and, as will be shown later, *h* does insert a deep effect through stress concentration during loading. Also it can be seen (Table 1-3) that the joint efficiency of AZ31 FSL welds are generally lower than those reported for FSL welds of aluminium alloys (Table 1-2).

Table 1-3 Summary of the FSLW conditions with maximum achieved σ_{Lap} in FSLW of magnesium alloys (data collected from literature)

Ref.	Base material	Welding speeds	Pin dimensions (mm)	Maximum σ_{Lap}(N/mm)	Loading configuration	Joint efficiency (%)
[17]	AZ31B-H24 (2 mm)	ω = 2000 rpm v = 300-1800 mm/min	Cylindrical pin $D_{shoulder}$ = 19 $D_{pin=}$ 6.35 $L_{pin=}$ 2.75	290	Advancing loaded	49
[12]		ω =500-2000 rpm v =1200 mm/min	Cylindrical pin $D_{shoulder}$ = 19 $D_{pin=}$ 6.35 $L_{pin=}$ 2.75	347	Advancing loaded	59
[7]		ω =1500-2500 rpm v =100-500 mm/min	Cylindrical pin(CP) Triangular pin(TP) $D_{shoulder}$ = 12-14 $D_{pin=}$ 4-6 $L_{pin=}$ 3.2	(CP) 240 (TP) 400	Retreating loaded	(CP) 40 (TP) 66

Figure 1-17 shows the reported values of σ_{Lap} (obtained from literature) plotted as function of *h* for FSL welds of AZ31B-H24. Strong dependence of σ_{Lap} on *h* can be seen, however when *h* is small or zero, scatters are large. The macrographs of the welds which have achieved the high σ_{Lap} values of 347 and 400 N/mm are shown in Figure 1-18. The weld shown in Figure 1-18a, with obtained σ_{Lap} value of 347 N/mm, has been tested in advancing loading configuration. Close examination of the hook on advancing side (Figure 1-18b) reveals that the hook has deflected downward from the original lapping interface into the bottom plate. Furthermore, the welds shown in Figure 1-18 c-d, with obtained σ_{Lap} values of 400 N/mm, have been tested in retreating loading configuration. It can be seen that the lapping interface on retreating side has also deflected downward and extended well into the stir zone. However the value of *h* for the welds shown in Figure 1-18 has been reported to be zero [7, 12]. That is due to the common definition of hook size, which specifies the *h* as the distance from original lapping interface to the hook tip at top plate. Thus when the hook was located in bottom plate, for instance those shown in Figure 1-18, *h* has simply been ignored and assumed to be zero, which is confusing.

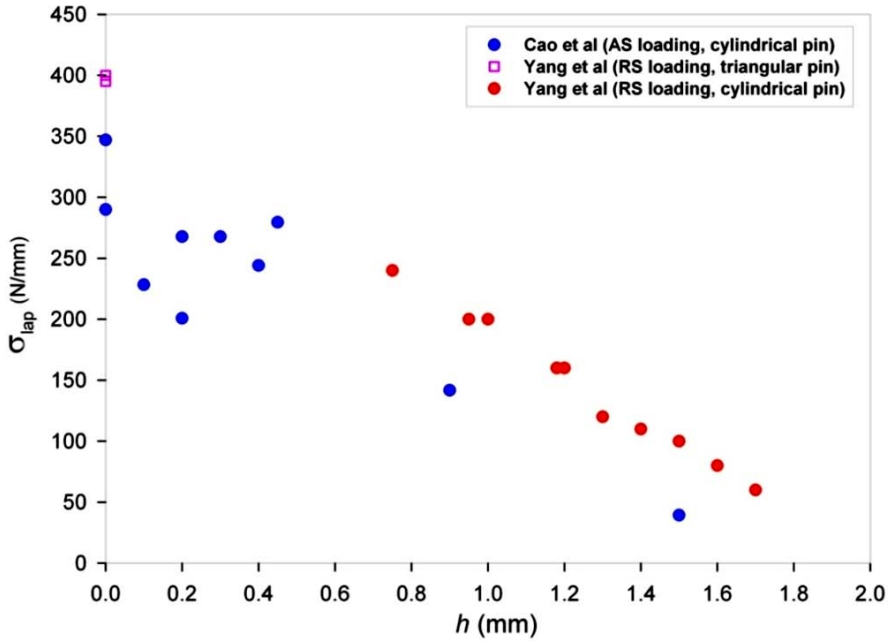

Figure 1-17 σ_{Lap} plotted as function of *h* for FSL welds of AZ31B-H24, data collected from literature [7, 12]

To take into account the presence of hooks when they deflect downward from the lapping interface, *h* is defined as the distance from the lapping interface to the hook tip, as shown in Figure 1-19b. However a minus sign is given to *h* value of downward deflected hooks (hereafter called negative hooks as illustrated in Figure 1-19b) in order to distinguish them from the commonly observed upward deflected hooks (hereafter called positive hooks as illustrated in Figure 1-19a).

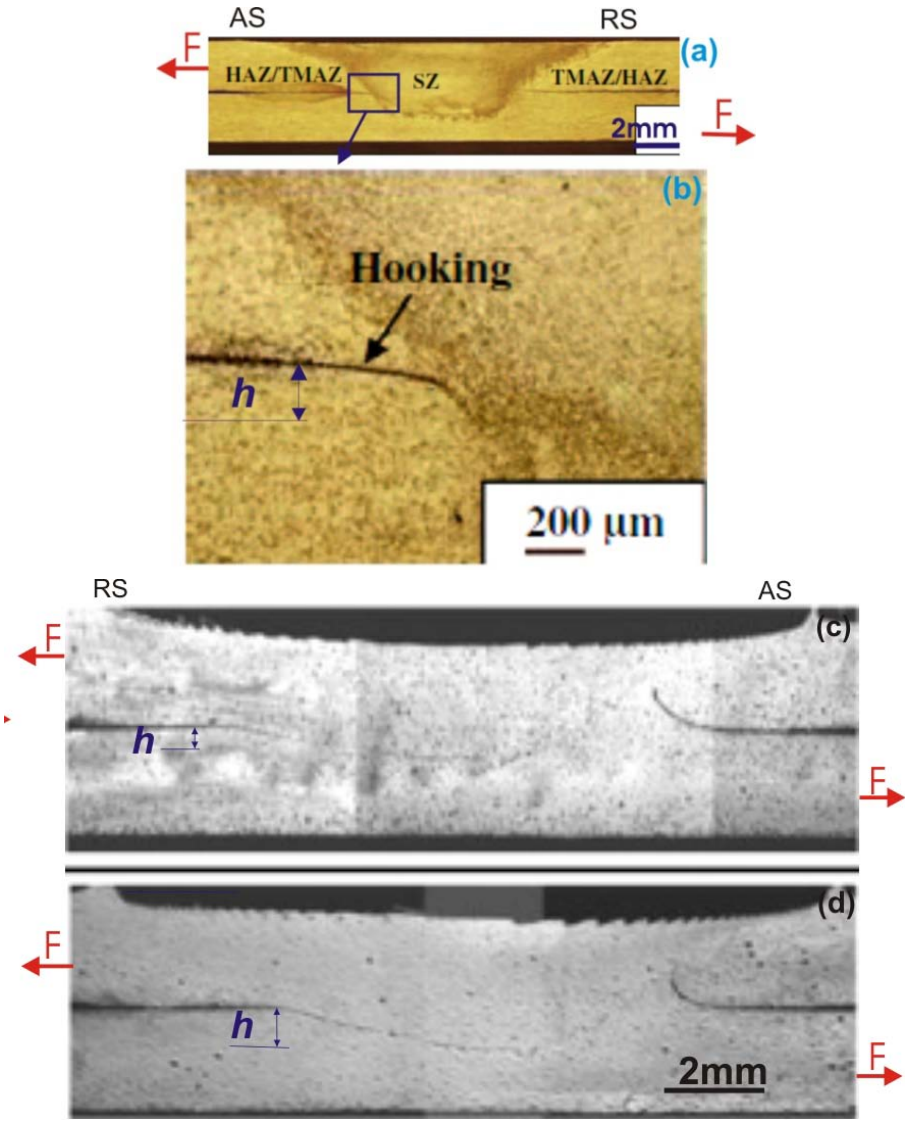

Figure 1-18 Transverse cross section of AZ31 FSL welds: (a) a weld made using ω =1000 rpm, ν =1200 mm/min and cylindrical pin, (b) higher magnification image of hook at advancing side of Figure 1-18a [12], (c) a weld made using ω =2000 rpm, ν =350 mm/min and a triangular pin and (d) a weld made using ω =2000 rpm, ν =500 mm/min and a triangular pin [7]

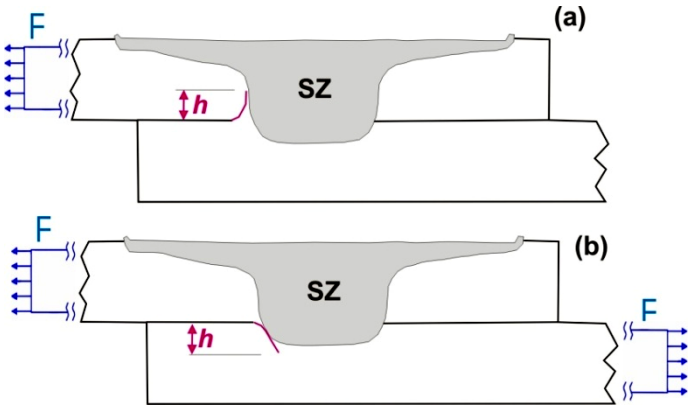

Figure 1-19 Schematic illustration: (a) positive hooking and (b) negative hooking

The reported values of σ_{Lap} has been re-plotted again as function of *h* (Figure 1-20), however the *h* value has been re-measured for the negative hooks shown in Figure 1-18. It can be seen that higher σ_{Lap} values were obtained for the welds which had negative *h* value. In other words, negative hooking resulted in a significant increase of σ_{Lap}. Cao et al [12] suggested that a downward deflected hook profile is likely to cause reduced stress concentration at hook location and thus positively influences the crack propagation during tensile shear testing. However this suggestion is not based on conducting quantitative stress analysis and hence it is not clear how the stress distribution and subsequent crack propagation, during tensile shear testing, is affected by the hook orientation. Therefore, how negative hooking improves the σ_{Lap} of AZ31 welds needs to be further studied.

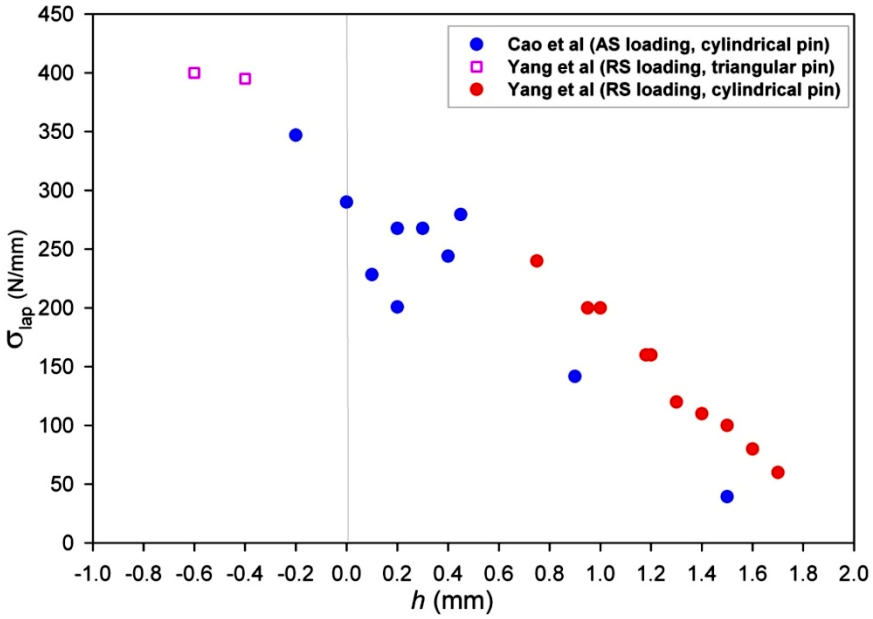

Figure 1-20 σ_{Lap} plotted as function of *h* for FSL welds of AZ31B-H24, with *h* re-measured for the negative hook welds [7, 12]

Furthermore, mechanisms of deformation preceding failure are known to affect the fracture behaviour of a material under loading. An available example of how an AZ31 FSL weld fractures during tensile shear testing is presented in Figure 1-21. It should be noted that tested sample in Figure 1-21a has been loaded in retreating loading configuration. The microstructure of left side of fracture surface (region V in Figure 1-21a) is shown in Figure 1-21b. Intensive twinning is observed immediately next to the fracture surface, and twinning is progressively reduced as the distance from the fracture surface increases. Based on this observation, it has been suggested [7] that plastic deformation was localized when the weld was loaded to failure. However twinning is known to be an important deformation mechanism in plastic deformation of magnesium alloys [43-47] and is not only limited to tensile shear testing of AZ31 welds. Moreover the twin formation in magnesium alloys depends on number of parameters including loading mode, grain orientation, grain size and temperature [44-54], which will be discussed further in the next section.

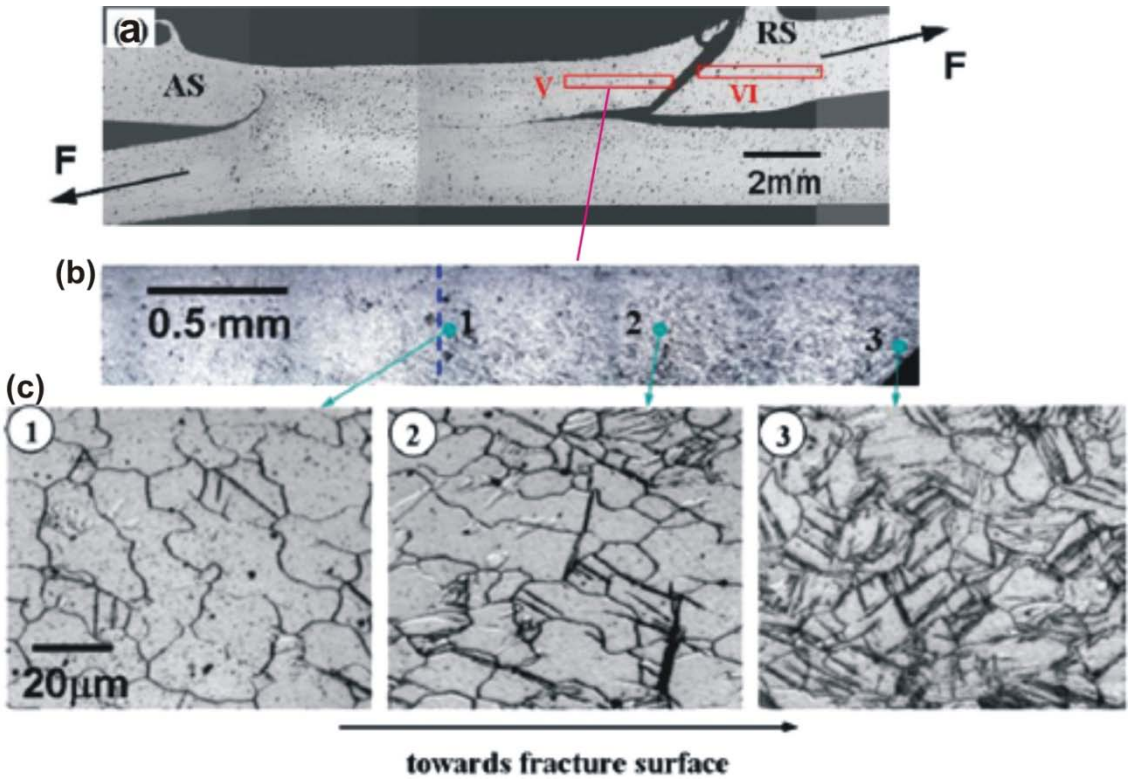

Figure 1-21 Macro and microstructure of a AZ31 FSL weld made using ω =2000 rpm, ν =350 mm/min (a) transverse cross section of the tensile shear tested specimen, (b) microstructure of failed weld near the fracture surface (region V in Figure 1-21a) and (c) micrographs taken as indicated in Figure 1-21b [7]

The microstructural evolution induced by FSLW and also non-uniform stress distribution during tensile shear testing can influence the plastic deformation and thus failure of AZ31 welds. However the current literature lacks the detailed investigation on deformation mechanism during tensile shear testing of magnesium alloys FSL welds. Therefore how the microstructure evolution and non-uniform stress distribution (during testing) affects the plastic deformation and failure of AZ31 welds needs to be studied further.

Deformation mechanism in magnesium alloys, under different loading conditions, have been intensively investigated in literature, however as pointed out by Agnew at al [55] many fundamental questions in relation to plastic deformation of magnesium alloys remain un-answered. In the next section, as it is relevant to this study, a brief review on deformation mechanisms of magnesium alloys at room temperature and how they are affected by the loading mode, grain orientation and grain size viewed necessary and is discussed.

1.3.4 Dislocation Slip and Twinning in Magnesium Alloys

Magnesium has a hexagonal close packed (HCP) crystallographic structure with a c/a ratio of 1.624. The unit cell of magnesium is shown in Figure 1-22. The most important crystallographic planes, which play an essential role in the deformation of magnesium, are the {0001} basal plane, the $\{10\bar{1}0\}$ prismatic plane, the $\{10\bar{1}1\}$ pyramidal plane, and the $\{1\bar{2}12\}$ second order pyramidal plane [56, 57]. All of these planes are illustrated in Figure 1-22. In metals plastic deformation usually occurs by the gliding of dislocations along definite crystallographic planes, called slip planes. The movement of dislocations only occurs once the critical resolved shear stress (CRSS) applied on the slip plane and in the slip direction exceeds a critical value. For magnesium, the movement of dislocations is easiest on basal slip systems at ambient temperature, because they need lowest CRSS to be activated. While basal slip is expected to dominate at room temperature, small amounts of non-basal slip can also occur [47, 49, 58]. With increase of temperature the CRSS for the non-basal slip systems decreases and the prismatic and pyramidal slip systems become more active which results in more ductility of magnesium alloys. Consequently, metal forming of magnesium alloys are mostly carried out at elevated temperatures [58-61].

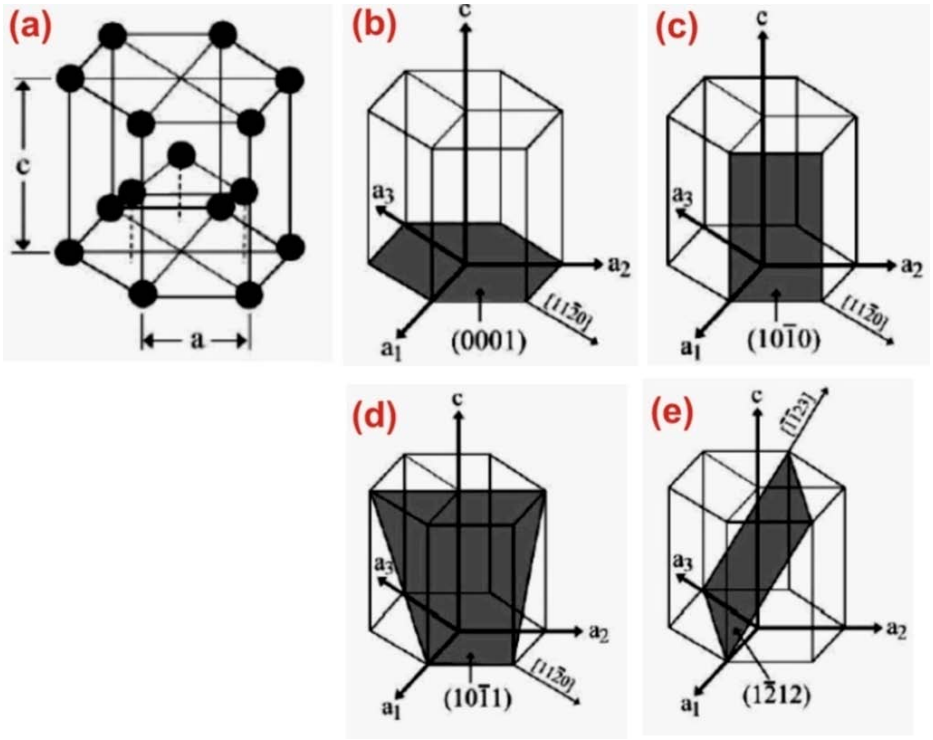

Figure 1-22 Illustration of magnesium slip systems: (a) Magnesium unit cell, (b) basal slip systems, (c) prismatic slip systems, (d) pyramidal slip systems and (e) second order pyramidal slip systems [56]

According to Von Mises criterion, five independent slips are necessary for homogeneous plastic deformation in a polycrystalline material. Metals with face center cubic (FCC) crystallographic structure (such as aluminium), have 12 slip systems, thus can easily satisfy the Von Misses criterion. However magnesium with its HCP crystallographic structure has only two independent slip systems at room temperature, which is insufficient to meet the Von Misses criterion. Under these conditions, dislocation slip cannot continue as the only deformation mode and thus deformation twinning becomes operative [43, 45, 50, 51].

There are two main deformation twin types for magnesium. The first one is the extension twin which occurs on $\{10\bar{1}\,2\}$ plane in $< \bar{1}011 >$ direction (Figure 1-23a) and second one is the contraction twin which occurs on $\{10\bar{1}\,1\}$ plane in $< 10\bar{1}\bar{2} >$ direction (Figure 1-23b). The atoms within a twinned crystal move into their new positions by a process of homogeneous shear parallel to the twinning plane. Thus the twined area is the region of the grain that became reoriented with respect to the matrix grain. Generally extension twins are preferred when there is an extension strain component parallel to the c-axis of crystal or when contraction is being applied perpendicular to the c-axis. Contraction twinning, conversely, it is activated when there

is a contraction strain component parallel to the c-axis or when extension is being applied perpendicular to the c-axis [46, 62].

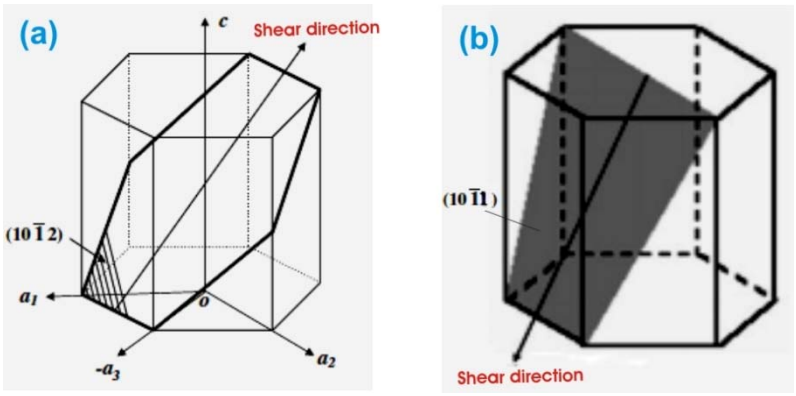

Figure 1-23 Illustration of main twinning systems in magnesium: (a) extension twin and (b) contraction twin [56, 63]

There have been number of studies [44, 45, 52] on twin formation during both compressive and tensile testing of AZ31 alloy. Figure 1-24 shows the microstructure of AZ31 specimens, with large grain size of 70 μm, compressive-deformed to ε=2 and 11% and tensile-deformed to ε=2 and 8%. For the compressive-deformed specimens, many twins with thick-lenticular morphology formed at ε= 2% (Figure 1-24a). Generally the twins with thick-lenticular morphology are recognized as extension twins [45, 46]. However it can be seen that extension twins apparently vanished at ε= 11% during compressive testing and fine recrystallised grained formed (Figure 1-24b). It has been suggested that dynamic recrystallisation at twins may have be responsible for decrease of twins [45, 53].

For the tensile-deformed specimens, there were no twins at ε= 2% (Figure 1-24c) however many narrow banded type twins generated at strain ε= 8% (Figure 1-24d). The twins with narrow banded morphology are generally recognized as contraction twins [43, 45-47]. As no deformation twins formed at an initial stage of tensile test (ε = 2%) hence it has been suggested that dislocation slip was the dominant deformation mechanism during the tensile testing. However formation of extension twins at the early stage of compressive testing (Figure 1-24a) suggest that twin formation was the dominant deformation mechanism during compressive testing [45].

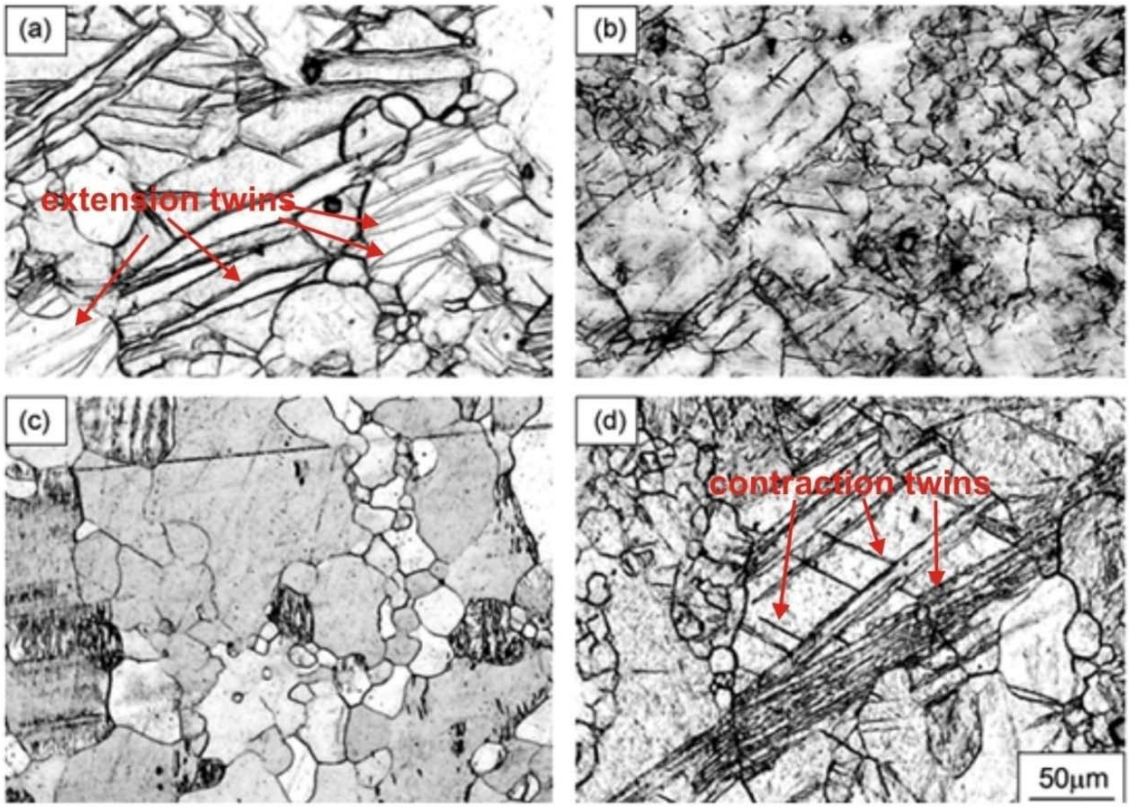

Figure 1-24 Microstructure of the AZ31 specimens with average grain size of 70 μm at (a) ε =2%, compressive deformed, (b) ε =11%, compressive deformed, (c) ε =2%, tensile deformed and (d) ε =8%, tensile deformed [45]

Figure 1-25 shows the microstructure of the AZ31 specimens, with small grain size of 8 μm, compressive-deformed to ε=2 and 20% and tensile-deformed to ε=2 and 20%. It can be seen that there are a few twins even at high strain of 20% for the both tensile-deformed and compressive-deformed samples. Therefore the twin formation was significantly suppressed in the samples with fine grain size. It has been suggested that twin nucleation decreases with decrease of grain size, thus in fine-grained magnesium alloys twinning is decreased and non-basal dislocation slips are instead activated[44, 47]. On the other hand, formation of twins in coarse grain AZ31 specimens (figure 1-24) suggests that deformation mechanism changes from dislocation slip to twinning as the grain size becomes larger.

The stress–strain curves of tensile and compressive tests for the AZ31 specimens of either large grain (70 μm) or small grain (8 μm) is shown in Figure 1-26. For the specimen with large grain size (Figure 1-26a), there is considerable tensile-compressive anisotropy and the tensile yield stress is about three times larger than the compressive yield stress. This anisotropy of mechanical properties is due mainly to a pronounced crystallographic texture of alloy as shown in Figure 1-27. The pole figure shown in

Figure 1-27 indicates that c-axis of grains is mostly parallel to ND (perpendicular to loading direction). It should be noted that similar textures have been reported for the rolled plates of AZ31 alloy [64, 65]. This orientation of grains (Figure 1-27) is highly favourable for extension twinning when compressive load is applied to specimens, resulted in comparably low compressive yield stress [44]. However formed extension twins act as a barrier for dislocation motions, resulting in notable strain hardening [63]. On the other hand, this texture is more favourable for basal slip when tensile load is applied [44]. Therefore it has been suggested that tensile-compressive anisotropy is closely related to the difference in twinning behaviour between tensile and compressive tests[44].

Furthermore it can be seen that the tensile–compressive anisotropy for specimen with small grain size (Figure 1-26b) has considerably reduced. This has been attributed to the effect of grain refinement on suppression of twinning which otherwise cause tensile-compressive anisotropy [44, 63].

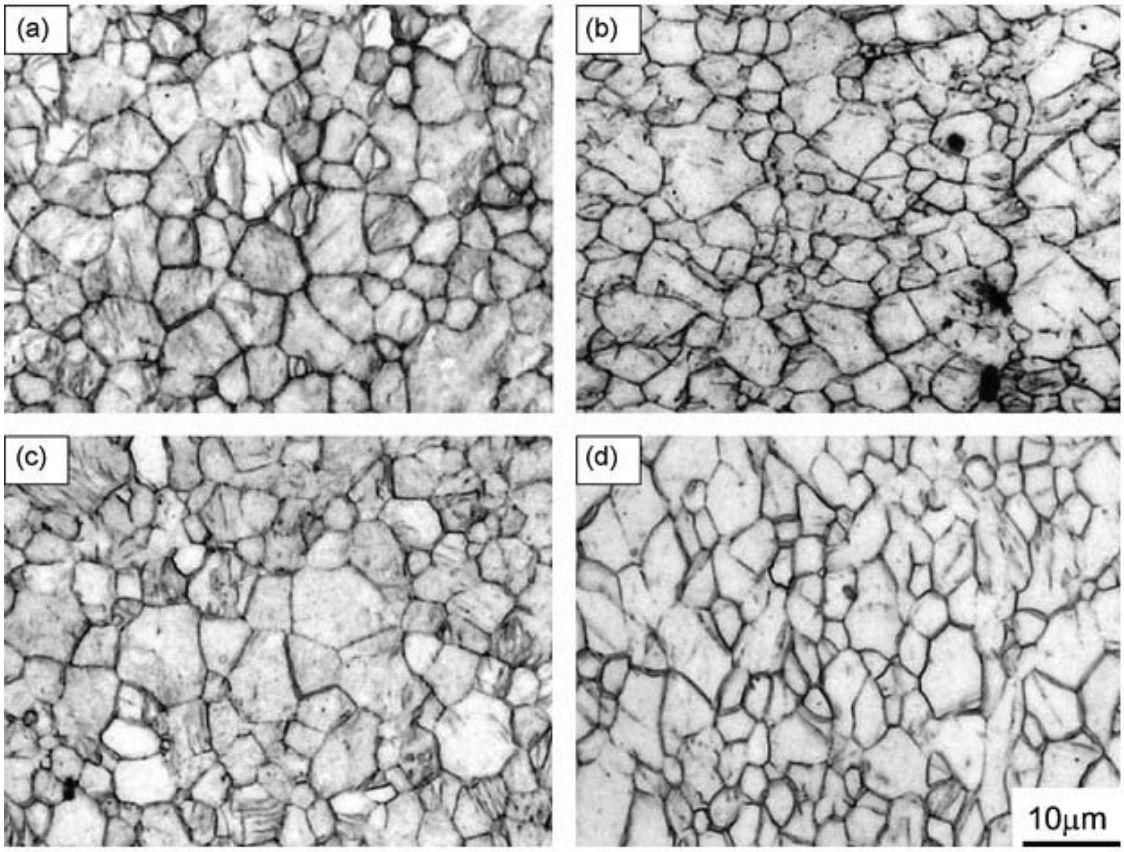

Figure 1-25 Microstructure of AZ31 specimens (with average grain sizes of 8μm) at (a) ε =2%, compressive deformed, (b) ε =20%, compressive deformed, (c) ε =2%, tensile deformed and (d) ε =20%, tensile deformed [45]

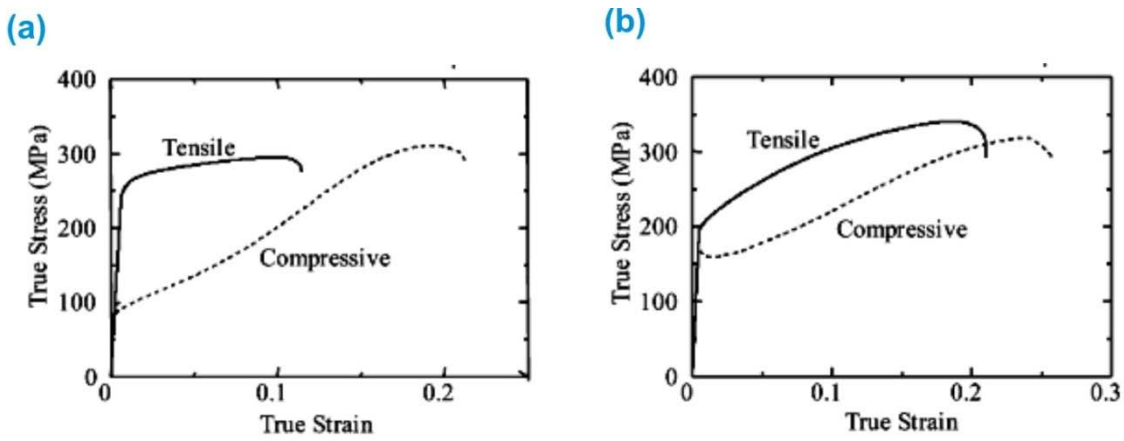

Figure 1-26 True stress-strain curves by the tensile and compressive tests for (a) specimen with large grain size of 70 μm and (b) specimen with small grain size of 8 μm [45]

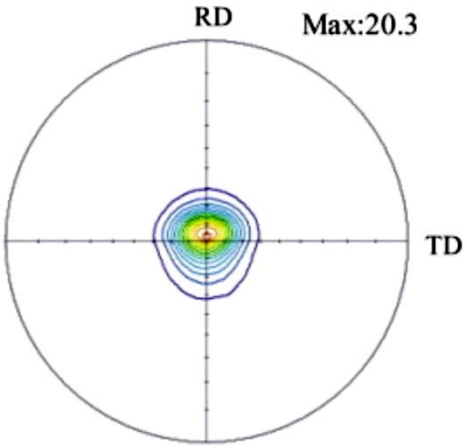

Figure 1-27 (0002) pole figure for rolled AZ31 specimens [44]

In summary, the brief review given above demonstrates that deformation mechanism (either dislocation slip or twinning) and mechanical behaviour of AZ31 alloy are strongly affected by number of parameters including crystallographic texture, grain size and loading direction. Therefore as described earlier, the microstructural evolution induced by FSLW (which alters the original material microstructure), and also non-uniform stress distribution during tensile shear loading (which varies across the welded specimen), is expected to affect the plastic deformation and failure of AZ31 welds and thus warrants further study.

1.4 FSLW of Dissimilar Materials

In this section, a detailed review on microstructure of interface region and fracture strength of Al/Steel FSL welds is given first. Then interface microstructure and fracture strength of Al/Ti FSL welds is presented. These two interface couples are representatives of FSLW of joint couples with large melting point difference and joint established by diffusion.

1.4.1 FSLW of Aluminium alloys to Mild Steels

There have been a number of studies on FSLW of Al/Steel [8, 27, 66-69]. Brief descriptions of FSLW conditions and maximum achieved σ_{Lap} (reported in literature) are given in Table 1-4. Early investigation by Elrefaey et al [27] on Al/Steel FSLW clearly established that the tool pin slightly (~0.1 mm) penetrating to steel is a condition for a metallurgical joint to be established at the Al/Steel interface, resulting in a good joint strength. Although detailed quantification was not done in their study, it was clear from their micrographs (as shown in Figure 1-28) that the interface region of welds made with pin penetration is a highly irregular structure of mix layers.

Table 1-4 Summary of the FSLW conditions with maximum σ_{Lap} achieved for Al/Steel FSL welds (data collected from literature)

Ref.	Base metals	Welding speeds	Pin dimension (mm)	Maximum σ_{Lap} (N/mm)
[27]	Al 1100 : low carbon steel (2 mm :1.2 mm)	ω=1000 - 2500 rpm v =200- 300 mm/min	$D_{shoulder}$ = 10mm $D_{pin=}$ 3 mm $L_{pin=}$ 2.1 mm	102
[66]	AC4C cast Al : low carbon steel (3 mm : 0.8 mm)	ω=800 rpm v =80 mm/min	$D_{shoulder}$ = 15 mm $D_{pin=}$ 5 mm $L_{pin=}$ 2.8 mm	163
[67]	AC4C cast Al : zinc-coated carbon steel (3 mm : 0.8 mm)	ω=1500 rpm v =60-120 mm/min	$D_{shoulder}$ = 15 mm $D_{pin=}$ 5 mm $L_{pin=}$ 2.8 mm	251
[68]	Al 5083 : SS400 steel (3 mm : 3 mm)	ω=225 - 1240 rpm v =24 - 85 mm/min	$D_{shoulder}$ = 20 mm $D_{pin=}$ 5 mm $L_{pin=}$ 3.1-3.4 mm	559
[8]	Al 6181-T4 : HC340LA steel (1.5 mm : 1.5 mm)	ω=1600 rpm v =180 mm/min	$D_{shoulder}$ = 13 mm $D_{pin=}$ 5 mm $L_{pin=}$ 1.6 mm	-
[69]	Al 5083 : St-12 (3 mm : 1.0 mm)	ω=750-1125 rpm v =70-230 mm/min	$L_{pin=}$ 3.1 mm	304

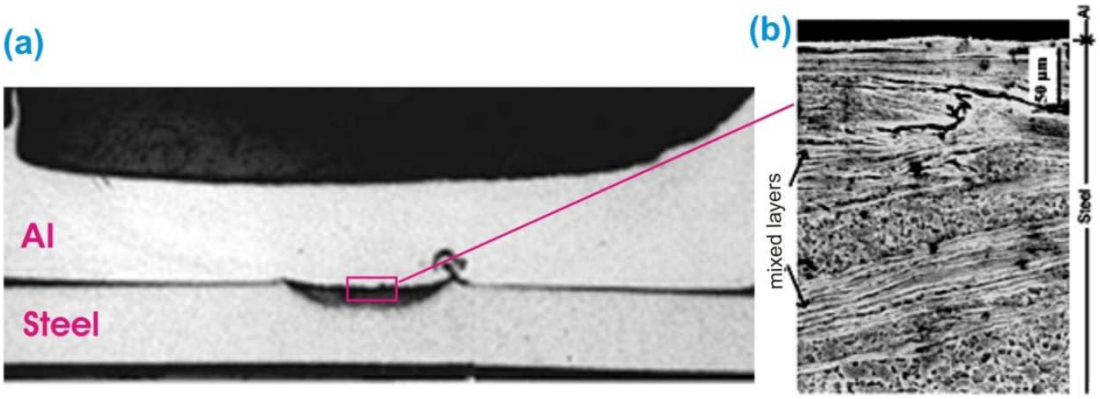

Figure 1-28 Macro/microstructure of an Al/Steel FSL weld, made using ω =2500 rpm and *v* =200 mm/min: (a) optical macrograph and (b) SEM image showing a highly irregular structure of mix layers [27]

Elrefaey et al [27] have suggested that intermetallic compounds Fe_2Al_5 and Fe_4Al_{13} formed at the mixed layers, based on X-ray diffraction patterns obtained from the fracture surfaces of tested samples, as shown in Figure 1-29. However it may view uncertain to identify structures using X-ray diffraction patterns of fracture surfaces where peaks from Fe-Al compounds are low in intensity and also many peaks may have overlapped.

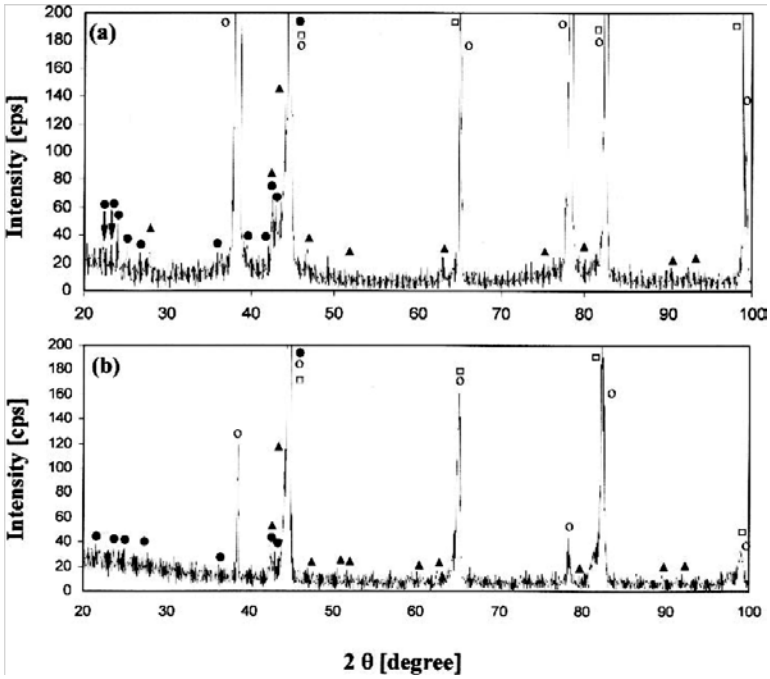

Figure 1-29 XRD patterns from fracture surfaces of a tensile shear tested Al/Steel FSL weld, (a) aluminum side and (b) steel side. Diffraction lines from Al, Fe, Al_5Fe_2,and $Al_{13}Fe_4$ were indicated by ○, □, ▲ and ● respectively

In the detailed analysis of Al/Steel welds made using FSLW with the condition of pin penetration, Coelho et al [8] names the irregular interface region as mixed stir zone. The thin layers, significantly less than 0.5 μm in thickness are laminated with recrystallised fine grains of α-Fe in this mixed stir zone, as shown in Figure 1-30b. An example of point analysis by TEM/EDS analysis (65.6at%Al and 33.0at%Fe, plus minor elements) may indicate that the thin layers are mainly $FeAl_2$ intermetallics, according to Al-Fe phase diagram (Figure 1-31).

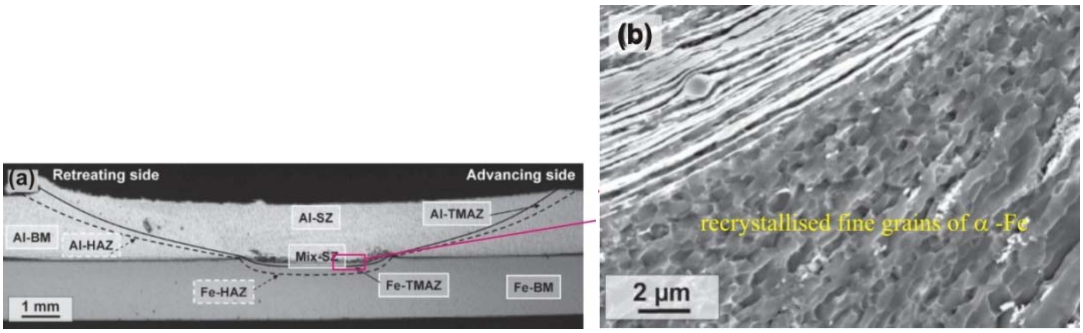

Figure 1-30 Microstructure of an Al/Steel FSL weld made using ω =1600 rpm and *v* =180 mm/min: (a) optical macrograph and (b) SEM image showing a highly irregular structure of mix layers laminated with recrystallised fine grains of α-Fe [8]

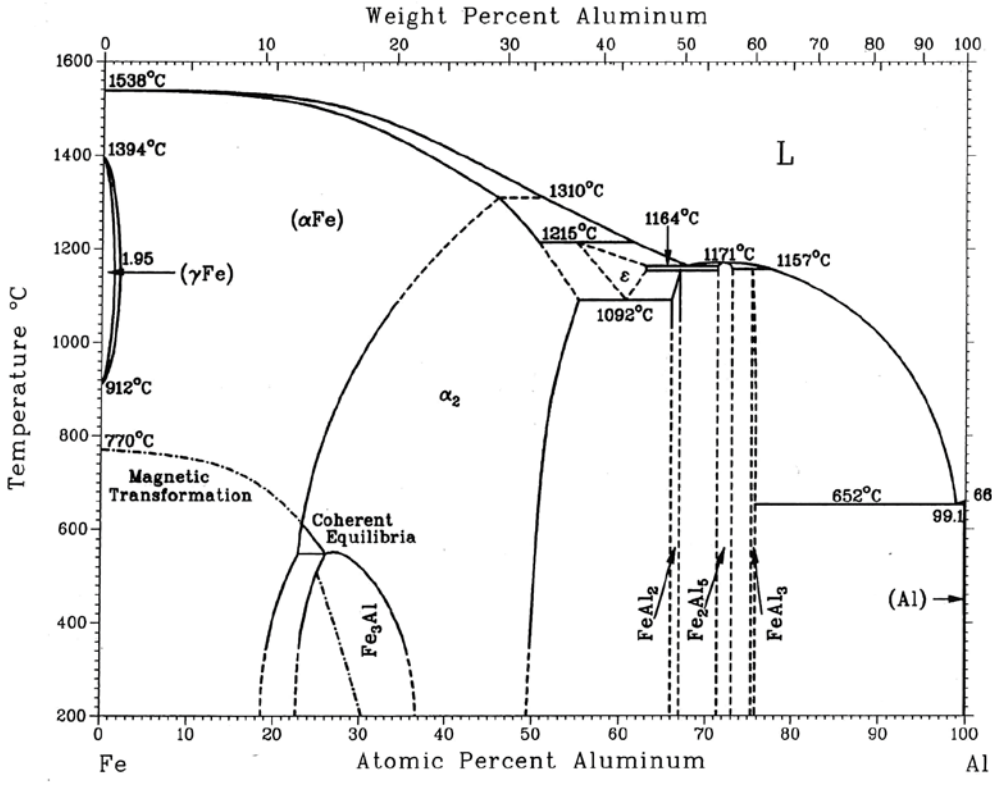

Figure 1-31 Binary alloy phase diagram of Al-Fe [70]

Early work by Kimapong et al [28, 68] was an attempt to correlate the σ_{Lap} to the thickness of the intermetallic layer, under the condition of pin penetration. Their data shows that in general increasing intermetallic compound thickness reduces σ_{Lap}, however the meaning of the referred intermetallic thickness is unclear and misleading. The micrograph of their welds (Figure 1-32a) clearly illustrates that the microstructure in the interface region is highly mixed. The irregular interface structure, with the absence of a single and uniform intermetallic layer to be measured, is in common to those observed earlier (Figure 1-28 and 1-30) when the condition of pin penetration was used. Furthermore, Kimapong et al [28, 68] reported that $FeAl_3$ and $FeAl_5$ formed at the interface region, based on SEM/EDS spot analysis. However it should be pointed out that assigning the structure of $FeAl_2$ or Fe_2Al_5 or $FeAl_3$ to a mixed region relying on SEM/EDS is not reliable due to the analytical spot size being large in SEM/EDS.

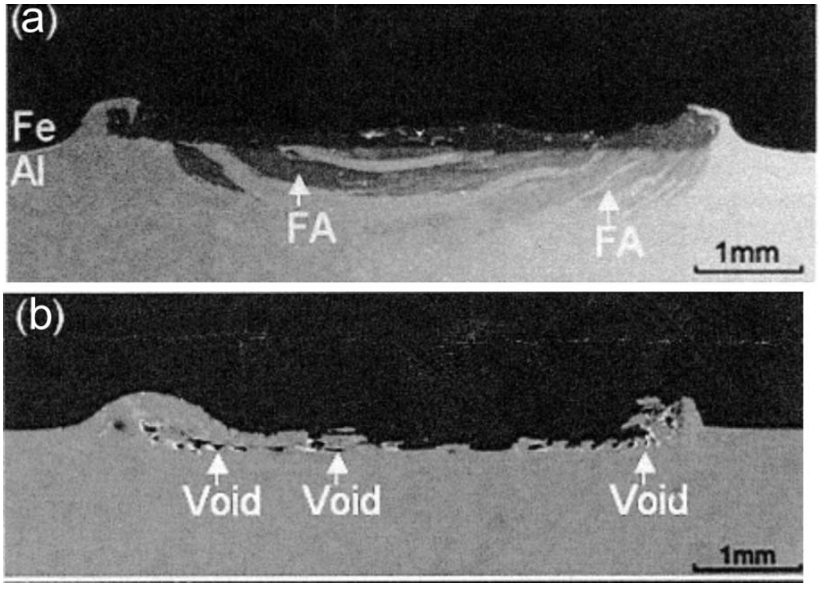

Figure 1-32 Cross sections of Al/Steel FSL welds made using (a) ω =1240 rpm and *v* =80 mm/min, (b) ω =225 rpm and *v* =45 mm/min [68]

In most studies on FSLW of Al/Steel, tensile shear testing has been used for evaluating the joint strength. Kimapong et al [68] reported σ_{Lap} values, ranging from 280 N/mm to 559 N/mm for a wide range of FSLW and pin penetrating conditions. However the reason is unclear as to why some of their welds displaying severe discontinuity with voids along the interface region (such as micrograph shown in Figure 1-32b), exhibited high values of σ_{Lap} (400 to 500 N/mm).

Chen et al [66] reported σ_{Lap} equal to 163 N/mm for Al/steel FSL weld when the pin did not penetrate to steel (bottom of pin was ~ 0.2 mm above the steel surface during FSLW). This is a very low σ_{Lap} value and from their micrographs (Figure 1-33c) a continuous bond in Al/Steel interface cannot be confirmed. However, metallurgical bonding was ensured when Zinc-coated steel was used, increasing σ_{Lap} to 251 N/mm (Figure 1-33d).

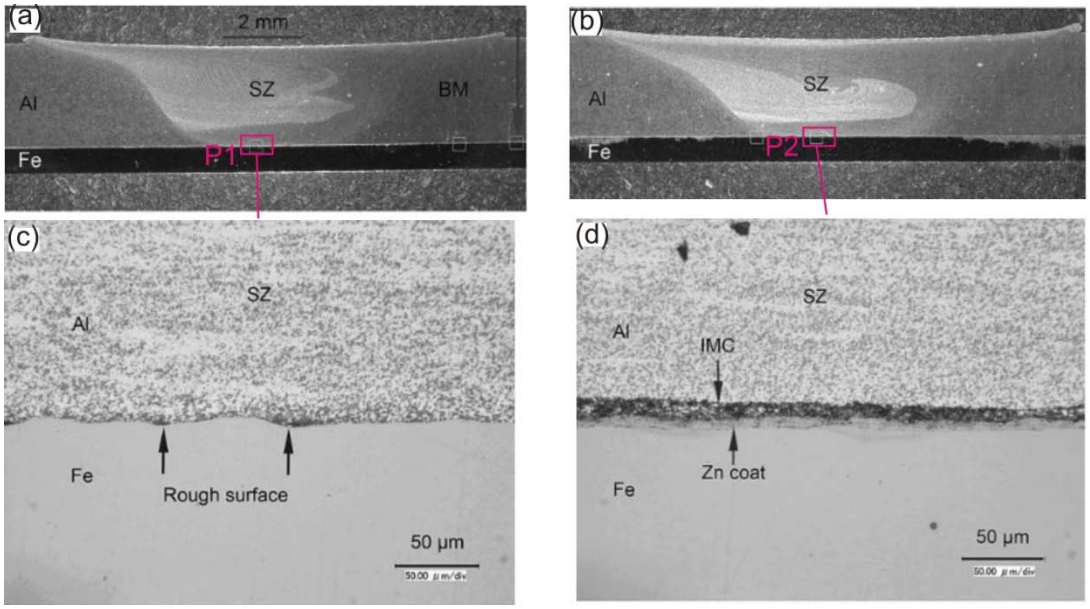

Figure 1-33 Cross sections of Al/Steel FSL welds made using ω =800 rpm and *v* =80 mm/min: (a) optical micrograph of weld made using uncoated steel, (b) optical micrograph of zinc-coated steel, (c) SEM image of region P1 in Figure 1-33a and (d) SEM image of region P2 in Figure 1-33b [66]

More recently, Movahedi et al [69] conducted Al/Steel FSLW experiments with pin sufficiently penetrated to steel and over a wide range of speed conditions. Their samples clearly showed mixed stir zones at the interface region. Their maximum σ_{Lap} value reached 304 N/mm for samples fractured along the joint interface.

Review of maximum attained σ_{Lap} values reported in literature (as summarised at Table 1-4) reveals that σ_{Lap} values differ substantially from one study to another. The reason for this is unclear as the relationship between Al/Steel interface structures, which is FSLW condition dependent, and the corresponding σ_{Lap} values is not understood well.

In the FSLW studies cited above [8, 27, 28, 68, 69] formation of Fe_2Al_5, $FeAl_3$ or both in welds were suspected to cause σ_{Lap} reduction, although pin penetrating condition for obtaining metallurgical bonding (through intermetallic formation) is also recognised as a condition for weld strength. However as has been explained, structure identification of Fe_2Al_5 and $FeAl_3$ in welds made using FSLW up to now may not be sufficiently reliable. Therefore it is not clear how the presence of intermetallics in Al/Steel interface region actually affect fracture behaviour and σ_{Lap} of welds. It should be pointed out that although Fe_x-Al_y intermetallic compounds are generally known to be brittle at room temperatures [71, 72], the hardness and ductility of these intermetallic phases is not the same [72, 73]. Therefore fracture behaviour and σ_{Lap} of welds can also be influenced by type of intermetallic compounds formed at the interface region.

Furthermore as has been explained, the pin penetration to steel appears to be accepted as a condition for promoting σ_{Lap} of Al/Steel FSL welds [8, 27, 28, 68, 69]. Thus the examination on Al/Steel interface structures and the corresponding σ_{Lap} values, for tool positioning so that the bottom of the pin very close to or in contact (without penetrating) with the lower steel plate (during FSLW) has not been explored and needs to be investigated further.

1.4.2 FSLW of Aluminium Alloys to Titanium Alloys

Recently there has been a number of studies on FSLW of Al/Ti [10, 74] . Brief descriptions of FSLW conditions and maximum achieved σ_{Lap} are given in Table 1-5. Early investigation on feasibility of Al/Ti FSLW was conducted by Chen and Nakata [10] and micrographs of their welds are presented in Figure 1-34. It can be seen that when the pin penetrated to the titanium plate (Figures 1-34 and 1-34b), the stir zone near Al/Ti interface exhibited a mixture of aluminium and titanium particles pulled away from the titanium surface by the tool stirring effect. Moreover, many void defects formed at the side of titanium because of insufficient flow behaviour of titanium during FSLW. However when the pin did not penetrate the titanium plate (as indicated in Figures 1-34d and 1-34e) the joint exhibited high σ_{Lap} value of 469 N/mm. All the welds fractured along the Al/Ti interface during tensile shear testing, as shown in Figures 1-34c and 1-34f.

Table 1-5 Summary of the FSLW conditions and maximum σ_{Lap} achieved for FSL welds of A/Ti (data collected from literature)

Ref.	Base metal	Welding speeds	Pin dimension (mm)	Maximum σ_{Lap} (N/mm)
[10]	Cast Al ADC12 : pure titanium (4 mm : 2 mm)	ω=1500 rpm v =60,90,120 mm/min	$D_{shoulder}$ = 15mm $D_{pin=}$ 5 mm $L_{pin=}$ 4 mm	469
[74]	LF6 Al alloy : Ti-1.5Al-2Mn alloy (2 mm : 2 mm)	ω= 600, 950,1500 v = 60-150 mm/min	$D_{shoulder}$ = 15mm $D_{pin=}$ 4 mm $L_{pin=}$ 2.1 mm	224

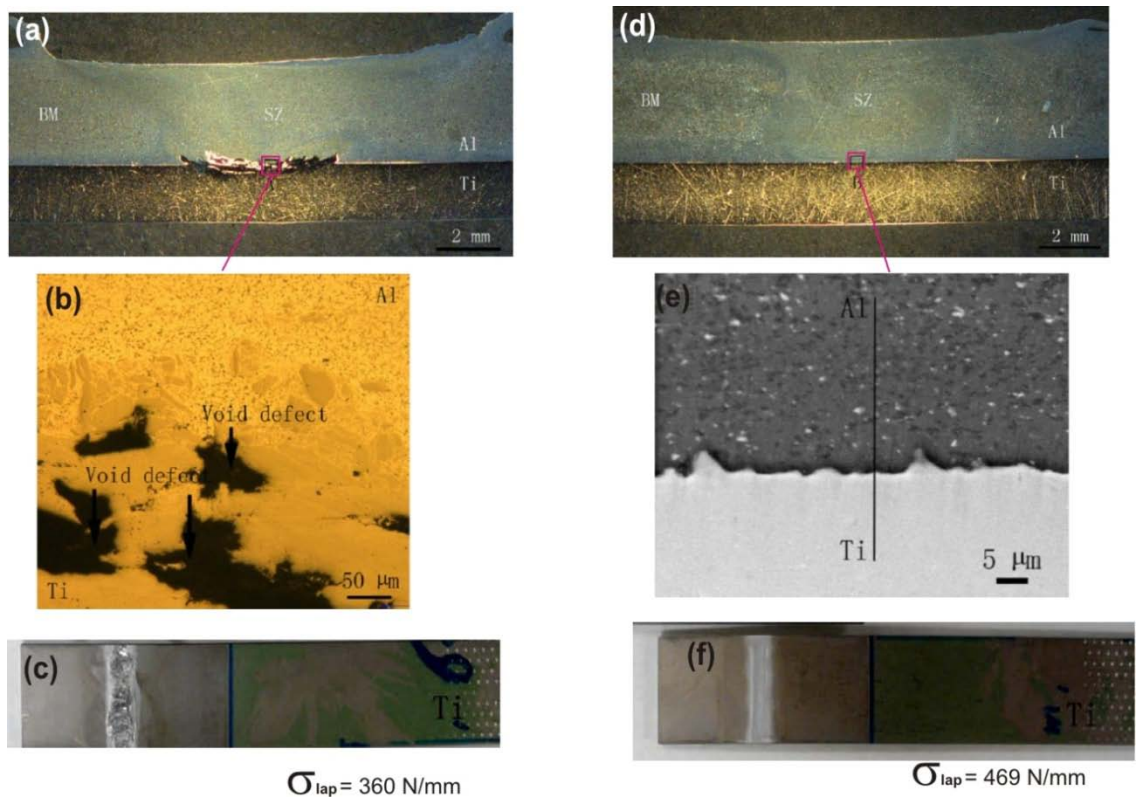

Figure 1-34 Macro/microstructure of Al/Ti FSL welds made using ω=1500 rpm and: ν =60 mm/min, (a) macrograph (b) microstructure of interface region (c) image of fractured tensile shear tested specimen. ν =90 mm/min: (d) macrograph (e) SEM image of interface region (c) image of fractured tensile shear tested specimen [10]

The achieved high σ_{Lap} value of 469 N/mm indicates the formation of strong bonding at Al/Ti interface. Chen and Nakata [10] suggested that $AlTi_3$ intermetallic phase formed at the interface region, based on x-ray diffraction patterns (Figure 1-35) obtained from the fracture surfaces of tested samples. However their results may not be accurate as no visible intermetallic layer can be seen in SEM micrograph of the interface region (Figure 1-34e).

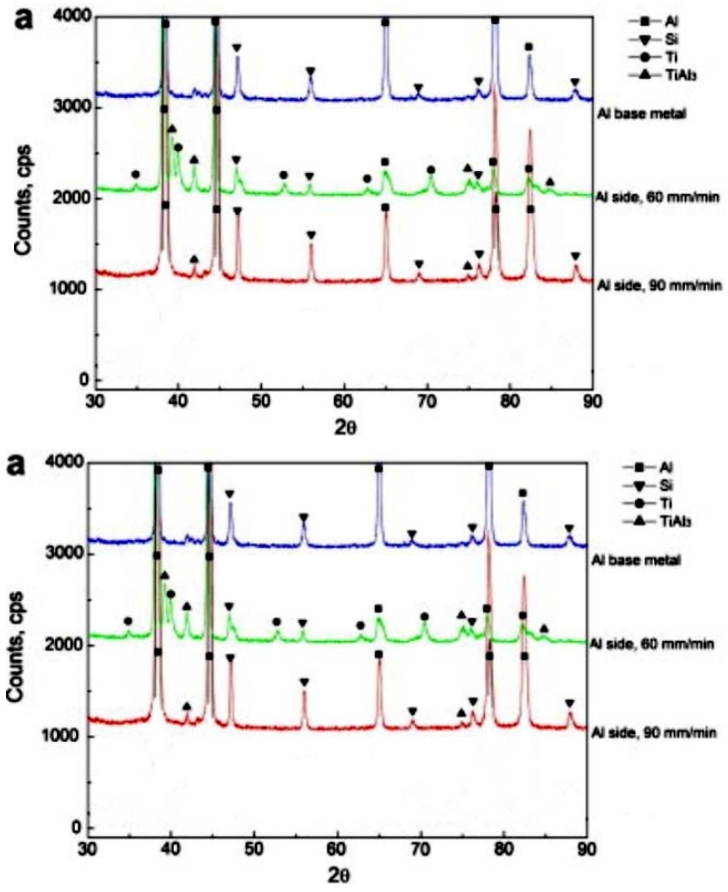

Figure 1-35 XRD patterns from different fracture surfaces of Al/Ti FSL welds: (a) from Al side and (b) from Ti side [10]

Further to formation of $AlTi_3$ at the Al/Ti interface, it has been suggested [9, 10] that aluminium metal is pushed into concavities of titanium surface (by the stirring action of rotating pin) resulting in formation of micro-mechanical bonding at the interface. However the contribution of this so-called micro-mechanical bonding to σ_{Lap} of welds is not clear.

More recently, Chen et al [74] conducted Al/Ti FSLW experiments using pin penetration condition. Although detailed quantification was not completed in their study, it can be seen from their micrographs (Figure 1-36) that the interface region of welds is a highly irregular structure of mix layers. An example of point analysis by SEM/EDS analysis (58.9at%Al and 41.1at%Ti) may indicate that the thin layers are mainly Ti_3Al_5 intermetallics, according to Al-Ti phase diagram (Figure 1-37). However assigning the structure of either Ti_3Al_5 or $AlTi_3$ to a mixed region relying on SEM/EDS is not reliable due to the analytical spot size being large in SEM/EDS. Also a number of micro-cracks can be seen in the interface region of the welds (Figures 1-36b and 1-36d). All their samples fractured along the Al/Ti interface region and their maximum σ_{Lap}

value reached 224 N/mm which is significantly lower than the σ_{Lap} value (469 N/mm) reported by Chen and Nakata [10] made using non pin penetrating condition.

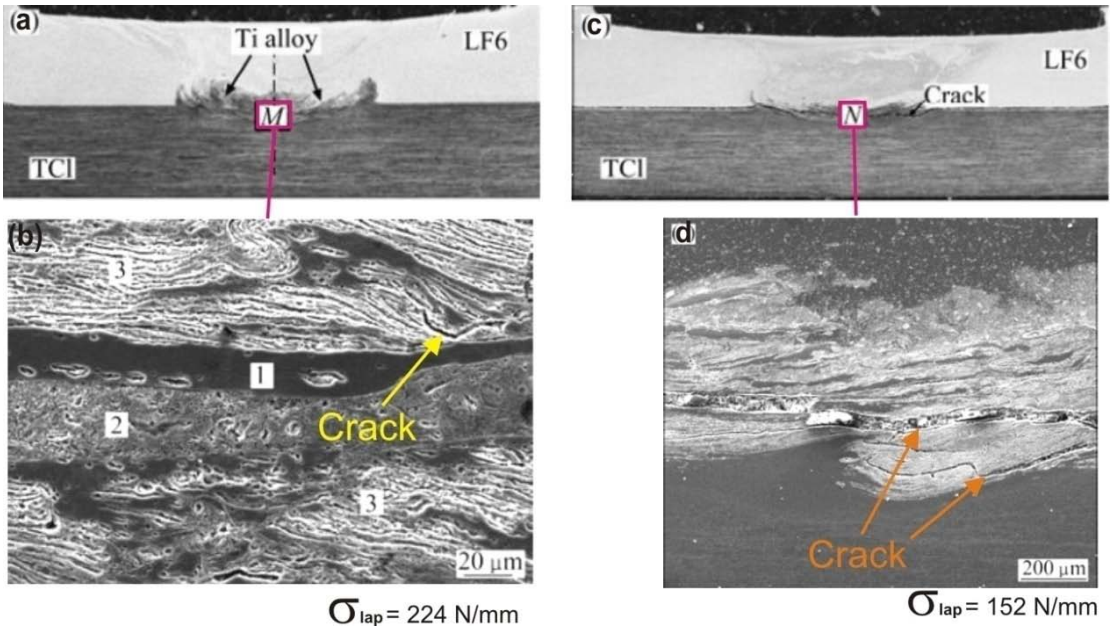

Figure 1-36 Macro/microstructure of Al/Ti FSL welds made using ω=1500 rpm and: ν =60 mm/min, (a) macrograph, (b) microstructure of interface region. ν=150 mm/min, (c) macrograph, (d) microstructure of interface region [74]

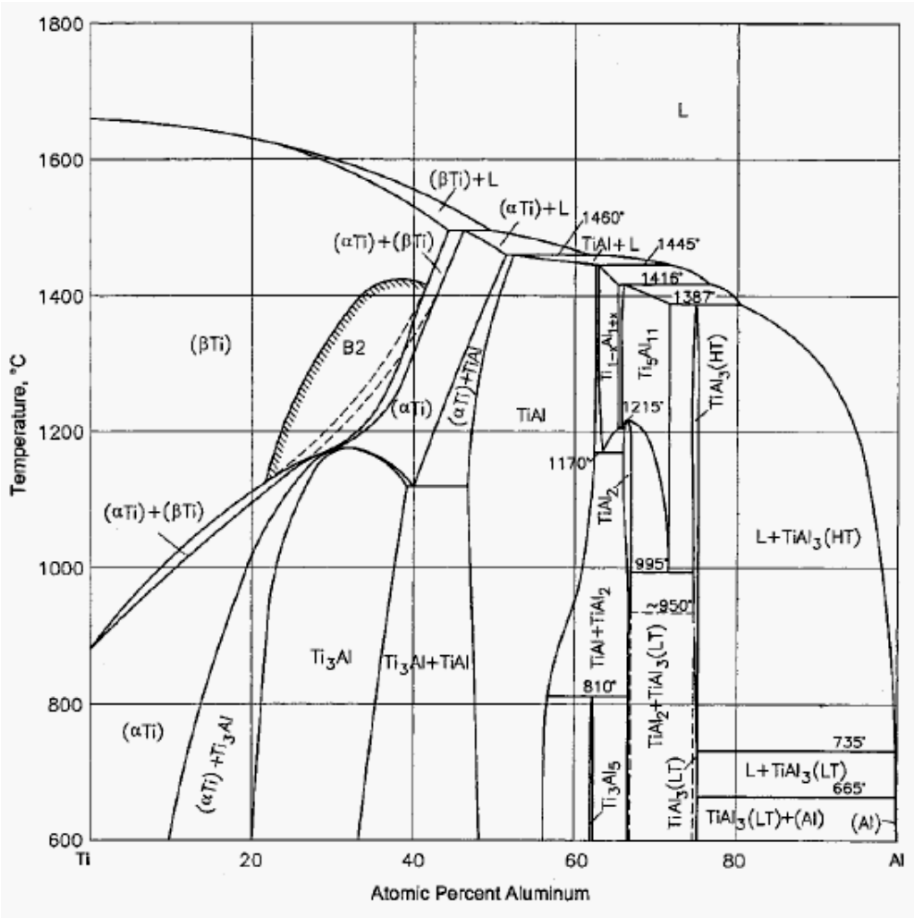

Figure 1-37 Al-Ti binary phase diagram [75]

The considerable difference in maximum σ_{Lap} values reported by Chen and Nakata (469 N/mm) and Chen et al (224 N/mm), and also a comparison of their corresponding micrographs in Figure 1-34e with Figure 1-36b, suggests that difference in interface structures of these welds is the reason for variation of σ_{Lap} values. However, details of how Al/Ti interface microstructure relate to the fracture behaviour and strength of welds have not been given.

Review of literature on other solid-state joining techniques such as diffusion bonding [76] and friction welding [76-80] shows that $TiAl_3$ intermetallic layer formed at the Al/Ti interfaces. However the intermetallic layer has been reported to be very thin (less than one micron) due to insufficient thermal energy for intermetallics growth. On the other hand, formation of several micron thick $TiAl_3$ intermetallic layers has been commonly observed in fusion welding of Al/Ti welds [81, 82]. That is because fusion welding techniques are all conducted at temperatures above the melting point of aluminium, and thus higher peak temperature of welding together with presence of liquid aluminium enhance the diffusion rate of Al-Ti atoms and thus faster growth of intermetallic layer. Therefore formation of $TiAl_3$ phase at the Al/Ti interface is widely recognised to provide metallurgical bonding in Al/Ti joints.

Furthermore, $TiAl_3$ intermetallic phase is commonly known to be brittle [83], however it has been reported that the detrimental influence of $TiAl_3$ intermetallic phase on joints mechanical properties only becomes apparent when a critical intermetallic layer thickness is exceeded [78, 84]. This critical thickness reported to be 5 μm for the Al/Ti joints made using friction welding [84], based on a comparison of as welded and post-weld heat treated joint samples.

1.5 The Scope of the Present Research

It is clear from the above literature review that in FSLW of aluminium alloys, a detailed thermomechanical explanation (supported by corresponding experimental data) on how process speeds (ω, v) relates to hooking has not been fully given. The relative role of hooking and softening (affected by the FS heat) on fracture behaviour of welds is not clear. The quality of hook (actual shape and continuity of hook, rather than just the vertical distance) has not been described and how it affects σ_{Lap} has not been

considered. Furthermore the state of stress distribution in tensile shear specimens (under loading) has been unclear and thus the effect of stress distribution on fracture behaviour of aluminium FSL welds is not understood.

For FSLW of magnesium AZ31 alloy, whether the hook formation and quality of hooks (shape and continuity) would differ from those in aluminium FSL welds is not clear in literature. It is not clear however why the joint efficiency of AZ31 FSL welds is generally lower than that of aluminium FSL welds. How the hook orientation and subsequent stress distribution, during tensile shear testing, affects the fracture behaviour of AZ31 FSL welds has not been described. Furthermore, the effect of tensile shear loading on local plastic deformation and fracturing is not understood.

For dissimilar FSLW of aluminium to steel alloys (Al/Steel) and aluminium to titanium alloys (Al/Ti), how the microstructure of the interface region is affected by the various pin positions in relation to bottom plate (of either steel or titanium) during FSLW, may been seen insufficiently understood. More importantly how the joint interface structures are related to the fracture behaviour and thus σ_{Lap} of FSL welds remains unclear and needs to be clarified.

Thus, the overall aim of the present research is to more systematically study and understand the thermomechanical and metallurgical phenomena relating to FSLW and how the various joint features affect the fracture strengths of the welds. More specifically, the objectives of present research are:

A. In FSLW of aluminium alloy 6060-T5, the quantitative effects of ω and v on material flow volumes related to hooking and temperature of SZ (during FSLW) will be investigated to obtain a more detailed thermomechanical explanation on effect of process conditions on *h*. Relative role of hooking and softening on fracture behaviour will be studied through examination of the ways that tensile shear samples fracture under loading. The role of hook shape and continuity on σ_{Lap} will also be evaluated. Furthermore, the effect of lap joint geometry on the state of stress distribution, under loading, will be numerically analysed and its effect on fracture behaviour and thus σ_{Lap} will be studied.(chapter 3)

B. In FSLW of magnesium alloy AZ31B-H24, hook formation and quality of hooks will be examined and results will be compared with those obtained in FSLW of aluminium alloy 6060-T5. Also the mechanical performance of AZ31 welds, under tensile shear loading, will be compared with those of Al 6060-T5 welds. Numerical modelling and artificial hook testing experiments will be conducted to investigate the effect of hook orientation on stress distribution and fracture behaviour of AZ31 specimens, during tensile shear testing. Effects of tensile shear loading on activation of deformation twinning and in turn fracturing and σ_{Lap} will be studied. (chapter 4)

C. In dissimilar FSLW of Al/Steel and Al/Ti, microstructures of the interfacial region affected by various pin positions will be characterized. Two special force monitored FSLW experiments will be conducted where the tool pin could be positioned to contact without penetrating the bottom plate (steel or Ti6Al4V). Through tensile shear testing and analysis of fracture surfaces, the effects of pin position dependent interfacial microstructures on fracture and on σ_{Lap} of welds will be studied and clarified.(Chapter 5)

2. Experimental Design and Procedures

In this chapter, the three large series of FSLW studies are first outlined. Then FSLW conditions and monitoring systems are described in detail followed by the description of metallurgical examination and analysis. This is followed by describing testing methods for evaluation of mechanical properties. Finally the description of finite element method analysis used is explained.

2.1 Outline of FSLW Experiments

Three series of FSLW experiments were conducted in the present study. Summary of materials and workpiece dimensions used in each series is given in Table 2-1. In series 1 and 2, FSLW experiments were conducted on aluminium alloy 6060-T5 and magnesium alloy AZ31B-H24, respectively. Series 3 experiments involved FSLW of dissimilar materials of Al 6060-T5 to mild steel and Al 6060-T5 to Ti6Al4V. In series 3 experiments, the use of sufficiently thick top plate (6 mm) was to prevent fracturing in HAZ of Al 6060-T5 (top plate) during mechanical testing. The nominal chemical compositions of all materials used in FSLW experimental series are presented in Table 2-2.

Table 2-1 Summary of material types and workpiece dimensions used in FSLW experimental series

Series	Materials	Top plate thickness (mm)	Bottom plate thickness (mm)	Plate dimensions (mm)
1	Al 6060-T5 to Al 6060-T5	3	3	240 x 100
2	AZ31B-H24 to AZ31B-H24	2.5	2.5	240 x 100
3	Al 6060-T5 to mild steel	6	2	240 x 100
	Al 6060-T5 to Ti6Al4V	6	2.5	240 x 100

Table 2-2 Nominal chemical composition of materials used in FSLW experiments

Alloy	Al %	Zn %	Si %	Mg %	V %	Fe %	Ti %	C %	Mn%
Al 6060-T5	Bal.	0.15	0.35	0.35-0.6	0.3-0.6	0.1-0.3	0.05	-	0.1
AZ31B-H24	2.5-3.5	0.7-1.3	0.05	Bal.	-	0.005	-	-	0.2
mild steel	-	-	0.35	-	-	Bal.	-	0.15	1
Ti6Al4V	5.5-6.7	-	-	-	3.5-4.5	0.25	Bal.	0.08	

2.2 FSLW Experimental Set up, Conditions and Monitoring Systems

2.2.1 FSW Machine and Clamping System

A retrofitted Lagun milling machine was used for all the FSLW experiments. Rotation and linear speed were controlled by step increments. To restrain the thermal expanding and thus bulking behaviour of plates, which could otherwise be encountered during normal FSLW conditions, a bolted clamping system (as shown in Figure 2-1), was used in all experiments. A support plate (of the same thickness of bottom plate) was placed underneath the top plate. This support plate is referred to as “lower support plate” in Figure 2-1. Also a support plate (of the same thickness of top plate) was placed above the bottom plate. This support plate is referred to as “upper support plate” in Figure 2-1, and its role was to help align and stabilize the lapping plates during FSLW. As the tendency of bulking (due to thermal expansion) is higher in the middle of the plates, two standard M6 bolts were used to fasten the lapping plates onto the backing plate (25 mm carbon steel plate). Also to enhance weld consolidation, the tool was tilted 2.5 ^{o}C from the normal direction of the plate towards the trailing side of the tool during experiments.

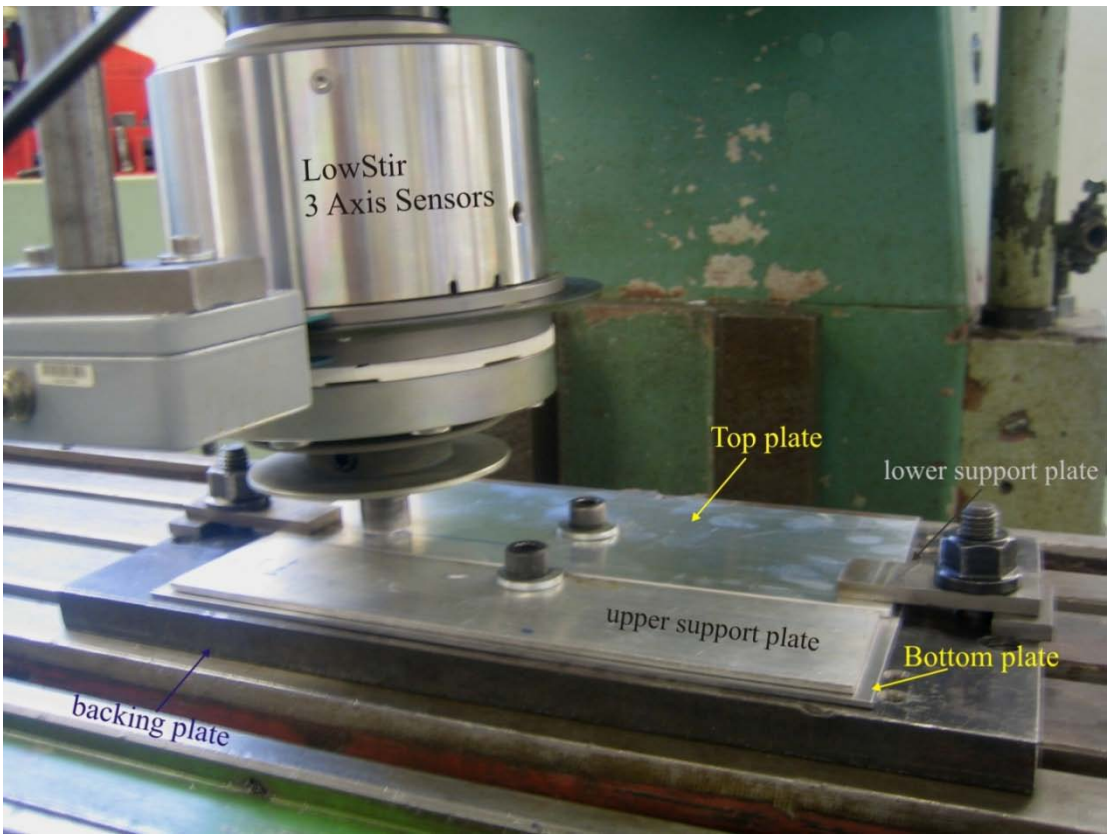

Figure 2-1 A retrofitted milling machine used for FSLW experiments. Bolted clamping system was used to restrain the plates during FSLW. The LowStir™ unit was installed to monitor the forces during experiments.

2.2.2 Tools Preparation

All the tools used in this study were CNC machined from H13 tool steel bars. Following making the tools, heat treatment was conducted with the following conditions:

a. Austenizating at 1050 ^{o}C for one hour and then water quenched

b. Tempering at 600 ^{o}C for one hour and then air cooled.

The hardness of the tools after heat treatment is approximately 48 HRC. Tools with various pin lengths and shoulder diameters were used in this study for each series of experiments and Table 2-3 summarise the key dimensions of the tools used. In series 1 and 2 experiments, a cylindrical tool pin with the same $D_{shoulder}$ and D_{pin} were used, as the workpiece materials was in comparable thickness range indicated in Table 2-1. However in series 3 experiments, the $D_{shoulder}$ were increased in accordance with the thicker top plates used (6 mm Al 6060-T5) in experiments. It should be noted that in all series of experiments, the tool rotation direction were kept unchanged so that the left-handed threaded pins were rotating clockwise.

Table 2-3 Summary of dimensions of the tools used in FSLW experiments

Series	Purpose	L_{pin} (mm)	D_{pin} (mm)	$D_{shoulder}$ (mm)	Pitch (mm)	D_{thread} (mm)
1	FSLW of Al 6060-T5	3.2 4.2 5.2	6	18	1	0.6
2	FSLW of AZ31B-H24	2.7 3.7	6	18	1	0.6
3	FSLW of Al 6060-T5 to mild steel	5.2 5.5 5.8 6	6	25	1	0.6
	FSLW of Al 6060-T5 to Ti6Al4V	6	6	25	1	0.6

2.2.3 Selection of FSLW Conditions (ω, ν, L_{pin})

All FSLW conditions used in this study are summarised and presented in Table 2-4. As described earlier, series 1 and 2 experiments involved performing FSLW on similar alloys of Al 6060-T5 and AZ31B-H24, respectively. These series of experiments were conducted using a relatively wide range of FSLW parameters (ω, ν, L_{pin}) in order to determine the effects of process parameters on hook formation and fracture strength/behaviour of the welds. In series 1 experiments, three L_{pin} values (3.2, 4.2 and 5.2 mm) used. Considering that workpiece material was 3 mm thick Al 6060-T5 plates, the L_{pin} values of 3.2, 4.2 and 5.2 mm represents slightly, moderate and excessive bottom plate penetration respectively. However for series 2 experiments, two L_{pin} values (2.7, 3.7 mm) used which represents slightly and moderate bottom plate penetration, respectively (for AZ31B-H24 plates with thickness of 2.5 mm).

Furthermore, a number of bead on 3 mm plate FS experiments were conducted on Al 6060-T5 to obtain the fracture strength of Al 6060-T5 welds in butt joint geometry. A cylindrical tool pin, with the same $D_{shoulder}$ and D_{pin} as the one used for series 1 FSLW experiments, used however L_{pin} value was 2.8 mm. In these FS experiments ω ranged from 500-2000 rpm and ν ranged from 112-630 mm/min which is similar to (ω, ν) range used for series 1 FSLW experiments when L_{pin} value of 4.2 mm used (as shown in Table 2-4).

Series 3 experiments (FSLW of Al6060/Steel and Al6060/Ti6Al4V) were performed using a few selected conditions, as the focus was to investigate the effect of pin positioning dependent microstructures on fracture strength of FSL welds. More details of tool positioning for series 3 FSLW experiments is given in next section.

Table 2-4 Summary of FSLW experimental conditions used in this study

Series	**No**	L_{pin} **(mm)**	**v (mm/ min)**	**ω (rpm)**	**Series**	**No**	L_{pin} **(mm)**	**v (mm/ min)**	**ω (rpm)**
1 (Al 6060-T5)	1	3.2	112	500	**2** (AZ31B-H24)	1	2.7	112	500
	2		112	1000		2		112	1000
	3		224	500		3		224	500
	4		224	1000		4		224	1000
	5	5.2	112	500		5	3.7	112	500
	6		112	1000		6		112	1000
	7		224	500		7		112	1400
	8		224	1000		8		224	500
	9	4.2	112	500		9		224	1000
	10		112	1000		10		224	1400
	11		112	2000		11		450	500
	12		224	500		12		450	1000
	13		224	1000		13		450	1400
	14		224	2000	**3** (Al6060/Steel)	1	5.2	80	710
	15		315	500		2	5.5	80	710
	16		315	1000		3	5.7	80	710
	17		315	2000		4	6	80	710
	18		630	500		5	6	80	1400
	19		630	1000		6	6	20	1400
	20		630	2000	**3** (Al6060/Ti6Al4V)	7	6	20	1400
						8	6	80	1400

2.2.4 Tool Positioning and Force Monitoring

A LowStir^{TM} device, as shown in Figure 2-1, was used to monitor the down force (F_z) applied to the tool pin during FSLW experiments. The data captured by the LowStir^{TM} was transmitted to a signal processing module, which converted the data into digital format such as Microsoft Excel file. The measurement frequency was kept constant at 300 HZ, i.e. five sets of measurements per seconds.

All FSLW experiments were conducted using displacement (position) control mode. The position was first ascertained by lowering the non-rotating tool downwards until the bottom of the pin touched the surface of the top plate and the $F_Z \approx 1$ KN was registered by using LowStir^{TM} device. In this way, the pin would leave a very shallow indentation mark if the tool was lifted without further plunging. Then the vertical control handle of FSW machine was assigned zero. Subsequently the rotating pin will be moved downwards for the required plunge depth which is equal to L_{pin}. The movement of vertical control handle can be controlled with an accuracy of ±0.05 mm.

In series 1 and 2 experiments for FSLW of similar materials, the L_{pin} value was always larger than thickness of top plate and hence the pin penetrated into bottom plate, as shown schematically in Figure 2-2a. In series 3 experiments for FSLW of dissimilar materials, the L_{pin} values was first selected to have either slightly penetrated or non-penetrated situation. A schematic illustration of Al/Steel FSLW, where L_{dis} is defined as the distance between bottom of pin and steel surface is shown in Figure 2-2b. In this case, positive values of L_{dis} ($L_{dis} > 0$) represent the conditions where the pin does not touch the steel surface during FSLW. On the other hand, $L_{dis} = 0$ or $L_{dis} < 0$ represent the conditions where the bottom of pin just touches or penetrates into the steel surface, respectively.

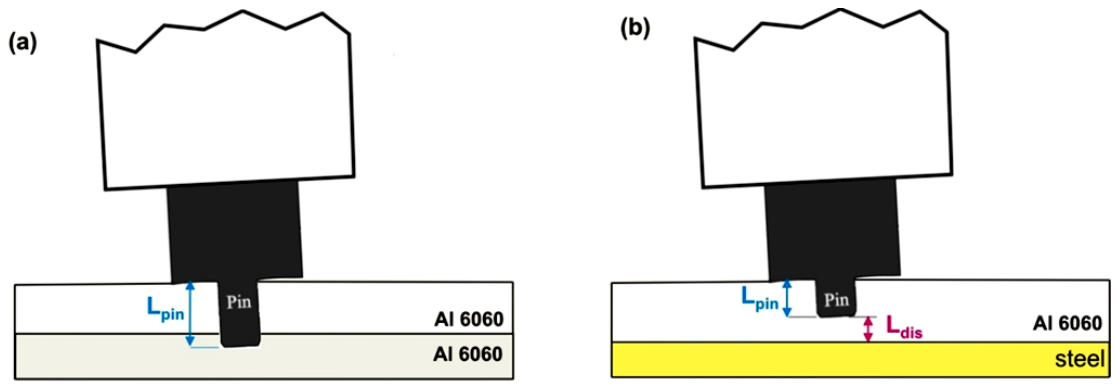

Figure 2-2 Schematic illustration: (a) FSLW of Al 6060 where pin has penetrated into bottom plate and (b) Al/Steel FSLW where L_{dis} is defined as the distance between bottom of pin and steel surface

To obtain information on position of bottom of pin with reference to the steel surface (either penetrated or non-penetrated), the down force (F_z) applied on the tool pin was monitored during FSLW, using LowStir^{TM} device. Figure 2-3 shows the measured F_z for the two welds made using same ω=710 rpm, v=80 mm/min but different L_{dis} of 0.5

and -0.1 mm representing a non-penetrating and penetrating conditions, respectively. For L_{dis}= 0.5 mm, tool plunging started from ~12 s and finished at ~19 s. During pin plunging F_z increased rapidly, but when the tool was fully immersed into the plate at ~19 s, then F_Z experienced a drop due to material softening around pin, caused by the FS heat. Shortly when tool forward motion started, F_z increased again until it reached a stable condition at ~40 s. The stable condition after ~40 s indicates that pin did not penetrate to steel. However for L_{dis} = - 0.1 mm, F_z value after manual plunging at ~ 30s is highly unstable with some big spikes on F_z curve, confirming that the pin penetrated to the steel. The above results clearly shows that F_z – time curves can be used to ascertain the position of bottom of pin, either penetrated or non-penetrated to steel surface, over the welded length.

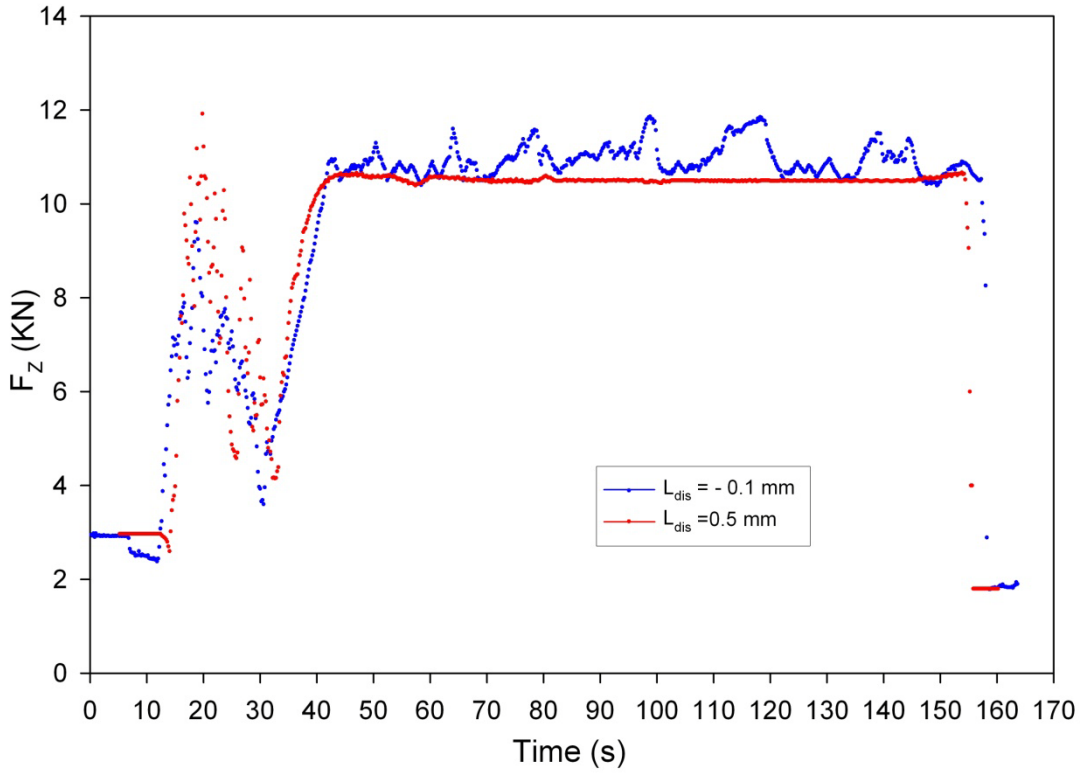

Figure 2-3 F_Z – time curves obtained for the Al/Steel FSL experiments made using same ω =710 rpm and ν =80 mm/min but different L_{dis} as indicated

Furthermore in series 3 experiments (either Al/Steel or Al/Ti) two force monitored FSLW experiments were performed so that $L_{dis} \approx 0$ was aimed in order for the pin bottom to just reach the bottom plate (steel or titanium) without penetration. An example is shown in Figure 2-4 for an Al/Steel FSL Weld in which the tool was

lowered slightly in later stage of FSLW, thus $L_{dis} \approx 0$ (Region 1) and $L_{dis} > 0$ (Region 2) were obtained in one experiment, as indicated in Figure 2-4.

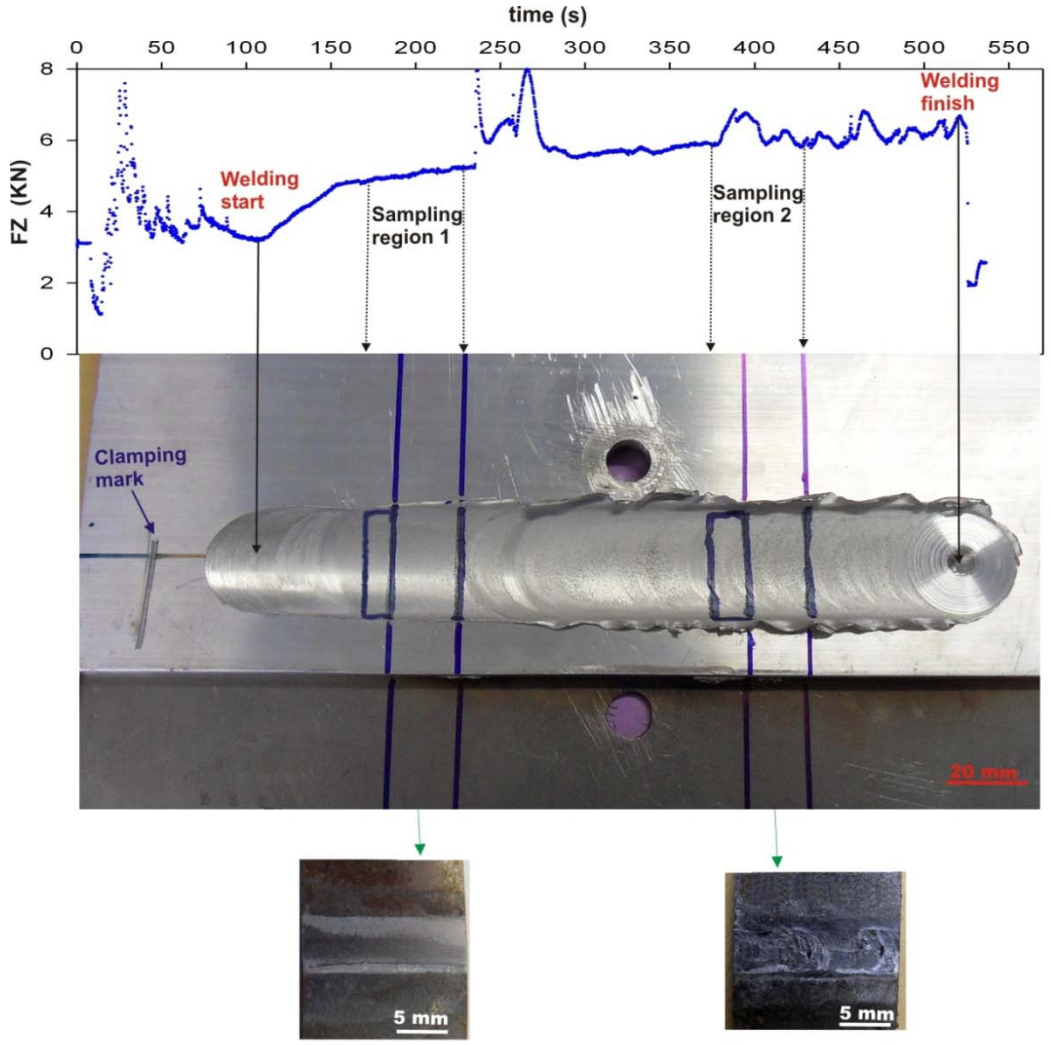

Figure 2-4 An Al/Steel FSL weld made using ω =1400 rpm and ν =20 mm/min with F_z – time curve superimposed. Location of tensile shear and metallographic samples from Region 1 and 2 are also marked. Macrographs of steel side of tensile shear tested samples are also shown below the associated samples

In Figure 2-4, F_z values before ~ 110s correspond to the manual plunging and careful positioning. When the tool forward motion started F_z increased but later at ~ 150s the rate of increase became very low, signalling a close to stable condition. After a sufficient time had elapsed, at ~ 235 s, the pin was manually lowered slightly so that the pin penetrated to steel caused a rapid increase in F_z. In a later part of welding, at ~ 375s, the pin was again manually lowered slightly to ascertain a slight penetration of the pin to steel. F_z –time curve indicates that in the sampling region 1, pin has not penetrated the steel surface as the F_z showed a stable condition. This is in agreement with

macrograph of steel side of tested sample (region 1 sample), as shown in Figure 2-4, in which no evidence of pin penetration can be seen on steel surface. However highly unstable F_z condition at sampling region 2 indicates the pin penetration at that region. The cutting marks made by the penetrating pin can be clearly seen on fractured surface of steel, as shown in Figure 2-4. Details of the examination will be given later in the section 5.1.3.

2.2.5 Temperature Monitoring

Twisted K type thermocouple wires (0.25 mm diameter) were used in this study for measuring temperature during FSLW. The thermocouples wires are capable of measuring temperatures up to maximum 1260 ^{o}C. An USB-2416-4AO personal Daq temperature measurement system was used in all temperature measurements experiments. The measuring frequency was 50 HZ which gives sampling interval of 0.02 s. The placement of thermocouple wires aimed at measuring temperature at the lapping interface of top and bottom plates, as shown in Figure 2-5b. Narrow grooves with depth of 0.5mm were made (using a small milling cutter) on the bottom plate to accommodate the twisted thermocouple wires, as shown in Figure 2-5a. Thermal conducting paste was also inserted into the grooves in order to enhance the thermal contact between plates and thermocouple wires. The temperature data was obtained simultaneously from two separate thermocouple wires (Figure 2-5a), in each experiment, hence the validity of data can be verified if the results obtained from both thermocouple wires are the same.

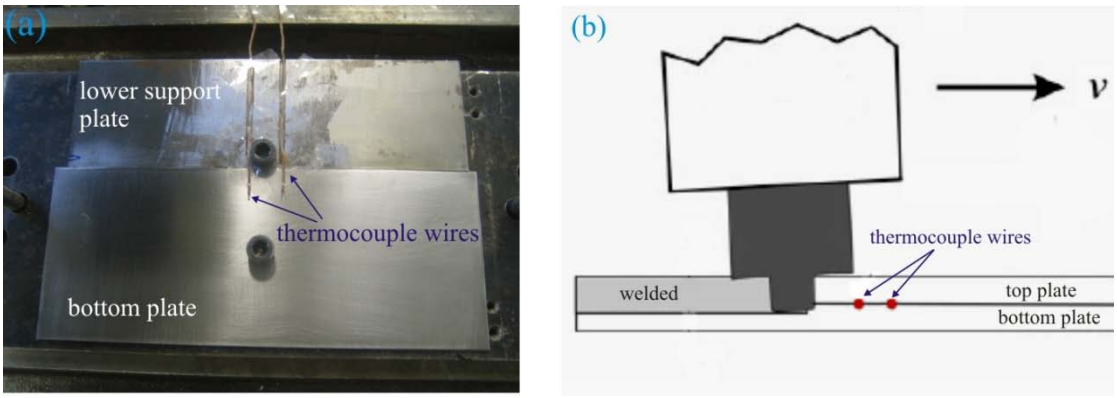

Figure 2-5 Thermocouple wires placement during FSLW experiments, (a) image showing thermocouple wires positioned at narrow grooves made on bottom plate before FSLW and (b) schematic illustration of thermocouple positions during FSLW

2.3 Metallurgical Examination

2.3.1 Sample Preparation

All FSL welds were sectioned normal to welding direction, and an example is given in Figure 2-6. FSL Welds of Al 6060-T5 (series 1 experiments) were sectioned using a vertical band saw. FSL Welds of AZ31B-H24 (series 2 experiment) were sectioned using a CNC wire cutting machine. For series 3 experiments (Al6060/Steel and Al6060/Ti6Al4V) a water-jet cutting machine utilised, due to thick (6 mm) top plate Al 6060-T5 alloy used. It should be noted that metallography samples were mounted so that the cross section of the welds could be examined. For series 1 and 2 experiments, phenolic hot mounting resin were used (mounted at 150 ^{o}C), while epoxy cold mounting resins were used for series 3 experiments. Wet coarse and fine grinding was conducted on rotating disks with 180, 500, 800, 1200 grit silicon carbide papers successively. Samples were then fine polished using a TegraPol-25 automatic polishing machine, provided by Struers, on cloths of 6µm, 3µm and finally 1µm successively. The metallographic samples polished to produce mirror like finish. Polished samples were then cleaned with ethanol using an ultrasound cleaning machine for 1 minute.

Figure 2-6 An Al/Steel FSL weld, with lines drawn indicating sectioned perpendicular to welding direction

Chemical etching procedures varied depending on the samples. For series1 experiments (Al 6060-T5 FSLW) samples were etched for 5 minutes in 'Keller's reagent containing 6 ml HCl, 3 ml HNO_3, 6 ml HF and 150 ml H_2O to obtain clear macrograph of the welds. In series 2 experiments (AZ31B-H24 FSLW), samples were etched for 5 seconds

in ‘Acetic-Picral’ reagent containing 6g picric acid, 5mL saturated acetic acid and 100 ml ethanol to reveal the general microstructure and deformation twins. For series 3 experiments (Al/Steel FSLW) samples were etched in ‘2% Nital’ reagent containing 2ml HNO_3, 100 ml H_2O for 5 seconds. Also ‘Kroll’ reagent containing 1ml HF, 1.5 ml HCL, 2.5 ml HNO_3 and 95 ml H2O were used for series 3 experiments (Al/Ti FSLW) which could reveal the general microstructural of Ti6Al4V.

Special steps have been included during specimen preparation for EBSD studies. As the electrons diffracted and detected by the EBSD camera emanated mostly from the top 50-100 nm of the specimen; a sample surface free of distortion, oxide or reaction products layers is essential. The polishing procedure followed the same steps as for optical metallography. However further polishing step, using 0.05 μm colloidal silicon suspension, was performed (for 3 minutes) using TegraPol–25 automatic polisher. Thereafter, freshly polished samples were immersed face down in etching solutions to remove the surface reaction layers. For Al 6060-T5 specimens, etching solution ‘0.5 % HF’ were used for 1 minute, and for Mg AZ31B-H24 specimens, a solution containing 10ml HNO_3, 30ml acetic acid, 40ml water and 120ml ethanol were used for 10 seconds right before conducting EBSD.

2.3.2 Optical and Electronic Microscopy

A Nikon optical microscope (FX-35A) and Olympus stereomicroscope (SZX9) have been used for macro and microstructure observations in low magnification range. Scanning Electron Microscope used in this study is FE Hitachi SU-70. Energy Dispersive Spectrometer (EDS) was used to analyse the chemical composition microanalysis. This SEM also equips with Nanotrace Si (Li) EDS detector and Quasor EBSD Detector.

2.3.3 Electron Backscatter Diffraction

Electron Back Scatter Diffraction (EBSD) is a technique by which an SEM can be used to evaluate the microstructure of a sample based on crystallographic analysis. It is a quantitative technique that can be used for revealing grain size, grain orientation, texture and phase identification. EBSD operates by arranging a flat, finely polished sample at a 70^{o} angle to the incident electron beam. A typical arrangement of EBSD system is shown in Figure 2-7. The SEM stage tilts the plane of the sample to this shallow angle. With moderate to high electron beam accelerating voltages (10 to 30 KV), the electron

beam is diffracted by the crystal lattice of the sample at the point where incident beam strikes on the sample surface. With the beam stationary, an electron backscatter diffraction pattern (EBSP) emanates spherically from this point in all directions. If an EBSP detector is placed close to the incident beam point, it intersects a portion of this diffraction pattern. The detector is in fact a digital camera similar which is contained within a vacuum compatible and retractable body. The camera's CCD (charged-coupled device) chip is illuminated by the phosphor screen that intersects the spherical diffraction pattern. The phosphor converts the diffracted electrons into light suitable for the CCD camera to record.

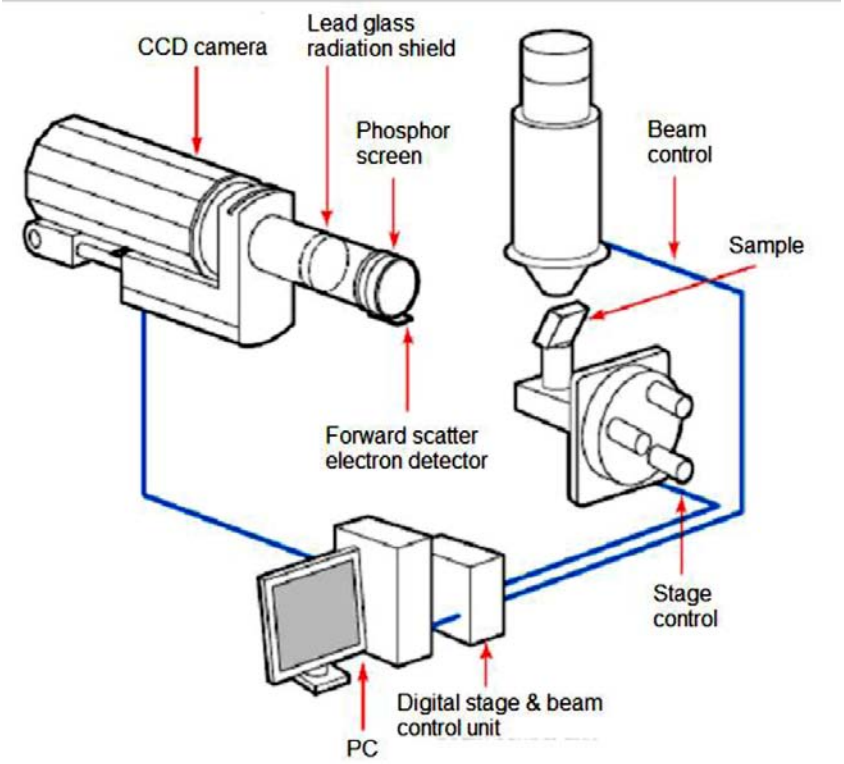

Figure 2-7 Diagram showing the principle components of an EBSD system [85]

With the stationary beam on a point of sample surface, the EBSP is analysed and stored by the EBSD-control computer. The EBSP is uniquely defined by the lattice parameters of the particular crystal under the beam, and by its orientation in space. By selecting the expected crystal phases from a phase databases, all possible identities and orientations of the crystal under the beam are matched to the EBSP until the best fit is found. The pattern is then considered indexed, and the best-fit orientation and phase is reported as the orientation and phase of the point on the sample. When the speed of pattern analysis

increases, it becomes practical to scan the beam over multiple points on the sample to create an orientation map (OM). Schematic illustration of the principle of orientation mapping is shown in Figure 2-8, in which the beam is scanned in a grid across a polycrystalline sample and crystal structure and orientation are analysed at each point. The resulting map will reveal the grain morphology, orientations, and boundary.

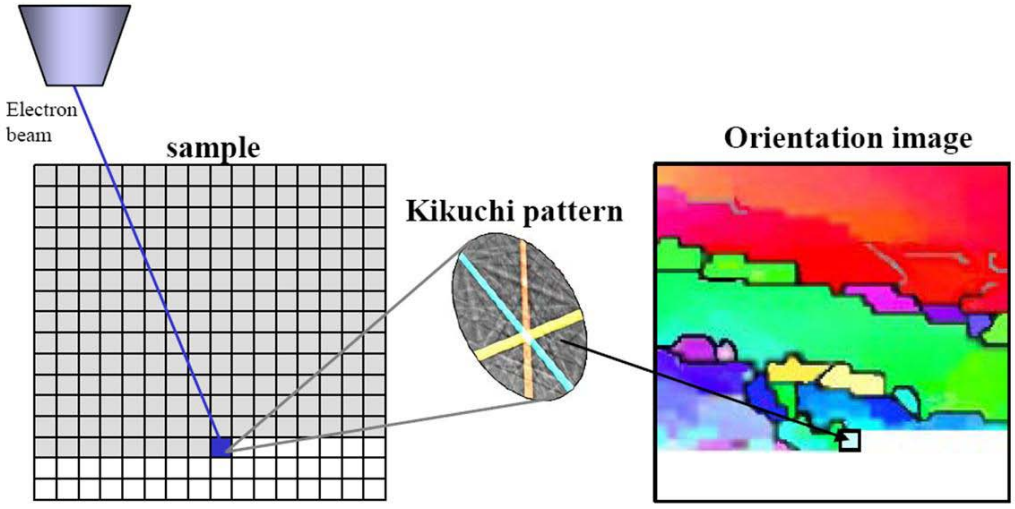

Figure 2-8 Schematic illustration of the principles of orientation imaging [86]

An acceleration voltage of 20 KV, together with a working distance of 26 mm and a sample tilt angle of 68º were selected to maximize backscattered electron diffraction. Additionally, the step size was chosen in order to maintain a ratio of 1:3 between the step size and the size of the smallest feature of interest. The EBSD patterns collected from the scans carried out in the FE Hitachi SU-70 were processed using the fully automated data acquisition programs 'NSS^{TM}'.

2.3.4 Quantifying Flow Volume in the Bottom Stir Zone ($A_{B\text{-}SZ}$)

As has been described in section 1.2.2, during FSLW the material around the rotating pin will be sheared and driven downwards by the thread space. Due to this downward material flow, the material originally located at bottom plate is pushed outward as well as upward towards the top plate. This mechanical push-up causes the original lapping surfaces to curve upward in thermomechanical affected zone and hence forming the hook. Therefore it is reasonable to suggest that the flow volume in the bottom stir zone ($A_{B\text{-}SZ}$), as shown in Figure 2-9, correlates to the amount of pushing up the original lap.

For example, the cross section macrograph of an Al 6060-T5 FSL weld, made using v=224 mm/min ω=1000 rpm, is given in Figure 2-9. This macrograph has been taken

using a stereo-microscope from the etched specimen. The total stir zone which includes material that has gone through noticeable deformation has been outlined by the white dashed curves. The yellow dashed line separates the $A_{B\text{-}SZ}$ (at bottom plate) from rest of stir zone at top plate. The clear boundary between SZ and TMAZ, as shown in Figure 2-9b, is used in measuring $A_{B\text{-}SZ}$ .To quantify the $A_{B\text{-}SZ}$, a fine mesh grid (as shown in Figure 2-9c) was superimposed onto the macrographs and then flow area was manually counted.

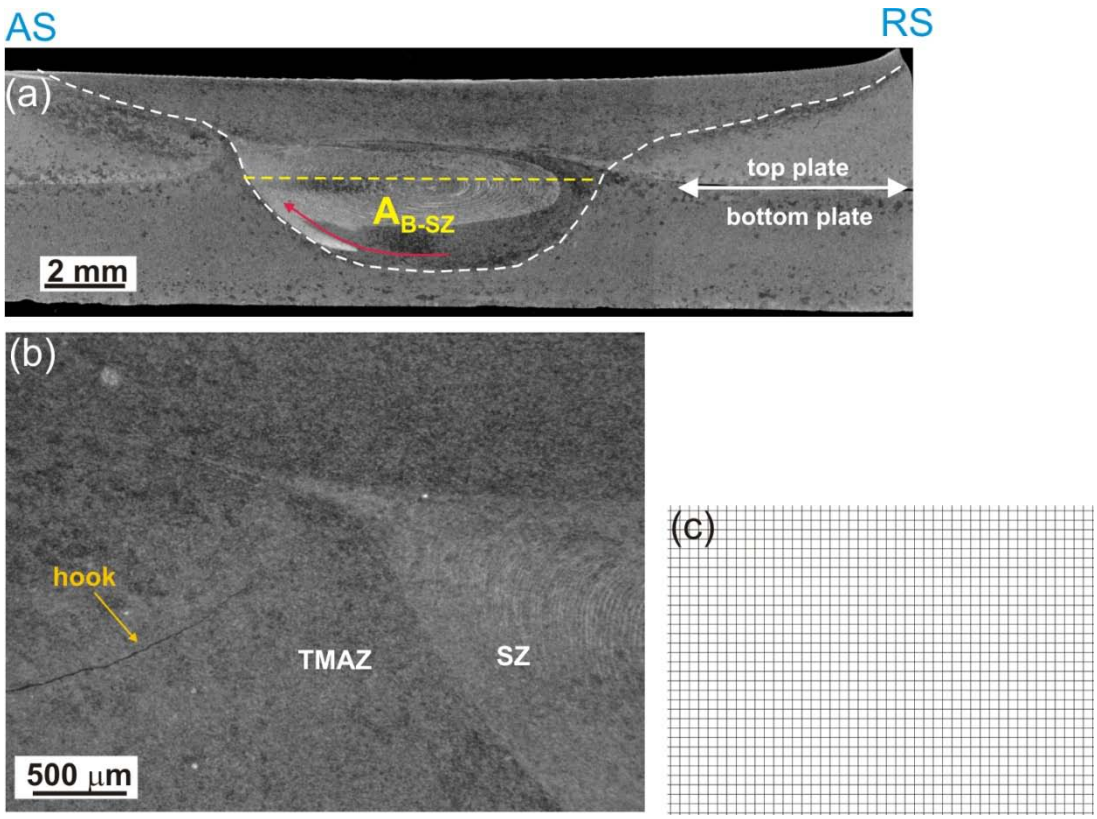

Figure 2-9 (a) Cross section of Al 6060-T5 FSL weld made using ν =224 mm/min and ω =1000 rpm. The white dashed curve outlines the total stir zone, and the area below the yellow dashed line is $A_{B\text{-}SZ}$, (b) an enlarged view of hooking region on advancing side and (c) mesh grid with a unit area representing 0.3 mm by 0.3 mm

2.4 Mechanical Properties Evaluation

2.4.1 Tensile Shear Testing of FSL Welds

Mechanical performance of FSL welds, under static loading, is commonly determined using tensile shear testing [6, 7, 12, 15-18, 20-22, 26-29]. Fracture strength (σ_{Lap}), corresponding to the maximum load in a test over the sample width, is the widely used

strength value. Schematic illustration of a tensile shear testing arrangement is given in Figure 2-10. To align the test samples (balance the offset axes of the lap members), two packing pieces (aluminium or steel) were used in clamping grips, as indicated in Figure 2-10. The testing was carried out at room temperature using a 50 KN Tinus Olsen tensile machine, with the crosshead speed fixed at 3 mm/min. For series 1 and 2 experiments, three specimens were tested for each weld to obtain the average σ_{Lap}.

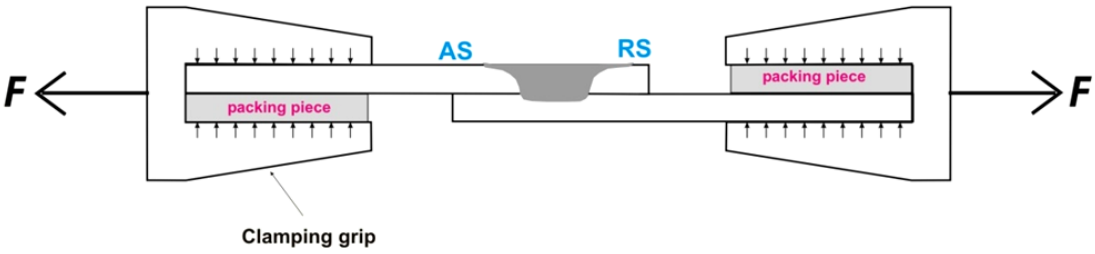

Figure 2-10 Schematic illustration of a tensile shear testing arrangement, with packing pieces and loading directions indicated

As has been described in section 1.2.2, due to asymmetry in profile of hook (on advancing side) and cold lap defect (on retreating side) FSL welds can be loaded in two different ways. In advancing loading configuration, the advancing side of a lap weld on the upper plate is placed under loading while in retreating loading configuration, the retreating side of a lap joint on the upper plate is loaded. In this study, all tensile shear testing experiments performed in advancing loading configuration, as illustrated in Figure 2-10.

2.4.2 Tensile Shear Testing of AZ31B-O Specimens

As the attempt to produce AZ31 FSL welds with negative hooking (on advancing side) were not successful using attainable FSLW conditions and cylindrical tool pins, a number of tensile shear testing specimens were made out of AZ31B-O using a wire cutting machine to systematically investigate the effect of hook orientation on fracture behaviour. Figure 2-11 shows the photos of these specimens, with *h* (artificial hook size) indicated on each specimen. It can be seen that for positive hook specimens *h* varies from 0 to 1.2 mm and for the negative hook specimens *h* varies from -0.27 to -1.17 mm. The tensile shear testing carried out at room temperature using a 50 KN Tinus Olsen tensile machine, with the crosshead speed fixed at 3 mm/min.

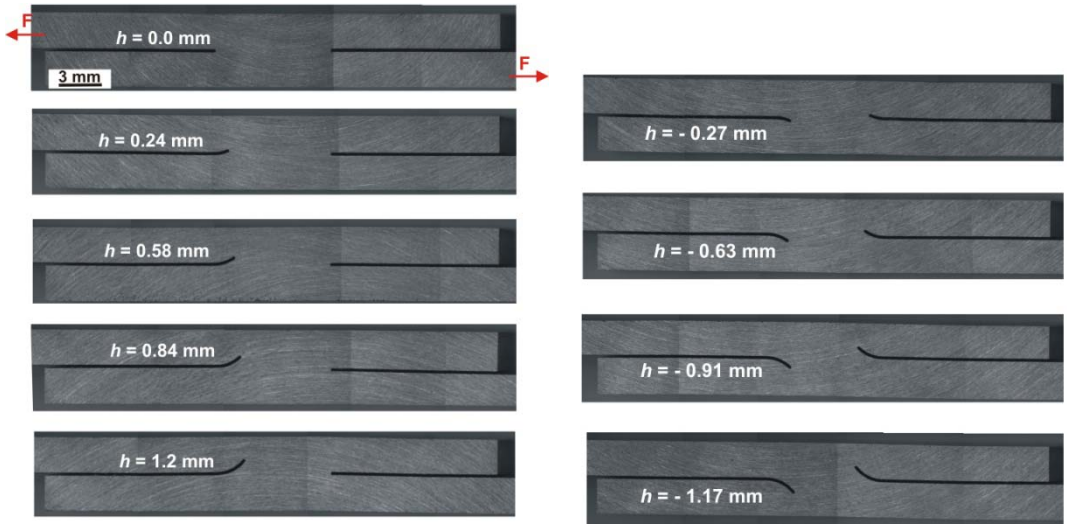

Figure 2-11 AZ31B-O tensile shear testing specimens with different artificial hook orientation and *h* as indicated (loading direction during tensile shear testing is indicated using arrows)

2.4.3 Micro-Hardness Measurement

Knoop indentation tests were conducted, using a micro-hardness tester (Model LECO M-400-G1) and following the procedure outlined in the ASTM standard E384. In series 1 and 2 experiments, an indentation load of 50gf at constant dwell time of 20 seconds have been used.

2.5 Finite Element Method

2.5.1 Brief Introduction to Finite Element Method (FEM)

FEM is one of the most widely used numerical methods for analysis of stress and strain in complex structures. It is based on the idea of dividing the complicated structure into smaller pieces which are called elements. Therefore the first step of any finite element simulation is to discretize the actual geometry of the structure using a collection of finite elements. Each finite element represents a discrete portion of the physical structure and the finite elements are joined by the shared nodes. The collection of nodes and finite elements is called the mesh and number of elements used in particular mesh is referred to as mesh density.

After describing the behaviour of physical quantities on each element (material dependent), the solver (computer) assemble the element at nodes to forms an approximate systems of differential equations for the whole structure, then solves the systems of equations involving unknown quantities at the nodes (e.g. displacement).

Afterwards the solver goes back and uses them to calculate the desired quantities (e.g. stress and strains) at the selected elements.

2.5.2 FEM Procedures Using ABAQUS™

In current study, FEM models were constructed using commercial software ABAQUS™ to analyse the stress distribution during tensile shear testing of FSL welds. ABAQUS is divided into different modules, where each module defines an aspect of the modelling process. As we move from a module to module, we build the model from which ABAQUS generates an input file which will be submitted to ABAQUS solver for analysis [87]. The brief descriptions of modelling modules are as follows:

(a) Part module: individual parts are created by sketching their geometry.

(b) Property module: materials physical and mechanical properties (such as yield strength, elastic modulus) are defined and assigned to the regions of the parts.

(c) Assembly module: when a part is created, it exists in its own coordinate system, independent of other parts in the model. In assembly module instances of the parts are created and then positioned relative to each other in global coordinate system. A model can only contain one assembly.

(d) Step module: analysis steps are created and configured. Then output requests (such as stress and strain variables) are defined for each step.

(e) Load module: In this step, applied loads and boundary conditions are specified. Load and boundary conditions are step dependent, which means we must specify the analysis steps in which they are active.

(f) Mesh module: A finite element mesh is generated by selecting type and size of elements for different regions of the part.

(g) Job module: once all the tasks involved in defining a model is finished, the job is submitted for analysis. ABAQUS first generates an input file representing the model, and then performs analysis using content of that file. The ABAQUS solver computes the values of variables (such as stress and strains) and then writes them on output databases.

(h) Visualisation module: this module provides graphical display of finite element models and results data such as stress contours.

2.5.2.1 Description of Model Geometry and Boundary Conditions

Figure 2-12 shows a schematic plot of a 3D FEM model used in current study. Key geometric dimensions used in the model, as shown in Figure 2-12, were selected to coincide as exactly as possible with the actual dimensions of tensile shear testing samples. Un-welded lap and hooking features were considered as sharp cracks, according to metallographic observation of FSL welds. A uniform tensile load applied on left edge surface of specimen, as indicated by the bold arrows in Figure 2-12. Also for the region A, as indicated in Figure 2-12, the displacement in the y-axis and z-axis directions is constrained to represent the clamping conditions (by the gripping jaws) in the tensile shear testing. It should be noted that Figure 2-12 shows a FEM model with zero hook size (h=0 mm), as an example to illustrate. FEM modelling was also performed for positive hook (h > 0 mm) and negative hook (h< 0 mm) samples, as will be shown later in section 4.3.1.

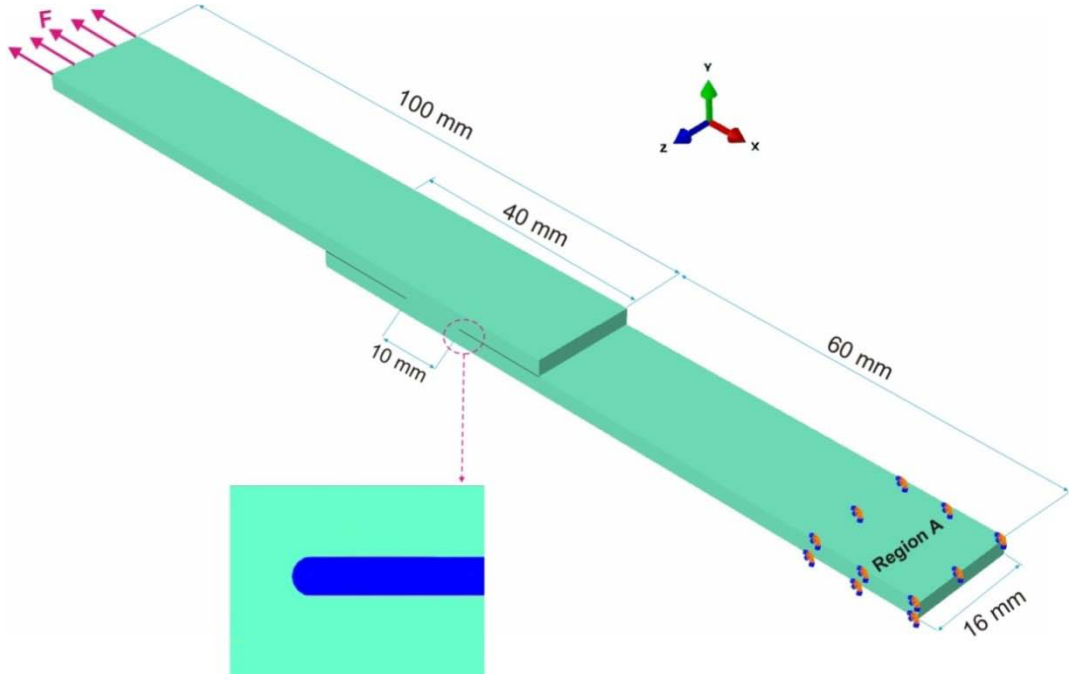

Figure 2-12 Schematic plot of a tensile shear sample, used in 3D FEM modeling, with uniform tensile load applied to the left edge surface of specimen shown as bold arrows.

2.5.2.2 Materials Properties

In current study, the base materials and welded regions were assumed to have isotropic material properties, showing linear elastic material behaviour. Details of mechanical properties inputs used in FEM modeling are presented in Table 2-5.

Table 2-5 Mechanical properties inputs for the materials used in FEM modelling

Material	**Young's modulus E (GPa)**	**Poisson's ratio, *v***	***YS* (MPa)**	***UTS* (MPa)**
Al 6060-T5	70	0.33	176	210
AZ31B-H24	45	0.35	202	310
Mild Steel	210	0.3	230	317

2.5.2.3 Meshing Details

Figure 2-13 shows a complete enmeshed FEM model, consisting of 62580 elements. 3D hexahedral reduced integration elements were selected for meshing, as they are best element types for obtaining accurate stresses at reduced computation time [87]. Due to formation of large stress concentrations around the notches, a very fine mesh size has been applied to the tip of un-welded lap, as shown in Figure 2-13b. The very fine meshes used at the tip of un-welded lap region, caused the later to appear black in Figure 2-13b compared to surrounding area. Finally the mesh verification was performed to ensure that the elements in the mesh were not inappropriately distorted.

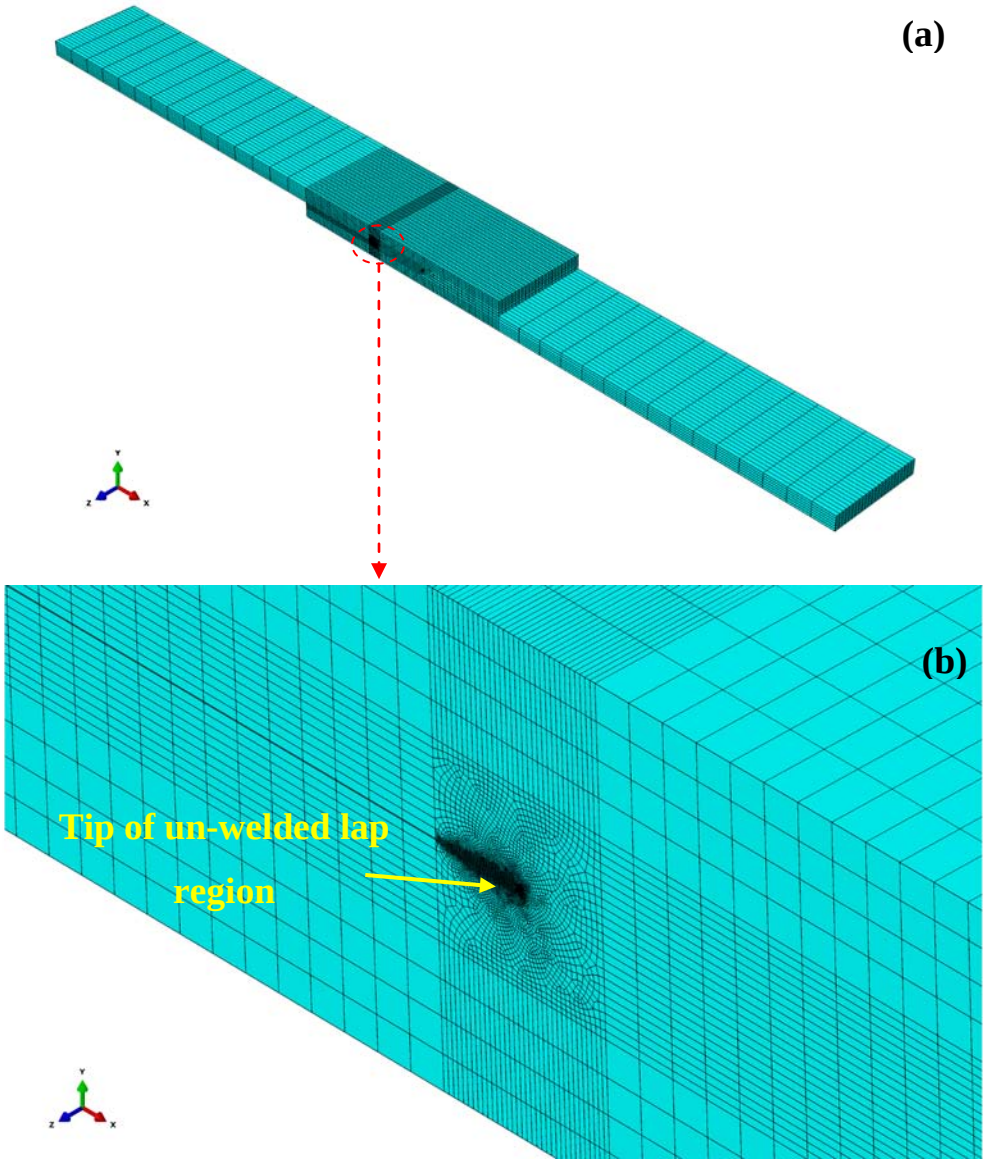

Figure 2-13 Schematic plot of a tensile shear sample, used in 3D FEM modelling, (a) the enmeshed model and (b) a close-up view of mesh near the tip of un-welded lap region

3. Hooking and Fracture Strength of Al 6060-T5 FSL Welds

In this chapter, fracture strength of "bead-on-plate" FS welds is presented first to serve as basis for strength comparison. Then the effect of the L_{pin} on the joint structure, and the manner in which the FSL welds fractured during testing are presented and discussed. A thermomechanical explanation on how ω and v affect hook formation is also presented. Then effects of hook size, shape and continuity, and also FS softening on fracture location and σ_{Lap} of FSL welds are discussed. FEM simulation results are presented and discussed for better understanding of how stress distribution, under tensile shear loading, affects the σ_{Lap} of FSL welds. Finally the mechanism of local deformation in FSL weld samples under tensile shear loading is presented.

3.1 Fracture Strength of Al 6060-T5 Bead-on-plate FS Welds

As described in section 1.2.1, Al 6060-T5 is an age hardened alloy (T5 is equivalent to T6 in this alloy), and thus FS heat causes softening in different regions of the weld. A number of bead-on-plate FS welds (as explained in section 2.2.3) were made and tensile tested to obtain the fracture strength values for FS welds in butt joint geometry. This strength data is then compared later to the strength values of FSL welds (using same ω, v) with *h* tending to zero.

All bead-on-plate tensile samples fractured in the heat-affected zone (HAZ), an example of which is shown in Figure 3-1a. Ultimate tensile strength (*UTS*) of the as-received base metal was measured at 211 MPa. Fracture strength (σ_{BoP}) of FS samples, given in Figure 3-1b, ranged from 128 to 150 MPa, thus 61% to 71% of the *UTS* value of the base metal. Higher v at the low ω condition resulted in higher σ_{BoP}. This is in line with well established results found in literature [2].

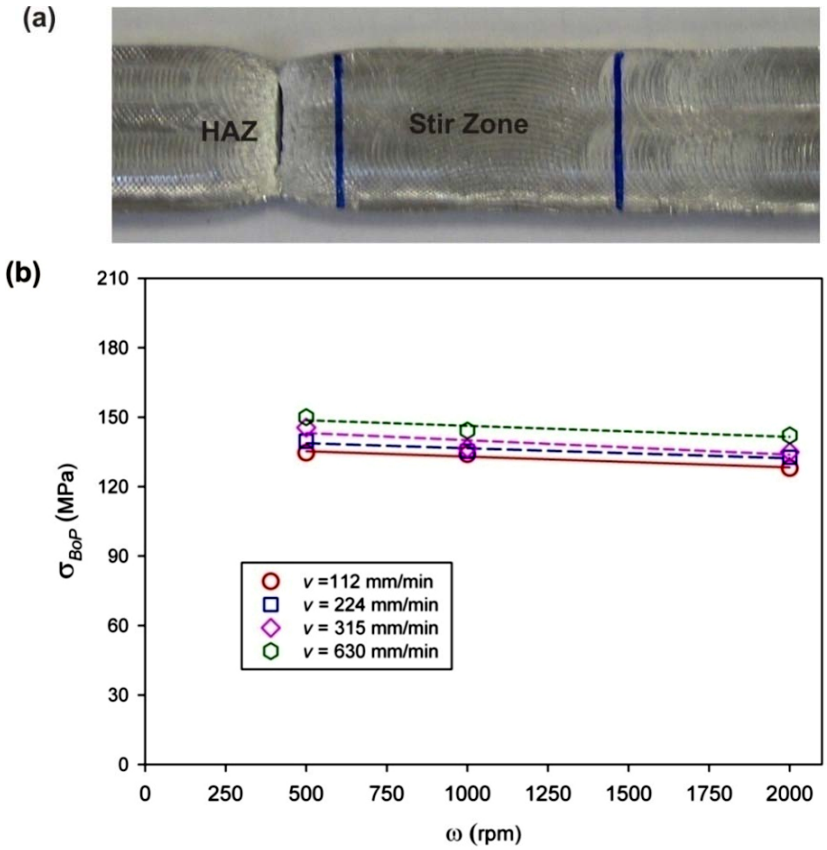

Figure 3-1 FS bead-on-plates tested results, (a) a typical test sample showing an extensive necking and fracture in HAZ outside the FS zone marked by the two lines and (b) σ_{BoP} plotted against ω for various v values

As explained in section 1.2, ω and ν are the fundamental parameters of FS, which significantly affect the weld zone temperature and material flow during FSLW. The L_{pin} value can also affect the material flow volume during FSLW. Thus, the effects of these parameters on the degree of hooking and σ_{Lap} of the FSL welds are presented in following.

3.2 The Effect of L_{pin} on Joint Structure and Strength

The first series of FSLW experiments were conducted using three L_{pin} values (3.2, 4.2 and 5.2 mm). Considering that the workpiece material was 3 mm thick Al 6060-T5, L_{pin} values of 3.2, 4.2 and 5.2 mm represent slight, moderate and excessive bottom plate penetration respectively. The values of σ_{Lap} plotted as function of L_{pin} are shown in Figure 3-2. It is clear that σ_{Lap} is highly process parameters dependent. Also the trends of the data in Figure 3-2 suggest that, for three out of four ν-ω conditions, σ_{Lap} varied quite considerably when L_{pin} was changed from 3.2 to 4.2 mm. However, for each of the

four v-ω conditions σ_{Lap} did not change significantly when L_{pin} increased from 4.2 to 5.2 mm. Furthermore for the welds made using L_{pin} values of 4.2 and 5.2 mm (representing moderate and excessive penetration) higher ω or lower ν resulted in lower σ_{Lap}, in a general agreement with that found in literature [15, 16, 21]. However the use of L_{pin}= 3.2 mm (representing slight penetration) was very different regarding the effect of ν and ω.

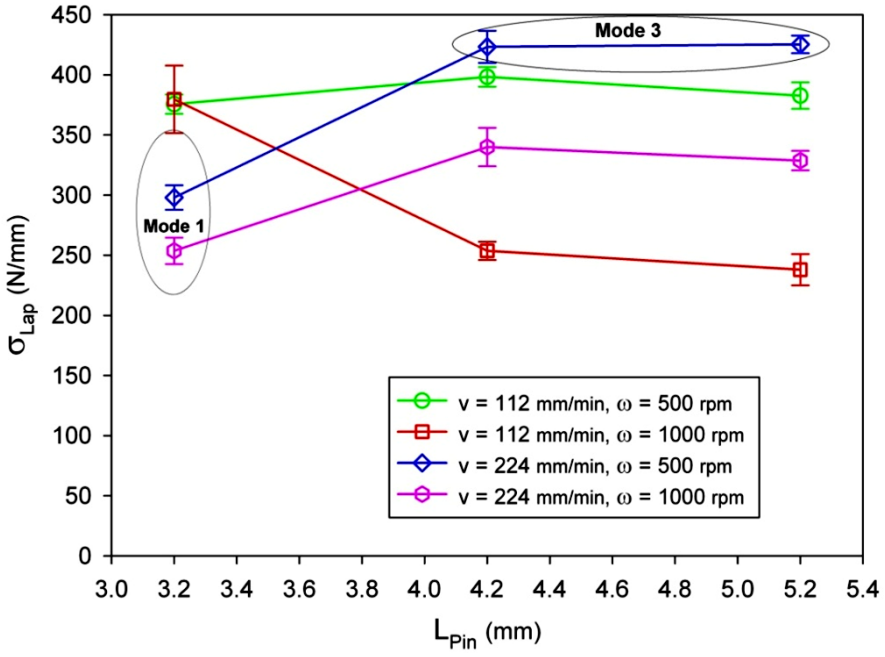

Figure 3-2 σ_{Lap} (and one standard deviation) plotted as a function of L_{pin} for various ν and ω combinations. Mode 1 and Mode 3 indicate modes of fracture for those samples included in the marked areas. The rest of samples fractured with Mode 2, which is not labelled

Prior to a further discussion on the effect of L_{pin} on σ_{Lap}, the way in which the tensile shear samples deformed and fractured needs to be discussed. A feature of interest in tested samples is local bending and rotating before fracturing. This is clearly shown in the selected tested samples in Figure 3-3, regardless of how subsequently a sample fractured. Samples fractured in three different manners. Fracturing of a joint could proceed without necking and the failure was simply by fracturing across the bottom part of the nugget and along or near the original lapping surfaces of the whole joint. This is Mode 1 and an example is given in Figure 3-3a. Mode 2 represents fracturing that is similar to a normal tensile fracture (after local bending) but the crack originated from the hook, as shown in Figure 3-3b. Mode 3 also represents a fracture that is similar to a

normal tensile fracture (after local bending), however the failure occurred in HAZ, as shown in Figure 3-3c.

The maximum achieved σ_{Lap} value, as shown in Figure 3-2, was ~ 422 N/mm. This maximum attainable σ_{Lap} value (422 N/mm) is actually slightly higher than that of FS bead-on-plate samples ($\sigma_{BoP} \approx 140$ MPa $\times$ 2.9 mm = 406 N/mm) using the same ω and v, given in Figure 3-1b. The FSL weld samples with maximum σ_{Lap} fractured in Mode 3 which, as explained earlier, is the same mode of deformation and fracture as that of bead-on-plate samples. This also means σ_{Lap} is just under 70% of *UTS* of the base metal, which is almost the same as the values obtained using the best FSLW conditions [15, 21].

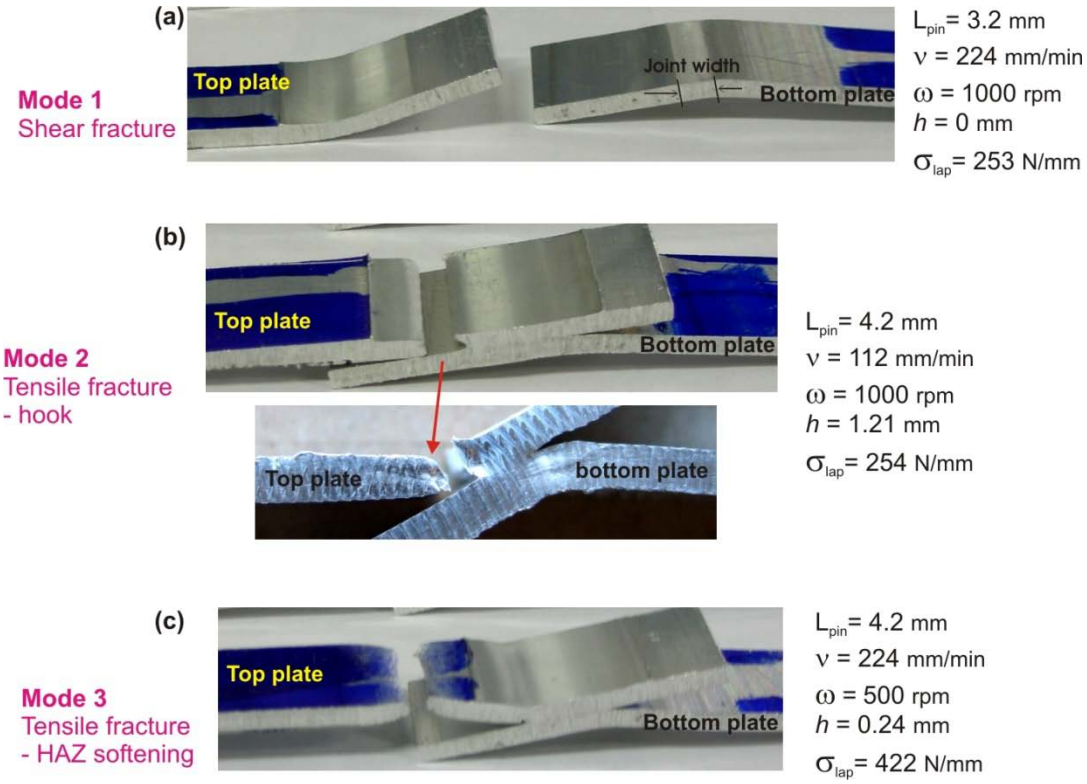

Figure 3-3 Various modes of fracture, (a) Mode 1: shear fracturing along the top and bottom joint interface, (b) Mode 2: tensile fracture with the crack propagated from the hook and (c) Mode 3: tensile fracture in HAZ

Returning to Figure 3-2 and examining the effect of L_{pin} on σ_{Lap}, Mode I fracture occurred in samples made using the low value of L_{pin} = 3.2 mm (representing slight penetration) and the higher value of v = 224 mm/min. It is generally understood that higher v should result in both lower stir zone temperature and lower volume of stir

material per unit length. Thus, when L_{pin} was almost the same as the top plate thickness, the stir material did not penetrate sufficiently to disrupt the original lapping interfaces (hereafter called un-welded lap) and did not strongly bond the top and bottom plates together. The cross sectional views of a weld made using v=224 mm/min (for L_{pin} = 3.2 mm) is shown in Figure 3-4. It is clear that the un-welded lap was not disrupted by the material flow during FSLW, and instead was slightly pushed into the bottom plate, due to the downward material flow induced by the rotating pin. Therefore the samples readily fractured, under loading, along the insufficient bond which was the un-welded lap (Mode 1) with low σ_{Lap}. It should be noted that advancing side in all of the cross-sectioned images (in this study) is kept on the left hand side.

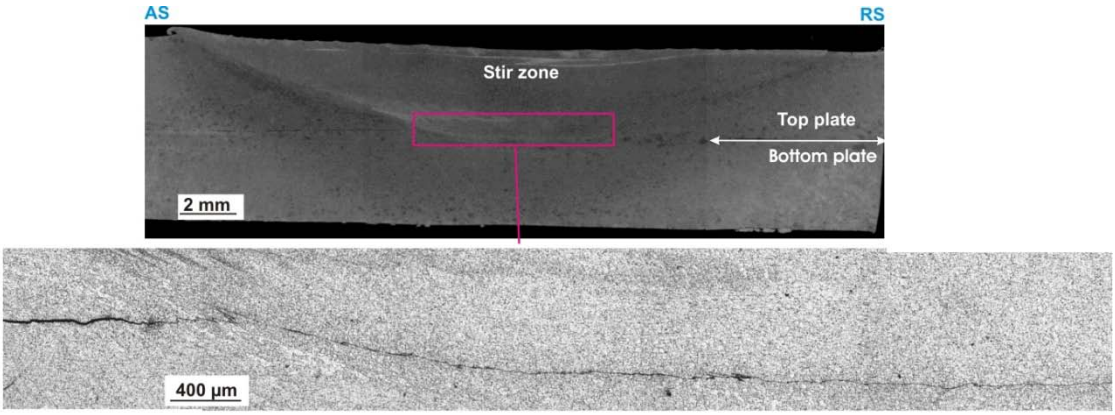

Figure 3-4 Cross sectional views of a Al 6060-T5 FSL weld made using L_{pin}=3.2 mm, ω =500 rpm and ν =224 mm/min, showing that original lapping interface were not disrupted by the material flow during FSLW and caused the subsequent fractured in Mode 1

Reducing *v* from 224 to 112 mm/min for L_{pin} = 3.2 mm had a large effect on increasing σ_{Lap} (Figure 3-2) with all samples fractured in Mode 2. This agrees with the general FS feature that with a lower *v* value, both stir zone temperature and stir volume increase facilitating a better bonding of the lapping plates. Cross sectional views of a weld made using v=112 mm/min (for L_{pin} = 3.2 mm) are shown in Figure 3-5. It is clear that un-welded lap was disrupted (at stir zone) by the material flow during FSLW and thus the top/bottom plates bonding were sufficiently high to force the fracture in Mode 2 manner with higher σ_{Lap} (compared to the specimens fractured in Mode 1).

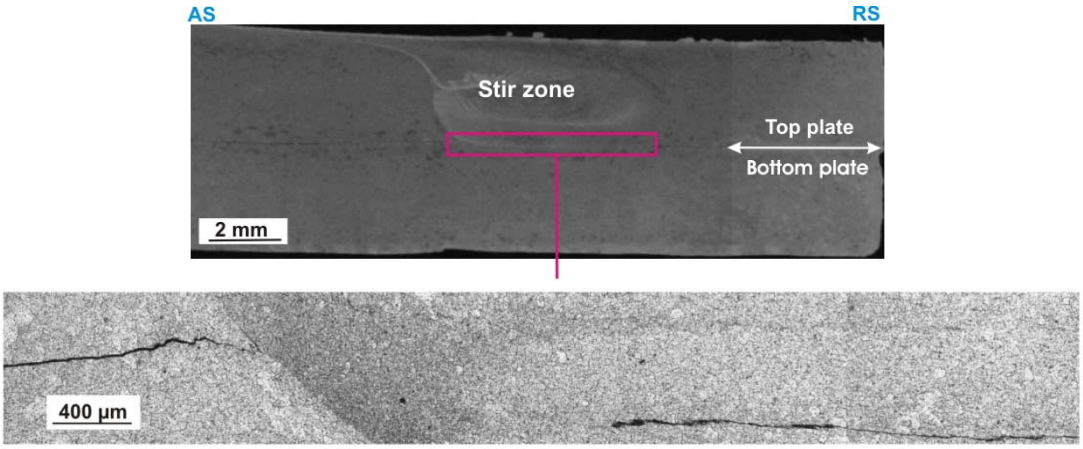

Figure 3-5 Cross sectional view of a Al 6060-T5 FSL weld made using L_{pin}=3.2 mm, ω =1000 rpm and ν =112 mm/min, showing original lapping interface were disrupted by the material flow during FSLW and caused subsequent fractured in Mode 2

When L_{pin} increased to 4.2 mm, a sufficient pin penetration was achieved. As already stated and shown clearly in Figure 3-2, the mode of fracture and σ_{Lap} did not change significantly from moderate (L_{pin}= 4.2 mm) to excessive penetration (L_{pin}= 5.2 mm) when *v* and ω were kept the same. This suggests that, once pin penetration is sufficient, the partial flow volume that causes the up-lift and thus hooking is largely the same, if other FSLW conditions are the same. Thus for the subsequent work of studying the details of hooking and how they affect σ_{Lap}, as presented in the following, only L_{pin} = 4.2 mm was used.

3.3 The Effect of ω and v on Hooking

General features of hooking are illustrated in Figure 3-6a using a FSL weld sample, where the stir zone has been outlined by the white dotted line and the formation of a hook outside, but very close to, the pin induced portion of the stir zone (nugget) is shown. In the nugget the commonly observed ring structure is apparent. As described in section 1.2.2, during FSLW the material around the rotating pin is sheared and driven downwards by the thread space. Due to this downward material flow, the material originally located at bottom plate is pushed outward as well as upward towards the top plate (on advancing side). This mechanical push-up causes the un-welded lap to curve upward in thermomechanical affected zone and hence forming the hook. Therefore it is reasonable to suggest that the flow volume in the bottom stir zone (indicated as $A_{B\text{-}SZ}$ in Figure 3-6a) correlates to the amount of pushing up the un-welded lap and thus hook size (*h*).

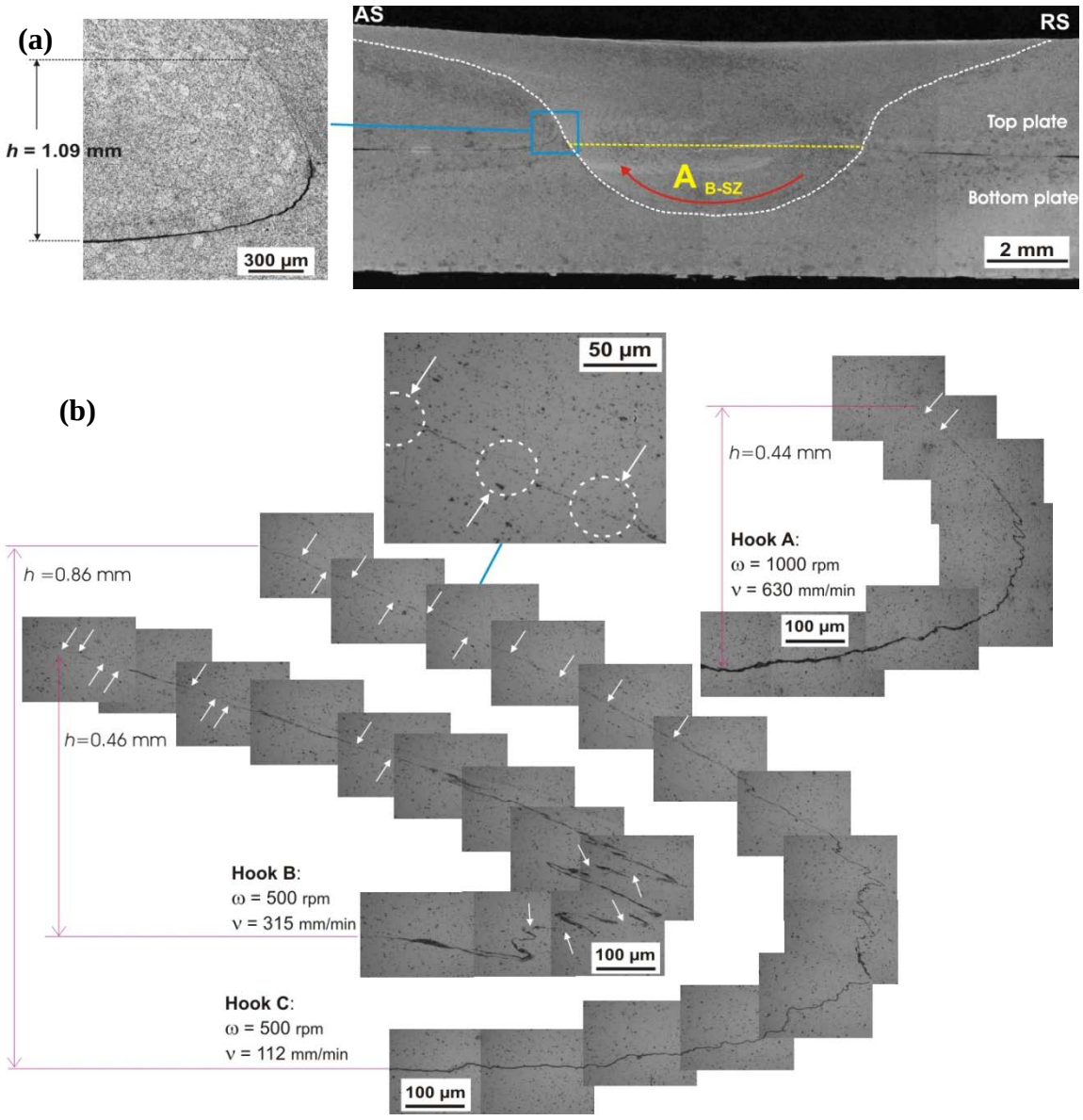

Figure 3-6 Cross sectional views of Al 6060-T5 FSL welds (a) the whole view of the weld made using ω = 1000 rpm and *v* = 224 mm/min showing hooking on the advancing side and next to the stir zone as outlined and indicating the flow direction in the stir zone during FS and (b) three hooks of welds made with various ω and *v* values as indicated. The small arrows point to locations of hook discontinuity

An *h* value only represents the vertical distance of the hook and has been used in literature for simplicity. It does not represent the length, the shape, the orientation and the continuity of the hook. To understand the features of hooking rather than just the vertical distance, three further hooks are shown in Figure 3-6b. Comparing Hook A in Figure 3-6b to that in Figure 3-6a, using the same ω =1000 rpm, *h* is lower with the higher *v* but both have a similar hook shape. Hooks B and C, both for the same ω = 500 rpm, in Figure 3-6b illustrate that they both curve more to the advancing side and a

large portion of each hook is quite discontinuous in locations pointed to by small arrows. This discontinuity is better shown in the higher magnification micrograph for Hook C where there is almost no un-welded lap inside the circled locations. A close examination shows the discontinuity even outside those circled regions.

The effect of ω on *h* for various *v* values are given in Figure 3-7. The general trend of increasing *h* when either ω increases or *v* decreases, in common with literature [15, 16, 21] is evident, but not totally when considering the whole ω and *v* ranges for the present data. There appears to be a maximum *h* value (h_{Max}) at ~ 1.2 mm. For the low to mid range of *v* (112-315 mm/min), ω=1000 rpm may resulted in *h* to have reached or close to h_{Max} and thus doubling ω (to 2000 rpm) had not changed significantly *h*. The top plate was 3 mm thick and, as h_{Max} is only ~ 1.2 mm, there must be a limit to which the upward flow in the lower portion of the stir zone during FSLW could push the un-welded lap vertically up to. For the case of very high *v* (630 mm/min), ω higher than 2000 rpm was needed for *h* to reach h_{Max}.

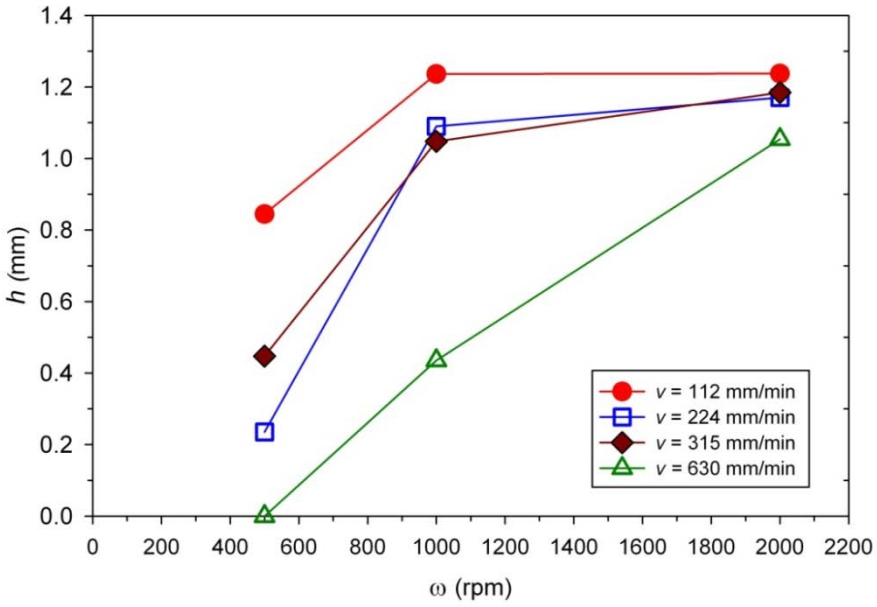

Figure 3-7 *h* plotted as a function of ω for various v values

To understand further the physical nature of hooking in relationship to stir flow, three traces of hooks together with their relative locations to the pin, and measured $A_{B\text{-}SZ}$ values are shown in Figure 3-8 (see section 2.3.4 for the meaning of $A_{B\text{-}SZ}$). The distances of the hooks to pin are ~ 2 mm or higher, meaning that the width of the nugget is significantly larger than the pin diameter for each case. The extent to which the hook has been pushed and the values of $A_{B\text{-}SZ}$ in Figure 3-8 suggest that increasing ω

increased the pin induced stir volume, in agreement with what is generally understood. However, an increase in stir volume due to the increase in ω did not necessarily result in an increase in *h*. This is clear for the cases of ω=1000 and ω=2000 rpm that values of *h* are basically the same but $A_{B\text{-}SZ}$ values are significantly different.

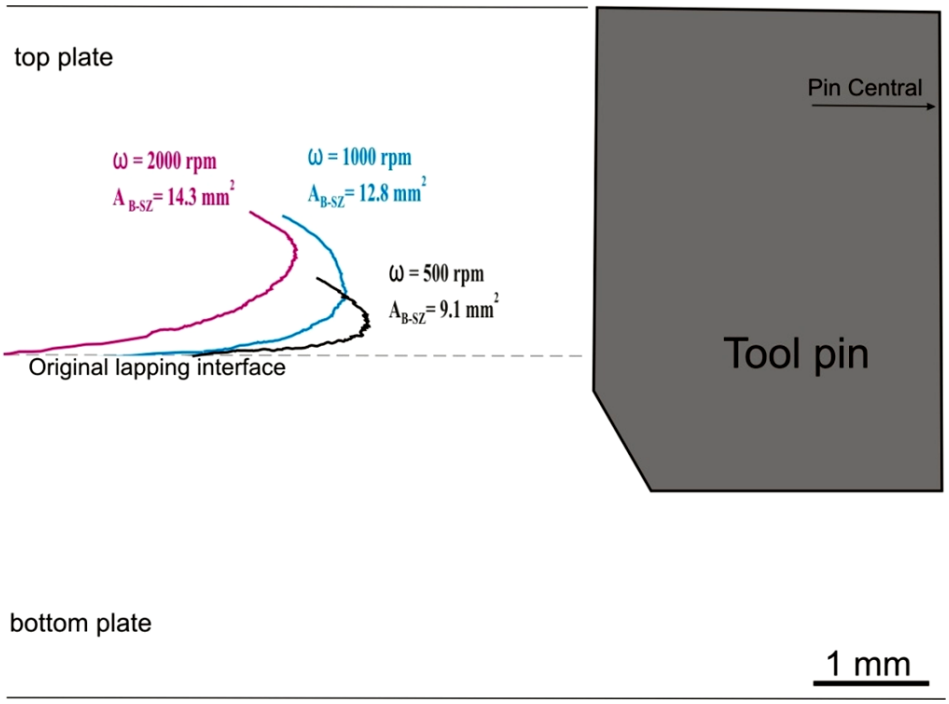

Figure 3-8 Traces of hooks formed in welds made using *v* = 112 mm/min and ω as indicated. Also the relative location of the pin is indicated and the measured $A_{B\text{-}SZ}$ values are given

Values of $A_{B\text{-}SZ}$ are plotted against ω for the various *v* values in Figure 3-9. Extrapolating all the data to ω= 0 rpm, $A_{B\text{-}SZ}$ seems to reach to a value close to the area of pin penetration to the bottom plate ($A_{pin\ penetration}$) which is ~ 7.2 mm^2 ($D_{pin} \approx 6$ mm $\times$ 1.2 mm = 7.2 mm^2). $A_{B\text{-}SZ}$ increased as ω increased and the rate of increase ($dA_{B\text{-}SZ}/d\omega$), when ω increased, was higher in the low-mid ω range (500-1000 rpm) than that when ω was high (1000-2000 rpm). The stir volume affecting *h* is illustrated by plotting *h* values from all the samples against $A_{B\text{-}SZ}$ in Figure 3-10. The initial increase in the extra bottom flow volume assisted greatly the up-lift flow and thus *h*. However, there was a definite stir volume ($A_{B\text{-}SZ} \approx 10$ mm^2) at which *h* reached h_{Max}, and further increase of stir volume did not result in increasing *h*.

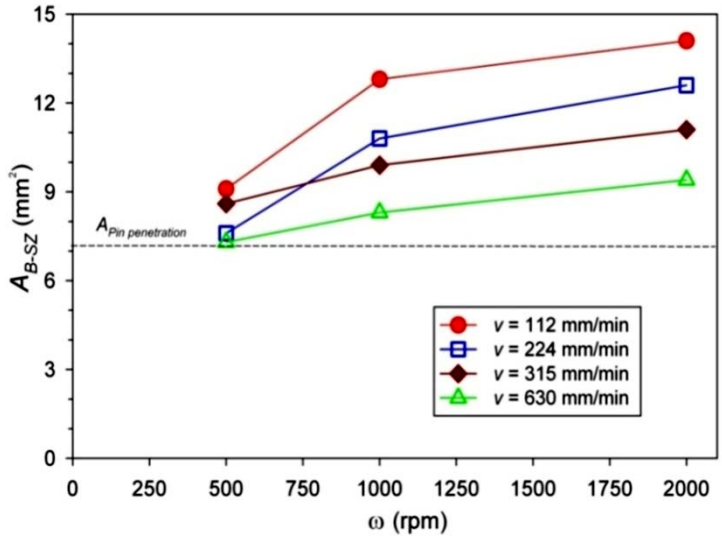

Figure 3-9 $A_{B\text{-}SZ}$ plotted as a function of ω for various ν values

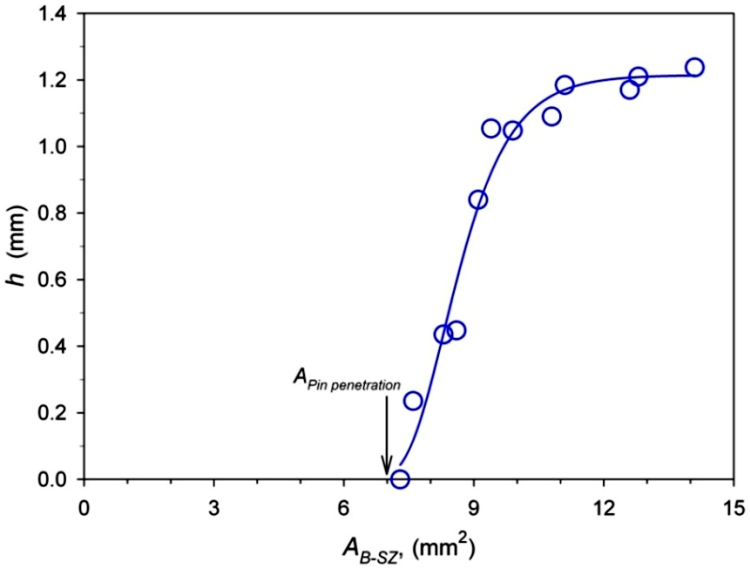

Figure 3-10 Measured *h* plotted as a function of $A_{B\text{-}SZ}$

It is clear by examining the hook traces in Figure 3-8, if a hook was to be unfolded back along the original lapping surfaces, the end of the hook would not reach the pin. This means that for each case a portion of the un-welded lap had been stirred and had disappeared. Therefore, on one hand, a higher stir volume caused more up-lift. Whilst on the other hand a larger stir volume was associated with more stir and mixing, thus more dispersal of the un-welded lap and shortening more the length of the hook. Therefore when *h* reached ~ 1.2 mm, further higher stir volume may have helped efficiently disrupt and disperse the un-welded lap, resulting in no further increase in *h*.

Selected traces of stir zone temperature (T_{SZ}) are given in Figure 3-11. In each trace, there are disturbance in the peak temperature region because the thermocouple was

pushed slightly by the lower stir flow when the pin approached the thermocouple. These traces show that the peak temperature of the stir zone ($T_{SZ\text{-}P}$) increased as ω increased and also suggest that the rate of increase ($dT_{SZ\text{-}P}/d\omega$), when ω increased, was high in the low-mid ω range (500-1000 rpm) and low when ω was high (1000-2000 rpm). This is consistent with the exponential rise of T_{SZ} as a function of ω, observed in FSW of aluminum alloys [88, 89].

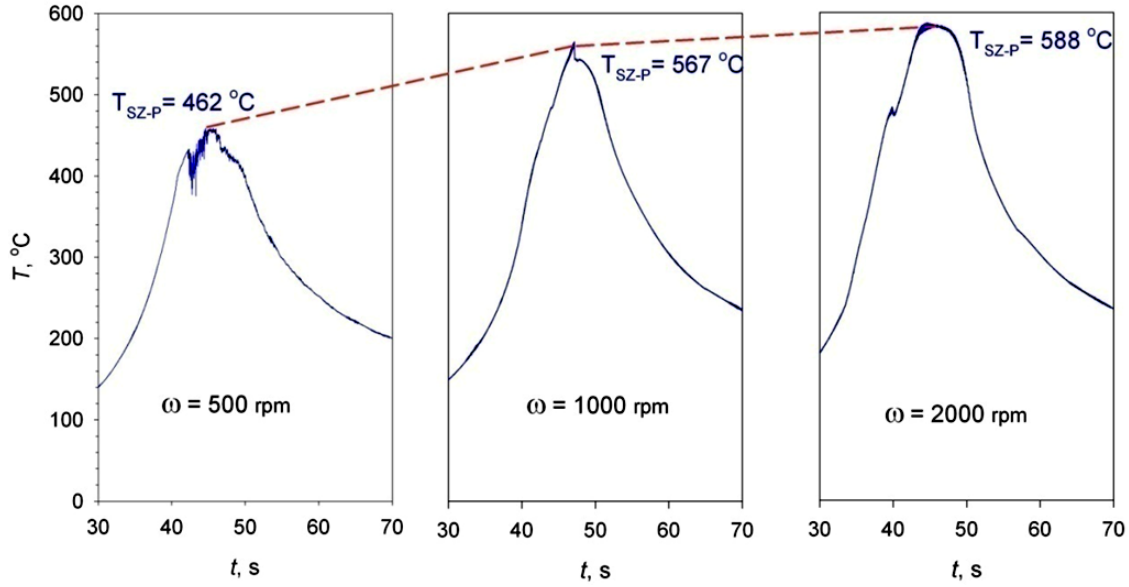

Figure 3-11 T_{SZ} measured during FSLW using v = 112 mm/min and various ω values as indicated. Increasing $T_{SZ\text{-}P}$ as ω increased is also indicated

Returning to Figure 3-9, if the mechanical effect of a higher ω was dominant for increasing the stir volume, as suggested by Lee et al [22], this effect diminished when ω increased as demonstrated by the decrease in $dA_{B\text{-}SZ}/d\omega$ with the increase in ω. The reason for this is unclear. Comparison of the peak temperature trace in Figure 3-11 (for 112 mm/min) to the curve for 112 mm/min in Figure 3-7, showed similarities in that the rate (either $dT_{SZ}/d\omega$ or $dA_{B\text{-}SZ}/d\omega$) of increase was high when ω was low and in that the rate diminished as ω increased. Thus, as reasoned by Dubourg et al [6], increasing temperature to enhance plasticity for a higher stir volume is reasonable. However, their reasoning of a higher stir volume results in a higher amount of up-lift and thus a larger h value is only partially correct, as already explained and shown in Figures 3-10 and 3-11.

An EBSD map of hooking region (for the weld made using v=112 mm/min and ω=1000 rpm) is presented in Figure 3-12. In the orientation map (Figure 3-12b) individual grains are coloured according to their crystallographic orientations relative to WD, with an

orientation code triangle being shown in the bottom. For simplicity, the trace of hook (as seen in Figure 3-12a) has been superimposed on the orientation map in Figure 3-12b. It is clear that grain orientation at TMAZ and SZ (affected by the material flow during FSLW) is notably different from that of HAZ region. However the shape of hook (being curved toward the advancing side) and grain orientation along the vertical part of hook indicates that material flow during FSLW has not only lifted up the un-welded lap, but also pushed it toward the advancing side.

As described in section 1.2.2, during FSW, immediately next to the pin the plasticized material is driven downward by the rotating threads. Due to this downward material flow, the material originally located at the lower plate is pushed upwards (forming the nugget zone) and thus causes the up-lifting of un-welded lap (Figures 3-12c). Later, the shoulder flow zone is formed (by the rear portion of the tool shoulder) [14] and the material at top of nugget is transported around the pin from retreating side to the advancing side. Due to this shoulder-induced material flow, the up-lifted un-welded lap is pushed and curved toward the advancing side (Figure 3-12d), resulting in further shearing, stretching and disrupting of un-welded lap which causes the hook to become shortened and discontinuous. These results suggest that a hook is depressed by the shoulder flow thus limiting the h_{Max} value.

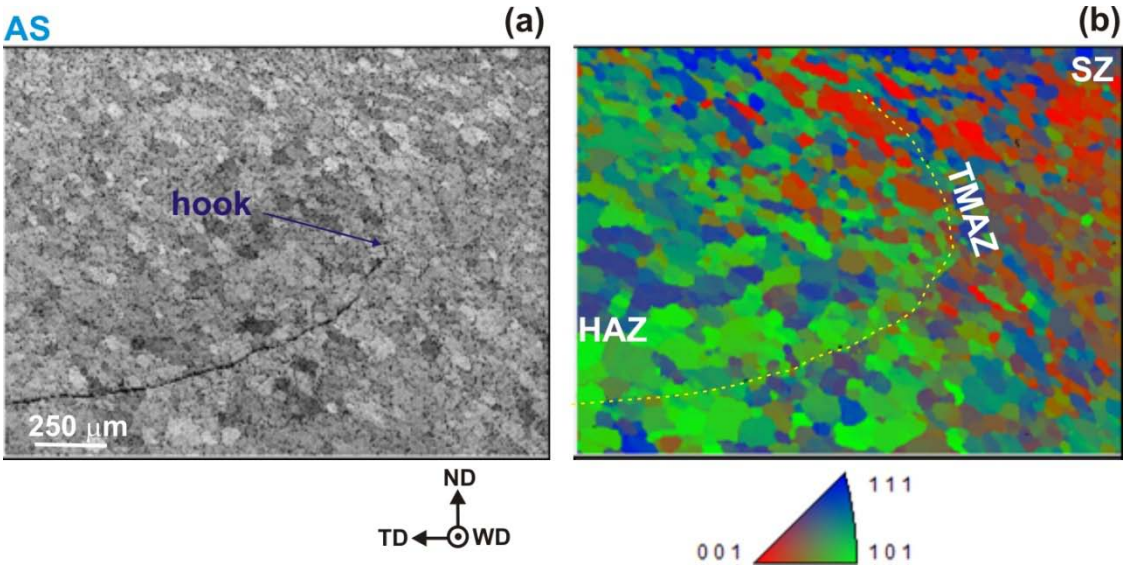

Figure 3-12 EBSD map of hooking region for the weld made using ν =112 mm/min and ω =1000 rpm (a) image quality map, (b) image orientation map, (c) schematic illustration of pin-induced flow, lifting up the un-welded lap in nugget zone and (d) schematic illustration of shoulder-induced flow, pushing the un-welded lap towards advancing side

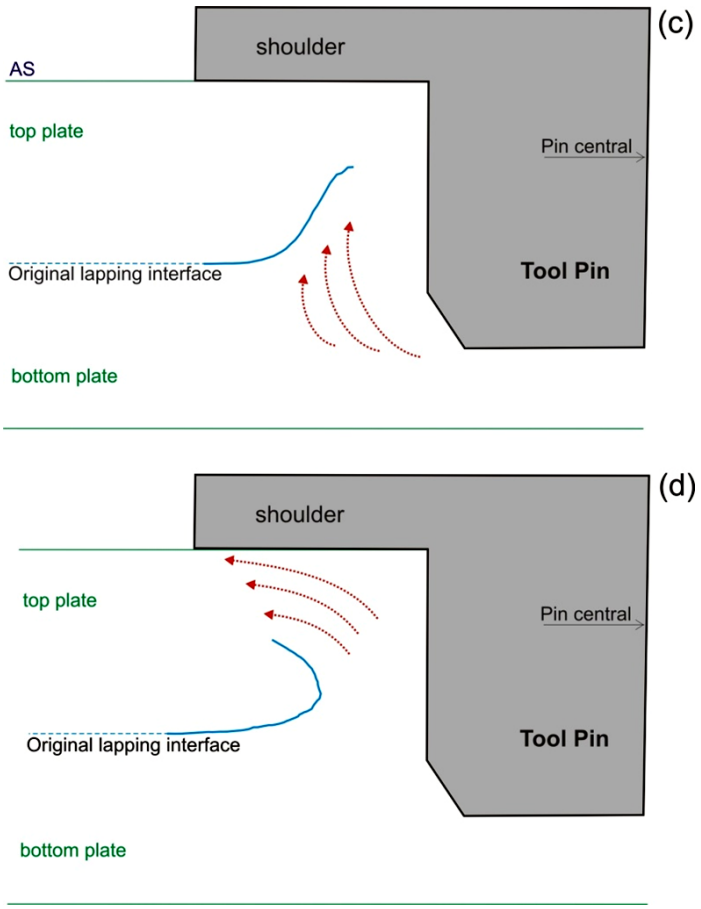

Figure 3-12 continued.

3.4 The Effect of ω and *v* on Joint Strength

Values of σ_{Lap} are plotted versus ω for various *v* values, as shown in Figure 3-13. A general trend of decreasing σ_{Lap} with increasing ω may be seen, although the trend is not followed for the whole ω range when *v* is either too low or too high. Samples made using ω=1000 and ω=2000 rpm fractured in Mode 2 manner. Samples made using ω=500 rpm fractured in various manners. Samples of ν=112 mm/min and ν=224 mm/min fractured in Mode 2 and 3, respectively. Samples of ν=315 mm/min and ν=630 mm/min fractured in Mode 3a and Mode 1a, respectively. Mode 3a is basically the same as Mode 3 in that the fracture is located in HAZ, with the former in HAZ of the bottom plate and the latter in the top plate HAZ. Mode 1a is largely the same as Mode 1 in the way of fracturing across the lower part of the nugget, with the slight difference being that in Mode 1a the fractured path is well inside the bottom plate. An example of this mode of fracture is shown in Figure 3-14, where we can clearly see a lack of joint. This is the consequence of the *v* value being too high and an insufficient flow for a complete

bonding, resulting in slightly lower σ_{Lap} comparing to σ_{Lap} values of samples made using lower *v* values.

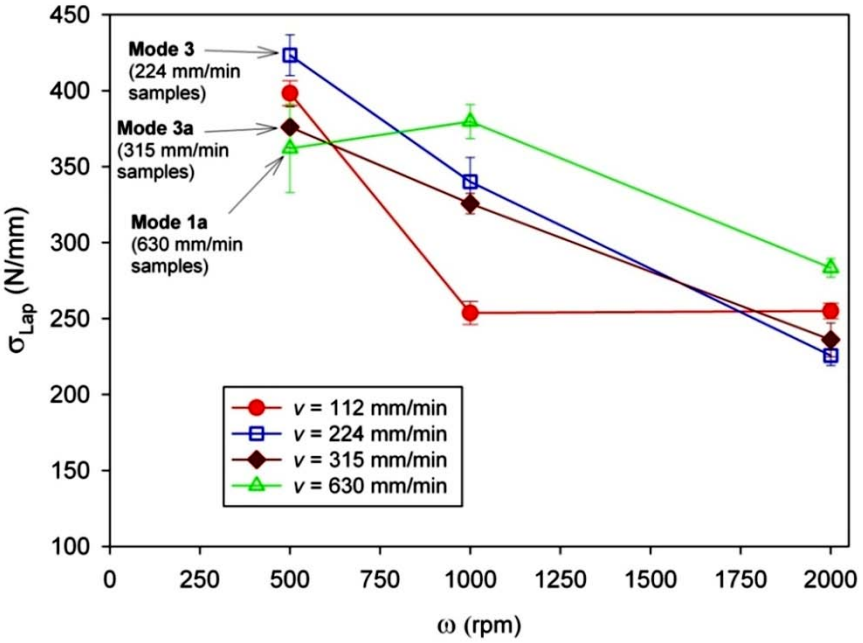

Figure 3-13 σ_{Lap} plotted as a function of ω for various *v* values as indicated. Modes of fracture are indicated as Mode 1a and Mode 3/3a and for the rest of samples fractured in Mode 2 (not labelled)

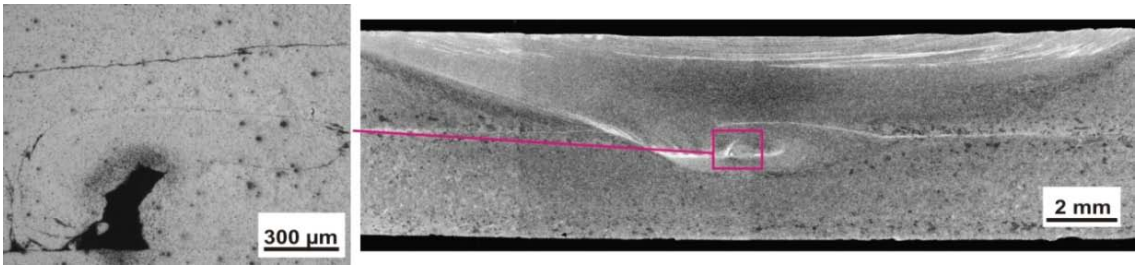

Figure 3-14 Cross sectional view of the FSL weld made using ω =500 rpm and *v* =630 mm/min, displaying lack of joint at nugget zone

The effect of *h* on σ_{Lap} is now examined using data plotted in Figure 3-15. Data from samples fractured in Mode 1a and Mode 3/3a are also plotted for comparison. The high σ_{Lap} for samples fractured with Mode 3 has suggested that the presence of small hooks (with *h* up to 0.2 mm) is not necessarily the dominant factor affecting σ_{Lap}. Softening in HAZ is another important factor determining where local deformation occurs leading to fracture. The strength of material in the hook location can be significantly higher, forcing deformation and fracture to occur in the softest location in the HAZ. As

explained in section 3.2, for a weld (224 mm/min and 500 rpm) with a small *h* and fractured in Mode 3 manner, σ_{Lap} = 422 N/mm is slightly higher than σ_{BoP} (406 N/mm) for the bead-on-plate sample (made using same ν, ω). This shows that the strength of material in the HAZ of a lap weld can be slightly different from that in a bead-on-plate weld.

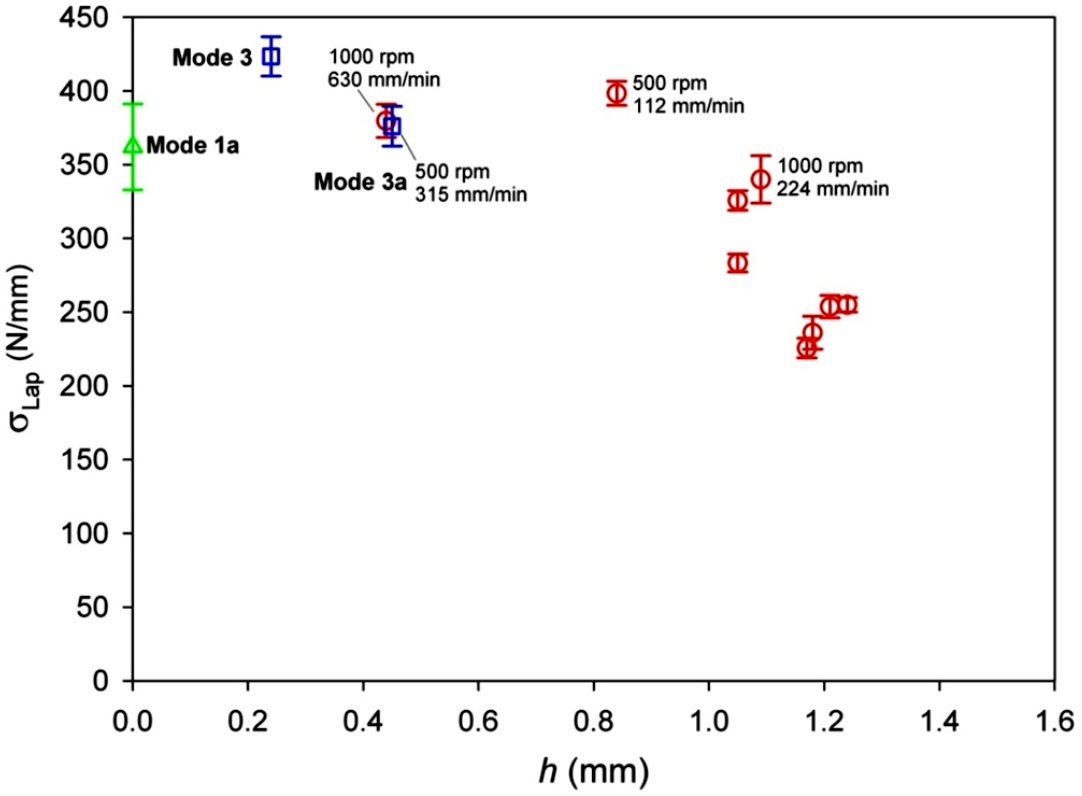

Figure 3-15 σ_{Lap} plotted as a function of *h*. Modes of fracture are indicated as Mode 1a and Mode 3/3a and for the rest of samples fractured in Mode 2 (not labelled). Some speed conditions are also indicated.

Data in Figure 3-15 also suggests that strength reduction due to hooking only becomes more significant when *h* reached a critical value. In the present case, as shown in Figure 3-15, such critical *h* ($h_{Critical}$) was ~ 0.9 mm. This is a large value, considering that the top plate was only 3 mm in thickness. The fact that σ_{Lap} is not very sensitive to *h* when $h < h_{Critical}$ suggests again and strongly that *h* is not the only factor. Take for instance the samples made with ω = 500 rpm and *v* = 112 mm/min. As is clearly shown in Figure 3-6, *h* = 0.86 mm but a large portion of the hook is discontinuous and an effective *h*, although it is difficult to define, should be considerably lower. Furthermore, the hook extended to a larger angle to the tensile loading direction resulting in crack propagation

normal to the loading direction more difficult. These two factors must have contributed to the high σ_{Lap} although the measured *h* is high (Figure 3-15).

The two factors of hook shape and continuity can be discussed further by examining two selected cross sections of tensile shear loaded samples of the weld made using ω = 500 rpm and *v* = 112 mm/min. A hook in a cross section, as shown in Figure 3-6, is viewed as a thin, curved and discontinued line. As shown in Figure 3-16a, for the fractured sample, the original hook has opened but the main fracture was not due to the crack propagation from the tip of the hook. Rather, the main fracture path initiated in a distance behind the end of the hook. This suggests that this particularly orientated hook of the weld may not have affected σ_{Lap} significantly. For the sample shown in Figure 3-16b, loading was interrupted before fracturing. Although, the hook has opened but it is clear that a main fracture has not developed even at a high loading level which is slightly higher than (331/404) 80% of σ_{Lap}. This high load for the stage that is associated with the opening of the hook without fracturing means that the presence of that particular hook does not reduce significantly σ_{Lap}.

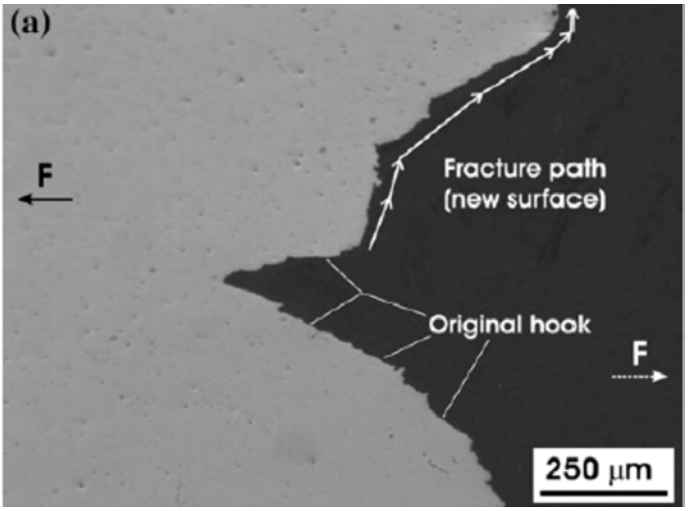

Figure 3-16 Cross-sectional views of hook regions after tensile shear loading of weld samples made using ω =500 rpm and v =112 mm/min, (a) sample loaded to fracture at σ_{Lap}= 404 N/mm showing that the main fracture path did not follow on the end of the hook and (b) sample loaded till σ = 331 N/mm showing the absence of the main fracture. In these images, the loading directions during testing are also indicated.

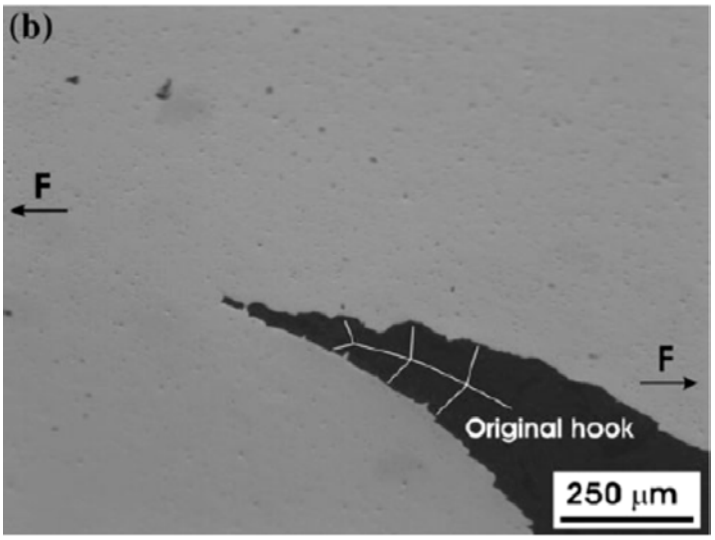

Figure 3-16 continued.

Another important factor, which affects fracture location and strength, is the strength of the material ahead of the tip of the hook. It should be noted that the correlation between hardness and yield strength of metallic materials has been widely studied in literature and positive relationship between the hardness and yield strength (either linear or curvilinear) have been reported [90]. Thus the local hardness of a material can be considered as an indication of local strength. Three hardness traces, measured at 0.1 mm above the tip of hook, are given in Figure 3-17. Hardness traces with similar profiles have been given in many studies of FSW of heat-treatable aluminium alloys, although a prediction of how ω and *v* affect the hardness values is difficult to make [32, 91, 92].

A important feature of Figure 3-17 is that for the sample made using ω= 500 rpm and *v*= 112 mm/min, the hook location is about 2 mm away from the lowest hardness location in HAZ. Thus, the local hardness, which is an indication of strength, of the material ahead of the hook is high. Although *h* is high at 0.86 mm, σ_{Lap} remains high (at 398 N/mm) due to the deformation and fracture ahead of the hook located in relatively stronger material. On the other hand, the hook is significantly closer (< 1mm) to the softest location for each of the other two samples and hardness and thus strength in hook location is also lower.

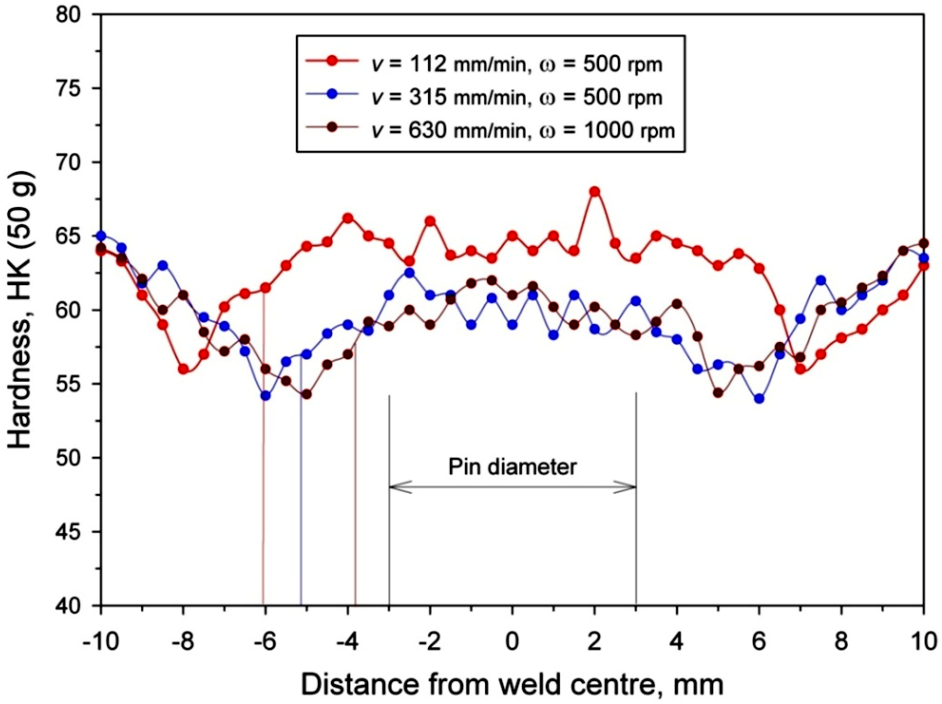

Figure 3-17 Knoop hardness distributions (transverse to welding direction measured at 0.1 mm above the tip of the hook) of welds made using *v* and ω values as indicated. The size of the pin is also indicated and each other vertical line indicates the location of the tip of hook.

Returning once again to hook quality, rather than just *h*, playing an important role in fracture, further explanation can be given by comparing Hook A (ω=1000 rpm, ν=630 mm) to Hook B (ω=500 rpm, ν=315 mm) in Figure 3-6b. Although both have a similar *h* value and a similar hardness profile near the hook and HAZ locations (Figure 3-17), the higher ω resulted in a more normal (to loading direction) hook and the lower ω resulted in a more torturous and discontinued hook. However, the more torturous and discontinuous hook did not result in a higher σ_{Lap} (Figure 3-15). This is because σ_{Lap} has been limited by the strength in HAZ in these samples, fractured with Mode 3a. On the other hand, using the same ω (1000 rpm), Hook A (Figure 3-6b) and the hook in Figure 3-6a are similar in shape but different in *h*. As a result, σ_{Lap} is lower with the higher *h*.

Thus, it can be concluded that when *h* is less than a certain value, which is not small and is about 30% of the plate thickness (t_{Plate}) in the present case, *h* is only partially indicative of how a hook affects σ_{Lap}. The orientation, continuity and how winding a

hook is, plays an important role, as has been explained. For this reason, there should also be a significant scatter of the data when considering simply how h affects σ_{Lap}, as is seen in Figure 3-15. However, when the measured h is higher than $h_{Critical}$, although there is still a significant scatter of data, the trend of a rapid decrease in σ_{Lap} as h increases is clear. This is likely the increasingly dominant effect of increasing h on decreasing the load bearing area. This decrease in σ_{Lap} is however soon self arrested as h does not keep increasing, as already explained. Instead, h only increases to h_{Max} (~ 1.2 mm) which is only moderately higher than $h_{Critical}$ (~ 0.9 mm).

3.5 Stress Distribution during Tensile Shear Testing and Joint Strength

As explained in section 2.5, finite element modelling (FEM) of tensile shear testing was conducted to understand how the stress distribution during testing affected the fracture behaviour of FSL welds. For illustration purposes, the simulation analysis of stress distribution conducted for the case of an ideal lap joint with zero hook (h = 0 mm). The modelling results, as shown in Figure 3-18a (the top illustration), show a high stress concentration initially (before local bending) in the regions of the un-welded lap tips. For the case of no softening, when the applied stress in locations of the sample close to the sample grip reaches only 50 MPa, the highest effective stress (misses stress) reaches ~180 MPa in stress concentration region, 3.6 times the applied stress. In a joint sample, as there is a local region of the lowest strength in HAZ, which is close to the un-welded lap tip, material in that region should deform, resulting in local bending and effective straightening of the sample being tested. This was the case for all tested samples and is shown in examples given in Figure 3-3.

After local deformation and strengthening, the geometry of the sample can be described as that given in Figure 3-18a (the bottom illustration). Samples fractured in Mode 2 and Mode 3 all displayed this geometry after local bending, as can be observed in the two examples in Figure 3-3 b-c. Then, as shown in the bottom illustration in Figure 3-18a, the magnitude of stress concentration has reduced considerably. The ratio of the highest stress to the applied stress may be seen at ~ 1.2. Thus, if the lowest strength location is a distance away from the un-weld lap tip (or the location of a small hook), and the strength is significantly lower (by more than ~ 20%), deformation can preferentially occur in that region (away from the un-weld lap tip); fracturing in Mode 3 manner.

However if the location of the lowest strength is very close to the un-welded lap tip (hooking location) then the sample should deform and fracture in Mode 2 manner.

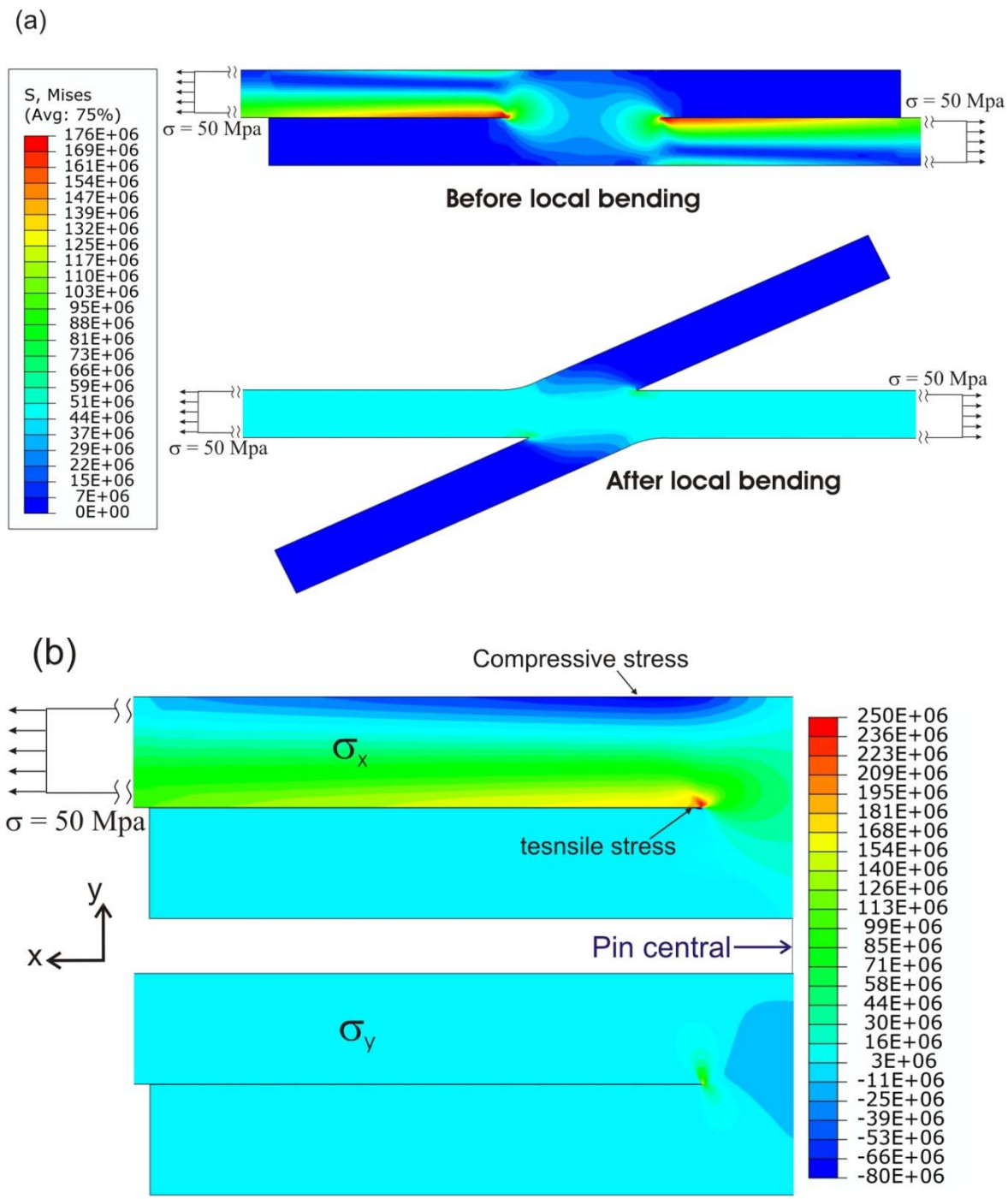

Figure 3-18 Simulation results showing distribution of stresses during tensile shear testing, (a) effective stress before bending (top) and after bending/straightening (bottom) and (b) normal stresses in horizontal and vertical directions (half sides shown)

Bending in tensile shear tested samples can be further explained by examining the simulation result in the form of normal stresses in both horizontal (x) and vertical (y) directions, shown in Figure 3-18b. High σ_x (tension) in the bottom of the top plate and σ_x gradually reducing to negative (compression) towards the plate surface of the top plate should mean bending upward to relax the stress concentration. The distribution of σ_y should also assist in the sample bending/rotating to the final sample testing geometry shown in the bottom illustration of Figure 3-18a.

3.6 Mechanism of Local Deformation during Tensile Shear Testing

Fracture surfaces of a tensile shear tested sample (taken from a weld with *h*=0.44 mm) are presented in Figure 3-19. The sample fractured in mode 2, with cracking initiated from the hook location. The fracture surface corresponding to hook location, as shown in Figure 3-19b, showed a highly brittle failure pattern. That is due to the presence of oxides along the hooking feature, which resulted in minimal bonding of material at that location and thus a brittle local failure. However at the locations away from the hook region, for instance location P2 and P3 as indicated in Figure 3-19a, fracture surfaces exhibited a highly ductile dimple pattern as seen in Figures 3-19 c-d. It is known that the dimple pattern is a typical feature of ductile fracture, which progresses by the process of void nucleation, growth and coalescence [93-95]. The above results indicate that the cross sectional area above the hooking region has sustained the tensile load, during testing, as evident by the ductile dimpled structure on the fracture surface.

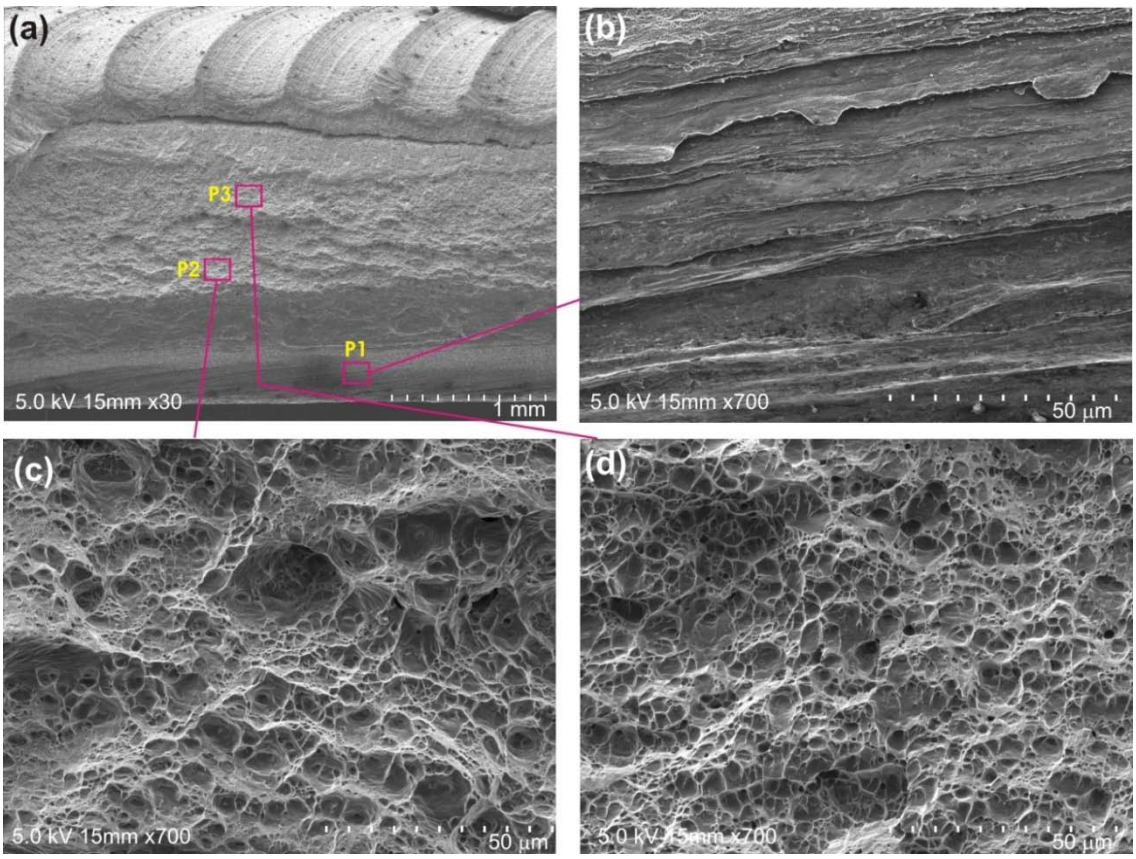

Figure 3-19 Fracture surface of a tested sample from a weld made using ν =630 mm/min and ω =1000 rpm, (a) fracture surface, (b) enlarged view of area P1 in Figure 3-19a where hook is located, (c) enlarged view of area P2 in Figure 3-19a which is located above the hooking region and (d) enlarged view of area P3 in Figure 3-19a

Local plastic deformation induced by the tensile shear loading was further investigated using EBSD study of the fractured and original (before testing) samples. Fractured sample and the location where EBSD maps were obtained, indicated by the red rectangle, is shown in Figure 3-20a. It can be seen that the selected area is sufficiently distant from the hooking region and thus represents the regions which fractured by the ductile dimpled structure (Figure 3-19 c-d), under loading. The EBSD maps obtained from the deformed sample is presented in Figure 3-20 b-d, and the EBSD maps corresponding to same location for the original sample is presented in Figure 3-20 e-g. In the presented orientation maps (Figure 3-20c and Figure 3-20f), individual grains are coloured according to their crystallographic orientations relative to WD, with an orientation code triangle being shown in the bottom.

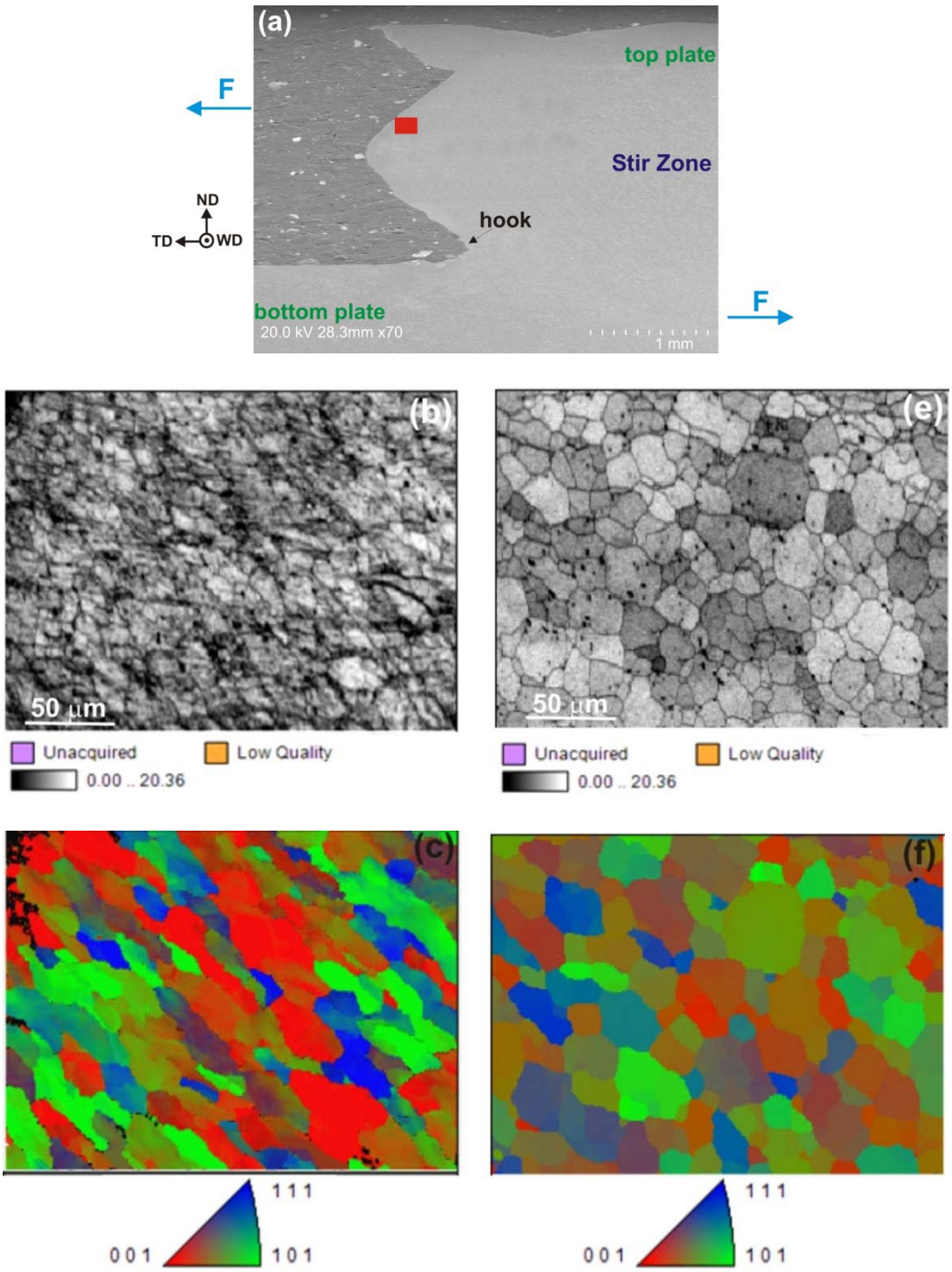

Figure 3-20 (a) Micrograph of fractured sample, location where EBSD maps were obtained is indicated using a red rectangle, (b) EBSD pattern quality map of deformed sample showing elongated grains, (c) EBSD orientation map of deformed sample, (d) EBSD grain boundary map of deformed sample, (e) EBSD pattern quality map of original sample showing fine and recrystallised grains, (f) EBSD orientation map of original sample and (g) EBSD grain boundary map of original sample

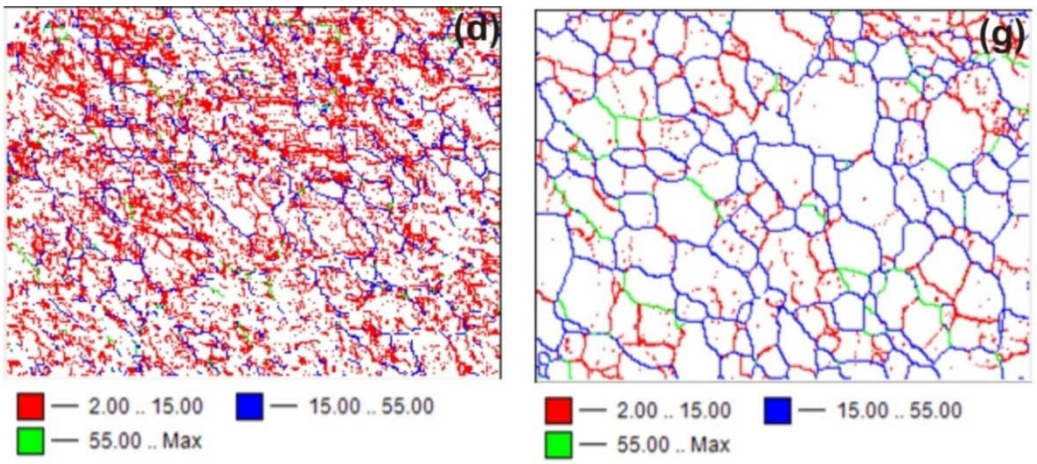

Figure 3-20 continued.

It can be seen from Figures 3-20 e-g that microstructure of the original sample (before testing) consists of the fine and fully recrystallized grains with dominant high angles grain boundaries (HAB), as marked by the blue lines in Figure 3-20f. This microstructure is consistent with general microstructure observed in stir zone of aluminium alloys friction stir welds [2, 96-98]. As during FSW, plastic deformation (induced by the rotating pin) and recrystallisation occur simultaneously at elevated temperatures, thus dynamic recrystallisation must have played a major role in obtaining that microstructure [97, 98].

On the other hand, the microstructure of the fractured sample (as seen in Figures 3-20 b-d) suggests that original grains have elongated (thinned) due to the strain imposed during loading. Also the generation of abundant low angle grain boundaries (LAB), as marked by the red line in Figure 3-20c, with corresponding notable changes of local crystallographic orientation within the individual grains indicates the grain subdivisions. It has been suggested [88, 89, 99] that a large number of grains rotate during tensile deformation and are divided into subgrains due to the operation of multiple slip systems (within the grains) to maintain the coherency of grains across their grain boundaries in relation to surrounding grains. The obtained EBSD results together with ductile fracture pattern achieved under loading are results of high ductility of aluminium alloys, provided by FCC crystallographic structure offering many slip systems for deformation.

3.7 Summary

When the pin only slightly penetrates the bottom plate, a sufficiently low welding velocity (v) allows for a sufficient bonding of the lap plates and for the joint strength (σ_{Lap}) to be close to the strength of FS bead-on-plate samples (σ_{BoP}). A more sufficient penetration allows for *v* to increase while maintaining σ_{Lap} to be close to σ_{BoP}.

When pin penetration is sufficient, increasing rotation speed (ω) or decreasing (v) increases a high stir volume per unit length in the bottom stir zone ($A_{B\text{-}SZ}$). The rate, either $dT_{SZ}/d\omega$ (T_{SZ} – stir zone temperature) or $dA_{B\text{-}SZ}/d\omega$, is high when ω is low and in both cases they diminish as ω increases. This suggests the effect of ω on $A_{B\text{-}SZ}$ more dominantly through the effect of ω on T_{SZ} and thus the plasticity of the stir zone. The initial increase in $A_{B\text{-}SZ}$ above the corresponding area of the rotating pin (which is equal to minimum $A_{B\text{-}SZ}$) rapidly increases the vertical distance of the hook (*h*) to a maximum value (h_{Max}), which was equal to 40% of the thickness of the top plate (t_{Plate}) in the present study. Evidences have suggested that a hook is depressed by the shoulder flow thus limiting the h_{Max} value.

When *h* tends to zero, despite the existence of un-welded lap acting as a pre-crack and high stress concentration around it due to the lap geometry (during tensile shear testing), σ_{Lap} is very close to σ_{BoP} (in butt joint geometry). This is due to significant specimen bending (during tensile shear testing), offered by the high ductility of aluminium alloy due to its FCC structure, and thus reorientation of the specimen to a testing geometry close to tensile test geometry; diminishing considerably the stress concentration.

It was found that *h* does not necessarily have a strong influence on σ_{Lap} when $h < \sim 30\%\ t_{Plate}$. This is because the end of a hook is not normally located in the lowest strength location of the HAZ, which competes with hooking as the preferred location of fracture. Also a more tortuous and discontinuous hook can reduce the effect of *h* on σ_{Lap}. When $h > \sim 30\%\ t_{Plate}$, σ_{Lap} decreases more sharply when *h* increases, due to the dominant effect of an increasingly larger reduction in load bearing area.

4. Hooking and Fracture Strength of AZ31B FSL Welds

In this chapter, the results are given to illustrate first the effect of FSLW parameters on the formation and characteristics of hooks in AZ31B-H24 welds. It will be shown that hooking for AZ31B-H24 welds differ significantly to that found for Al 6060-T5 welds. Then the effects of hook size, microstructural evolution, subsequent microhardness distribution and lack of bending during testing on fracture strength of AZ31 welds are presented in details. Different mechanical behaviours due to the use of different alloys are also explained. To further understand the effect of hook orientation on fracture strength, results of hook orientation experimentation/testing and subsequent FEM simulation of stress distribution during tensile shear testing are presented in detail. Finally, the effects of loading geometry on deformation mechanism and thus fracture behaviour are discussed following detailed observations of microstructure and fracture surface of tested samples.

4.1 Hook Formation

4.1.1 The Effect of ω, ν and L_{pin} on *h*

Values of *h* affected by various FSLW parameters (ω, ν, L_{pin}) are plotted in Figure 4-1. It can be seen that the use of low ω=500 rpm has resulted in small size hooks ($h < 0.4$ mm) for all L_{pin} and ν values used. Increasing ω from 500 to 1000 rpm caused a substantial increase in *h* value for low to medium ν range (112-224 mm/min). However further increase of ω from 1000 to 1400 rpm resulted in little increase in *h.* Also it can be seen that for ν=450 mm/min, ω did not affect *h* and the *h* values are low. The results (for 112-224 mm/min) are in agreement with general trends observed in FSLW of Al 6060 (section 3.3), in which either increasing ω or decreasing ν resulted in larger *h* value. Furthermore, comparing the *h* values for the welds made using the same welding speeds (ω, ν) but different L_{pin} values of 2.7 and 3.7 mm (representing slightly and moderate bottom plate penetration) reveals that use of L_{pin}=3.7 mm resulted in slight increase of *h.* This is also similar to the observations made in FSLW of 6060 (section 3.2).

As explained in section 3.3, in FSLW of Al 6060, the significance of ω on *h* is through its effect on the temperature of the stir zone and thus the plasticity of SZ, affecting the stir flow volumes which cause up-lifting of lapping interfaces. However as explained in section 1.3.2, the current literature on magnesium alloys FSLW lacks the experimental

data on how welding speeds are related to the temperature of SZ during welding. Therefore the temperature of SZ was recorded during all FSLW experiments and results are discussed in following.

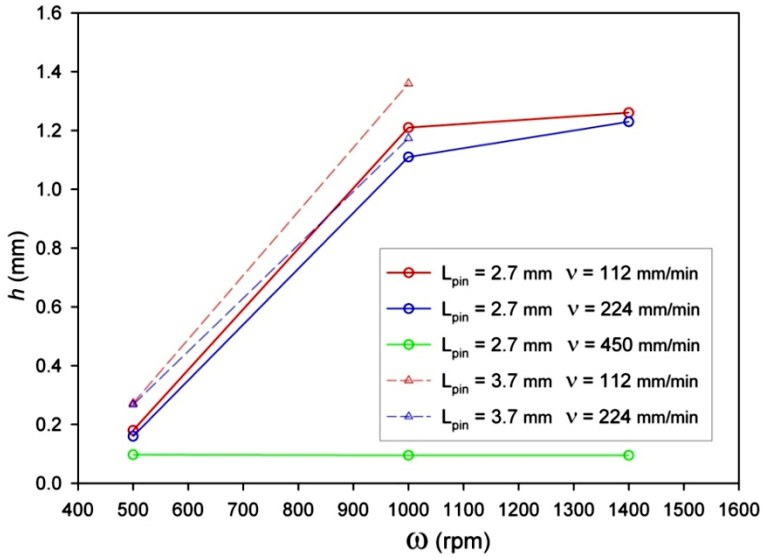

Figure 4-1 *h* as function of ω for AZ31 welds made using various ν and L_{pin} values

In Figure 4-2 the peak temperature of the stir zone ($T_{sz\text{-}p}$) at the lapping interface location, as described in section 2.2.5, are plotted as function of ω for the welds made using same L_{pin} value of 2.7 mm. It is clear that $T_{sz\text{-}p}$ increased as ω increased. Also it can be seen that the rate of increase ($dT_{SZ\text{-}P}/d\omega$), when ω increased, was high in the low-mid ω range (500-1000 rpm) and low when ω was high (1000-1400 rpm). As it was described in section 3.2, this trend is consistent with the exponential rise of T_{SZ} as a function of ω, observed in FSW of Al alloys [88, 89].

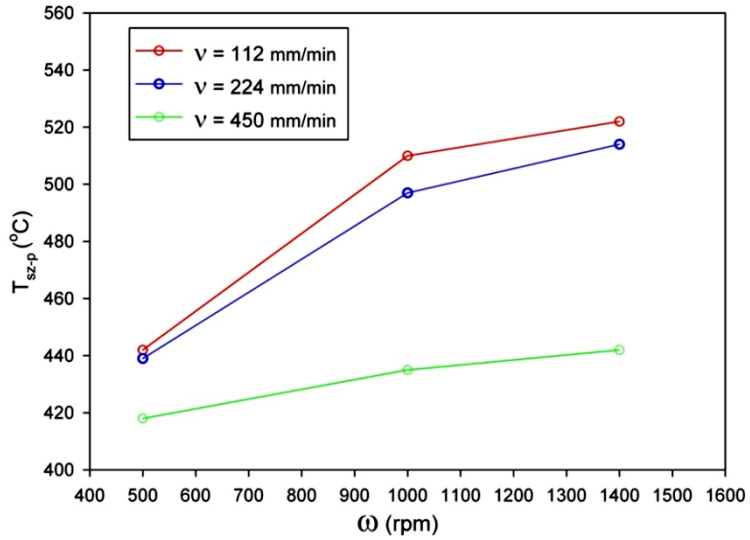

Figure 4-2 Effect of ω on $T_{sz\text{-}p}$ for the welds made using L_{pin} =2.7 mm

Comparing the $T_{sz\text{-}p}$ curves (for 112-224 mm/min) in Figure 4-2 to the corresponding curves (for 112-224 mm/min) in Figure 4-1, it is clear that substantial increase of *h* by varying ω from 500 to 1000 rpm is associated with considerable increase of $T_{sz\text{-}p}$. Furthermore the rate (either $dT_{SZ\text{-}p}/d\omega$ or $dh/d\omega$) of increase was high when ω was low and in both cases the rate diminished as ω increased. These results are in agreement with those found in FSLW of Al 6060 (section 3.3) and hence supporting the suggestion made earlier (section 3.3) that increasing SZ temperature lead to a higher stir volume, which cause lapping interface up-lifting, through enhancing flowability of material (due to material softening) during FSLW.

However comparing the $T_{sz\text{-}p}$ curve (for 450 mm/min) in Figure 4-2 to the corresponding curve in Figure 4-1, it can be seen that slight increase of $T_{sz\text{-}p}$, when ω increased, did not result in an increase of *h.* Also traces of the hooks in relation to the pin location for these welds are illustrated in Figure 4-3. It is clear that all hooks are located at the same position and also very close to the pin location. The measured $A_{B\text{-}SZ}$ (representing the stir flow volume related to interface up-lifting) in these welds is low as minimum attainable value of ~ 1.2 mm^2 which is equal to the area of pin penetrated to the bottom plate. Therefore the resultant low stir flow volumes, as indicated by the low value of $A_{B\text{-}SZ}$, were not sufficient to cause the interface up-lifting and consequently a low *h* value of 0.1 mm was obtained in these welds.

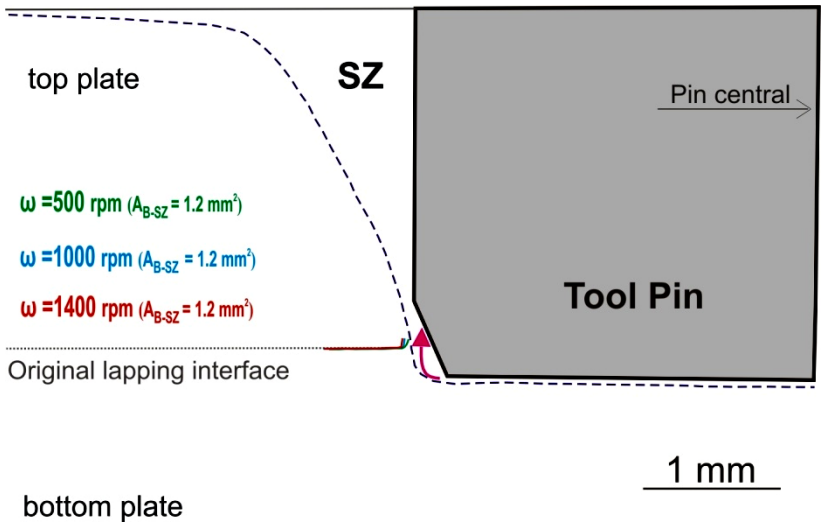

Figure 4-3 Traces of hook in relation to the pin location for AZ31 welds made using ν =450 mm/min, L_{pin} =2.7 mm and ω as indicated. Direction of material flow causing the interface up-lifting is schematically illustrated by the curved arrow. Stir zone is also schematically outlined.

As can be seen in Figure 4-2, for the low to medium ν range (112-224 mm/min), $T_{sz\text{-}p}$ increased significantly when ω increased from 500 rpm to 1000 rpm. However for high ν range (450 mm/min), $T_{sz\text{-}p}$ increased slightly with increase of ω. This is because when the tool pin is travelling fast (in case of ν=450 mm/min) during FSLW, the major frictional heat generated by the contact of tool shoulder and workpiece (at surface of top plate) must not have fully transferred/conducted to the location of lapping interface (where the $T_{sz\text{-}p}$ was measured during FSLW) and the cooling rate increases with increase of welding speed [4]. It is well known that frictional heat produced by the contact of tool shoulder and workpiece is the major source of heat generation during FSW and the tool shoulder dominates the heat generation during welding [3, 4, 100].

Figure 4-4 shows the h value plotted as function of $T_{sz\text{-}p}$, including all AZ31 welds. It can be seen that for welds with small hook size (h < 0.4 mm), $T_{sz\text{-}p}$ has not exceeded 450 ^{o}C. However for welds with large hook size (h > 1.0 mm), $T_{sz\text{-}p}$ is at ~ 500 ^{o}C or higher. These results suggest that to produce a weld with small hook size, it is necessary to select welding speeds which do not result in $T_{sz\text{-}p}$ higher than 450 ^{o}C during FSLW. It is likely that when $T_{sz\text{-}p}$ exceeds 450 ^{o}C, the plasticity of the stir zone is significantly increased by a further increase in temperature, facilitating up-lifting of original lapping interfaces. Hook characteristics (shape and continuity) and how they are affected by material flow during FSLW is discussed in following section.

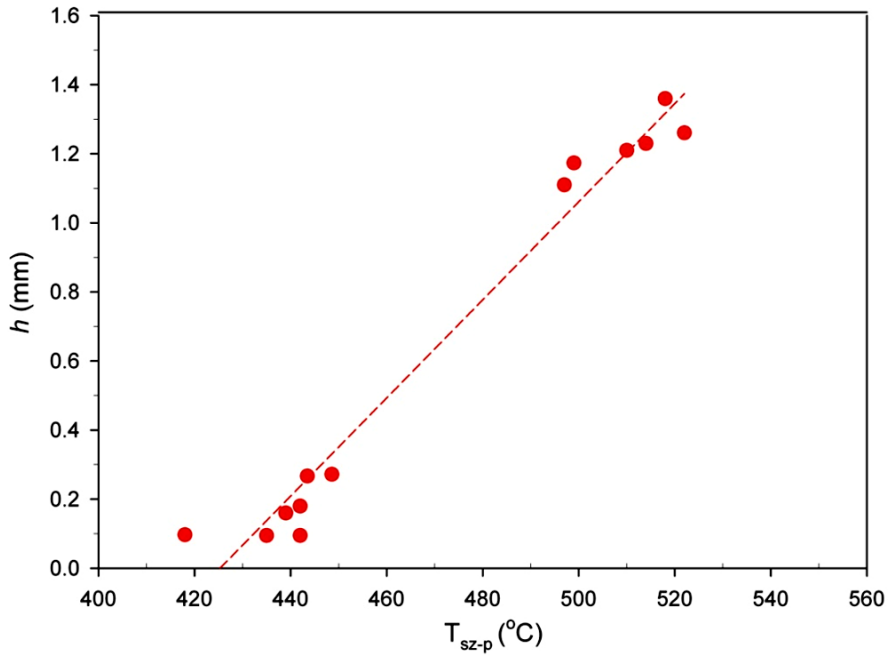

Figure 4-4 Relationship between $T_{sz\text{-}p}$ and h (including welds made using both L_{pin}=2.7 and 3.7 mm)

4.1.2 Hook Shape and Continuity

Traces of the hooks in relation to the pin location for the two selected AZ31 welds is shown in Figure 4-5a. Traces of the hooks for Al 6060 welds, made using same process speeds (ν, ω) used for AZ31 welds, are also shown in Figure 4-5b for comparison. It should be noted that in either AZ31 or Al 6060 welds (in Figure 4-5), the pin penetrated 1.2 mm into bottom plate, representing a moderate bottom plate penetration.

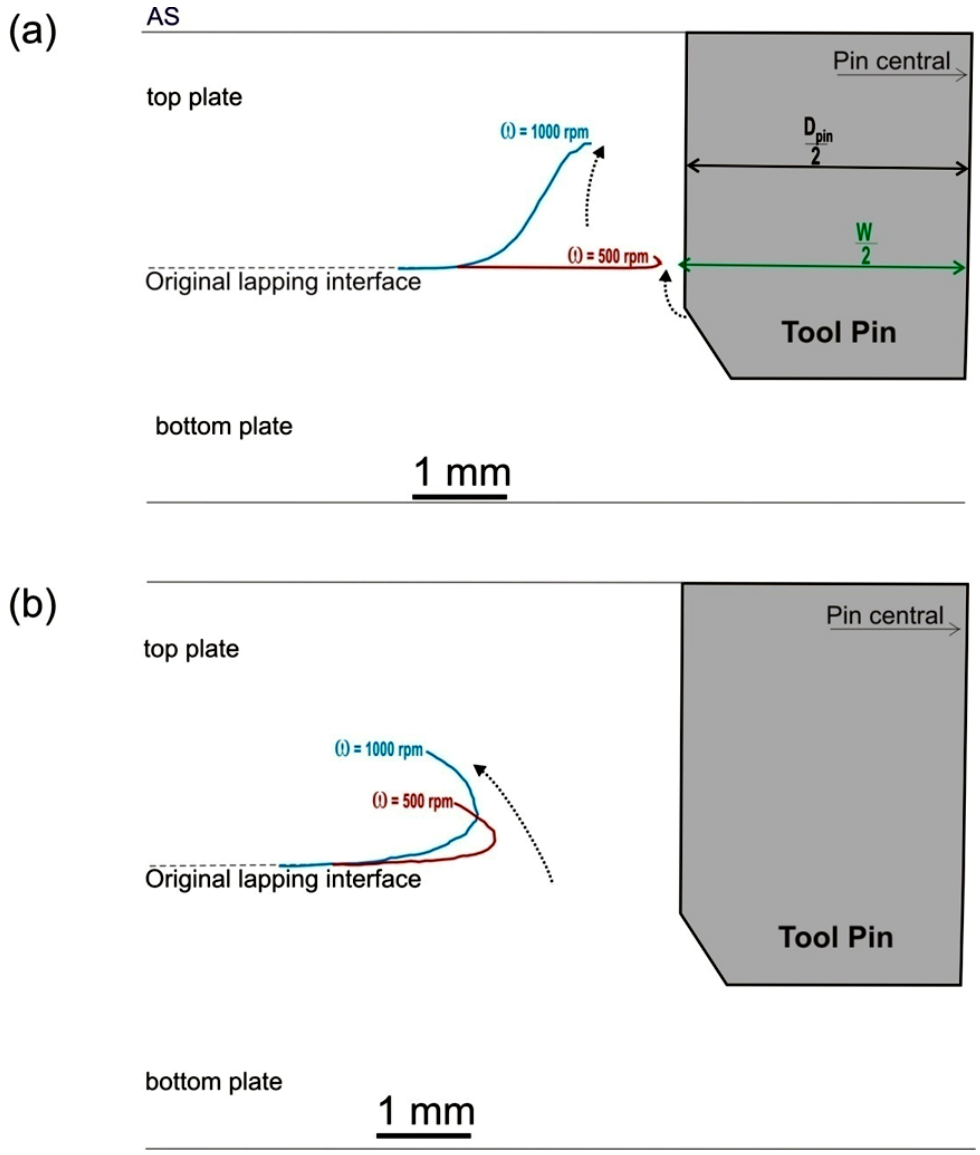

Figure 4-5 Traces of hooks in relation to the pin location for the FSL welds made using ν =112 mm/min and ω as indicated in: (a) AZ31B-H24 welds, L_{pin}=3.7 mm and (b) Al 6060-T5 welds, L_{pin}=4.2 mm. Direction of material flow causing the hook formation is schematically illustrated by the curved dotted arrows. SZ width (W) for AZ31B-H24 weld made using ω=500 rpm is also indicated in Figure 4-5a.

As can be seen in Figure 4-5, at the same ω the hook in AZ31 weld is located much closer to the pin, compared to the hook in Al 6060 weld. This indicates the formation of smaller stir zone in AZ31 welds. The formation of smaller SZ is better seen for the hook at ω=500 rpm (Figure 4-5a), in which if the hook is folded back along the line of the original lapping interface, the hook would end approximately where the edge of the pin is; which means SZ width at the location of lapping interface (as indicated by W in Figure 4-5a) is almost equal to the size of the pin (D_{pin}).

Formation of smaller SZ in AZ31 welds, compared to Al 6060 welds, indicates that a smaller volume of sufficiently softened material (by the FS heat) has been deformed/stirred by the rotating pin, during FSLW. The material flow stress (σ_{flow}) in hot working conditions (such as FSW) is known to be related to the temperature and strain rate through the Zener-Holloman relationship [101, 102]:

$$\mathrm{Z} = \dot{\varepsilon}\exp(-\frac{\mathrm{Q}}{\mathrm{RT}}) = A(\sinh \alpha\, \sigma_{\mathrm{flow}})^2 \qquad 1\text{-}2$$

Where $\dot{\varepsilon}$ is the strain rate, Q is the activation energy, R is the gas constant, T is the temperature and n, α and A are the material constants. By rearranging the equation 1-2, the σ_{flow} can be solved:

$$\sigma_{\mathrm{flow}} = \alpha^{-1} \sinh^{-1}\{[\dot{\varepsilon}\exp(\mathrm{Q/RT})\, A^{-1}]^{1/n} \qquad 1\text{-}3$$

Equation 1-3 indicates that σ_{flow} decreases with either increase of temperature or decrease of strain rate. However it is important to note that accurate σ_{flow} distribution in the stir zone cannot be achieved in this study. That is due to the difficulty of the experimental set up and also complex numerical modelling required for estimation of temperature and strain rate distribution in stir zone [103, 104]. Nevertheless, it is generally known that the peak temperature (during FSW) gradually decreases from the weld center toward the HAZ (at both sides of weld) [104] thus according to equation 1-3, σ_{flow} would increase from the weld center toward the HAZ.

Al 6060 and AZ31 have different thermal properties and the thermal conductivity of AZ31 (76.9 $Wm^{-1}k^{-1}$) is significantly lower than that of Al 6060 (200 $Wm^{-1}k^{-1}$) [105, 106]. Assuming that the thermal input is the same during FSLW of Al 6060 and AZ31, due to the same ν-ω and tool pin size used, the lower thermal conductivity of AZ31

results in higher temperature gradient in the stir zone of AZ31 welds according to the Fourier's Law of thermal conduction:

$$\nabla T = \frac{q}{-k} \qquad 1\text{-}4$$

Where the q is the local heat flux (Wm^{-2}), k is the thermal conductivity ($Wm^{-1}k^{-1}$) and ∇T is the temperature gradient (Km^{-1}). The higher temperature gradient in stir zone of AZ31 welds, compared to Al 6060 welds, suggests the development of higher σ_{flow} gradient in the stir zone of AZ31 welds according to equation 1-3. Thus the σ_{flow} increases more rapidly from the weld center toward the HAZ (at both sides of weld) resulting in formation of smaller stir zones in AZ31 welds.

Furthermore, heat treatable aluminium alloys, in high temperature (240-500^{o}C) tensile testing conditions, show strong work softening after reaching the peak stress values [107]. That is due to enhanced over-aging of original artificially-aged microstructure, resulting in intense material softening with plastic deformation. AZ31 alloy, on the other hand, does not show strong work softening in high temperature tensile testing conditions, and instead exhibits steady flow stress behaviour at higher temperatures [108]. Therefore it is reasonable to assume that Al 6060 (as heat treatable alloy), which experiences strong softening at increasing temperatures, will easily undergoes intense plastic deformation during FSLW, allowing a larger volume of softened material to be deformed/stirred by the rotating tool. As a result, a larger stir zone is expected to form in Al 6060 welds, compared to AZ31 welds made using the same FSLW conditions (ω, ν).

Macrograph of the AZ31 weld made using ω=1000 rpm and ν=112 mm/min is presented in Figure 4-6. It can be seen that the hook profile (on advancing side) is a simple consequence of a portion of the original lapping interface pushed and lifted due to the upward material flow in nugget, and hook has followed the shape of nugget (with clear onion ring structure) curving toward the weld center. This hook profile is very different from those in Al 6060 welds (Figure 4-5b) in which hooks lifted up and also curved toward the advancing side. The hook profile of Al 6060 welds suggest that the original lapping interface lifted up first by the upward material flow in the nugget zone and then pushed outward into the advancing side by the shoulder flow. However the hook profile in AZ31 welds indicates that although the original lapping interface lifted

up by the upward material flow in nugget zone but has not been pushed by the shoulder flow into the advancing side.

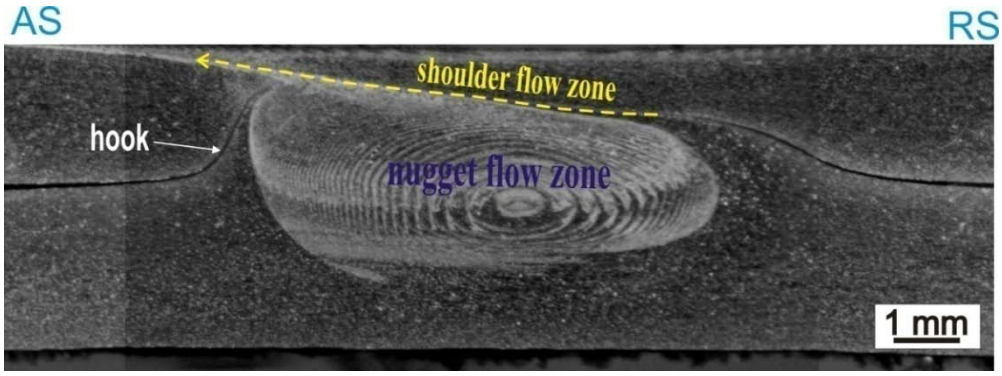

Figure 4-6 Cross sections of an AZ31 weld made using ω =1000 rpm and ν =112 mm/min showing nugget and shoulder flow zones. Shoulder flow direction is indicated by the yellow dashed arrow

It is known that the shoulder zone forms after the nugget zone during FSW [14]. This is illustrated back in Figure 2-2, which indicates the pin is in contact with the material first forming nugget zone, followed by the rear portion of the tool shoulder forming the shoulder zone. For AZ31 welds, the flow stress of hook location (after up-lifting by nugget flow) was still sufficiently high when the pin moved forward and rear of tool shoulder arrived (to form the shoulder flow zone). Thus the shoulder flow was not able to push the hook and hence the hook retained the original shape caused by the nugget zone. On the contrary, the hook profiles of Al 6060 welds suggest that flow stress of hook location (after up-lifting by nugget flow) was still sufficiently low when the rear of shoulder arrived and thus shoulder flow could push the hook toward the advancing side (Figure 4-5b). This is due to intense material softening of heat treatable aluminium alloys (such as Al 6060) at high temperatures of FSLW, which is caused by the over-aging of original artificially-aged microstructure [107], thus easily undergoes intense plastic deformation during FSLW. The observed difference in hook profiles of Al 6060 and AZ31 welds reflects the significant influence of the plastic properties of the base materials, at high temperatures of FSLW, on material flow during welding.

The higher magnification micrograph of the hook region at advancing side of Figure 4-6 is given as Hook A in Figure 4-7. It can be seen that the hook is quite continuous even at the hook tip region. This continuity of hook has also been observed in other AZ31 welds and Hook B in Figure 4-7 is another example of continuous hook. However it should be noted that the hook in AZ31 welds is different from the Al 6060 welds, in

which hooks can be quite discontinuous (section 3.2). The continuity of hooks in AZ31 welds indicates that original lapping surfaces were not highly stretched by the material flows forming the SZ. This is related to the insufficient material flow volumes produced during FSLW, evidenced by the smaller SZ formed in AZ31 welds as described earlier.

Furthermore as it was explained in section 3.2, for Al 6060 welds there was a limit on maximum *h* value (h_{Max}), as the hook was dispersed by the shoulder flow during FSLW. This is also the case for AZ31 welds. Close examination of the hook at Figure 4-6 clearly illustrates that the hook was arrested by the shoulder flow at the location where nugget and shoulder flow zones meet. In other words, h_{Max} depends on the maximum vertical distance that nugget flow zone can reach during FSLW, as can be seen in Figure 4-6.

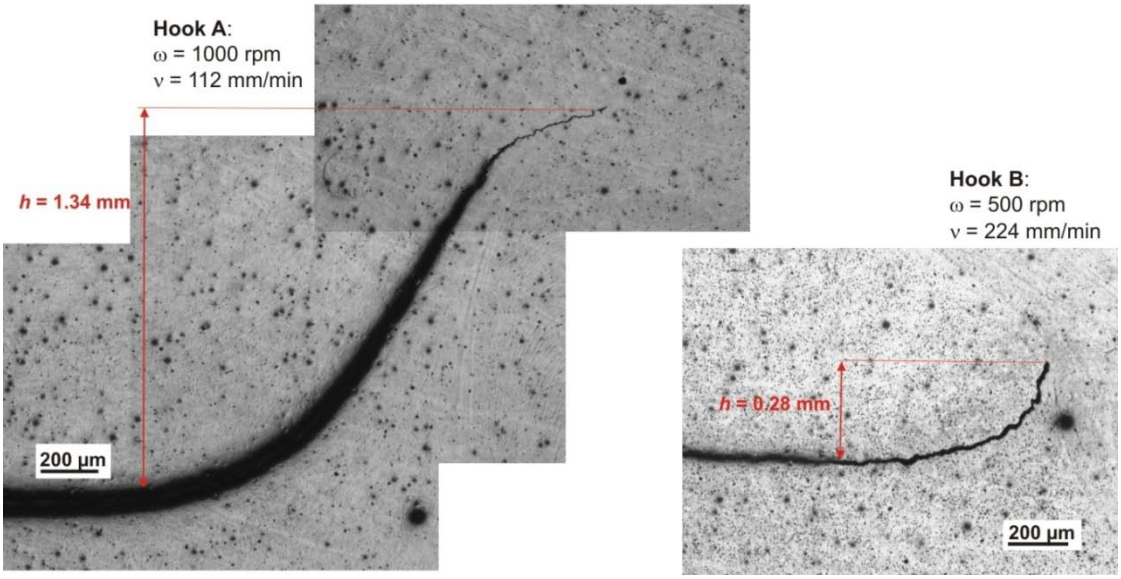

Figure 4-7 Micrographs showing the hooks in AZ31 welds made with various ω and *v* values as indicated

The results presented in this section demonstrated that in FSLW of AZ31, increasing SZ temperature facilitates interface up-lifting through enhancing the material's plasticity and thus higher stir flow volumes, similar to FSLW of Al 6060 (section 3.2). However the hook characteristics (shape, distance to weld center, continuity) in AZ31 welds are different from those in Al 6060 welds. That is related to the difference in plastic properties of these materials at the high temperatures of FSLW, affecting the material flow during welding.

4.2 Fracture Strength Relating to FS Macro/Microstructure

In this section, how the fracture location and strength of AZ31 welds are affected by the hook size, microhardness distributions in welds and also degree of deformation (bending) during testing is presented.

4.2.1 Fracture Strength as Function of *h*

Figure 4-8 presents the σ_{Lap} data plotted as function of *h* for AZ31 welds. It is clear that despite the scatter of data, there is a strong dependence of σ_{Lap} on *h*. This is consistent with literature as explained in section 1.3.3. It should be noted that FSLW parameters used in this study resulted in two groups of data as can be seen in Figure 4-8. The first group consists of the welds which obtained high *h* values ($h > 1.0$ mm) due the higher $T_{sz\text{-}p}$ achieved during FSLW, as explained in section 4.1.1. The second group consist of the welds which obtained low *h* values ($h < 0.4$ mm) due the lower $T_{sz\text{-}p}$ during FSLW.

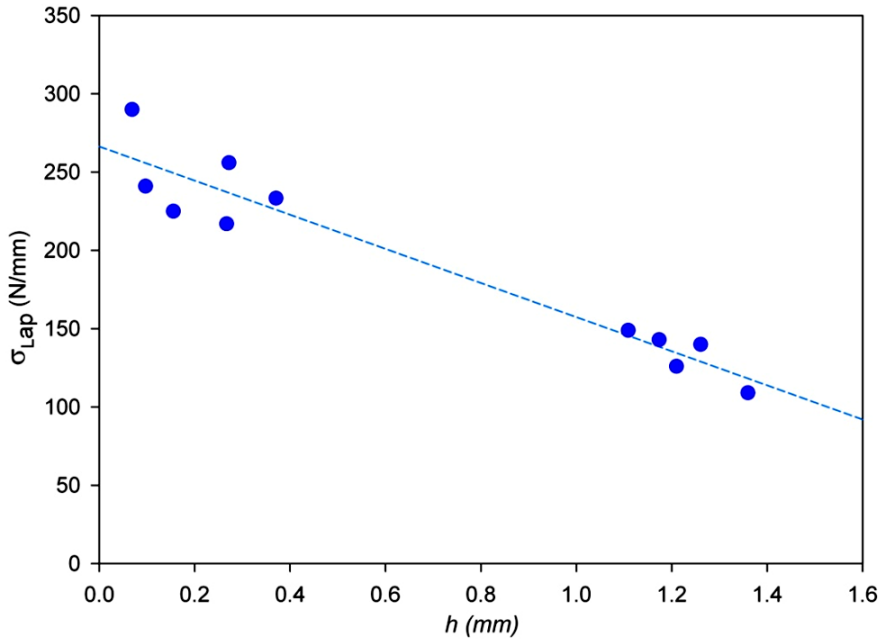

Figure 4-8 σ_{Lap} as function of h for AZ31 welds

The maximum of σ_{Lap} (290 N/mm) was obtained for the weld with $h = 0.07$ mm, as shown in Figure 4-9. This value (σ_{Lap} =290 N/mm) is the same as the maximum σ_{Lap} =290 N/mm reported by Cao et al [17] in which loading configuration was advancing loaded (similar to this study). However the micrographs presented in Cao et al study [17], as explained in section 1.3.3, suggest that their measurements of *h* were not been made accurately as the magnification of micrographs were not high enough to allow

accurate measurement of *h*. On the other hand, higher magnification micrographs of hooking region were used in this study for a more precise measurement of *h*, as can be seen in Figure 4-9.

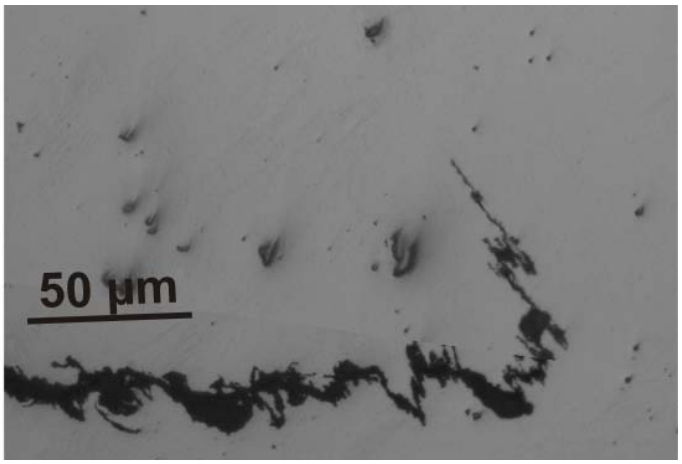

Figure 4-9 Micrographs showing the hook at advancing side for the weld made using ω =1000 rpm, v = 450 mm/min and L_{pin}=2.7 mm

4.2.2 Fracture Location and Hardness Distribution in Welds

During tensile shear testing, all the AZ31 welds fractured in the same mode in which the crack initiated from the tip of hook and then propagated through top plate, as shown in Figure 4-10. This is very different from Al 6060 welds where various fracture modes were observed. As was described in section 3.2, fracture due to HAZ softening becomes the dominant fracture mode in Al 6060 welds, when *h* is small. However this fracture mode was not observed in AZ31 welds, even when *h* was tending to zero. To examine the softening effect caused by FS heat on AZ31 welds, the hardness distributions for the two welds made using same v=112 mm/min but different ω=500 and 1000 rpm was obtained, as shown in Figure 4-11. It can be seen that for both welds, minimum hardness is located in SZ center, contrary to Al 6060 welds in which minimum hardness is always located at HAZ region.

As described in section 3.4, the correlation between hardness and yield strength of metallic materials has been widely studied in literature and positive relationship between the hardness and yield strength (either linear or curvilinear) have been reported [90]. Thus the local hardness of a material can be considered as an indication of local strength. Therefore the higher local strength (as indicated by hardness) in HAZ in comparison to the values in hook tip location (Figure 4-11) assisted the failure by crack

propagating from the tip of hook (softer region), even when *h* was small (Figure 4-10a). In contrast, in Al 6060 welds the HAZ softening limited the σ_{Lap} when *h* was small, meaning that HAZ softening and hooking could compete against each other for deformation and fracturing. As the hardness distribution in welds is related to the microstructural evolution during FSLW, the typical microstructure of AZ31 welds is presented in next section.

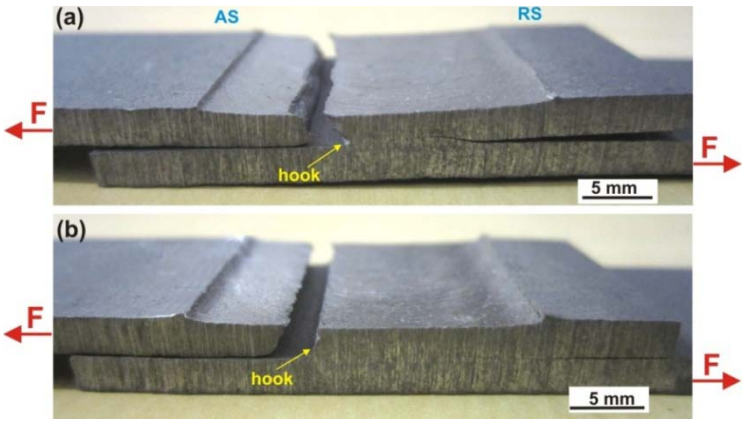

Figure 4-10 Mode of fracture in AZ31 welds with the crack propagated from the hook location in: (a) weld with *h*= 0.28 mm and (b) weld with *h*= 1.34 mm

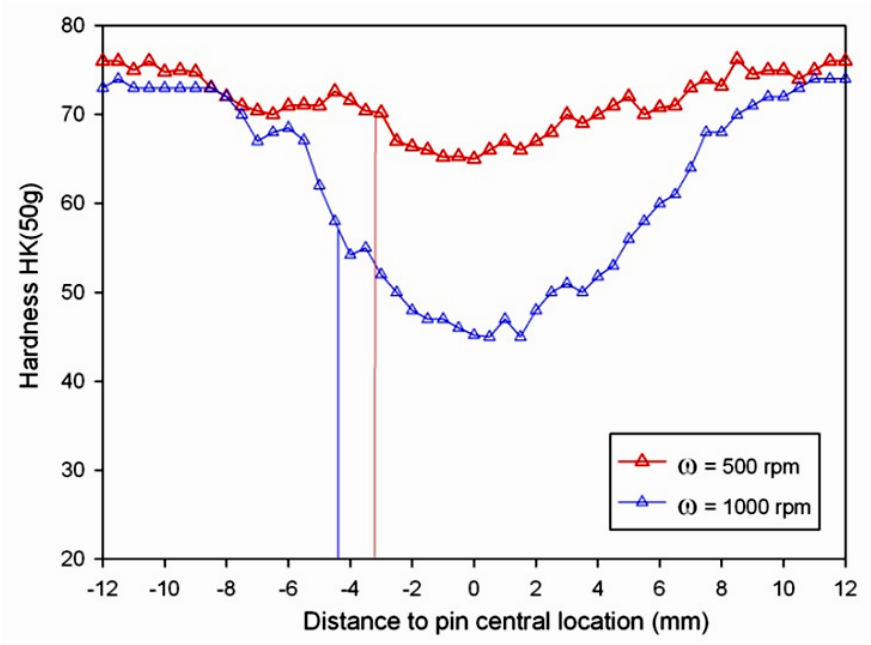

Figure 4-11 Knoop hardness distribution (transverse to welding direction measured at 0.1mm above the tip of hook) for the two welds made using *v* = 112 mm/min and ω as indicated (vertical lines indicate the location of the hook tip)

4.2.3 Microstructure and Hardness Distribution in welds

The microstructure of different regions of a weld made using ν=112 mm/min and ω=1000 rpm is shown in Figure 4-12. The microstructure of base metal (Figure 4-12a) consists of both equiaxed and deformed grains of various sizes. A number of deformation twins can also be observed (Figure 4-12b) which have formed during hot rolling of AZ31 plates. However the materials in TMAZ (Figure 4-12c) and SZ (Figure 4-12d) are fully recrystallized with no deformation twins. Also microstructure of TMAZ shows no obvious elongated and aligned grain structure, contrary to Al 6060 welds (section 3.3), indicating that the deformed microstructure readily recrystallised dynamically during welding as well as significant static recrystallization by the FS heat. That is because magnesium alloys dynamically recrystallize more easily than aluminium alloys. The recrystallization temperature of magnesium alloys are about 248 ^{o}C [13, 109] which is lower than that of the aluminium alloys in general.

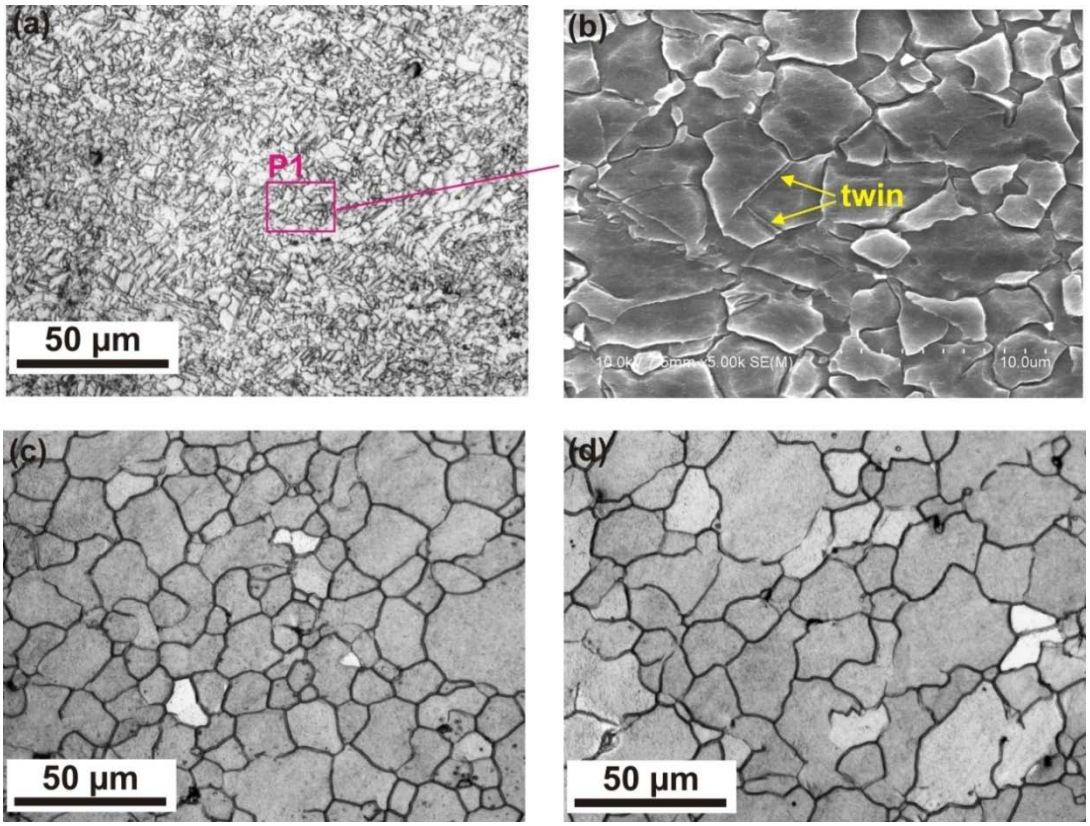

Figure 4-12 Microstructure of a weld made using ν =112 mm/min and ω =1000 rpm at various regions, (a) optical micrograph of base metal, (b) SEM image of area P1 in Figure 4-12a, (c) optical micrograph of TMAZ and (d) optical micrograph of SZ center

Also Figure 4-12 clearly shows that grain size has increased significantly from the base metal (with average grain size of 5 μm) to the stir zone (with average grain size of 20 μm). This substantial increase of grain size, from BM towards SZ, is in general agreement with hardness reduction from BM towards SZ, as illustrated in Figure 4-11. The hardness-grain size relationship has been plotted in Figure 4-13, showing hardness values as a function of the reciprocal of the square root of the grain sizes. The hardness values and grain sizes were taken at different zones of the weld. It is seen that Hall-Petch type linear relationship is followed and could be written as $HV=10.2+147\ d^{-1/2}$. Afrin et al [13] have also reported the Hall-Petch relationship with $HV=16.4+119.5\ d^{-1/2}$ in FSW of AZ31. It should be noted that the difference in intercept and slope of these equations are due to the different FSW parameters used in these studies. As the larger grains have less grain boundaries hence they would impose less restriction to the dislocation movement, resulting in lower hardness and local strength. Therefore the SZ exhibited the lowest hardness, compare to the other region, as it had the largest grains.

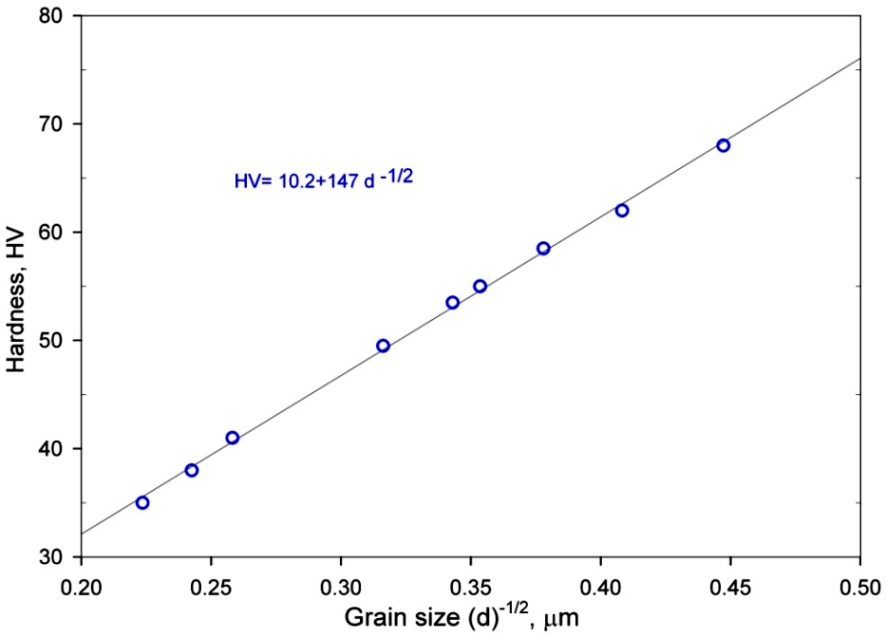

Figure 4-13 Plot of the Hall-Petch relationship for the AZ31 weld made using ω =1000 rpm and ν =112 mm

Referring back to Figure 4-11 it can be seen that hardness of SZ for the weld made using ω=1000 rpm is considerably lower than that of the weld made using ω=500 rpm. This is due to difference in grain size produced at SZ of theses welds, as shown in Figure 4-14. It is clear that the grains in the weld made using ω=1000 rpm is

considerably larger than the grains in the weld made using ω=500 rpm. Traces of temperature at SZ of these welds, during FSLW, are also presented in Figure 4-15. In each trace, there are disturbances in the peak temperature region because the thermocouple was pushed slightly by the lower stir flow as the pin approached the thermocouple. It is clear that the weld made using ω=1000 rpm has obtained higher peak temperature ($T_{sz\text{-}p}$ =510 ^{o}C) and spent longer time at the elevated temperatures, compared to the weld made using ω=500 rpm (with $T_{sz\text{-}p}$ =442 ^{o}C). Consequently the recrystallised grains at SZ of the weld made using ω=1000 rpm were allowed to grow more, resulting in larger grains with subsequent reduced hardness.

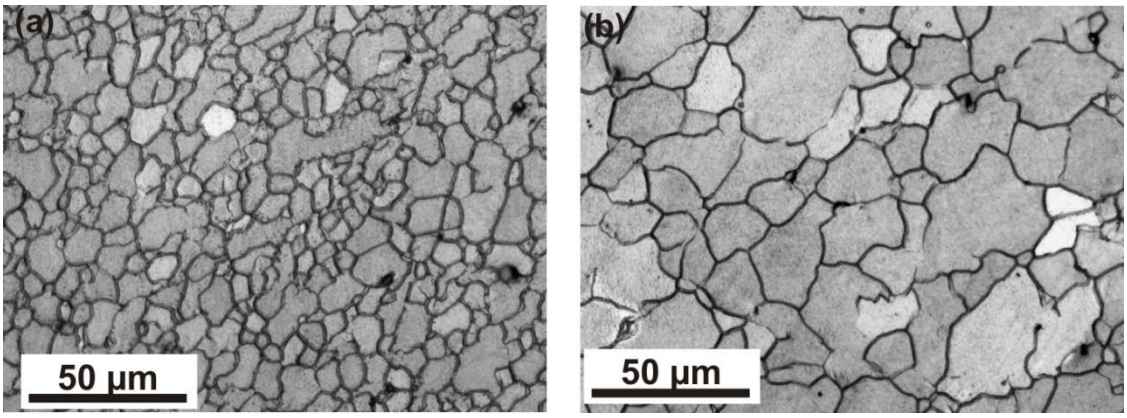

Figure 4-14 Microstructure of SZ for the welds made using same ν =112 mm/min and: (a) ω =500 rpm and (b) ω =1000 rpm

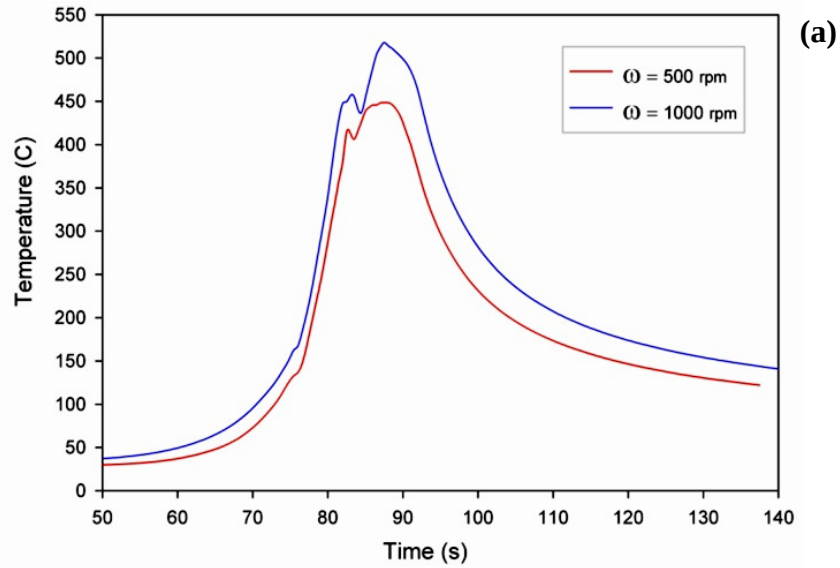

Figure 4-15 (a) measured temperature at SZ of welds made using same ν =112 mm/min and ω as indicated and (b) enlarged view of temperature reading at temperatures above 400 ^{o}C

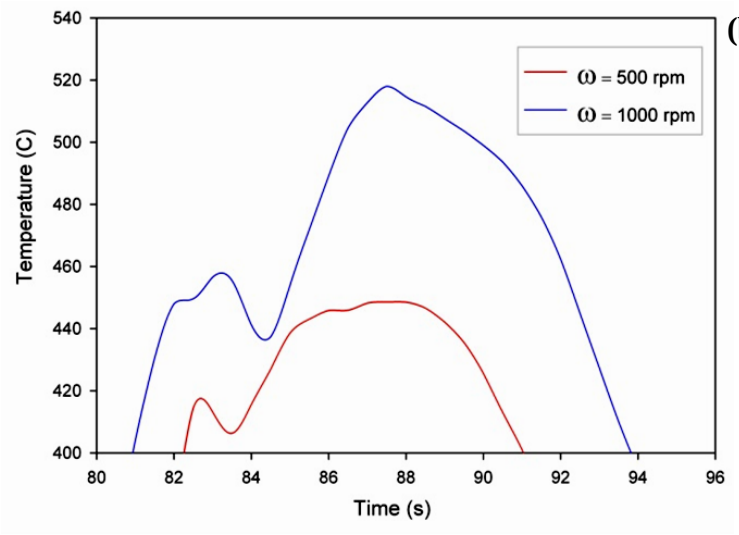

Figure 4-15 continued.

4.2.4 Fracture Strength and Deformation (Bending) during Testing

As described in section 4.2.1, the highest σ_{Lap} value obtained (in this study) for AZ31 welds was 290 N/mm. σ_{Lap}-strain curves for the highest strength AZ31 weld (σ_{Lap}=290 N/mm) and also as-received alloy of AZ31B-H24 are presented in Figure 4-16. Also σ_{Lap}-strain curves for the highest strength Al 6060 weld (σ_{Lap}=422 N/mm) and as-received alloy of Al 6060-T5 are shown in Figure 4-16, for comparison. It should be noted that tensile load per unit width has been used for the as-received alloys in order to be comparable to σ_{Lap} (load per unit of width) of welds. It is clear that Al6060-T5 is highly ductile with a moderate amount of uniform deformation (up to ~ 10%) and a further large local deformation after the start of necking. For AZ31B-H24, ductility by uniform deformation is also quite high (up to ~ 15%), but the fracture is sudden with little further local deformation and necking, as evident from σ_{Lap}-strain curves. The fractured samples of Al 6060-T5 and AZ31B-H24 are also shown in Figure 4-17. It can be seen that significant necking occurred on fracture location of Al 6060 sample while no necking can be observed for AZ31B-H24 sample.

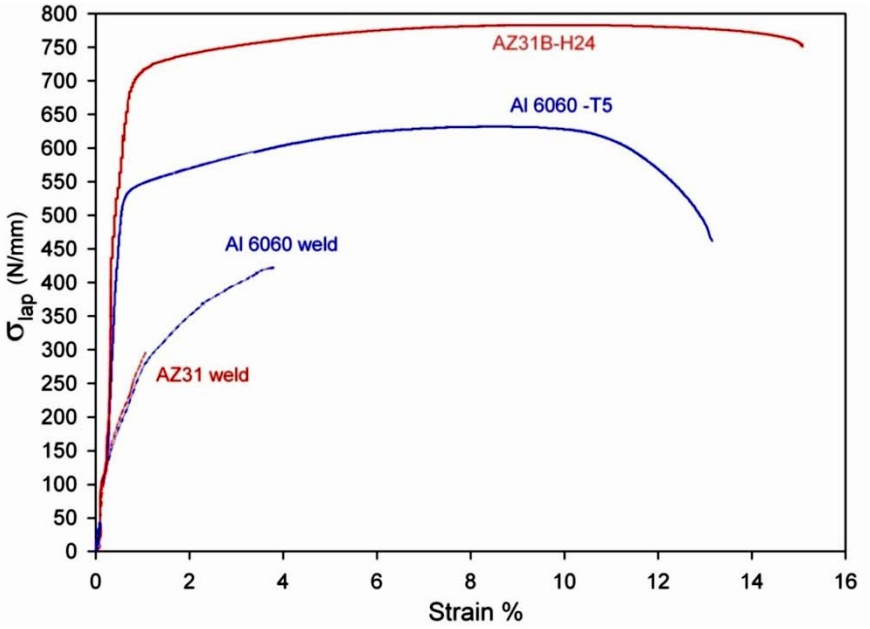

Figure 4-16 σ_{Lap} – strain curves for the as-received alloys of AZ31B-H24 and Al 6060-T5 (during tensile testing) and the highest strength FSL welds of AZ31 and Al 6060 (during tensile shear testing)

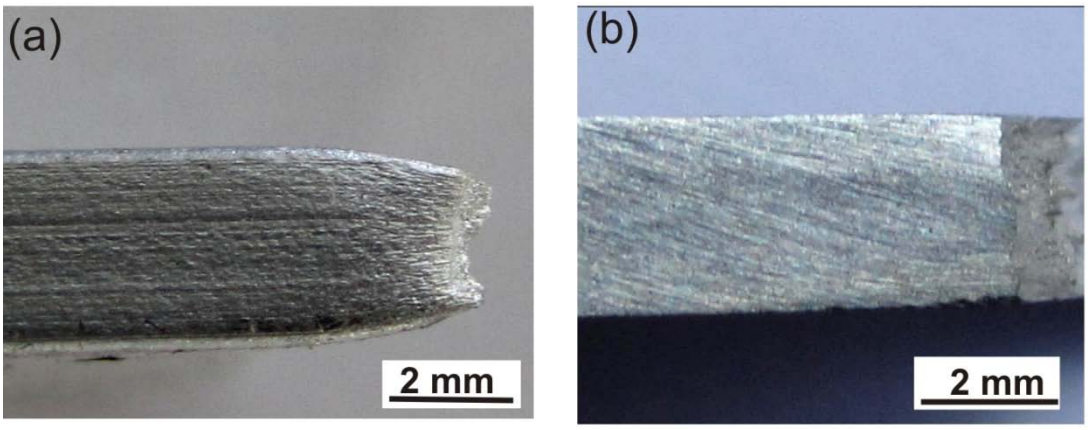

Figure 4-17 Fractured tensile tested specimens (a) Al 6060-T5 showing significant necking at fracture location and (b) AZ31B-H24 showing no necking at fracture location

For AZ31 weld, value of σ_{Lap}=290 N/mm is about 1/3 of strength of original AZ31B-H24 pulled in uniaxial tensile testing. This ratio is much lower than that for Al 6060 weld with $\sigma_{Lap} \approx$ 2/3 of strength of original 6060-T5 material. Tested samples for both Al 6060 and AZ31 welds are shown in Figure 4-18. It can be seen that Al 6060 sample has rotated locally in the lapping region to a large degree and straightened itself, aligned with direction of applied loads (Figure 4-18a). In this case, the final bended geometry of specimen resulted in diminished stress concentration, as explained in section 3.5. Also a

considerable amount of local plastic deformation could be observed in the fracture locations (Figure 4-18a) and thus it was possible that a significant amount of strain hardening proceeded before fracture, leading to a high σ_{Lap}. On the other hand, AZ31 sample displayed little rotation before the fracture; therefore has maintained the stress concentration caused by tensile shear testing (at the un-welded lap tips), resulting in a lower σ_{Lap}. It should be noted that the lack of local bending, during tensile shear testing, indicates the lack of local ductility of AZ31 alloy; as the AZ31 alloy was not able to locally deform/bend to relax the stress concentration caused by tensile shear testing. This lack of local ductility was also observed in tensile tested AZ31 alloy (Figures 4-16 and 4-17b), in which fracture was sudden with little further local deformation and necking. The deformation mechanisms associated with this lack of local ductility are discussed later (section 4.4).

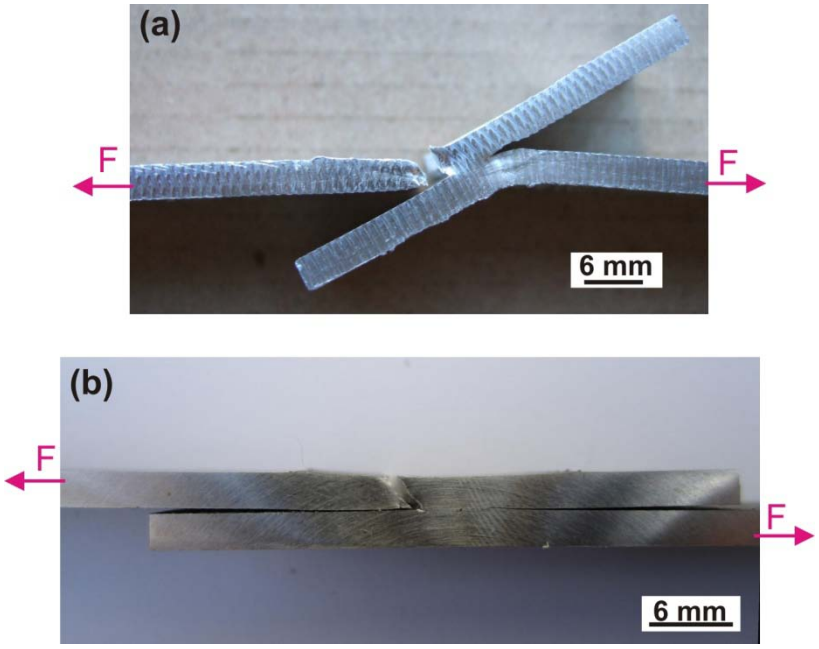

Figure 4-18 Fractured tensile shear tested specimens of (a) an Al 6060 weld showing large degree of rotation before fracture, *h*=0.25 mm and (b) an AZ31 weld showing little rotation before fracture, *h*=0.1 mm

The negative effect of stress concentration, due to lack of local ductility and bending during tensile shear testing, on σ_{Lap} of AZ31 welds was discussed earlier. Also it has been suggested in literature [12, 17] that change in hook orientation from positive hooking to negative hooking (as described in section 1.3.3) is likely to reduce the stress concentration at hook location (during tensile shear testing) and hence may increase the σ_{Lap} of AZ31 welds. However this suggestion is not based on conducting quantitative

stress analysis and hence is not clear how stress concentration and subsequent fracture strength varies by changing hook orientation. These are addressed in the following section.

4.3 Hook Orientation and Fracture Strength

4.3.1 Modelling of Stress Distribution Affected by Hook Orientation

Figure 4-19 shows the simulated effective stress (von misses stress) distribution for the specimen with positive hook of *h*= 0.2 mm. It can be seen that ahead of the hook tip there is an area where the effective stress reached the yield stress (area in red colour), with an applied stress of only 40 MPa, indicating significant stress concentration produced at the hook tip. As explained in section 4.2.2, the local hardness (strength) of the hook region is lower than that of HAZ region for AZ31 welds. Therefore high stress concentration together with lower local strength at hook location, force the fracture to occur at the hook tip. This is in agreement with the common failure mode observed during tensile shear testing of AZ31 welds (Figure 4-10).

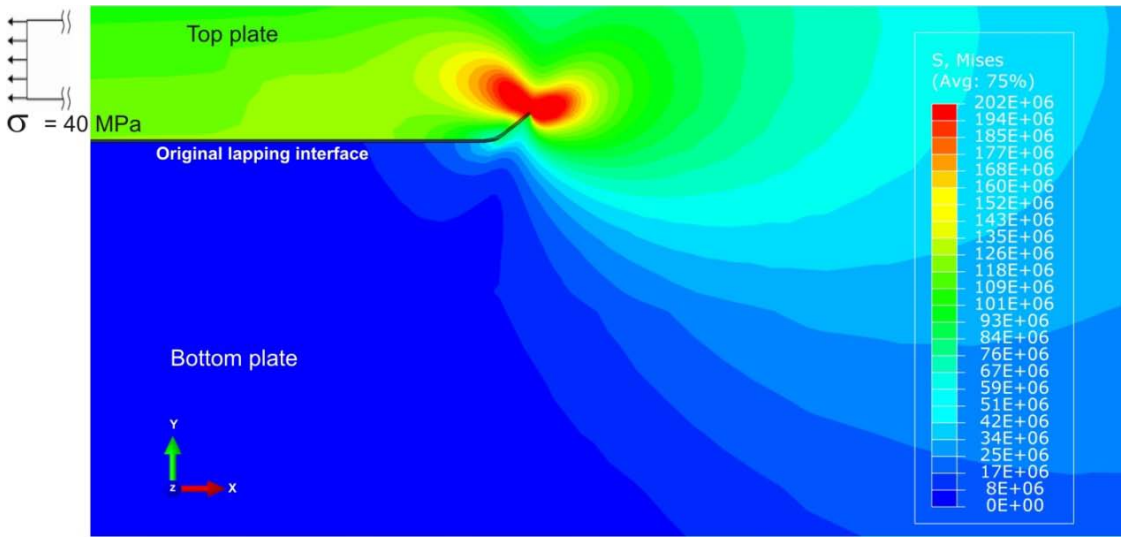

Figure 4-19 Effective stress distribution for the specimen with positive hook of *h*= 0.2 mm, under applied load of 40 MPa during tensile shear testing

A simulated effective stress distribution for the specimen with zero hook (*h*= 0 mm) is presented in Figure 4-20, showing high stress concentration in the location of lapping interface end. As described earlier, the local hardness (strength) of the hook region is lower than that of HAZ region for AZ31 welds. Therefore high stress concentration

together with lower local strength at hook location, force the fracture to initiate at the lapping interface end tip.

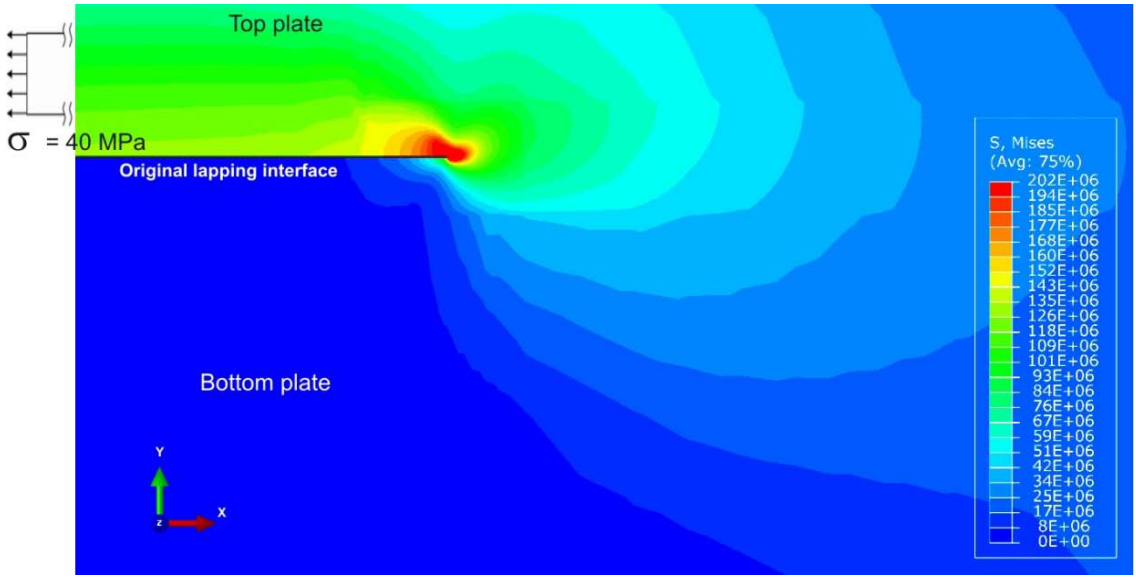

Figure 4-20 Effective stress distribution for the specimen with positive hook of *h*= 0.0 mm, under applied load of 40 MPa during tensile shear testing

Figure 4-21 shows the simulated effective stress distribution for a specimen with negative hook of *h*= - 0.2 mm, the minus sign indicates that hook has extended downward from the original lapping interface. It can be seen that ahead of the hook tip there is a small area where the effective stress reached the yield stress (area in red colour), however size of this area is much smaller than the one observed for the positive hook (Figure 4-19). It should be noted that in linear elastic material FEM modelling (used in this study) yield stress is the maximum stress that material can attain, as the strain hardening after yield stress is not defined in the modelling. Thus presence of a smaller red area at the hook tip of negative hook specimen (Figure 4-21), compared to the positive hook specimen (Figure 4-19), indicates the significant decrease of stress concentration at the hook tip. Nevertheless at the location where the hook starts to deflect downward (location B in Figure 4-21) considerable stress concentration has resulted instead. These results suggest that failure is more likely to initiate at location B, rather than the hook tip, as the high effective stress are mainly concentrated at that location.

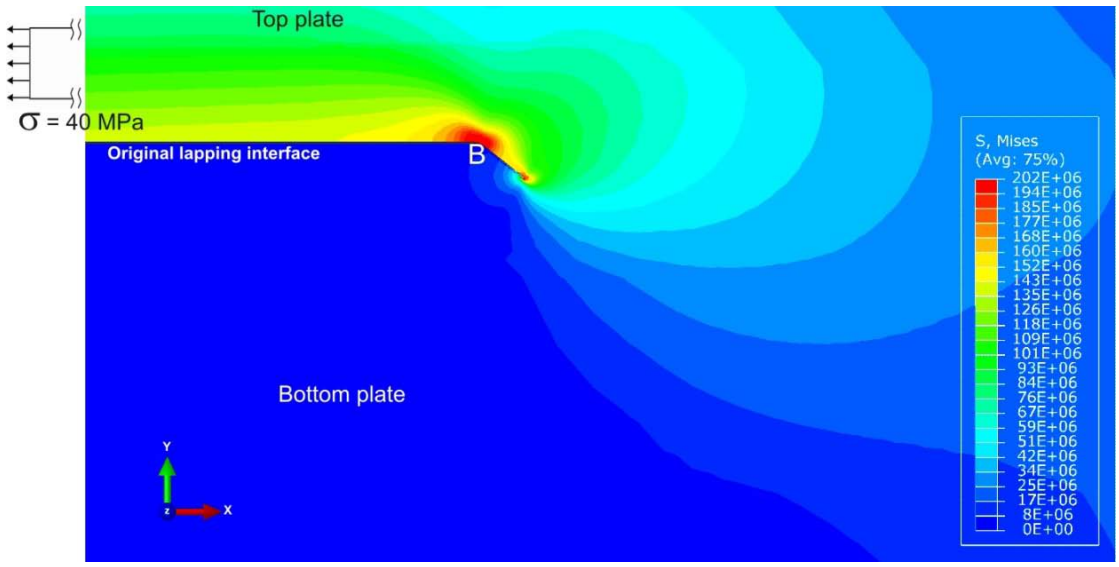

Figure 4-21 Effective stress distribution for the specimen with negative hook of *h*= -0.2 mm, under applied load of 40 MPa during tensile shear testing

Effective stress distribution for a specimen with larger negative hook of *h*= -0.6 mm is presented in Figures 4-22. It can be seen that effective stress at the hook tip has not reached the yield strength (no red area) indicating significant reduction of stress concentration at hook tip, compared to other specimens presented earlier. However at location where hook starts to deflect downward (location B in Figure 4-22) considerable stress concentration has formed. Therefore failure is expected to initiate at location B, rather than the hook tip.

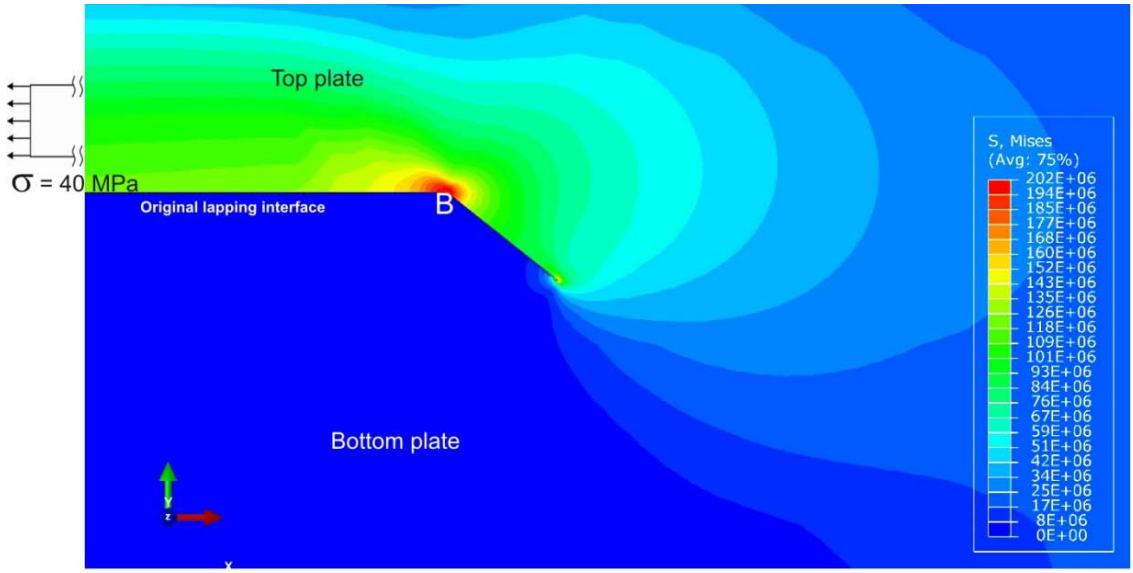

Figure 4-22 Effective stress distribution for the specimen with negative hook of *h*= -0.6 mm, under applied load of 40 MPa during tensile shear testing

Positive hooking reduces the load bearing area of the top plate (as illustrated in Figure 4-23a) during testing, resulting in significant stress concentration at the hook tip (Figure 4-19) thus facilitating crack initiation and decreases fracture strength. On the other hand, negative hooking increases the load bearing area of the top plate, as illustrated in Figure 4-23b, resulting in decrease of stress concentration at the hook tip (as shown in Figures 4-21 and 4-22). Therefore specimens with negative hooks are expected to display higher fracture strength during testing.

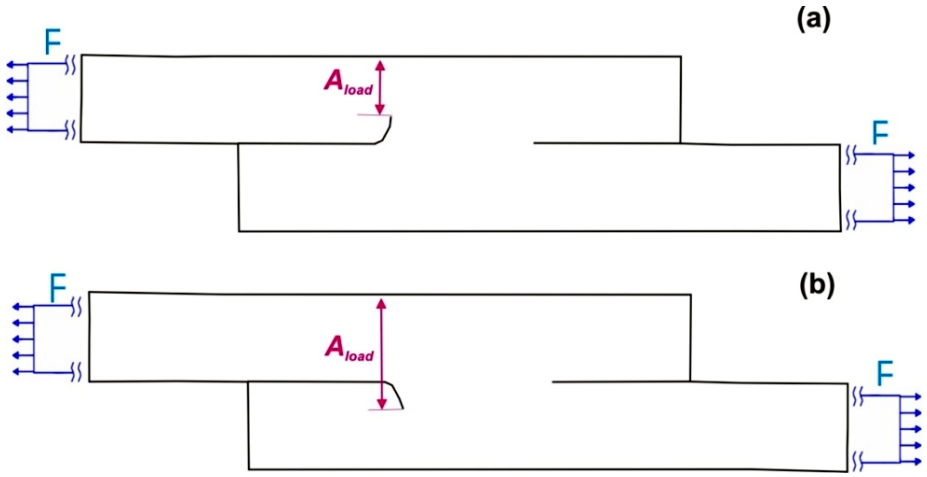

Figure 4-23 Schematic illustration of load bearing area (A_{load}) in (a) a positive hook specimen and (b) a negative hook specimen

The presented simulation results, demonstrated that specimens with negative hooking experience considerably less stress concentration at the hook tip region, due to the increased load bearing area of the top plate (provided by the hook orientation). However stress concentration due to testing geometry is unavoidable and thus significant stress concentration forms on location where hook start deflecting downward (from the original lapping interface); which makes this area susceptible for failure during tensile shear testing.

4.3.2 Effect of Hook Orientation on Fracture - using Artificial Hooks

In order to further and systematically investigate the effect of hook orientation on fracture behaviour, a number of tests were conducted on simulated hooking samples made from AZ31B-O (as explained in section 2.4.2). As illustrated back in Figure 2-11, for positive hook specimens *h* varies from 0 to 1.2 mm and for the negative hook specimens *h* varies from -0.27 to -1.17 mm.

σ_{Lap} data for AZ31B-O specimens, are plotted against the *h* (Figure 4-24). It can be seen that when *h* > 0 mm (positive hook specimens) σ_{Lap} has a strong dependence on *h* and in particular σ_{Lap} increases notably when *h* becomes zero. However when *h* < 0 mm (negative hook specimens) σ_{Lap} is no longer a strong dependence of *h* and increases only slightly with further increase of *h*. In other words, when hooks become negative, tensile shear specimen is reaching its strength limit.

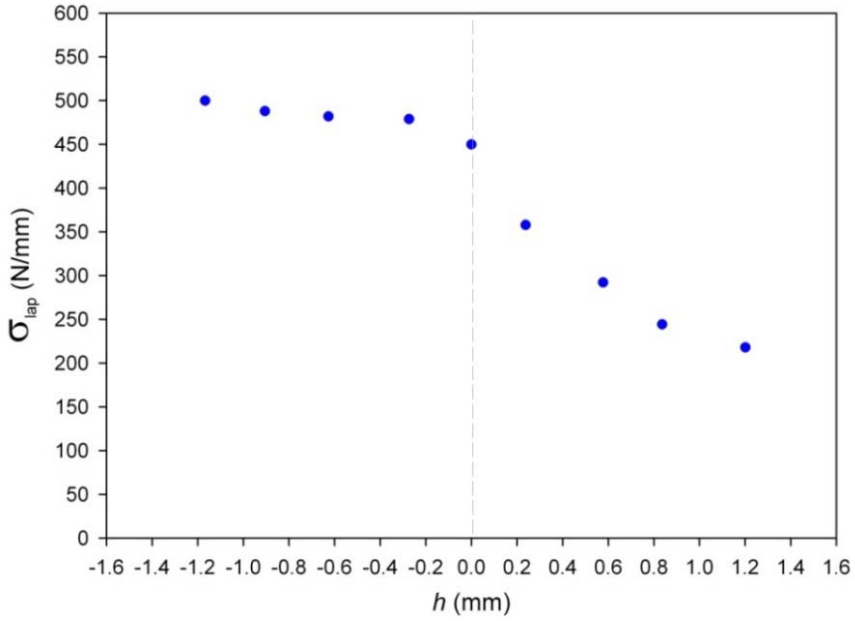

Figure 4-24 σ_{Lap} as function of *h* for AZ31B-O tensile shear specimens (as shown in Figure 2-11)

Figure 4-25 shows the images of three tensile shear tested samples representing positive, zero and negative artificial hook specimens respectively. For both of the positive *h* (Figure 4-25b) or zero *h* (Figure 4-25c) specimens, fracture initiated from the top of hook tip. However for the negative *h* specimen, fracture did not start from the hook tip and instead initiated at the location where the artificial hook starts deflecting downward. This fracture location is in agreement with results of FEM modelling which predict significant stress concentration at that location (indicated as location B in Figures 4-21 and 4-22).

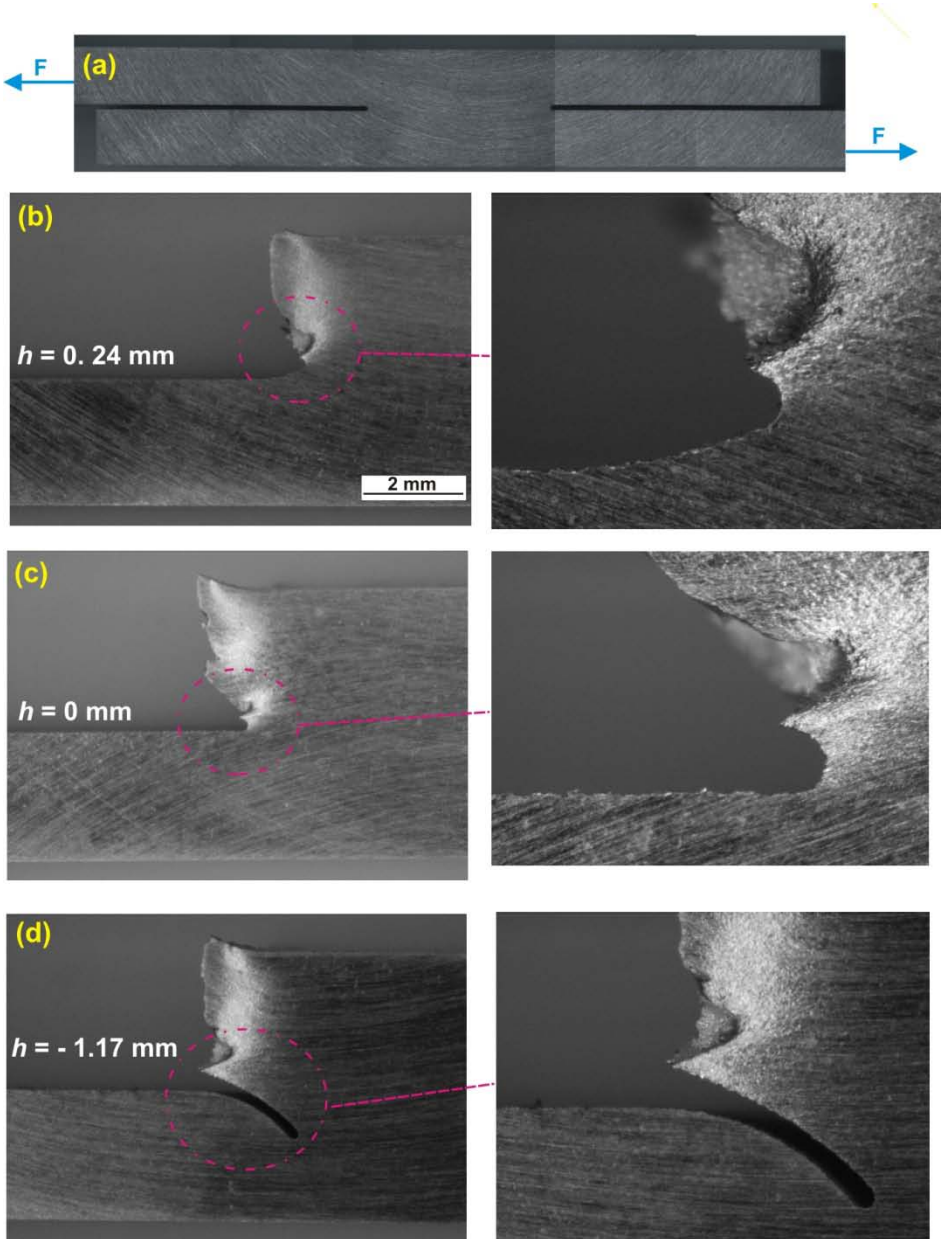

Figure 4-25 Images of fractured tensile shear tested specimens, (a) loading configuration, (b) positive *h* specimen, (c) zero *h* specimen and (d) negative *h* specimen

σ_{Lap}-strain curves for these tensile shear tested specimens are presented in Figure 4-26. Stress-strain curve for the as-received AZ31B-O alloy pulled in uniaxial tensile testing are also shown in Figure 4-26 for comparison. Tensile load per unit of width have been used for the as-received AZ31B-O alloy in order to be comparable to σ_{Lap} (load per unit of width). It can be seen that AZ31B-O alloy showed high global ductility with 24.5 % elongation to failure, but the fracture is sudden with little further local deformation and necking, as evident from σ_{Lap}-strain curve. However tensile shear specimens (with

artificial hooks) displayed considerably lower ductility in comparison to the uniaxial tensile tested AZ31B-O alloy.

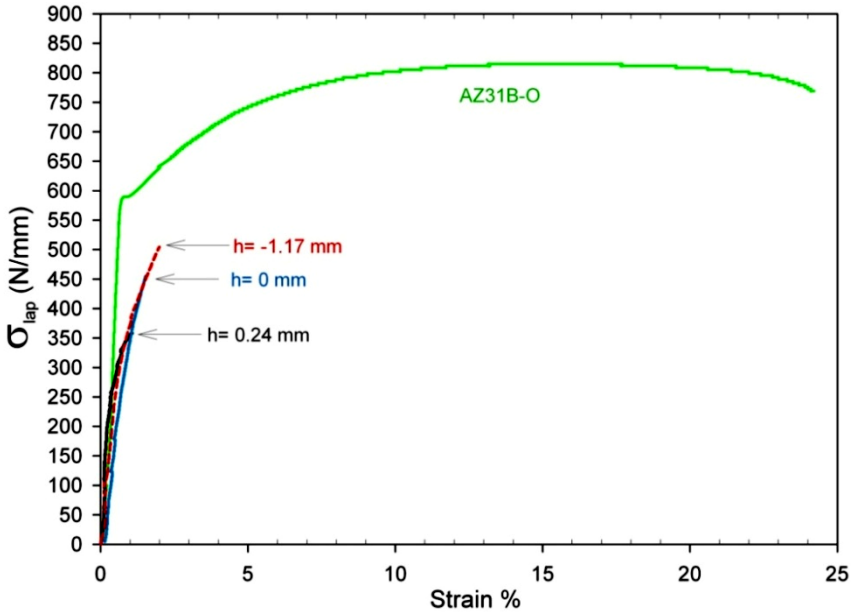

Figure 4-26 Stress-strain curves for tensile shear tested specimens (with different *h* as indicated) and AZ31B-O tensile sample

As described earlier, the actual fracture location of tensile shear specimens (with artificial hook) was in agreement with results of FEM modelling which predicts the failure location as a location with high stress concentration, under loading. Results of FEM modelling were further used to understand how stress distribution (during testing) relates to the crack growth, at early stage of fracturing. One of the most widely used methods in literature to describe the mixed-mode crack growth is based on maximal principal stress at the crack tip [94, 110-112]. The maximal principal stress criterion postulates that the direction of newly formed crack is perpendicular to the direction of maximal principal stress. The simulated distribution and tensor direction of maximal principal stresses for both positive and negative hook specimens are presented in Figure 4-27 and Figure 4-28 respectively.

For the positive hook specimen, it can be seen that maximal principal stress is highest at the hook tip (Figure 4-27a). Also the direction of maximal principal stress tensors (at hook tip) is almost at a right angle relative to the hook (Figure 4-27b). Thus according to maximal principal stress criterion, the crack is expected to grow parallel to the hook

at the early stage of fracturing. This is in agreement with the actual crack path observed, as shown in Figure 4-25b.

For the negative hook specimen, it can be seen that maximal principal stress is highest at location where hook deflected downward from lapping interface (Figure 4-28a). Also the direction of maximal principal stress tensors is almost parallel to the hook (Figure 4-28b). Thus the crack is expected to grow perpendicular to the hook, at location where started deflecting downward. This is also in agreement with the actual crack path observed, as shown in Figure 4-25d. It should be noted that simulated results (Figure 4-27 and Figure 4-28) are only valid for the early stage of crack growth, as the crack extension and geometric change (due to some degree of specimen rotation) results in variation of model geometry which requires further steps of FEM modelling and analysis.

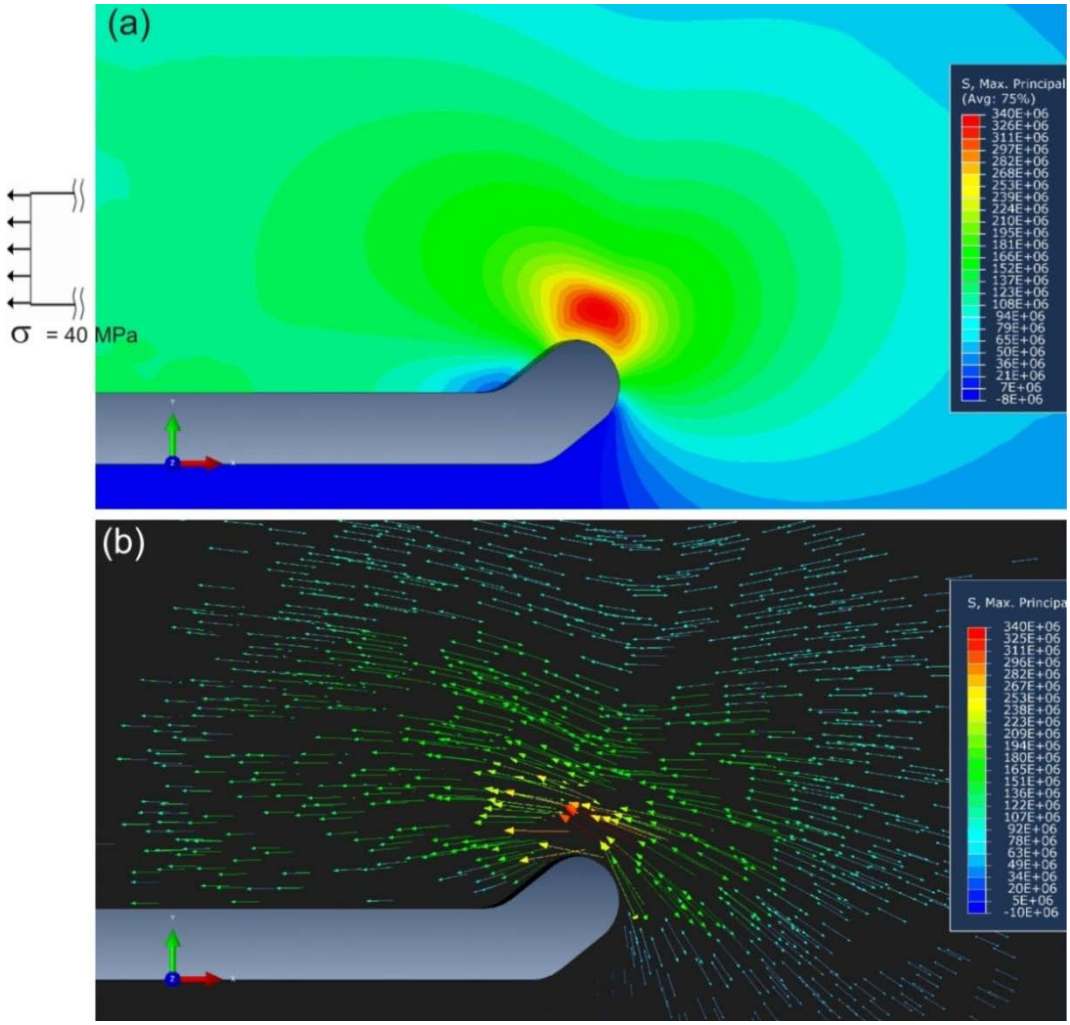

Figure 4-27 Distribution of maximal principal stress in a positive hook specimen with *h*=0.2 mm, (a) maximal principal stress values and (b) illustration of tensors of maximal principal stresses

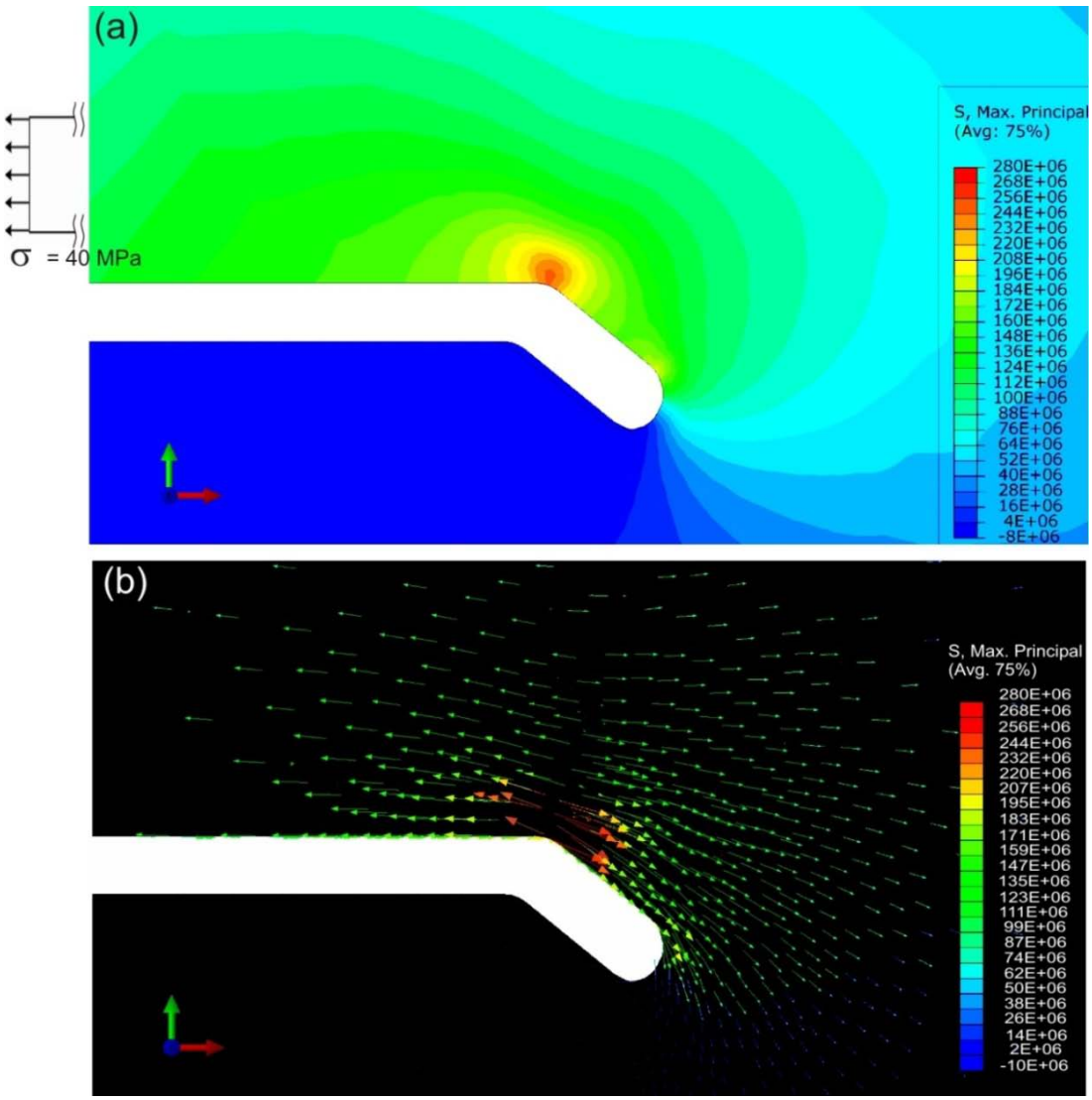

Figure 4-28 Distribution of maximal principal stress in a negative hook specimen with *h*= - 0.6 mm, (a) maximal principal stress values and (b) illustration of tensors of maximal principal stresses

The results presented in this section demonstrated that hook orientation is an important parameter affecting fracture location and strength of AZ31 tensile shear specimens. For the specimens with positive hooks, significant stress concentration forms at the hook tip region, facilitating the fracturing with low σ_{Lap}. However the specimens with negative hooking experience considerably less stress concentration at the hook tip region, thus resulting in increase of σ_{Lap}. Nevertheless the σ_{Lap} of negative hook specimens is not sensitive to *h* value and it increases only slightly with further increase of *h*. That is because stress concentration due to tensile shear geometry is unavoidable and thus considerable stress concentration forms at location where the hook starts to curve

downward (from the original lapping interface); which makes this area susceptible for failure during tensile shear testing. How the fracture behaviour is affected by other parameters such as microstructure and stress distribution during testing are discussed in next section.

4.4 Testing Geometry and Fracture Behaviour

In this section, how the testing geometry and stress distribution (during testing) affects the deformation mechanism and subsequent fracture of either AZ31B-O specimens or AZ31 FSL welds is presented.

4.4.1 Deformed Microstructures in AZ31B-O Tensile Tested Samples

The microstructure of AZ31B-O alloy (fully annealed) is shown in Figure 4-29, displaying fully recrystallised grains with no deformation twins. As it was explained in section 1.3.4, magnesium alloys with HCP crystal structure have limited slip systems at room temperature; therefore their mechanical performance shows texture dependence. Figure 4-30a shows (0002) pole figure of AZ31B-O alloy obtained using EBSD (as described in section 2.3.3). It can be seen that c-axis of grains is mostly parallel to ND of the sample. Thus, basal planes are extensively distributed parallel to plate surfaces (Figure 4-30b). The texture shown in Figure 4-30a is similar to those reported in literature for the rolled plates of AZ31 alloy [65, 113-115].

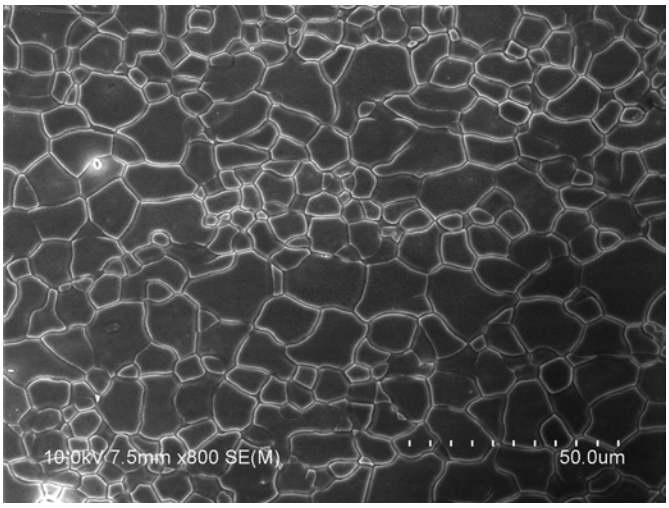

Figure 4-29 Microstructure of AZ31B-O showing fully recrystallized grains with no deformation twin

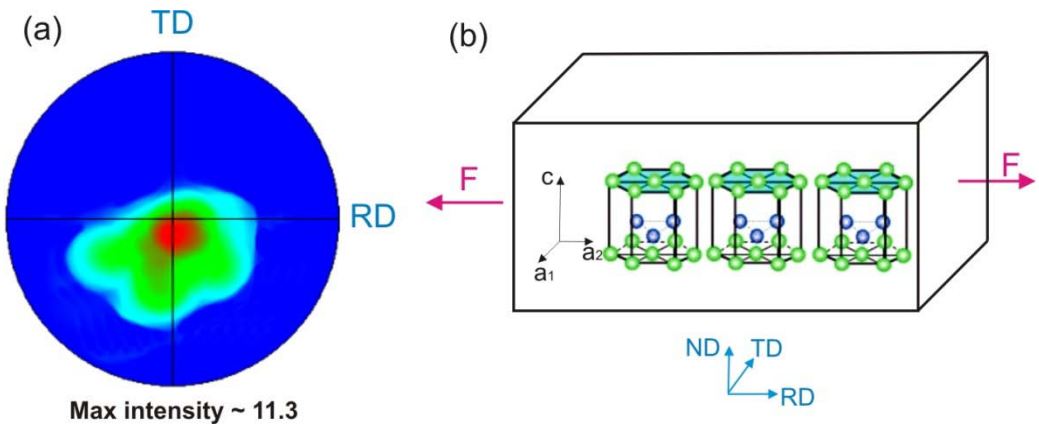

Figure 4-30 EBSD analysis of AZ31B-O, (a) (0002) pole figure and (b) schematic illustration of basal planes distribution in relation to tensile load direction

As explained in previous section, AZ31B-O showed high global ductility with 24.5 % elongation to failure. However the failure was sudden with little further local deformation and necking. Figure 4-31 shows the microstructure of AZ31B-O specimen, tensile deformed to fracture. Many narrow banded type twins formed near the fracture surface, as shown in Figure 4-31a. As described in section 1.3, the twins with the narrow banded morphology are recognized as contraction twins [45, 51]. The shear bands (group of parallel contraction twins) can also be seen at locations close to the fracture surface (Figure 4-31b). Furthermore, very fine recrystallized grains formed at the regions very close to the fracture surface (Figure 4-31c). Formation of these recrystallised grains is related to the contraction twins, as the contraction twins serve as preferred nucleation site in static recrystallisation [53]. The microstructure of a region ~ 10 mm away from the fracture surface is also shown in Figure 4-31d. It is clear that some contraction twins have also formed, however the twin density is considerably lower than the regions at vicinity of fracture surface (Figure 4-31a).

Figure 4-32 shows the fracture surfaces of a tensile tested AZ31B-O specimen. The fracture surface (Figure 4-32a) consisted of dimples, tear ridges and cleavage facets. The plate-like features, as indicated by the arrows in Figure 4-32b, suggesting cleavage fracture occurred likely along the twin boundaries [96, 97] . The size of these features matches the grain size of original alloy (Figure 4-29).

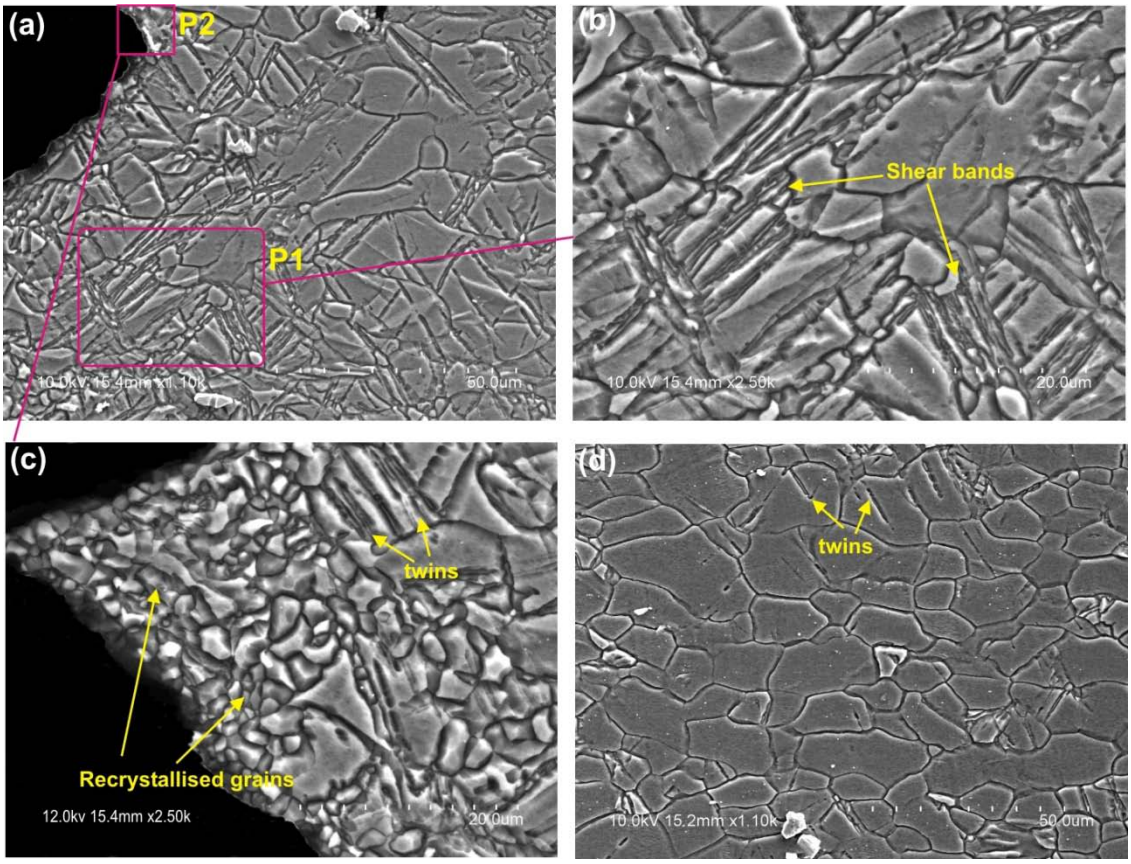

Figure 4-31 Micrographs of an AZ31B-O tensile test fractured sample, (a) SEM image showing contraction twins adjacent to fracture surface, (b) SEM image of location P1 in Figure 4-31a showing shear bands, (c) SEM image of location P2 in Figure 4-31a showing recrystallized grains and (d) micrograph of a location ~10 mm away from fracture surface

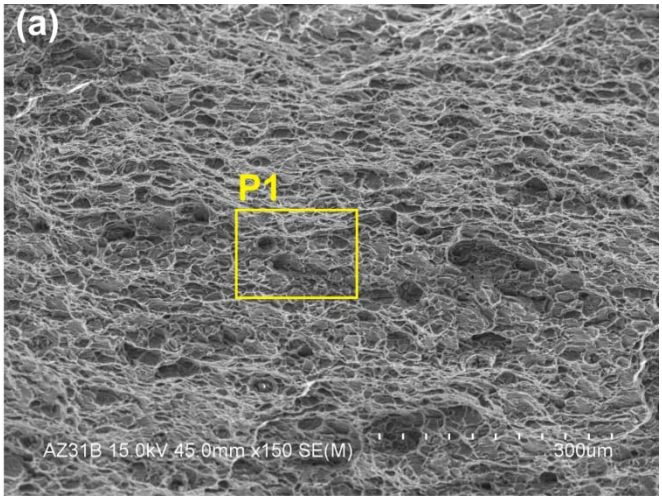

Figure 4-32 Fracture surface of AZ31B-O after tensile testing (a) showing ductile dimple pattern and (b) enlarged view of region P1

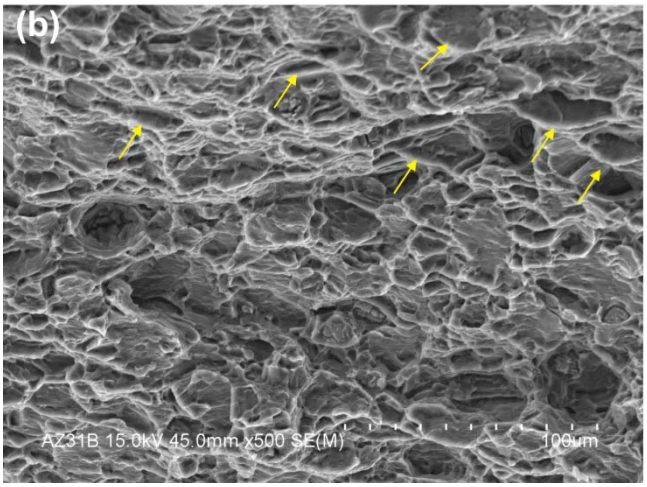

Figure 4-32 continued.

Koike [46] and Barnett [51] have reported that high tensile ductility of rolled AZ31 sheets (with a strong basal texture) is due to operation of basal <a> slip and prismatic <a> slip systems. Also at the early stage of deformation, $\{10\bar{1}\,2\}$ extension twins are formed in order to accommodate the concentrated stresses caused by dislocation pile-up. The activity of prismatic <a> slip brings about a large width strain, thus the tensile elongation can be compensated by the width reduction. However none of basal <a> slip, prismatic <a> slip and $\{10\bar{1}\,2\}$ extension twin provide <c> displacement component to accommodate the thickness strain. Therefore, contraction twins forms at the late stage of deformation to accommodate the thickness strain. It has been suggested that formation of contraction twins produces a highly localised shear-deformation region (within the twin) [43, 46, 51, 116] leading to strain incompatibility and eventual failure at twin interface. Therefore the dislocation slip systems are recognised as the major contributor to the macroscopic strain (elongation) of tensile loaded AZ31 specimens and the brittle nature of failure has been attributed to twinning.

4.4.2 Deformed Microstructures in Tensile Shear Tested AZ31B-O Samples

Microstructures of a tensile shear tested AZ31B-O specimen (Figure 4-25b) are presented in Figure 4-33. At location P1(Figure 4-33b), which is located 2 mm away from the fracture surface, no deformation twin can be observed. However at regions adjacent to the fracture surface, deformation twins can be seen clearly (Figures 4-33c and 4-33e). These results indicate that during tensile shear testing, twin formation is limited to the areas adjacent to fracture surface.

Figures 4-33c and 4-33d show the microstructure of region P2 (indicated in Figure 4-33a). It can be seen that some thick lenticular twins formed, together with narrow

banded twins (contraction twins). As described in section 1.3.4, the twins with thick lenticular morphology are known as extension twins [46, 50, 62]. It is known that extension twins are formed more easily than the other types of deformation twins (compression and double twins) because of its very low critical resolved shear stress [46]. The extension twins are the preferred twinning mode when there is an tensile strain component parallel to the c-axis of crystal [46, 62].

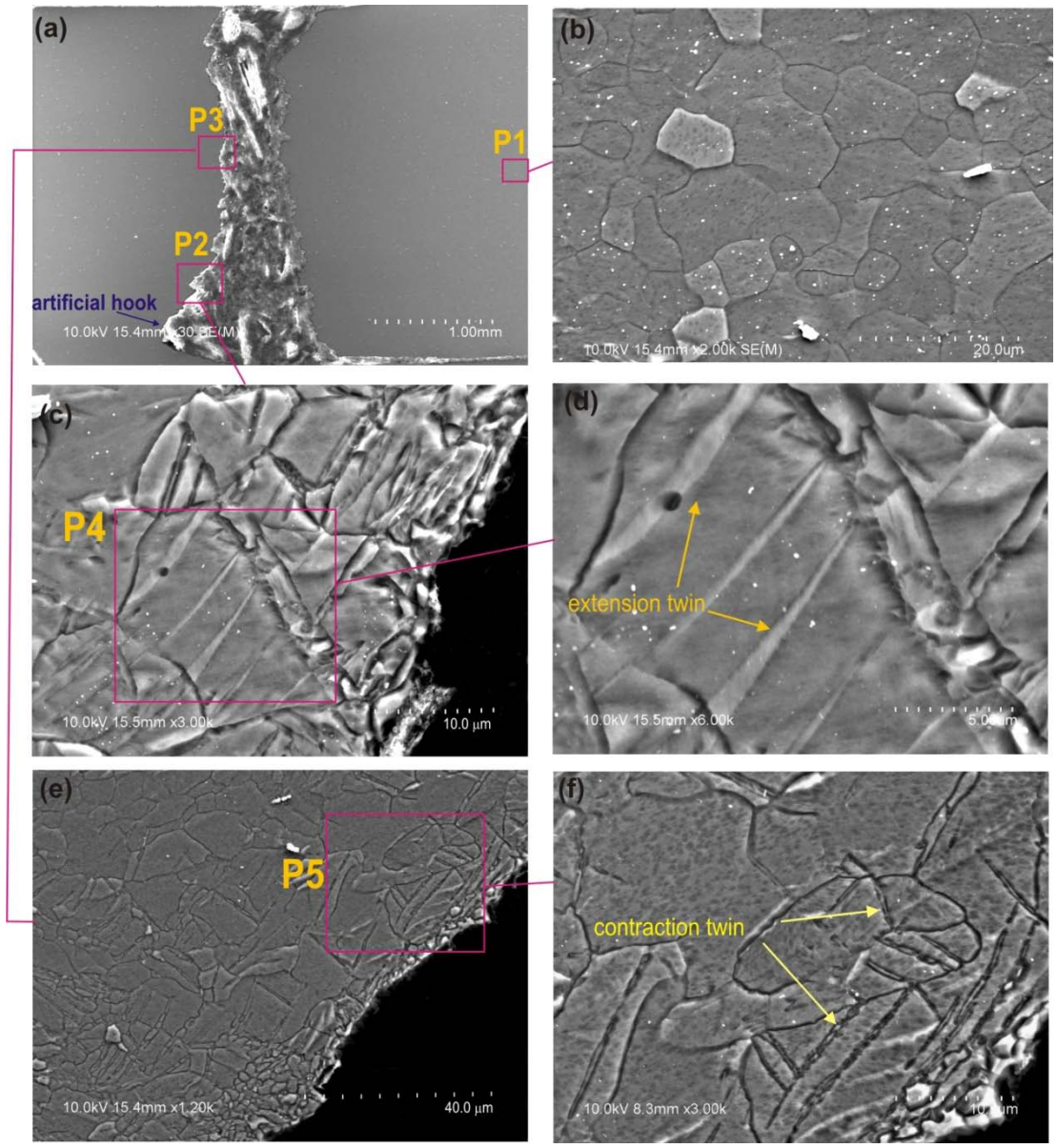

Figure 4-33 SEM micrographs of an AZ31B-O tensile shear test fractured sample, with artificial hook *h*=0.24 mm, (a) fractured specimen, (b) enlarged view of area P1 in Figure 4-33a, located 2mm away from the fracture surface, (c) enlarged view of area P2 in Figure 4-33a, (d) enlarged view of area P4 in Figure 4-33c, (e) enlarged view of area P3 in Figure 4-33a and (f) enlarged view of area P5 in Figure 4-33e

The extension twins observed in Figure 4-33c, are likely related to the stress distribution in tensile shear testing. As described earlier, AZ31B-O specimens have texture in which c-axis of grains are mostly distributed parallel to the thickness direction of plate (Figure 4-30). Also FEM modelling results shows that tensile shear loading produces a stress component parallel to the plate thickness direction (σ_y), as shown in Figure 4-34b. Therefore some grains become favourable for extension twinning, as the σ_y induce a strain parallel to the c-axis of grains.

Figures 4-33e and 4-33f show the microstructure of region P3 (indicated in Figure 4-33a). It can be seen that twins with narrow band morphology (contraction twins) formed, suggesting that the grain orientation and principal stress components at that region were more favourable for contraction twinning.

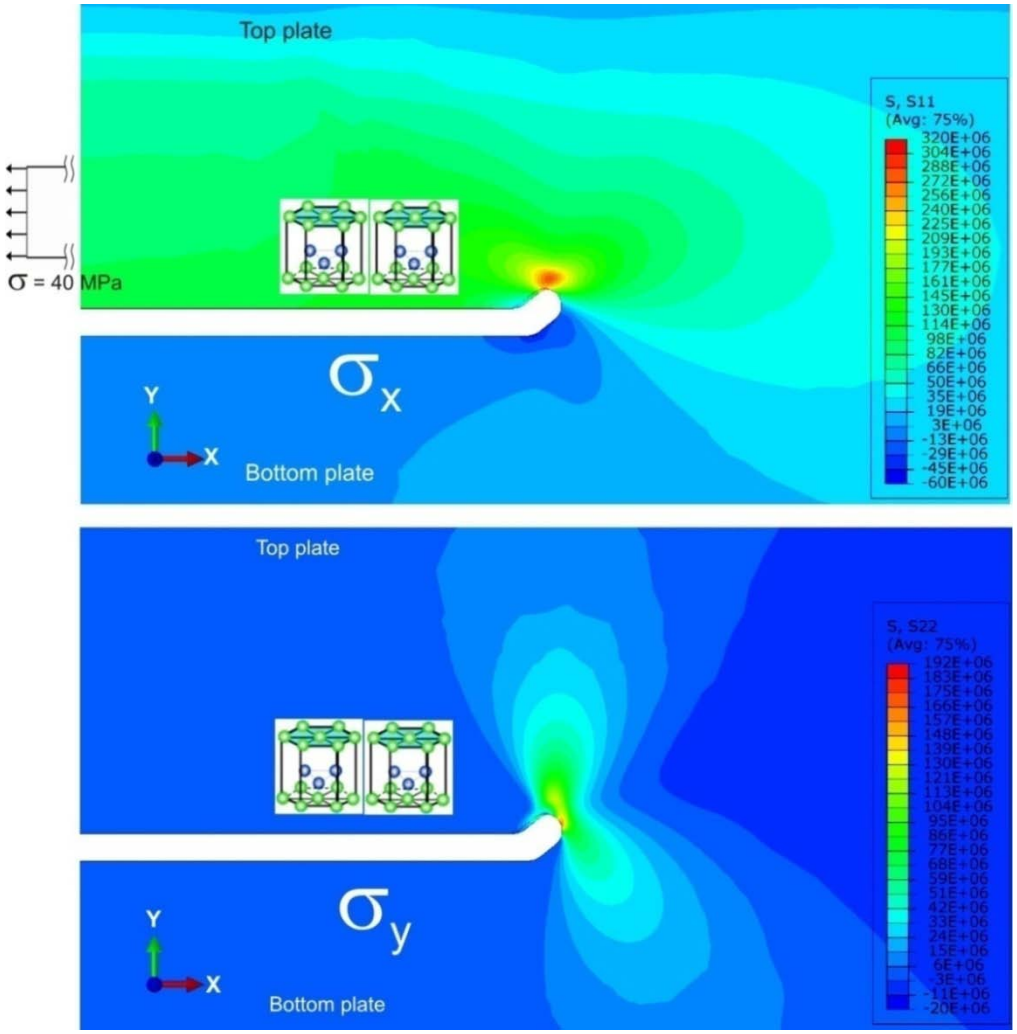

Figure 4-34 Simulation results showing stress distribution during tensile shear loading, (a) normal stresses in horizontal direction and (b) normal stresses in vertical direction. Dominant crystal orientation of grains schematically is illustrated.

The fracture surface of a tensile shear tested specimen is shown in Figure 4-35. In the area immediately next to the artificial hook tip (Figures 4-35a and 4-35b), directional cleavage features can be observed, reflecting a locally brittle fracture. However moving further toward the top plate (Figure 4-35c), the fracture surface consists of tear ridges, dimples and cleavage facets. The cleavage features associated with fracturing at twin boundaries are also indicated in Figure 4-35c. Formation of micro-cracks on fracture surface can also be seen in Figure 4-35c

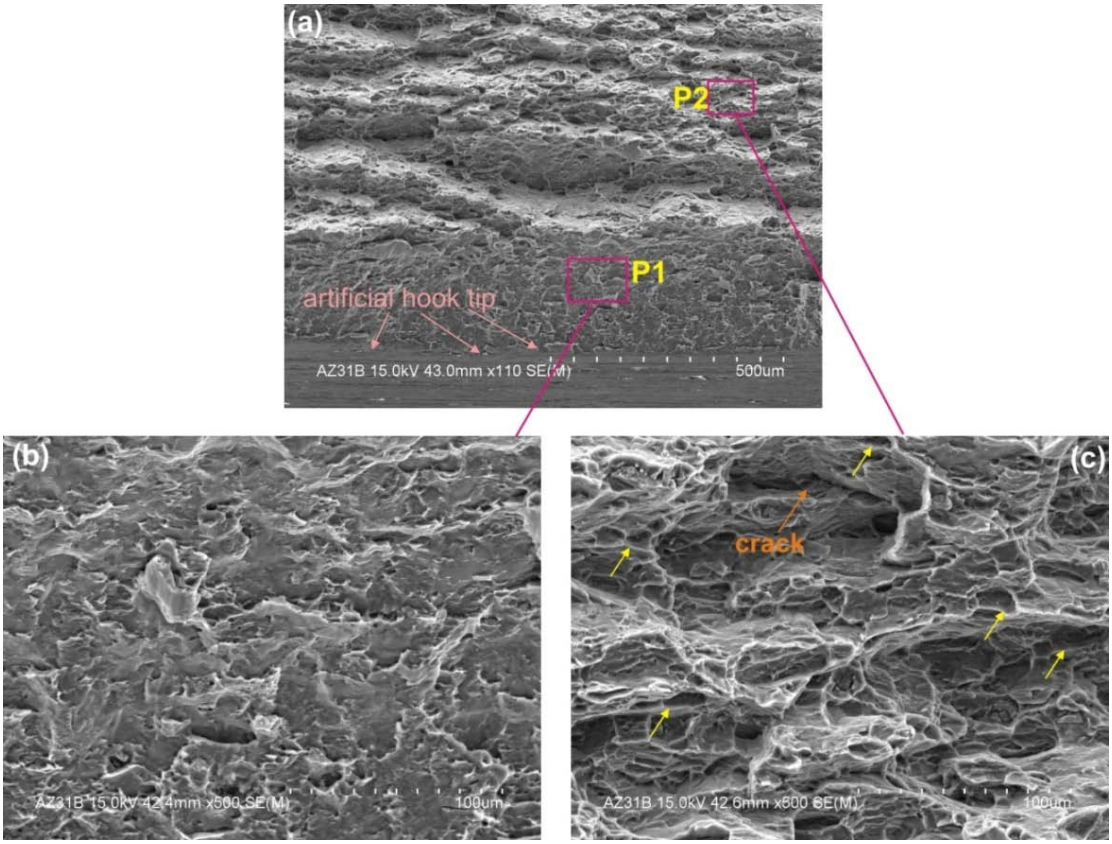

Figure 4-35 Fracture surface of an AZ31B-O tensile shear tested specimen with h=0.24 mm, (a) SEM image of fracture surface, (b) enlarged view of area P1 showing directional cleavage features and (c) enlarged view of area P2

As described in the previous section, high ductility of AZ31 alloy in uniaxial tensile testing is due to operation of dislocation slip systems as the major deformation mechanisms. However formation of contraction twins (at the late stage of deformation) produces a highly localised shear-deformation region (within the twin) leading to strain incompatibility and eventual failure at twin interface [43, 46, 51, 116].

In tensile shear loading, the non-uniform stress distribution caused by the lap geometry and also significant stress concentration at the hook tip region (Figure 4-34) forces the material to locally deform. Due to this highly localised stress concentration, twining is expected to be activated locally, when the twinning stress is exceeded. This is in agreement with observation made on microstructure of deformed sample (Figure 4-33) showing localised twinning at the regions adjacent to the fracture surface. As described earlier, the interface between the twin boundary and the matrix is generally considered as the origin or the propagation route of microcracks, during plastic deformation of magnesium alloys [43, 117, 118]. Therefore any situation which promotes the twin formation, such as localised stress concentration in tensile shear loading, can facilitate the fracturing. Thus it is reasonable to suggest that low ductility of AZ31B-O specimen during tensile shear testing (Figure 4-26) and subsequent brittle patterns observed on the fracture surface (Figure 4-35) are results of accelerated localised plastic deformation by twinning which has not been proceeded with considerable dislocation slip.

4.4.3 Deformed Microstructures in Tensile Shear Tested AZ31 FSL Welds

We now turn to the manner in which AZ31 welds fractured during tensile shear testing. Figure 4-36 shows the microstructure of different regions of a tensile shear tested AZ31 weld (h=0.25 mm). Microstructure of region P1 (Figure 4-36b), which is located 1.5 mm away from the fracture surface, is composed of fully recrystallised grains (due to dynamic recrystallisation during FSLW) with no deformation twins. However at other regions adjacent to the fracture surface (Figures 4-36c and 4-36d) narrow banded twins (contraction twins) formed. As described earlier, the confinement of twin formation to the regions adjacent to fracture surface indicates the localised plastic deformation induced by the twin formations. This is due to highly localised stress concentration produced at the hook tip region, where fracturing (cracking) initiated and propagated towards the top plate.

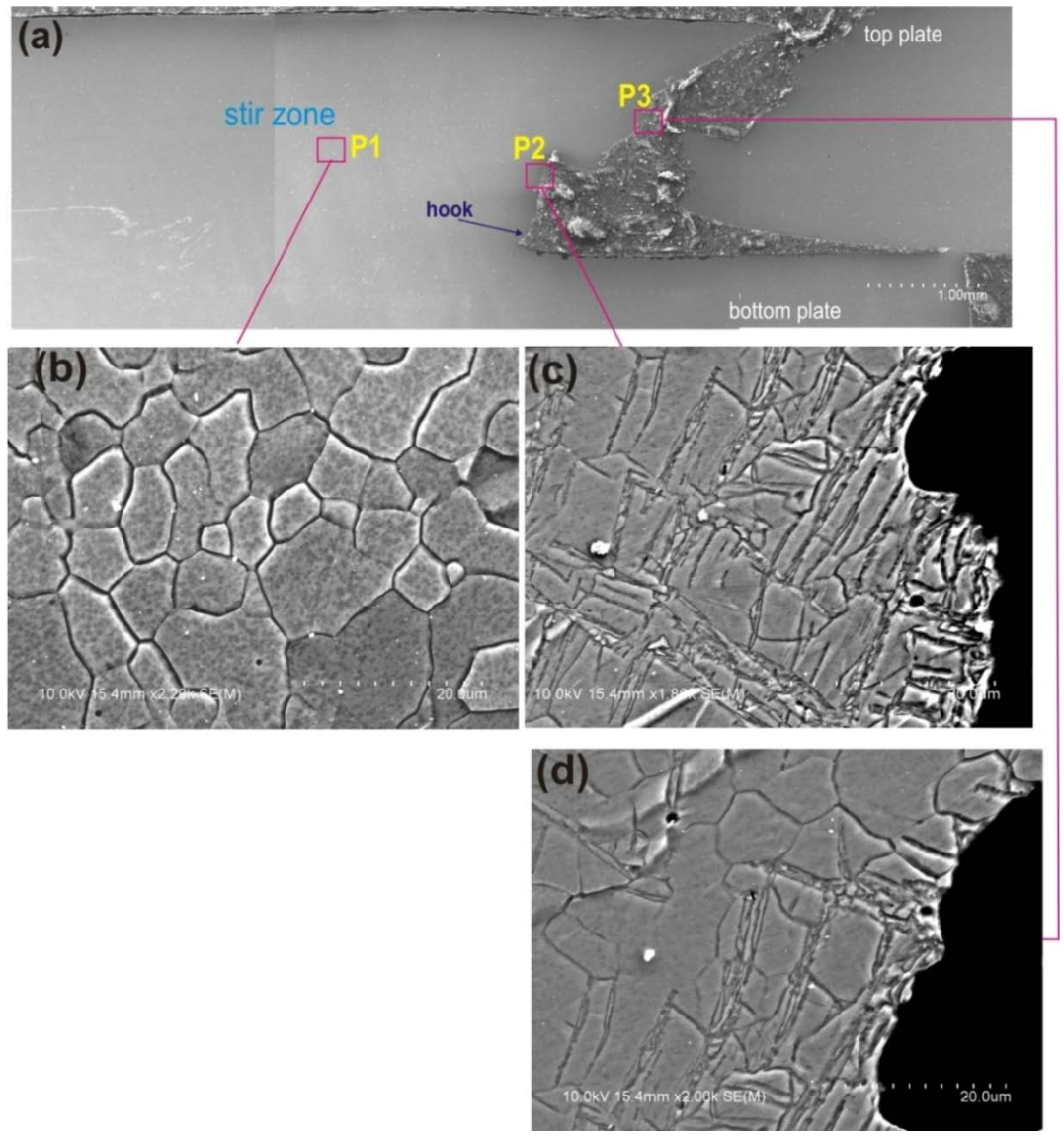

Figure 4-36 SEM micrographs of a AZ31 weld tensile shear sample tested to fracture, (a) fractured specimen, (b) enlarged view of region P1 in Figure 4-36a, which is located 1.5mm away from the fracture surface, (c) enlarged view of region P2 in Figure 4-36a and (d) enlarged view of region P3 in Figure 4-36a

Figure 4-37 shows the fracture surface of tensile shear tested AZ31 weld at different locations. Fracture surface morphology in the hook tip region (Figure 4-37c) is similar to the fracture surface observed in the artificial hook region of AZ31B-O tensile shear tested specimens (Figure 4-35b). However at region L2 (indicated in Figure 4-37a) which is located at middle of top plate, the fracture surface (Figure 4-37c) shows directional tear features indicating preferred cleavage along certain crystallographic planes [119]. Furthermore at region L3 (indicated in Figure 4-37a) which is close to the weld top surface, fracture surface pattern (Figures 4-37e and 4-37f) is completely

different from those observed at location L2 (Figure 4-37c). As the fracture behaviour of magnesium alloys shows texture dependence, thus the different fracture surface morphologies observed through the weld thickness suggests the variations of local textures at the different regions of the AZ31 weld. Recently Yuan et al [113] have investigated the local texture evolution in the stir zone of AZ31 weld and reported a severe gradient in crystallographic texture throughout the thickness of stir zone. It has been suggested [113] that the variation in local texture of stir zone is related to stress state and associated complex material flow during FSW resulting in rotation of the basal planes and thus variation of local textures.

As it has been explained in section 1.3.4, depending on loading mode and grains orientation, different deformation twinning and dislocation slip mechanisms can be activated. Thus it is likely that variation of local texture between adjacent regions of AZ31 welds results in an incompatible plastic boundary between these regions causing a local fracture (cracking) [120]. An example of crack formation between two regions with considerable difference in fracture surface patterns (and thus local textures) is given in Figures 4-37b and 4-37d. It can be seen that the region above the formed crack has different texture (as indicated by directional tear features) from the region below the crack. However the contribution of these cracks to the fracture strength is unclear.

σ_{Lap} as a function of *h* for both AZ31B-H24 FSL welds and AZ31B-O tensile shear specimens is presented in Figure 4-38. It can be seen that σ_{Lap} of both AZ31B-H24 FSL welds and AZ31B-O increases with decrease of *h*. However AZ31B-O specimens achieved considerably higher σ_{Lap} compared to AZ31B-H24 FSL welds. For instance when h=0.24 mm, the difference between σ_{Lap} of AZ31B-H24 weld and AZ31B-O tensile shear specimen is about 100 N/mm. The AZ31B-H24 welded samples and AZ31B-O specimens differ in number of ways which could affect their mechanical performance, including material temper, hook sharpness and crystallographic texture which are discussed in following.

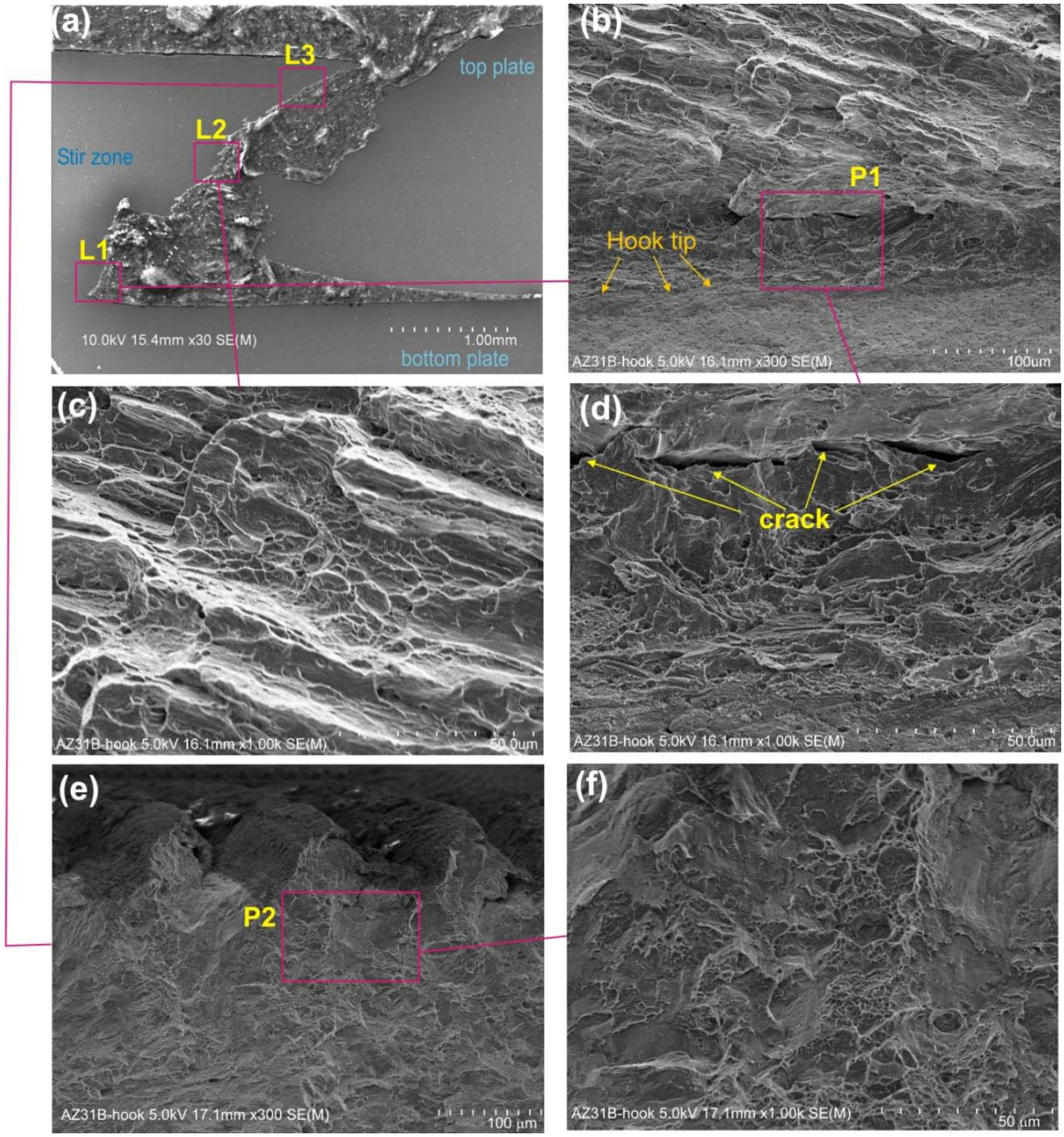

Figure 4-37 SEM micrograph of fracture surface of AZ31 weld (*h*=0.25 mm) tensile shear sample tested to fracture (a) fractured specimen, (b) fracture surface of region L1 in Figure 4-37a, where hook is located, (c) fracture surface of region L2 in Figure 4-37a, located at mid top plate thickness, (d) enlarged view of region P1 in Figure 4-37b, (e) fracture surface of region L3 in Figure 4-37a, located close to top plate surface and (f) enlarged view of region P2 in Figure 4-37e

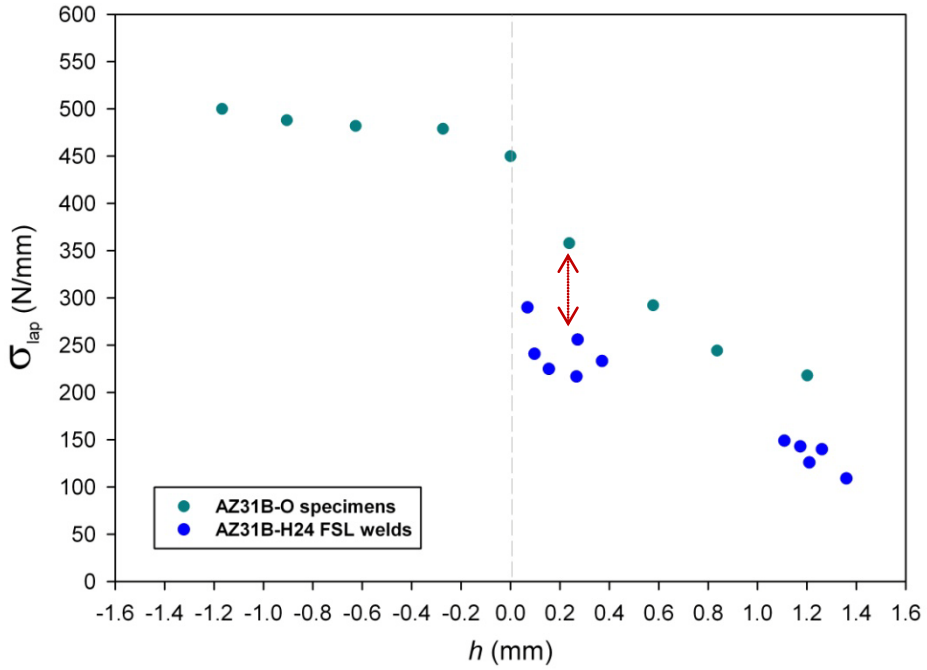

Figure 4-38 σ_{Lap} plotted as function of *h* for both AZ31B-H24 FSL welds and AZ31B-O tensile shear specimens

Figure 4-39 shows the stress–strain curves obtained for the two material tempers of AZ31, i.e. AZ31B-H24 and AZB-O. It is clear that AZ31B-H24 achieved considerably higher yield strength and *UTS* than AZ31B-O. That is because the AZ31B-H24 is strained-hardened material while AZ31B-O is fully annealed material and hence softer than the former. However as described earlier, the microstructure of the stir zone and TMAZ in the AZ31 welds is composed of fully recrystallised grains (Figure 4-12) and hence the microstructure can be considered as fully annealed. Also as the crack initiated at the hook tip and then propagated through the SZ (Figure 4-36a), at locations of fracture, material temper can be considered fully annealed. In other words at location of fracture, welded specimens have the same material temper as AZ31B-O tensile shear specimen. Consequently the difference in temper of AZ31 materials is not the reason for the considerable difference between σ_{Lap} of AZ31B-H24 weld and AZ31B-O tensile shear specimen.

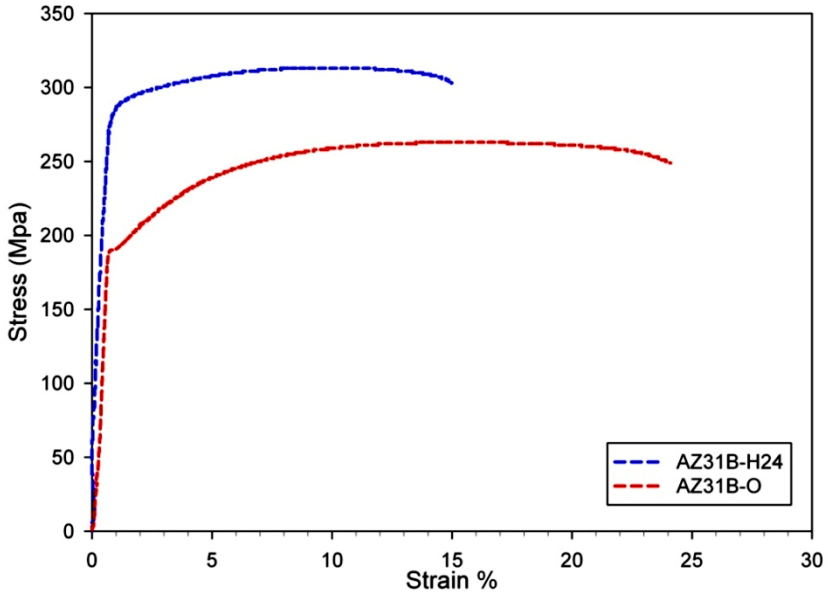

Figure 4-39 Tensile stress-strain curves of AZ31B-H24 and AZ31B-O alloys

In AZ31 welds, the hook are made of array of very thin oxides therefore it is considered as a very sharp crack. However for the AZ31B-O tensile shear specimen, the artificial hook tip had a radius of 0.2 mm thus it can be considered a blunted crack. Figure 4-40 shows the simulated stress distribution at the hook region for the two tensile shear specimens having same h=0.25 mm but different hook sharpness. It can be seen that under an applied load of 15MPa, maximum effective stress for the specimen with the sharp hook can reach the value of 202 MPa indicating significant stress concentration formed at the hook tip (Figure 4-40a). However the maximum effective stress at the blunted hook tip can only reach the value of 100 MPa (Figure 4-40b). Therefore the specimen with a sharp hook requires lower load for crack initiation at hook tip. However it should be noted that as the applied load to the specimen increases, the sharp crack blunts itself. Therefore the sharp hook present in AZ31 welds is partially accountable for their lower σ_{Lap} compared to AZ31B-O specimen with blunted artificial hooks.

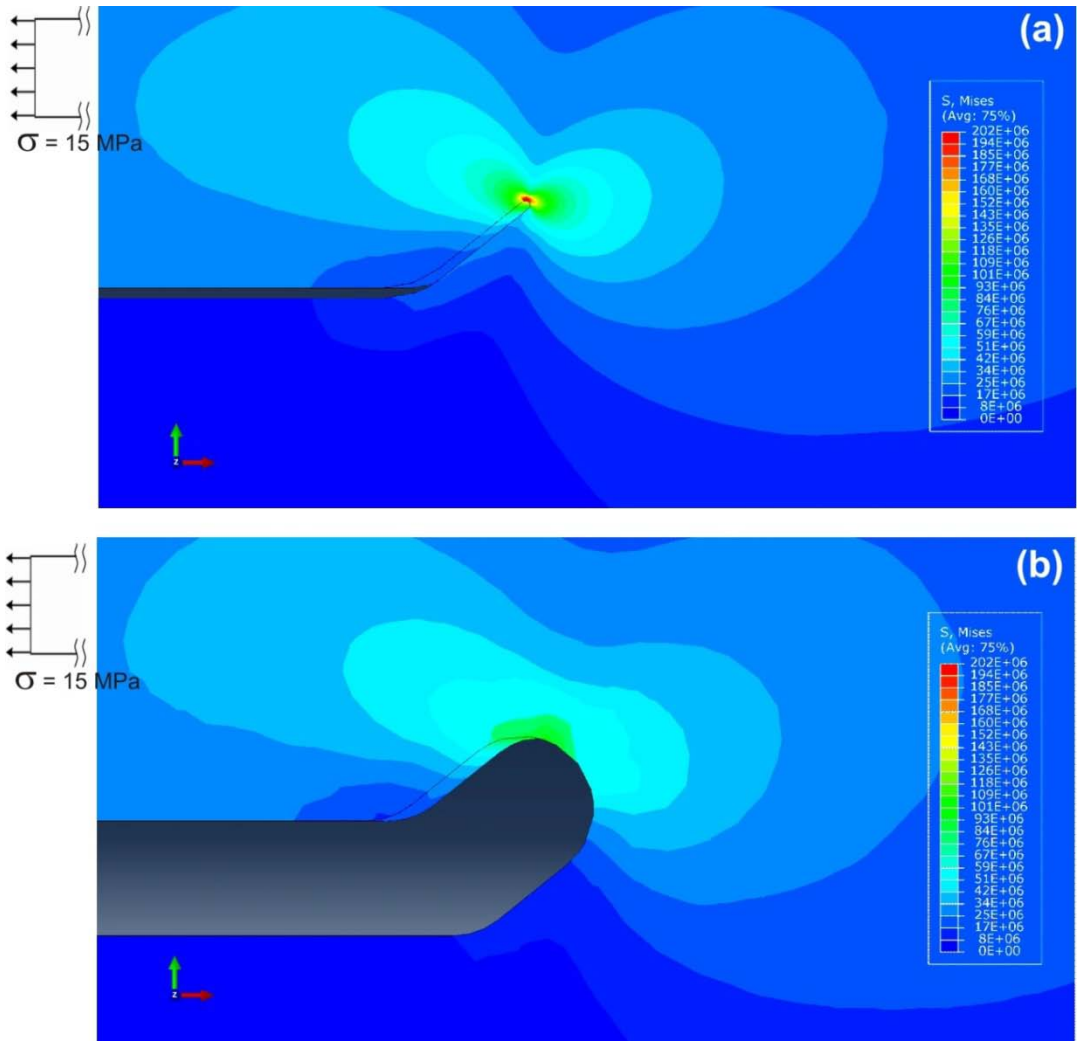

Figure 4-40 Simulated stress distribution at the hook region of two specimens having same *h*= 0.24 mm, (a) sharp hook with radius of 0.01mm and (b) blunted hook with radius of 0.2 mm

Also as described earlier, the AZ31B-O specimens had a texture with basal planes extensively distributed parallel to plate surfaces (Figure 4-30). However in AZ31 welds, material flow during FSW results in local texture variation throughout the stir zone [113]. Therefore as suggested earlier, it is likely that local texture variations (in FSL weld) may assist the fracturing through creating an incompatible plastic boundary between the adjacent regions. However as the effect of local texture variation on σ_{Lap} is not certain, thus the difference in the sharpness of hooks can be regarded as the major factor responsible for the difference in σ_{Lap} of AZ31B-H24 FSL welds and AZ31B-O tensile shear specimens (with the same hook size).

4.5 Summary

In FSLW of AZ31B-H24 alloy, the ω was also found to be the major parameter affecting *h*, in agreement with literature. Increasing ω resulted in increase of stir zone temperature and hence stir zone plasticity, affecting the stir flow volumes which cause interface up-lifting, similar to FSLW of Al 6060. However hooks in AZ31 welds are located much closer to the pin compared to hooks in Al 6060 welds, as a result of much smaller stir zone in AZ31 welds. Also hooks in AZ31 welds are quite continuous while a hook in Al 6060 can be highly discontinuous. The observed difference in hook characteristics (shape, distance to weld center, continuity) of AZ31 and Al 6060 welds is suggested to be related to the difference in plastic properties of these materials at the high temperatures of FSLW, affecting the material flow during welding.

During tensile shear testing, all the AZ31 welds fractured by the same mode in which the crack initiated from the hook location and then propagated through top plate. That is related to the hardness distribution in AZ31 welds in which the hook location had lower hardness (and thus local strength) than HAZ region. Therefore contrary to Al 6060 welds, when *h* is small, HAZ softening could not compete against hooking for deformation and fracturing. Thus, failure always occurred at hook location. Consequently σ_{Lap} of AZ31 welds exhibited a strong dependence on *h*.

The maximum achieved σ_{Lap} in AZ31 welds was about 1/3 of strength of original AZ31B-H24 alloy pulled in tensile testing. This ratio is much lower than that for Al 6060 welds with $\sigma_{Lap} \approx 2/3$ of strength of original 6060-T5 alloy. High local ductility of Al 6060 resulted in considerable specimen bending/rotation and thus diminishing stress concentration caused by tensile shear loading. On the other hand, lack of local ductility and specimen bending/rotation in AZ31 welds allowed for the stress concentration to be maintained during tensile shear loading and thus resulted in fracturing with lower σ_{Lap}.

It was found that hook orientation is an important parameter affecting fracture location and strength of AZ31 tensile shear samples. In tensile shear testing of the samples with positive hooks, significant stress concentration forms at the hook tip region, facilitating the fracturing with low σ_{Lap}. On the other hand, the samples with negative hooking experience considerably less stress concentration at the hook tip, thus resulting in increase of σ_{Lap}. For the case of negative hook specimens with h >-0.6 mm, the end of hook is almost stress concentration free, but in location where hook start curve downward (from the original lapping interface), significant stress concentration forms and thus fracture occurs.

High ductility of either AZ31B-O or AZ31B-H24 (with strong basal texture) during uniaxial tensile testing is due to operation of dislocation slip systems as the major deformation mechanisms. Therefore large amount of deformation took place by dislocation slips, prior to formation of contraction twins (to accommodate the strain in thickness direction) which produces a highly localised shear-deformation region, leading to failure. On the other hand, localised high stress concentration caused by tensile shear loading, force the material to locally deform, resulting in activation of deformation twinning at the regions of high stress concentration. The localised plastic deformation by twinning, which was not preceded with substantial deformation by dislocation slip, facilitated the fracturing with lower ductility and σ_{Lap}.

5. Interfacial Microstructure and Fracture Strength of Dissimilar FSL Welds

In this chapter, the effect of pin positioning on interfacial microstructure of Al/Steel FSL welds is given first. Then the effect of intermetallic formation and its distribution in interface region on fracture behaviour of Al/Steel FSL welds is presented in detail. Later the effect of pin positioning on interface microstructure and subsequent fracture behaviour of Al/Ti FSL welds is presented. It will be shown that when the bottom of pin contacts (without penetrating) the bottom plate (steel or titanium), formation of a single continuous intermetallic layer at interface resulted in the joints to fracture in a ductile manner during testing, thus considerably high σ_{Lap} values obtained.

5.1 Al 6060-T5 to Mild Steel FSL Welds

As has been explained in section 1.4.1, in current literature pin penetration to steel has been accepted as a condition for promoting σ_{Lap} of Al/Steel FSL welds [8, 27, 28, 68, 69]. However effects of non pin penetrating conditions (during FSLW) on Al/Steel interface structures and the corresponding σ_{Lap} values have not been systematically investigated. In next sections, results of pin positioning on interface microstructure and subsequent σ_{Lap} of Al/Steel FSL welds will be presented and discussed.

5.1.1 Microstructure of Interfacial Regions

The interfacial microstructures corresponding to L_{dis} (illustrated in Figure 2-2) varying from positive to negative values, i.e., from non pin penetrating to pin-penetrating conditions are first presented. Figure 5-1 shows the microstructure at the interfacial region of welds made using same ω=710 rpm and ν=80 mm/min with different L_{dis} values, as indicated. It can be seen that when L_{dis}=0.8 mm (Figure 5-1a), no visible intermetallic phase formed at the interfacial region. Consequently there is no metallurgical bonding between aluminium and steel plates, thus they separated during preparation of metallographic sample. However in welds made using L_{dis}= 0.5 mm (Figure 5-1b) and L_{dis}=0.3 mm (Figure 5-1c), small outbursts of Fe-Al intermetallics with the size of ~ 1.0 μm formed along the interface. It is clear that the number of formed intermetallic outbursts increased by decreasing L_{dis}.

As it was explained in section 1.1.2, stir material immediately next to the pin is driven downward by the rotating threads. This downward flowing material, if the pin is sufficiently close to steel surface, may rub the steel surface resulting in removal of the thin surface oxides. Therefore formation of discontinuous intermetallics (when L_{dis} > 0.3mm) indicates the early stage of interfacial intermetallic growth along the joint interface at high temperatures during FSLW. It should be pointed out that formation of Fe-Al intermetallic outbursts at the interface, resulting from the early stage of interfacial intermetallic growth in Al-steel couples at high temperatures, have commonly been observed [121, 122]. However the condition of $L_{dis} \geq 0.3$ mm has not insured a continuous intermetallic layer, suggesting a possible non-continuous metallurgical bond.

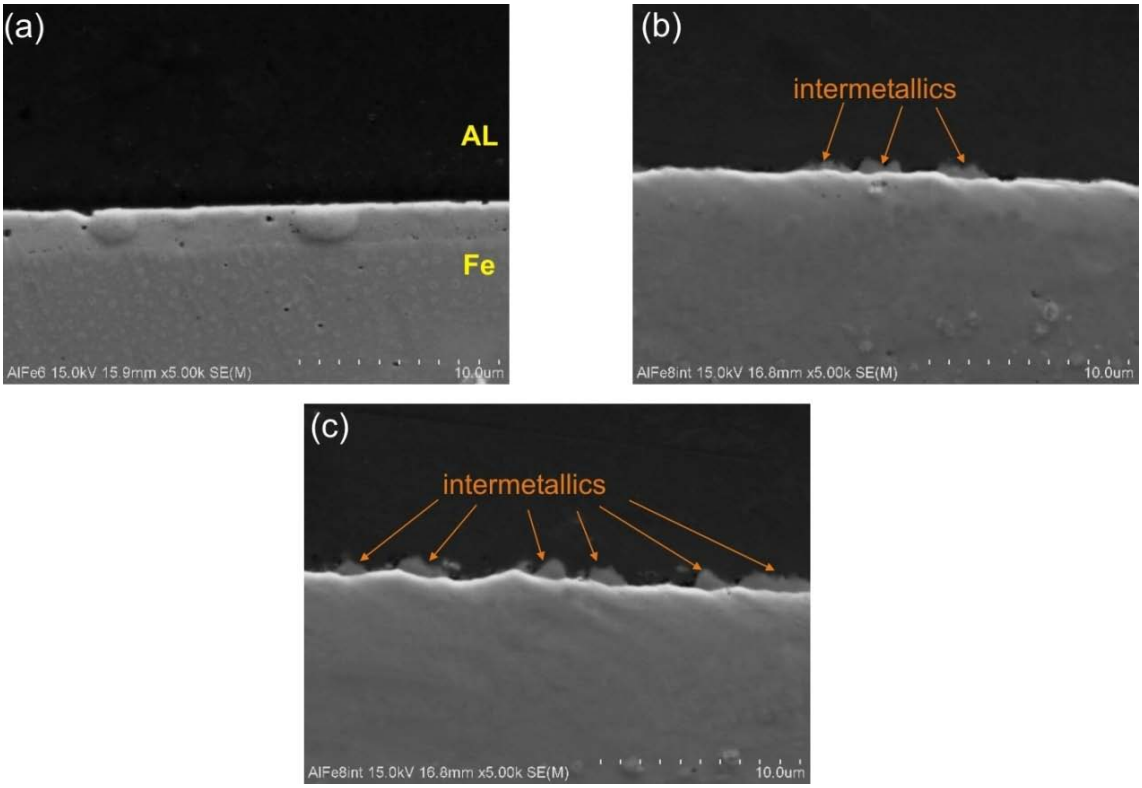

Figure 5-1 Micrographs showing microstructures of interface region for the welds made using ω =710 rpm, ν =80 mm/min and (a) L_{dis}= 0.8 mm, (b) L_{dis} = 0.5 mm and (c) L_{dis} = 0.3 mm

Interface microstructure changed considerably when the condition of pin penetration was used. This can be seen in Figure 5-2 showing the microstructures of interface region for a weld made using L_{dis}= -0.1 mm (representing a slight pin penetration).

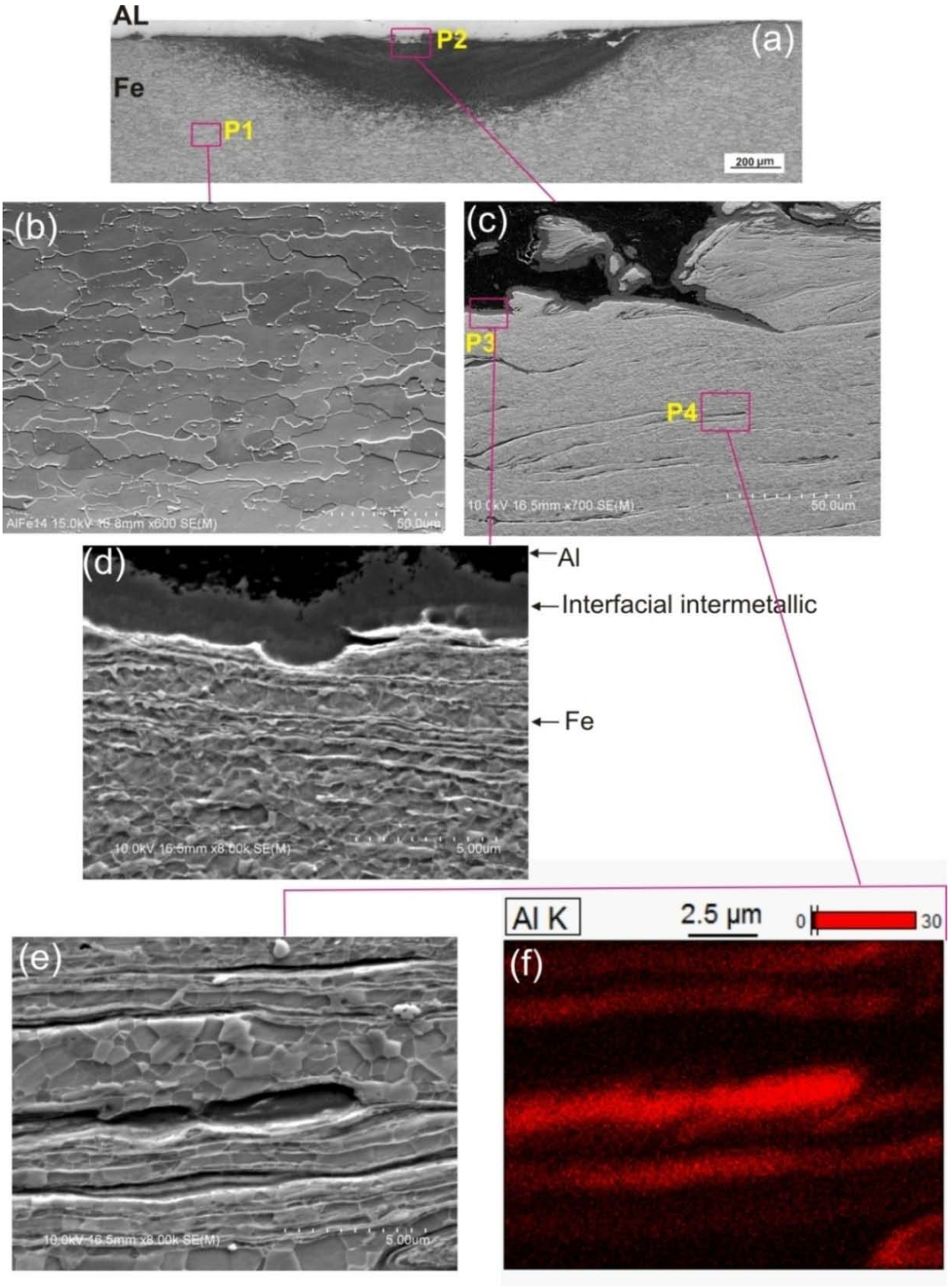

Figure 5-2 Microstructure of a weld made using ω =710 rpm, ν =80 mm/min and L_{dis}= -0.1 mm, (a) optical macrograph, (b) SEM micrograph of area P1 in Figure 5-2a showing original microstructure of steel, (c) SEM micrograph of area P2 in Figure 5-2a, (d) SEM micrograph of area P3 in Figure 5-2c, (e) SEM micrograph of area P4 in Figure 5-2c, (f) EDS map of Al for Figure 5-2e

Due to the pin penetration, a mixed stir zone developed in the steel which appears as dark in Figure 5-2a. Higher magnification images of this mixed stir zone (Figure 5-2c) and also results of EDS mapping (Figure 5-2 e-f) suggests that mixed stir zone is a irregular laminate of α-Fe and Fe-Al intermetallic layers. Also, close examination of Figure 5-2 c-d reveals that a continuous Fe-Al intermetallic layer formed at the interface between the mixed stir zone and aluminium. Thus, metallurgical bonding is continuous in this penetrated region.

Also, examination of mixed stir zone in Figures 5-2 d-e clearly shows that very fine equiaxed α-Fe grains (~ 0.5-1 μm) formed due to the dynamic recrystallization of steel grains after undergoing heavy plastic deformation (induced by the rotating pin) at high temperatures of FSLW. Original microstructure of mild steel with the average grain size of 30 μm is also shown in Figure 5-2b for comparison. Recrystallization of α-Fe grains in the mixed stir zone has also been reported by Coelho et al [8].

Formation of intermetallics layers at the mixed stir zone was further investigated using EDS spot analysis. Typical EDS spectra of intermetallic layers at the Al/Steel interface and inside the mixed stir zone (of the weld shown in Figure 5-2) is presented in Figures 5-3b and 5-3c, respectively. The chemical composition of 72.5at%Al and 27.5at%Fe in Figure 5-3b, may indicate that the thin layer at Al/Steel interface is mainly Fe_2Al_5 intermetallic, according to Al-Fe phase diagram (Figure 1-31). On the other hand, the chemical composition of 61.8at%Al and 38.2at%Fe in Figure 5-3c may indicate that the thin layer within the mixed stir zone is likely to be $FeAl_2$ intermetallic phase. However as explained in section 1.4.1, due to the analytical spot size being large in SEM/EDS hence assigning the structure of either $FeAl_2$ or Fe_2Al_5 to the small size intermetallic layers is not very reliable.

The microstructures shown in Figure 5-2 clearly shows that under the pin-penetrating condition, the interface region consist of intermix and irregular layers of intermetallics and deformed and recrystallised α-Fe. Furthermore, the thickness of intermetallic layers within the interface region is not constant. A similar microstructure was also described for Al/Steel FSL welds [8] when the pin-penetrating condition used.

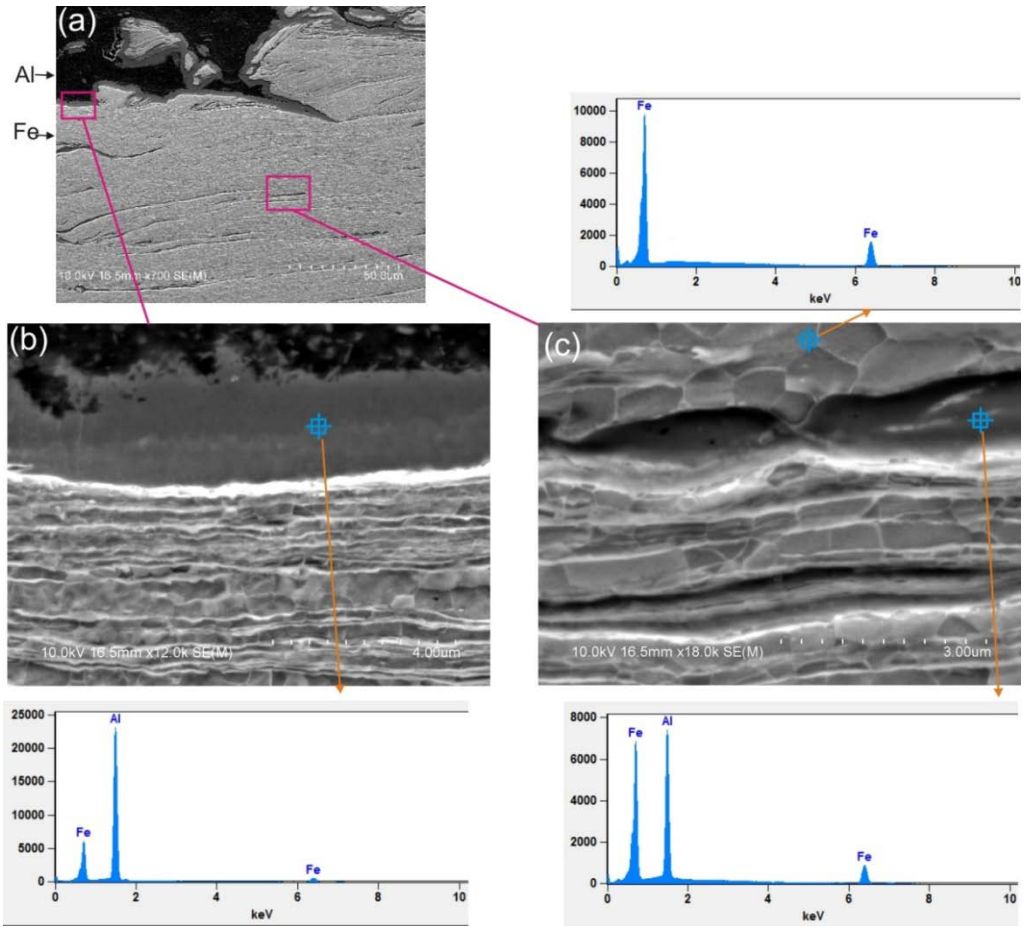

Figure 5-3 (a) microstructure of mixed stir zone for the weld shown in Figure 5-2, (b) SEM micrograph showing the intermetallic layer at Al/Steel interface, EDS spectra of intermetallic layer is also shown and (c) SEM micrograph showing the intermetallic layers within the mixed stir zone. EDS spectra of intermetallic layer and recrystallised α-Fe is also shown

5.1.2 Relationships between Interfacial Microstructures and σ_{Lap}

As illustrated in last section, the nature of interface (in terms of its macro and microstructure) affected considerably by varying L_{dis}. How the interface microstructures in turn affect the fracture strength of welds is analysed in this section. Figure 5-4 shows the average σ_{Lap} values of welds plotted as function of L_{dis}. It can be seen that the weld made using L_{dis}=0.8 mm has exhibited no strength (σ_{Lap}=0 N/mm). That is consistent with the observation that no intermetallic layer formed at the interfacial region (Figure 5-1a) and hence there is no metallurgical bonding to join the aluminium and steel plates. Decreasing L_{dis} to 0.5 mm resulted in formation of a few intermetallic outbursts (Figure 5-1b), and thus some strength (σ_{Lap} =72 N/mm) has developed. Further decreasing L_{dis} to 0.3 mm improved the average value of σ_{Lap} to 121 N/mm which is due to a higher

number of intermetallic outbursts and thus larger metallurgical bonding area along the interface (Figure 5-1c).

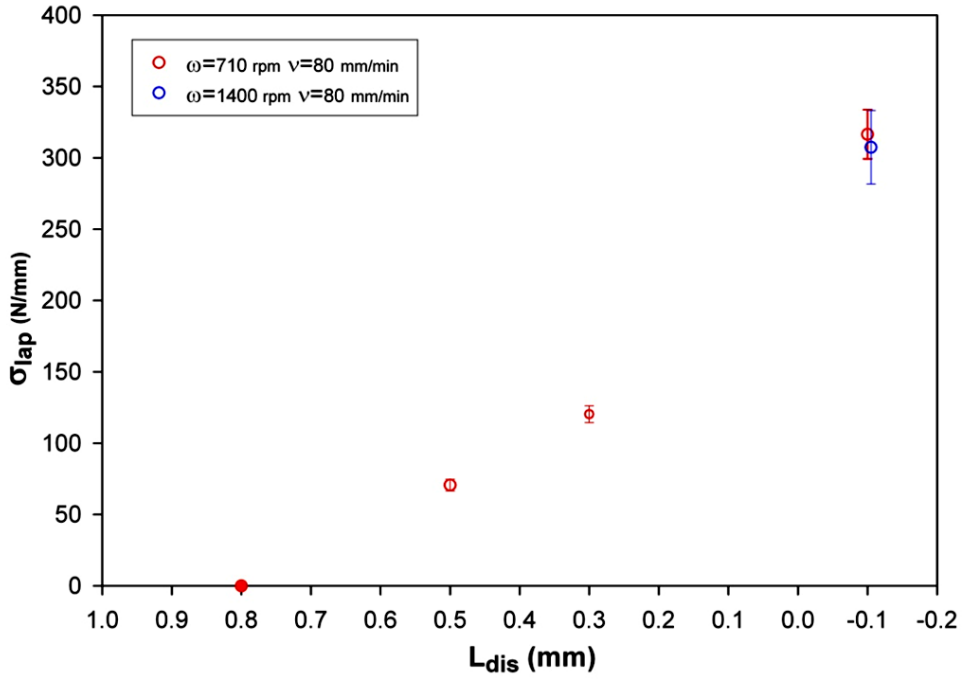

Figure 5-4 Values of σ_{Lap} (and one standard deviation) for the welds made using different L_{dis}, ω and ν as indicated

In the pin-penetrating condition (L_{dis} = - 0.1 mm), average value of σ_{Lap} increased significantly to 307 N/mm. The σ_{Lap} value at ~ 307 N/mm is a high strength value considering that, as has been explained in section 1.4.1, Movahedi et al [69] conducted a series of Al/Steel FSLW experiments with sufficient pin penetration and their maximum σ_{Lap} value was 304 N/mm. Figure 5-5 shows typical σ_{Lap}–strain curves, one for the weld made using L_{dis} = - 0.1 mm and the other L_{dis} = 0.3 mm. The fracture energy, represented by the area under the curve, of the slightly penetrated weld (L_{dis} = - 0.1 mm) is 42 times larger than that of the weld without penetration (L_{dis} = 0.3 mm). The low fracture energy for the weld made using L_{dis} = 0.3 mm indicates that tensile shear sample fractured without plastic deformation.

Since in pin-penetrating condition, as shown in Figure 5-2, intermix and irregular layers of intermetallics and recrystallized α-Fe formed at the interface region hence it is reasonable to suggest that formation of this interface structure (with irregular layers of intermetallics) is necessary to provide sufficient metallurgical bonding required for a

joint with reasonable σ_{Lap}. However as it will be shown later, this interface structure does not represent a joint condition for optimal σ_{Lap} to be obtained

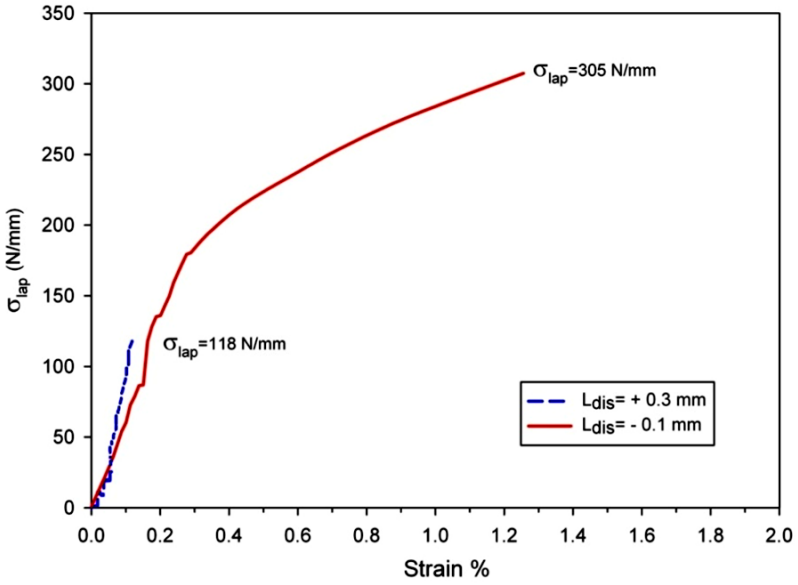

Figure 5-5 Tensile shear test curves for two sample, one taken from weld made using L_{dis}= +0.3 mm and the other using L_{dis}= - 0.1 mm

As Fe-Al intermetallic compounds are generally known to be brittle, they are commonly believed to adversely affect the joint strength; thus there has been attempts in literature [28, 68] to relate the joint strength to intermetallic layer thickness. Kimapong et al [28, 68] reported that in general increasing intermetallic layer thickness reduces σ_{Lap}, for the welds made using pin-penetrating condition. However as described in the previous section, under the condition of pin penetration, the interface region is not simply identified as a continuous intermetallic layer. Rather, there is an interface region consisting of intermix and irregular layers of intermetallics and recrystallised α-Fe. Furthermore, the thickness of intermetallic layers within the interface region is not constant. Therefore the relationship between intermetallic layer thickness and joint strength is not relevant in FSLW of Al/Steel, when the pin penetrates the steel.

Let us consider two welds made using different ω of 710 and 1400 rpm, under the same pin-penetrating condition (L_{dis} = -0.1 mm). The microstructure of interface region for these welds, as shown in Figure 5-6, clearly illustrates the formation of continuous intermetallic layer along the Al/Fe interface. The average thickness of these interfacial intermetallic layers is ~ 2.7 µm and ~ 1.4 µm for the welds made using ω of 1400 rpm and 710 rpm, respectively. The measured temperature of interfacial region, during

FSLW, for these welds is also shown in Figure 5-7. It is clear that weld made using higher ω (1400 rpm) spent significantly more time at higher temperatures compared to the weld made using lower ω (710 rpm). Higher temperature and thus higher diffusion rate caused faster growth of intermetallics along the Al/Fe interface, for the weld made using higher ω (1400 rpm), resulting in a larger in size intermetallic layer.

Although there is considerable difference in thickness of interfacial intermetallic layer for the two welds shown in Figure 5-6, both welds achieved similar values of σ_{Lap} (~ 307 N/mm) as shown in Figure 5-4. These results suggests that once a continuous interfacial intermetallic layer formed at the AL/Fe interface, providing a continuous metallurgical bonding, fracture strength is not affected by the thickness of interfacial intermetallic layer (for the interface region in the pin-penetrating condition).

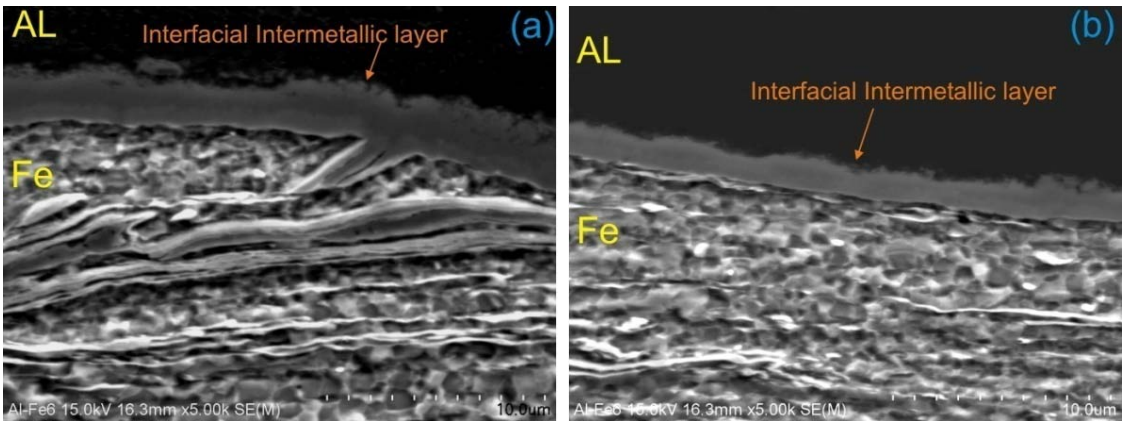

Figure 5-6 Interfacial microstructures for the welds made using L_{dis}= -0.1 mm and ν =80 mm/min (a) ω =1400 rpm and (b) ω =710 rpm

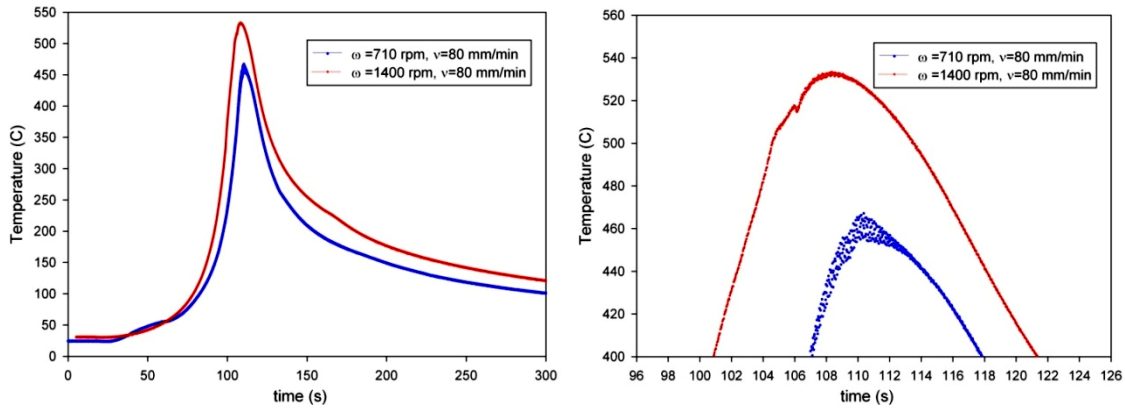

Figure 5-7 (a) measured temperatures at the interface region, during FSLW, for the welds made using L_{dis}= -0.1 mm and ω and ν as indicated and (b) enlarged view of temperature readings for temperatures > 400 ^{o}C

5.1.3 Further Experimentation to Study Joint Interface and Fracture Strength

There is a crucial point missing from the results presented in the last section. The interface was either one with discontinuous intermetallic outbursts then discontinuous metallurgical bond (in non pin penetrating conditions), or one that was an irregular layers and mixture of microstructure (in pin penetrating conditions). The question of what should be the strength value if the interface is a single continuous intermetallic layer could not be answered. Thus a specific force monitored FSLW experiment, as described in section 2.2.4, was performed so that a sample with $L_{dis} \approx 0$ could be obtained where the pin bottom just reaching the steel plate without penetration. It should be noted that during FSLW experiment the tool was lowered slightly in later stage, thus $L_{dis} \approx 0$ (Region 1) and $L_{dis} < 0$ (Region 2) were obtained in one experiment as indicated in Figure 5-8.

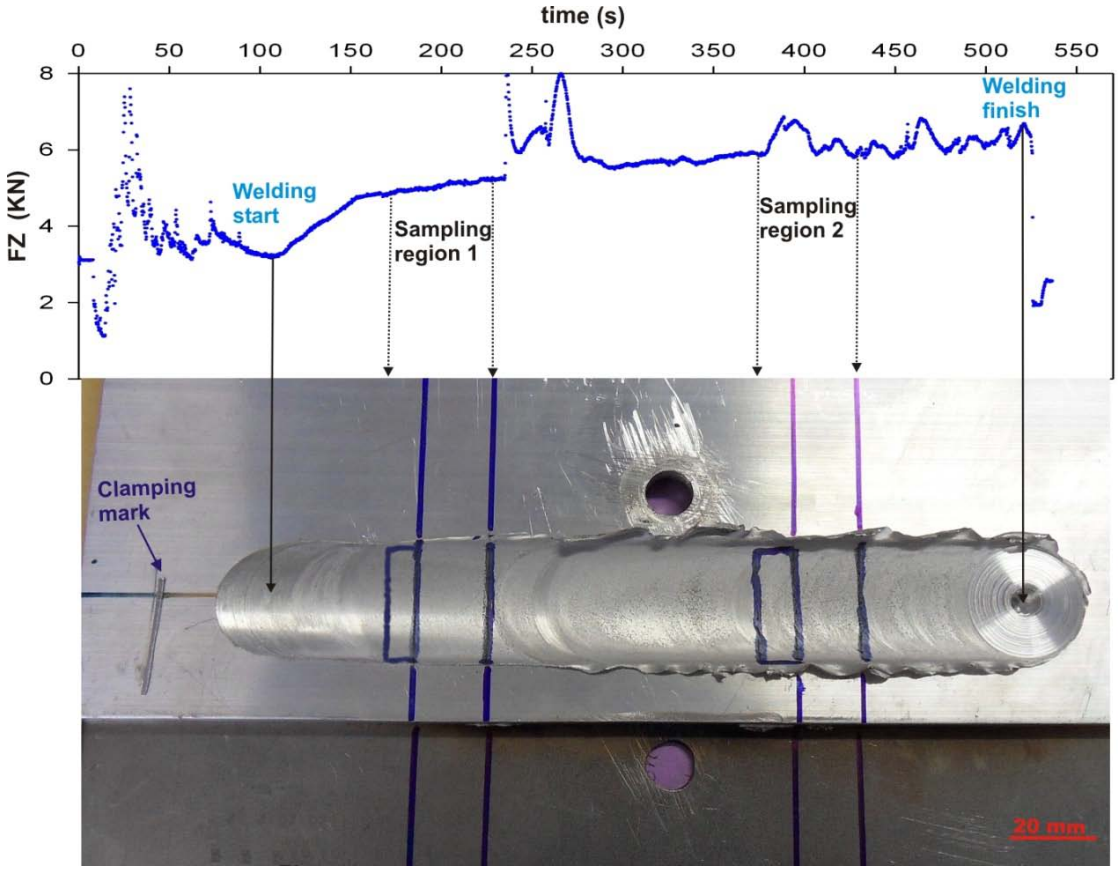

Figure 5-8 An Al/Steel FSL Weld made using ω =1400 rpm and ν =20 mm/min with F_z – time curve superimposed. Location of sampling region 1 and 2 is indicated.

σ_{Lap}–strain curves for the Regions 1 and 2 tested samples are presented in Figure 5-9. For the Region 2 sample, σ_{Lap} =299 N/mm is almost the same as those σ_{Lap} values of

the welds made using 0.1 mm penetration (L_{dis} = -0.1 mm) in this study and is also almost the same as the maximum σ_{Lap} value (304 N/mm) of defect-free joints with sufficient pin penetration from Movahedi et al [69]. This agreement suggests that the attainable value for the joint strength may not be significantly higher than 300 N/mm for the case of pin penetrating.

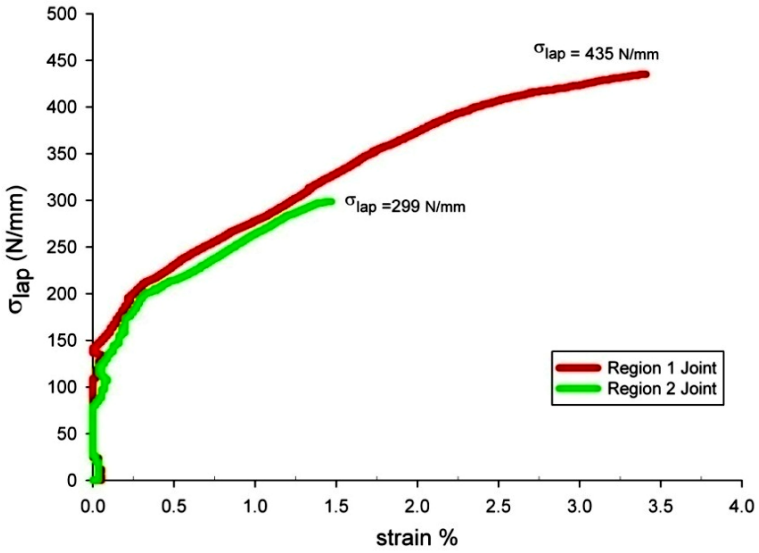

Figure 5-9 σ_{Lap} – strain curves for Region 1 and 2 tested samples (as indicated in Figure 5-8)

For Region 1, σ_{Lap} value is high of 435 N/mm. The fracture energy, which corresponds to the area under the curve, for the Region 1 sample is 3.1 times larger than that of Region 2 sample. A joint σ_{Lap} value of 435 N/mm is a high value. If a lap joint with σ_{Lap} value (435 N/mm) was made using a top sheet 2.8 mm thick, the resulting σ_{Lap} value of stir zone needs to be higher than 150 MPa to force the fracture in joint interface. A strength value of 150 MPa is close to the best attainable *UTS* values of Al 6060-T5 friction stir welds (section 3.1).

Microstructures corresponding to Region 2 sample are shown in Figures 5-10. The optical micrograph in Figure 5-10a clearly shows a pin penetration to steel with a sufficient depth. This condition resulted in an interface region consisting of intermix and irregular layers of intermetallics and recrystallised α-Fe, as indicated in Figures 5-10 b-e. This interface region is the same as those described in the previous section, thus σ_{Lap} is almost the same (~ 300 N/mm).

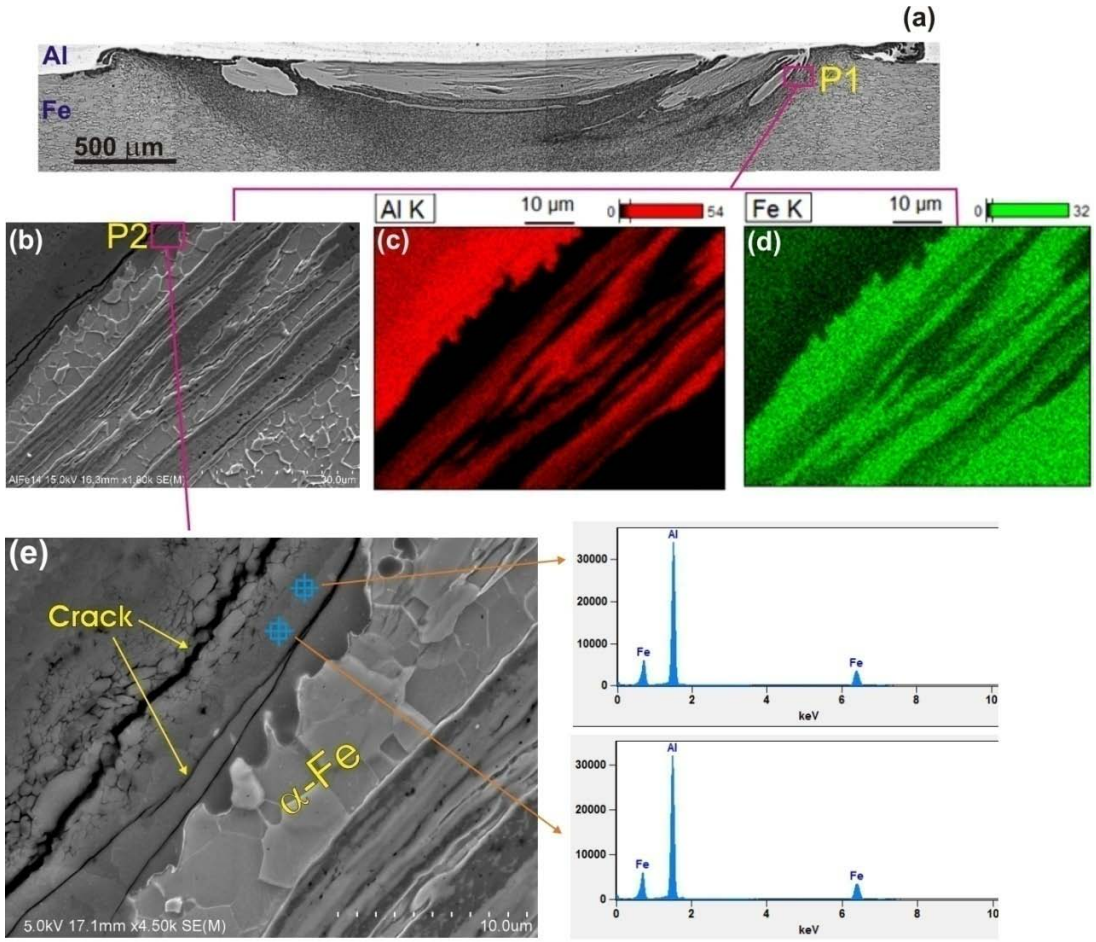

Figure 5-10 Microstructure of Region 2 sample as indicated in Figure 5-8, (a) optical macrograph, (b) SEM micrograph of area P1 in Figure 5-10a with associated, (c) EDS map of Al, (d) EDS map of Fe, (e) SEM micrograph of area P2 in Figure 5-10b, typical EDS spectra of intermetallic layer are also shown

Furthermore Figure 5-10e shows that microcracks formed along the intermetallic layer which is likely due to the strain caused by considerable difference in thermal expansion coefficients of steel and of aluminium during FSLW. The EDS spot analysis of intermetallic layer (Figure 5-10e) showed the average composition of 70.1at%Al and 29.9at%Fe, suggesting that intermetallic phase is Fe_2Al_5. For further verification of Intermetallics phase, EBSD point analysis conducted to identify the intermetallic type according to their crystallographic structure. Reliable phase identification of Al-Fe intermetallics using EBSD analysis has recently been reported by Wei-Jen et al [123, 124] where the authors have conducted extensive EBSD analysis on Fe-Al diffusion couples.

The typical diffraction patterns (kikuchi patterns) collected from several locations of the thick intermetallic layer, located in intermix region of the weld shown in Figure 5-10e,

are presented in Figure 5-11. These diffraction patterns analysed by the EBSD crystal software and were indexed to be Fe_2Al_5. Representative diffraction patterns corresponding to different Al-Fe intermetallic phases [123, 124] are also shown in Figure 5-12 for comparison. It should be noted that if the diffraction patterns shown in Figure 5-11c are rotated to certain angle, they would match well with the representative diffraction pattern of Fe_2Al_5 in Figure 5-12. As the crystal structure of each intermetallic phase is unique therefore the results of EBSD point analysis (Figure 5-11) confirms that Fe_2Al_5 intermetallic layer formed in the laminate region (penetrated region).

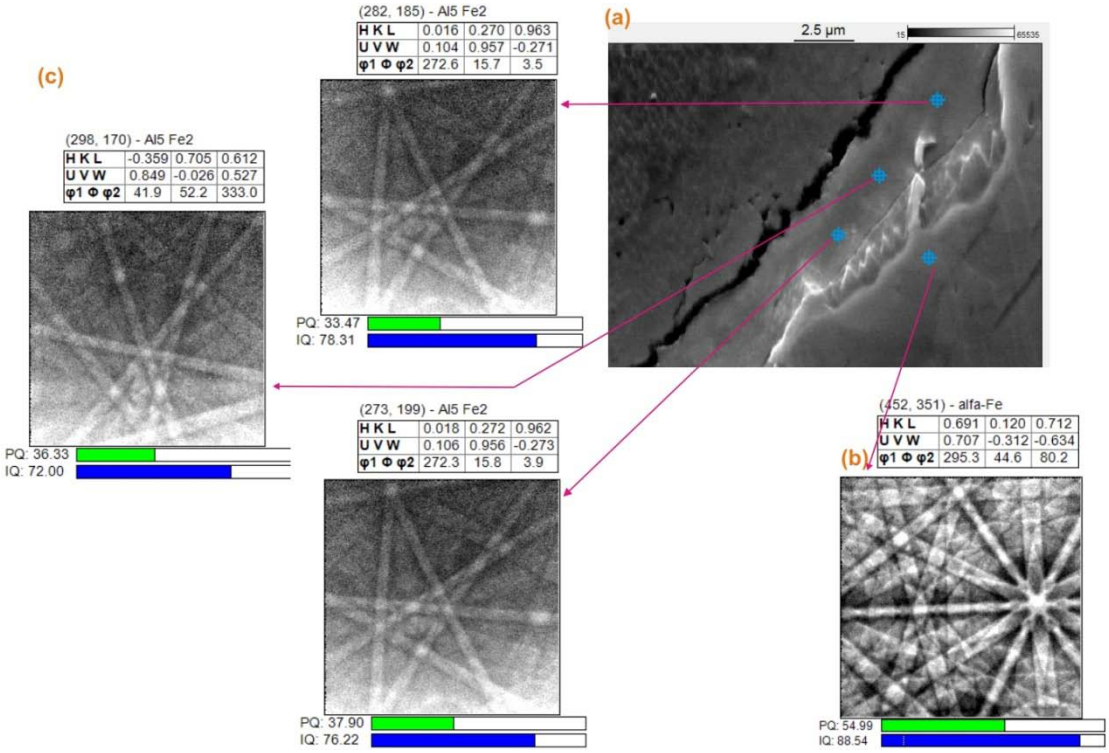

Figure 5-11 EBSD phase analysis: (a) the intermix area of Region 2 sample as indicated in Figure 5-10e, (b) indexed diffraction pattern corresponding to recrystallized α-Fe phase and (c) indexed diffraction patterns corresponding to Fe_2Al_5 intermetallic phase

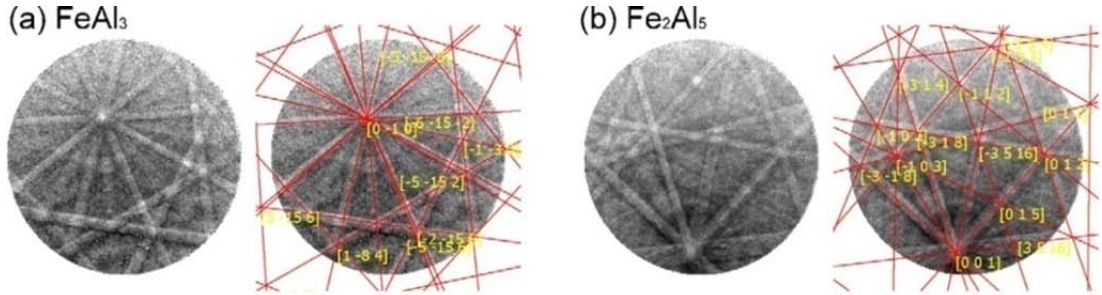

Figure 5-12 Representative indexed diffraction patterns of (a) $FeAl_3$, (b) Fe_2Al_5, (c) $FeAl_2$ and (d) FeAl or α-Fe [123]

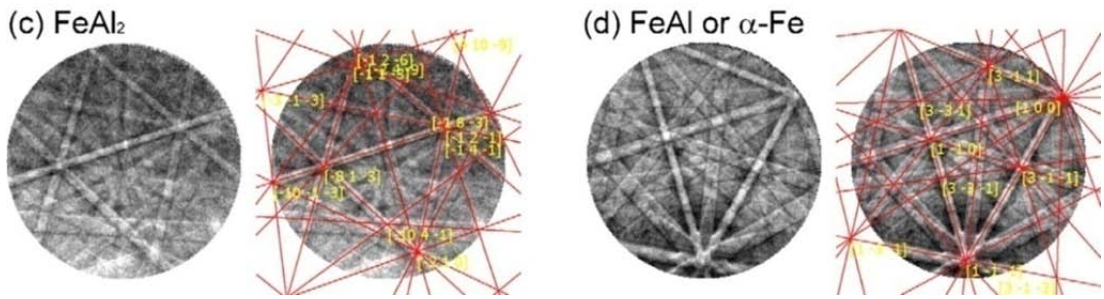

Figure 5-12 continued.

Microstructure corresponding to Region 1 sample is shown in Figures 5-13. The optical micrograph in the figure suggests no pin penetration for Region 1 sample; however a single continuous intermetallic layer (with thickness of 2 to 2.5 μm) can be seen in the SEM micrograph of interfacial region. It is expected that the pin was sufficiently close to the steel surface so that the thin surface oxides were removed and metallurgical reaction occurred resulting in formation of intermetallic layer. It worth noting that the microstructure of interface region for Region 1 sample (with a single continuous intermetallic layer) is quite different from that of Region 2 sample (with intermix and irregular layers of intermetallics).

The EDS spot analysis of intermetallic layer (Figure 5-13b) showed chemical composition of 69.5at%Al and 30.5at%Fe, suggesting that intermetallic phase is Fe_2Al_5. Intermetallic layer structure was further investigated using EBSD point analysis. The typical diffraction patterns collected from several locations of the intermetallic layer are presented in Figure 5-14. Although diffraction patterns corresponding to intermetallic layer obtained reasonable pattern quality (PQ), as shown in Figure 5-14d, however they could not be indexed by the EBSD crystal software. On the other hand, diffraction patterns corresponding to α-Fe (Figure 5-14b) and aluminium alloy (Figure 5-14c) were indexed with relatively high index quality (IQ). Careful comparison of diffraction patterns corresponding to intermetallic layer (Figure 5-14d) with those of aluminium alloy (Figure 5-14c), in terms of width of kikuchi bands and also the angle between the kikuchi bands, clearly shows that the pattern obtained from intermetallic layer are different from those corresponding to aluminium alloy. Therefore the intermetallic layer has different structure from the adjacent α-Fe (at bottom) and aluminium (on top), even though its structure was not indexed by the EBSD crystal software.

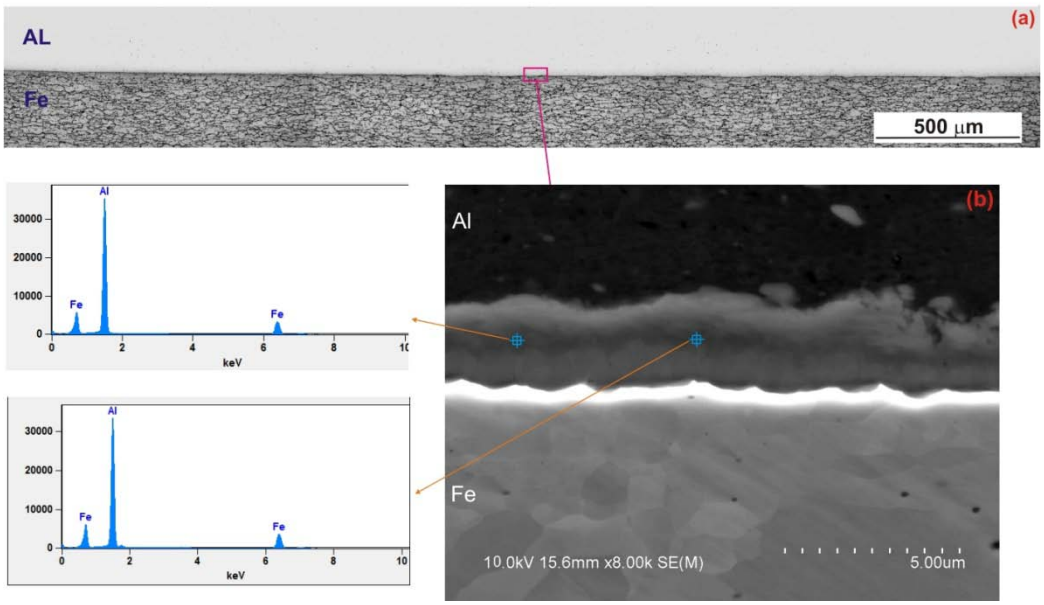

Figure 5-13 Microstructure of Region 1 sample as indicated in Figure 5-8, (a) optical macrograph and (b) SEM micrograph of Al/Steel interface showing formation of a single continuous intermetallic layer. Typical EDS spectra of intermetallic layer are also shown.

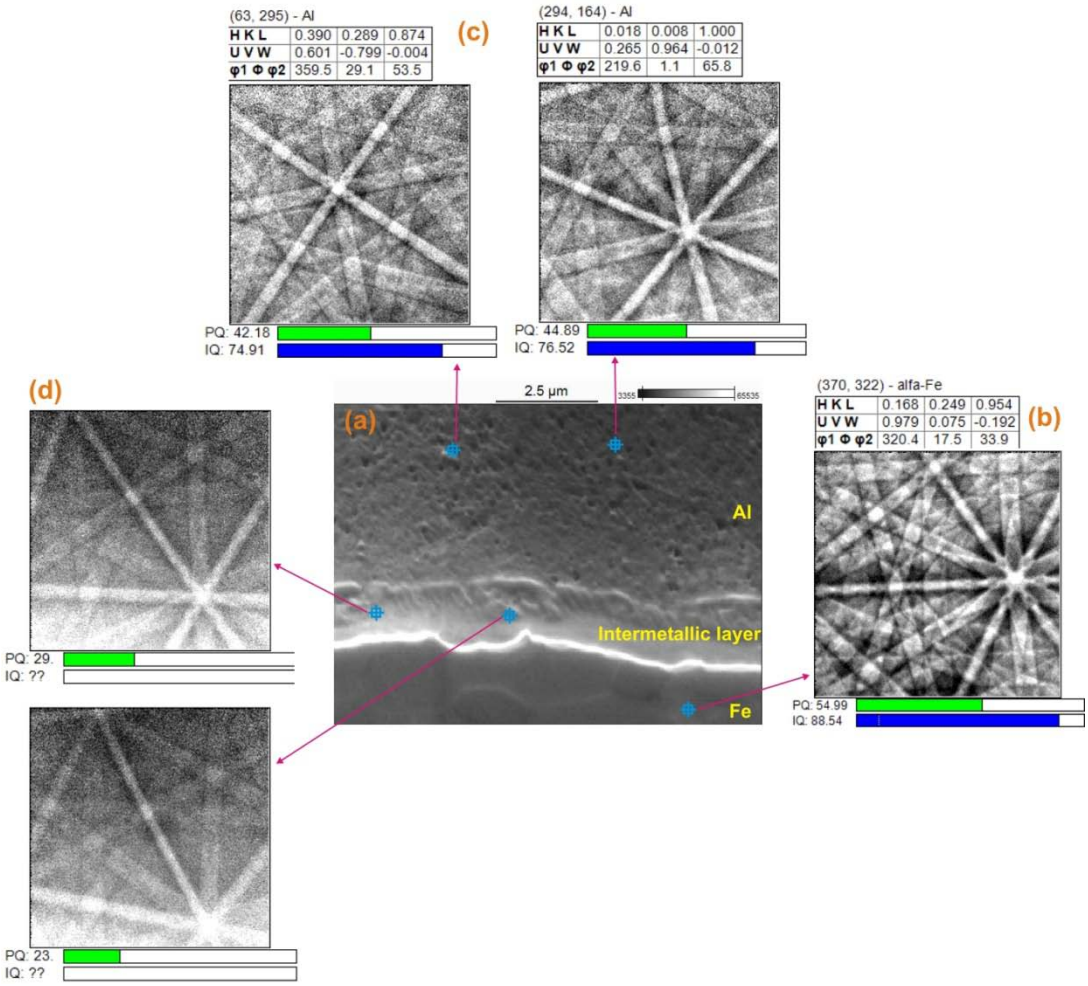

Figure 5-14 EBSD phase analysis: (a) SEM micrograph of interface for Region 1 sample, (b) indexed diffraction pattern corresponding to recrystallized α-Fe phase and (c) diffraction pattern corresponding to intermetallic layer

5.1.4 Effect of Interface Microstructure on Fracture Behaviour

Before a further discussion on the effect of interface microstructure on fracture behaviour, it is helpful to review three types of interface structures observed in this study, as shown in Figure 5-15. When the bottom of pin did not penetrate to steel ($L_{dis} > 0$), small outbursts of intermetallics formed at the interface region. This is called Type 1 interface and an example is given in Figure 5-15a. When the bottom of pin reached (without penetrating) the steel surface ($L_{dis} \approx 0$), a single continuous intermetallic layer formed at the interface region (Figure 5-15b), representing Type 2 interface. However slight pin penetrations into steel ($L_{dis} < 0$) resulted in formation of intermix and irregular layers of intermetallics at the interface region (Figure 5-15c), representing Type 3 interface.

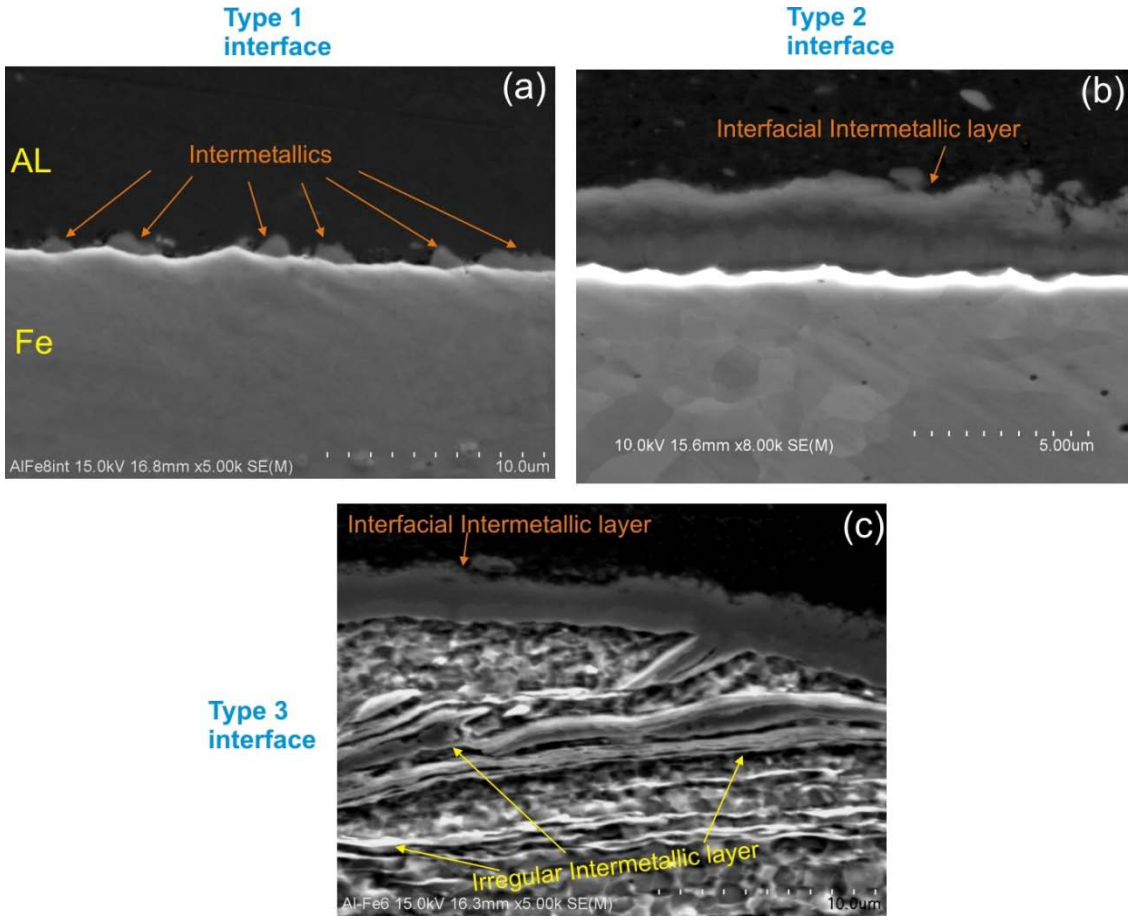

Figure 5-15 Types of interface structures for different pin positioning (a) Type 1: when $L_{dis} > 0$, small outburst of intermetallic formed, (b) Type 2: when $L_{dis} \approx 0$, a single continuous intermetallic layer formed and (c) Type 3: when $L_{dis} < 0$, intermix and irregular layers of intermetallics formed

As described in section 5.1.2, the welds with Type 1 interface, fractured with low values of σ_{Lap} (~70-120 N/mm) during tensile shear testing, due to non-continuous metallurgical bonding at the interface. Moreover low fracture energy of tested samples, as seen in Figure 5-5, indicates that tensile shear sample fractured without plastic deformation.

As described in previous section, interface microstructure of Region 1 sample (Figure 5-13) consisted of a single continuous intermetallic layer along the Al/Steel interface, representing Type 2 interface. During tensile shear testing, Region 1 sample fractured along the Al/Steel interface (Figure 5-16a). However considerable amount of specimen rotation occurred before failure indicating that interface layer can support a high load (σ_{Lap} = 430 N/mm), despite of stress concentration. Fracture surface of steel side of tested sample, as shown in Figure 5-16c, indicates that a ductile fracture is dominant with plastic (shear) deformation preceding failure mostly in aluminium adjacent to and on top of the interfacial intermetallic layer. The presence of smeared aluminium on top of fracture surface can be better seen in EDS maps of fracture surface (Figures 5-16 d-f). The parallel cracks seen in Figures 5-16 c-d are largely as thin as thickness of intermetallic layer and normal to the shear direction, thus contributing little to the shear deformation and fracturing. This ductile deformation is consistent with the σ_{Lap} –strain curve shown in Figure 5-9, displaying high σ_{Lap} value and fracture energy. Therefore these results suggest that Type 2 interface (with a single continuous intermetallic layer) is highly shear fracture resistant.

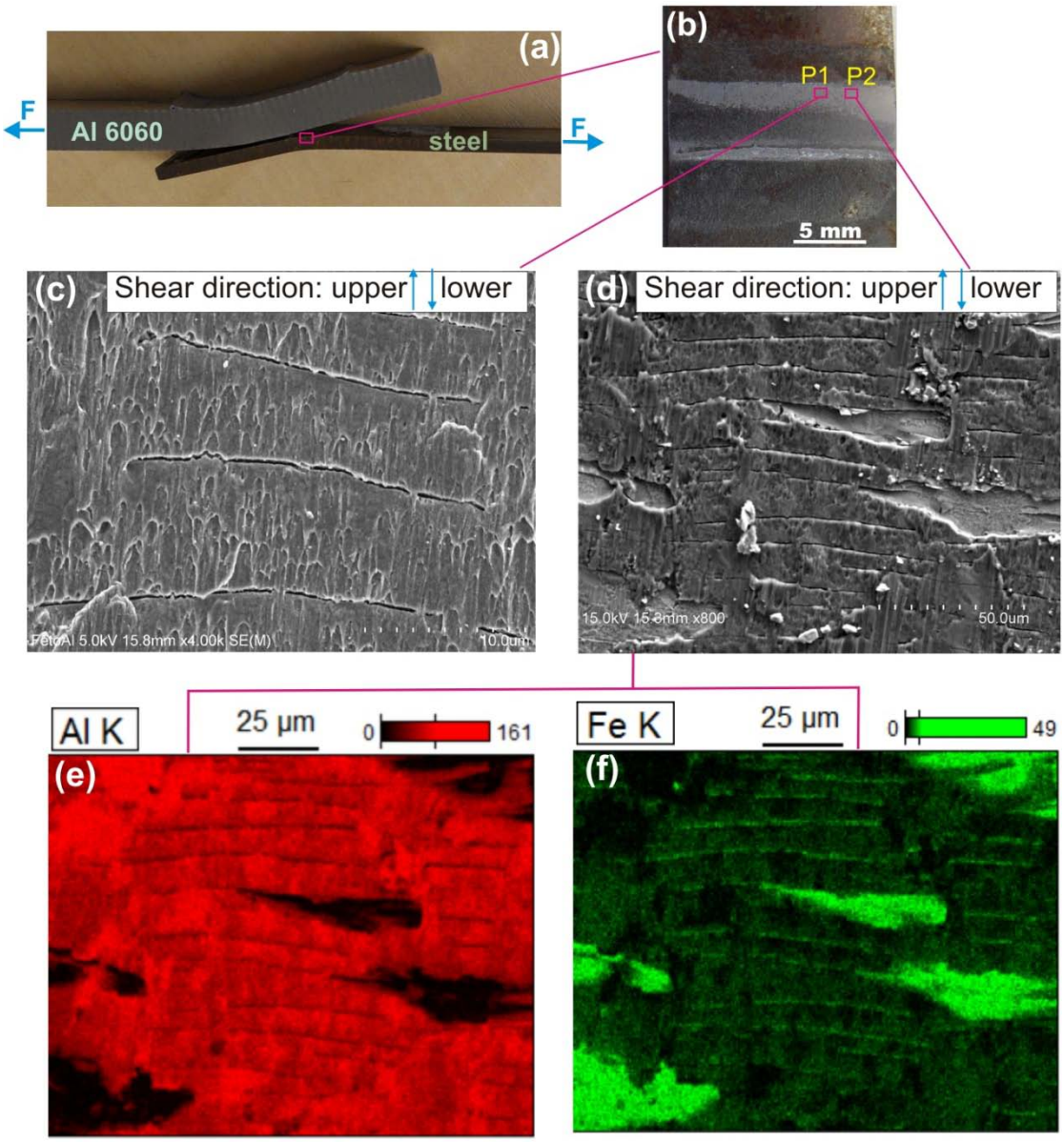

Figure 5-16 Fracture surface of Region 1 tested sample (a) fractured sample, (b) image of steel side of tested sample, (c) SEM micrograph of area P1 in Figure 5-16b showing the heavily deformed aluminium on top of the intermetallic layer, (d) SEM micrograph of area P2 in Figure 5-16b and associated, (e) EDS map of Al and (d) EDS map of Fe

As described in previous section, microstructure of Region 2 sample (Figure 5-10) was an irregular laminate of α-Fe and Fe-Al intermetallic layers, representing Type 3 interface. Figure 5-17 shows the Region 2 sample, tensile shear tested to fracture. It can be seen that a significant portion of the fracture surface displays brittle failure (Figure 5-17 c-d). The flake-like features formed on the fracture surface suggest that cracking propagated along (parallel to) the thin intermetallic layers in the laminate (penetrated) region during testing. This brittle nature is consistent with the σ_{Lap}–strain curve of Region 2 sample (Figure 5-9) displaying lower σ_{Lap} value (~ 300 N/mm) and fracture

energy. Therefore smaller amount of specimen rotation occurred before failure (Figure 5-17a), compared to Region 1 tested sample (Figure 5-16a).

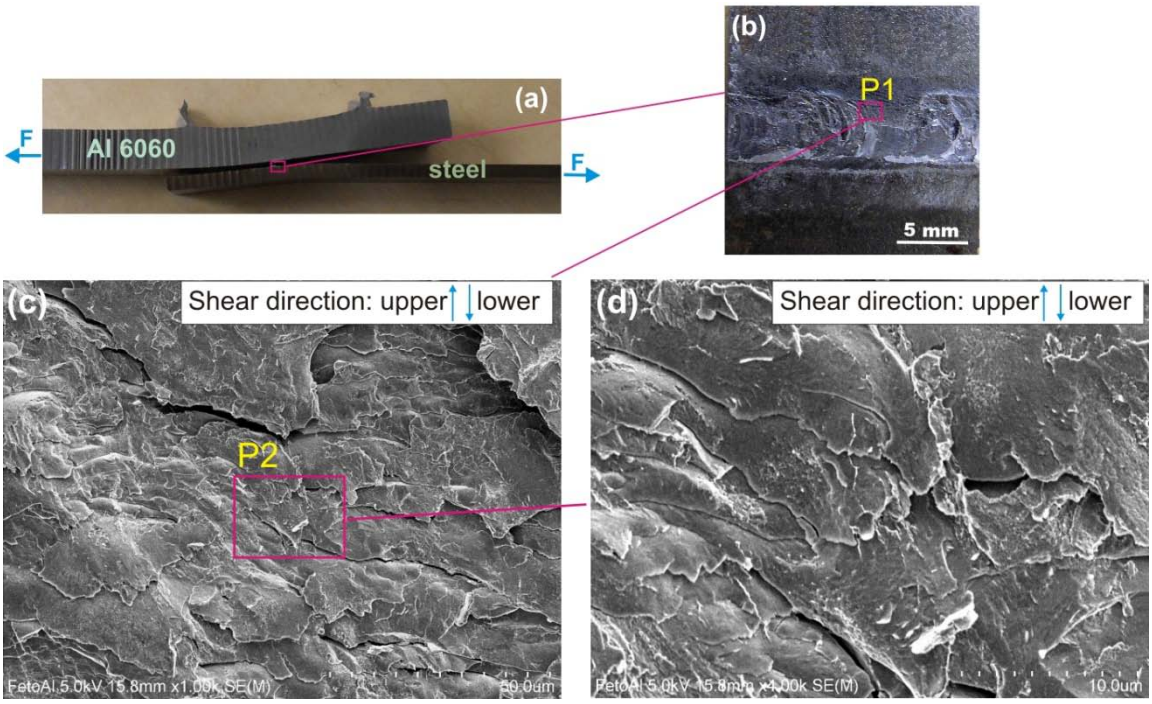

Figure 5-17 Fracture surface of Region 2 tested sample (a) fractured sample, (b) image of steel side of tested sample, (c) SEM micrograph of area P1, displaying brittle fracture patterns and (d) higher magnification micrograph of area P2

The brittle fracture associated with Type 3 interface (in pin-penetrating condition) was further investigated through interrupted tensile shear testing of another sample taken next to the Region 2 sample, as indicated in Figure 5-18. It can be seen that in the location of interrupted testing sample, F_z – time curve shows highly unstable condition indicating that the pin penetrated to steel. The new sample was loaded till 270 N/mm, equal to 90% value of σ_{Lap} (300 N/mm) for the Region 2 sample.

Microstructures of the interface region (after testing) are presented in Figure 5-19. It can be seen that although a continued interfacial intermetallic layer formed in the outer boundary of the irregular α-Fe/intermetallic laminate region (Figure 5-19b) but the crack propagated along the intermetallic layers embedded inside the laminate region. In other words, the intermetallic layers inside the laminate region are more favourable for crack propagation during testing. Also close examination of Figure 5-19d shows that the cracking occurred along the boundary of an intermetallic layer and α-Fe. These results confirm that brittle fracture observed in Type 3 interface (Figure 5-17) is due to

cracking along (parallel to) the intermetallic layers in laminate (penetrated) region, not along the most outer intermetallic layer (interfacial intermetallic layer).

The more favourable cracking along the intermetallic layers embedded inside the penetrated region (Figure 5-19b), rather than cracking along the interfacial intermetallic layer (in the outer boundary of the irregular laminate region), indicates that irregular intermetallics layers formed inside the laminate region are weaker than the interfacial intermetallic layer; as the cracks tends to propagates through the weakest point of joint. This could be related to the different types of intermetallics compounds formed at various locations of interface region. As explained in previous sections, intermetallic compounds formed in interface region can be of different forms of Fe_2Al_5 or $FeAl_2$ or $FeAl_3$ intermetallic compounds. Therefore the local metallurgical bond produced by each type of intermetallics can be different from the others, with one being stronger under loading. Furthermore it was demonstrated that for the Region 2 sample (representing Type 3 interface) some microcracks formed along the intermetallic layers in the laminate region (Figure 5-10). These pre-cracks can act as favourable cracking initiation source and facilitate the fracturing with lower σ_{Lap}.

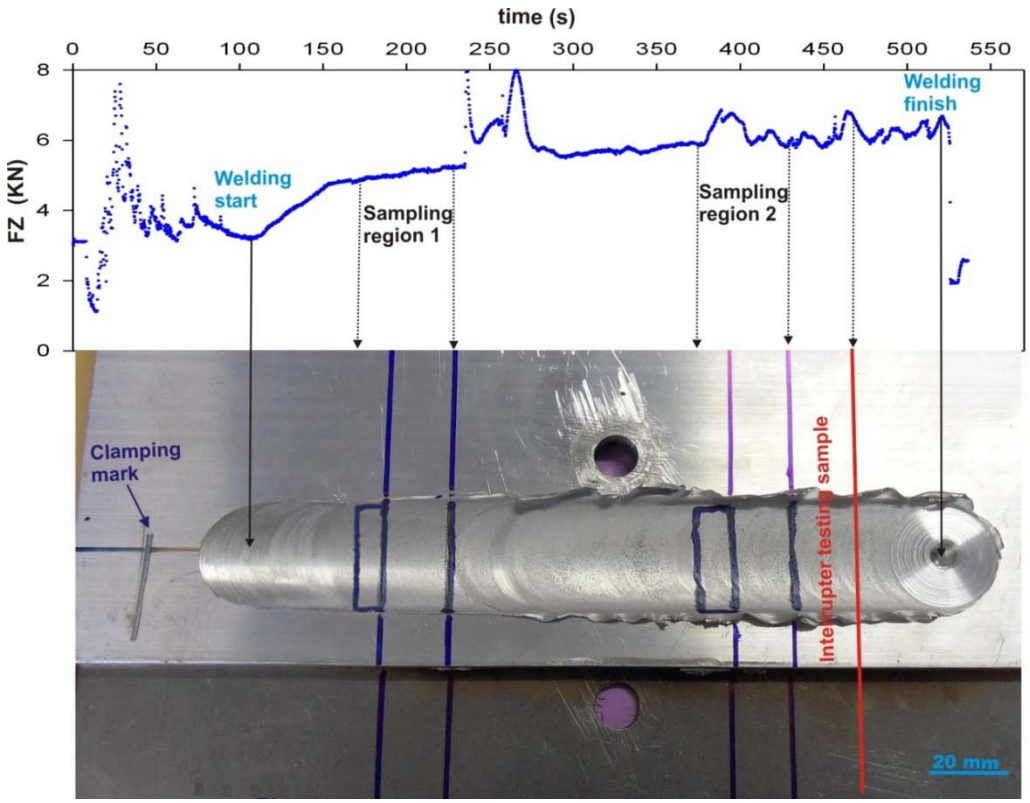

Figure 5-18 An Al/Steel FSL Weld made using ω =1400 rpm and ν =20 mm/min with F_z – time curve superimposed. Location of interrupted testing sample is indicated.

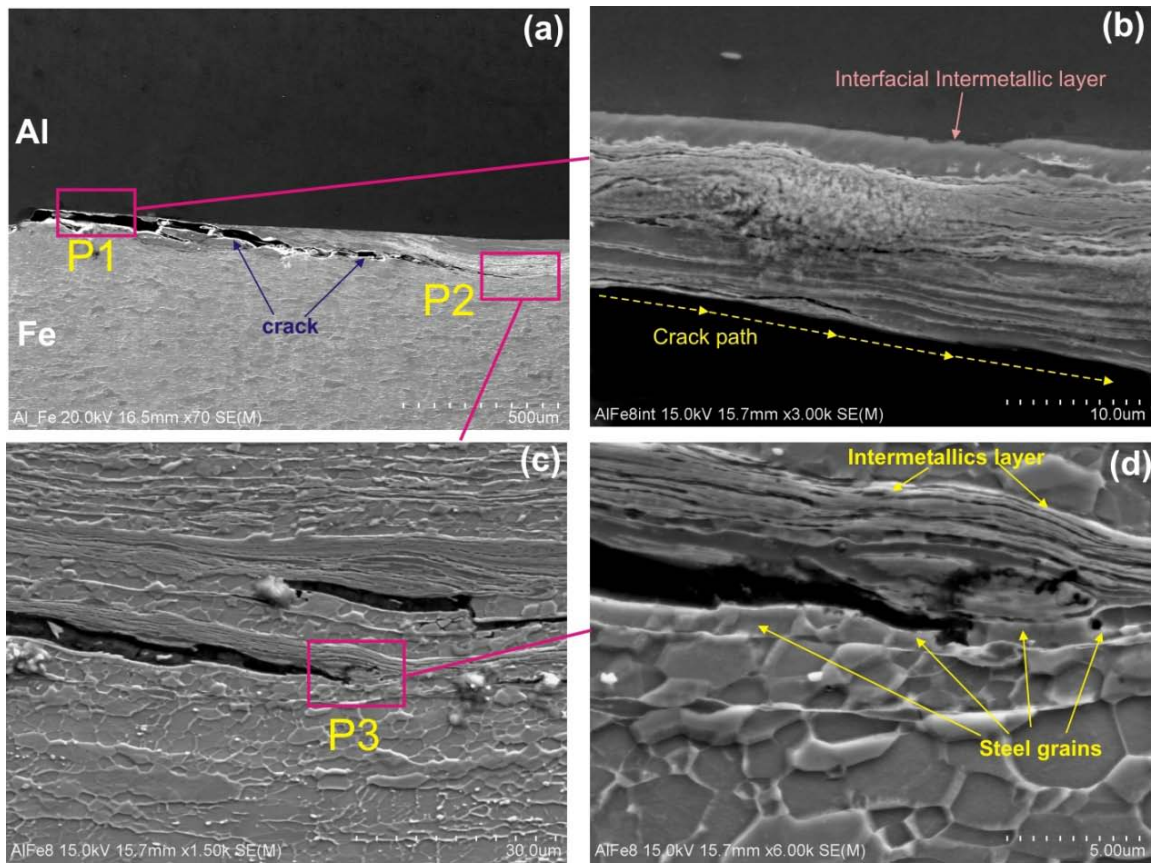

Figure 5-19 Microstructure of interrupted testing sample loaded till 270 N/mm: (a) macrograph, (b) SEM micrograph of area P1 in Figure 5-19a showing the crack propagated along the intermetallics layers embedded inside the laminate region, (c) SEM micrograph of area P2 in Figure 5-19a and (d) SEM micrograph of area P3 in Figure 5-19c

The photo of the tool pin, after being used in aforementioned FSLW experiment (shown in Figure 5-18) is presented in Figure 5-20. It is clear that pin tip has not deformed. This is due to the slight penetration of pin to mild steel plate, during FSLW.

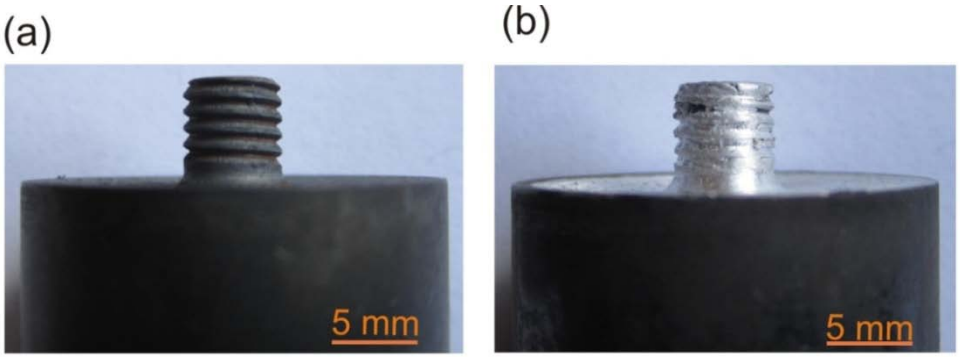

Figure 5-20 Photos of tool pin (a) before FSLW and (b) after FSLW

σ_{Lap} as function of L_{dis}, including the Region 1 sample, has re-plotted and shown in Figure 5-21. It is clear that for non pin penetrating ($L_{dis} > 0$) σ_{Lap} increased with decrease of L_{dis} and reached the optimal σ_{Lap} (435 N/mm) at $L_{dis} \approx 0$ mm (with Type 2 interface). However pin penetrating ($L_{dis} < 0$), with Type 3 interface, resulted in decrease of σ_{Lap} from the optimal joint strength obtained at $L_{dis} \approx 0$. Also the pin penetrating condition resulting in $\sigma_{Lap} \approx 300$ N/mm, although L_{dis} may differ for different samples, has suggested that the fracturing process along (parallel to) the irregular intermetallic layers in laminate region is common. In other words, σ_{Lap} is not very sensitive to the size of the interface region (with intermix and irregular intermetallic layers), once it forms.

The above results clearly demonstrated that σ_{Lap} of Al/Steel FSL welds is very sensitive to the pin positioning during FSLW. Therefore it is suggested that a force control mechanism of pin positioning can be effective for obtaining the high strength Al/Steel welds. By carefully controlling the pin positioning during FSLW make sure that the bottom of pin reaches the steel surface (without penetrating) to obtain optimal joint strength at condition of $L_{dis} \approx 0$ mm.

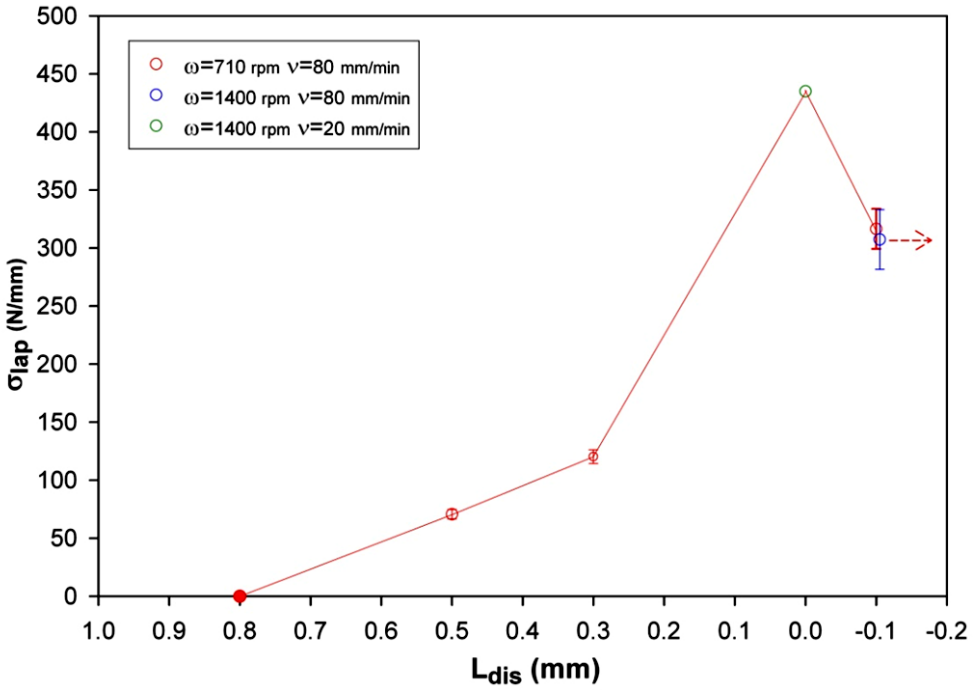

Figure 5-21 Values of σ_{Lap} for the welds made using different L_{dis} (ω and ν as indicated)

In summary, it was demonstrated that the suggestion made in literature on necessity of slight pin penetration to steel for promoting joint strength is valid as far as making sure a condition for a continuous metallurgical bond to be accomplished. However this condition does not represent a joint condition for optimal σ_{Lap} to be obtained. It was shown that by controlling the pin positioning during FSLW a thin continuous intermetallic layer can form and thus metallurgical bonding is established, without the pin penetrating to steel. The joint produced by this non pin penetrating condition displayed a high σ_{Lap} value (435 N/mm) which was ~ 42% increase in σ_{Lap} in comparison to the commonly observed maximum σ_{Lap} value (304 N/mm) for case of pin penetrating

5.2 Al 6060-T5 to Ti6Al4V FSL Welds

As just described in the previous section, the pin positioning and subsequent formation of intermetallic layers in the interface region can significantly affect the σ_{Lap} of Al/Steel FSL welds. As the Al/Ti FSL welds are also joined through formation of interfacial intermetallics ($TiAl_3$) [9, 10], therefore FSLW experiments is conducted so that effect of pin positioning on σ_{Lap} is examined to see if the condition of $L_{dis} \approx 0$ mm is the joint condition for optimal σ_{Lap} in Al/Ti FSLW, similar to Al/Steel FSLW.

The average values of σ_{Lap} for the two welds made using same ω=1400 rpm, but different ν of 20 and 80 mm/min is shown in Figure 5-22. During FSLW of both welds, as will be explained in next section, L_{dis} varied so that $L_{dis} \approx 0$ and $L_{dis} < 0$ could be obtained in one experiment. In general the average value of σ_{Lap} for both welds, 537 N/mm for the weld made using ν=20 mm/min and 466 N/mm for the weld made using ν=80 mm/min, are considerably higher than that of average value of σ_{Lap} (307 N/mm) in Al/Steel welds. Also as described in section 1.4.2, the maximum σ_{Lap} value reported for Al/Ti FSL welds in literature [10] is 469 N/mm which is in the comparable range with those obtained in this study.

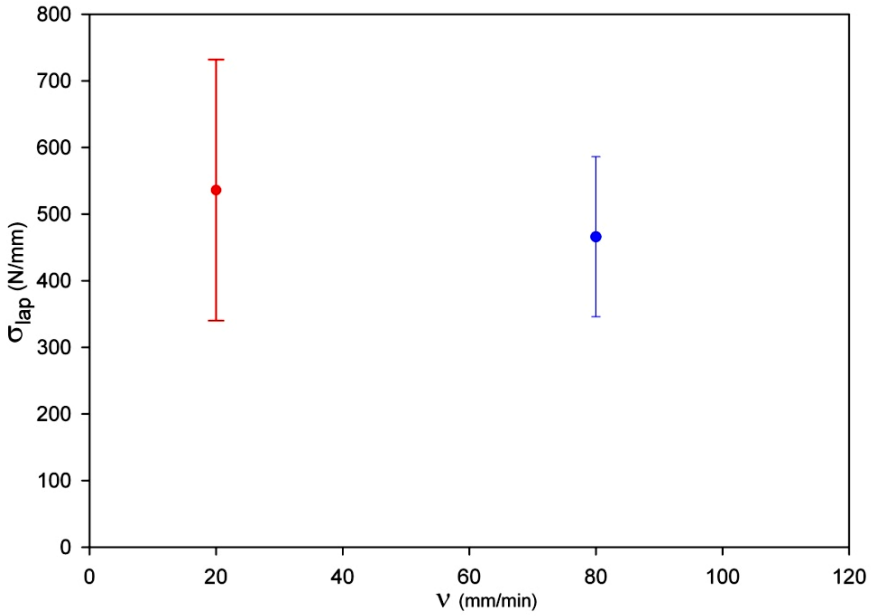

Figure 5-22 Average value of σ_{Lap} for two Al/Ti FSL welds made using ω =1400 rpm and ν as indicated. Two tensile shear specimens tested for each weld.

5.2.1 Relationships between Interfacial Microstructures and σ_{Lap}

Figure 5-23 shows the image of an Al/Ti FSL weld, made using ω=1400 rpm and ν=20 mm/min, with F_z–time curve superimposed. In this experiment, $L_{dis} \approx 0$ was aimed in order for the pin bottom just reaching the bottom plate without penetration. However during FSLW the tool was lowered slightly in later stage, thus $L_{dis} \approx 0$ (Region 1) and $L_{dis} < 0$ (Region 2) were obtained in one experiment as indicated in Figure 5-23.

The σ_{Lap}–strain curves for the Region 1 and 2 tested samples are shown in Figure 5-24. It can be seen that the Region 1 sample achieved a very high σ_{Lap} value (732 N/mm) compared to the σ_{Lap} value (340 N/mm) for Region 2 sample. A joint σ_{Lap} value of 732 N/mm is a very high value and is 1.5 times greater than the maximum σ_{Lap} value (469N/mm) reported in literature for Al/Ti FSL welds [10].

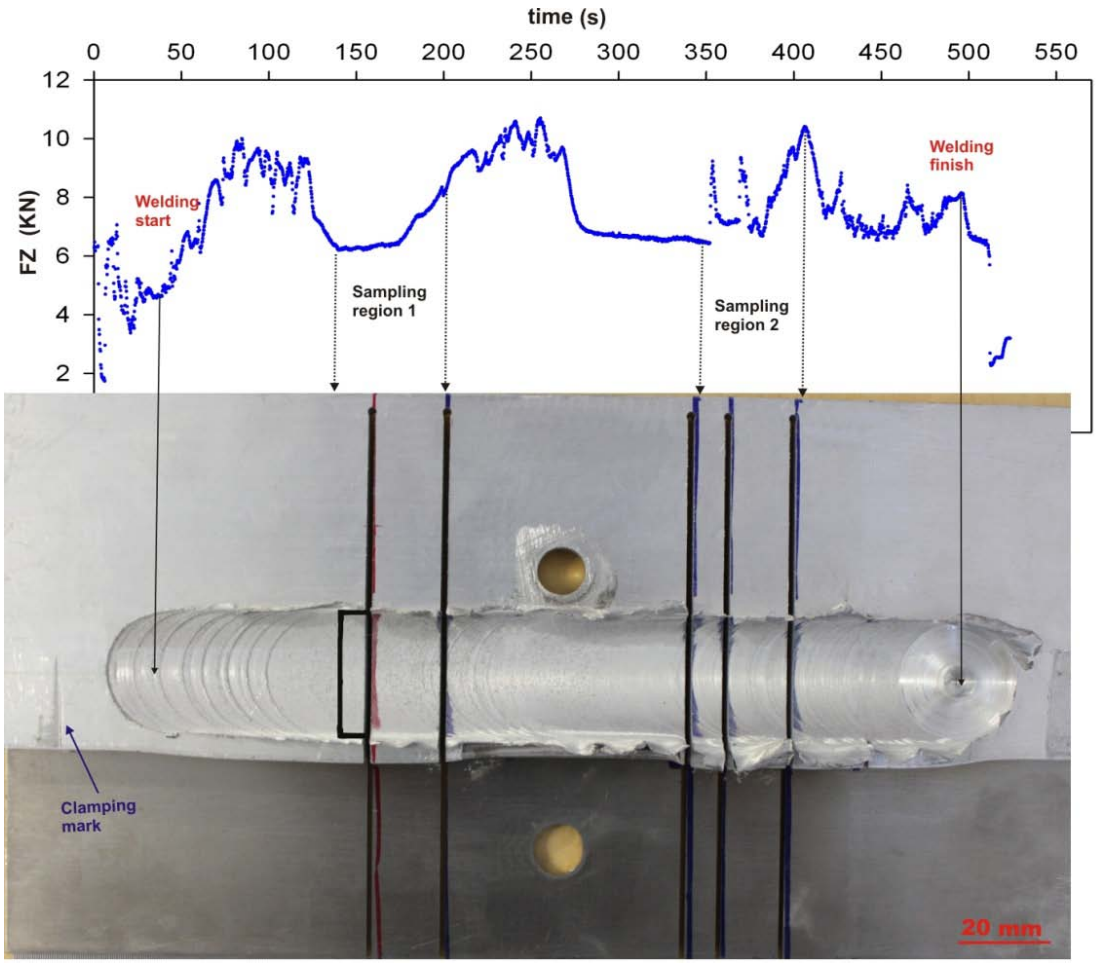

Figure 5-23 An Al/Ti FSL weld made using ω =1400 rpm and ν =20 mm/min with F_z – time curve superimposed. Sampling region 1 and 2 are also indicated.

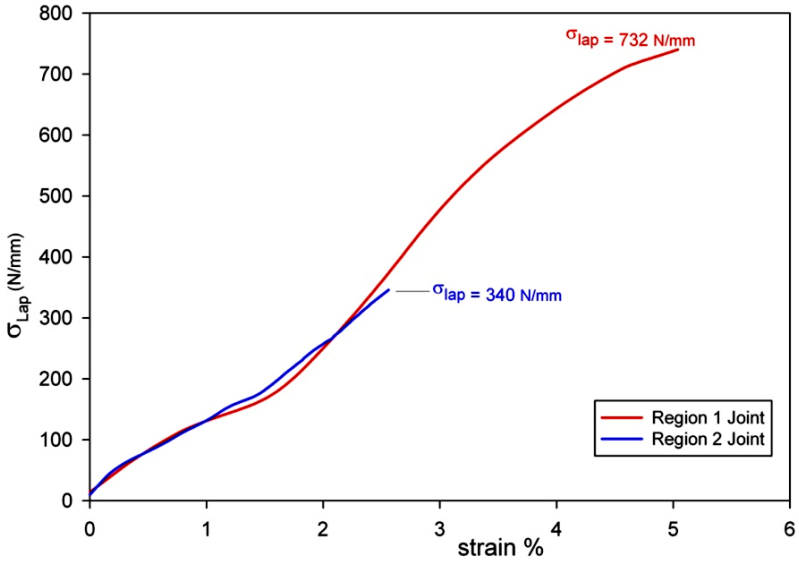

Figure 5-24 σ_{lap}–strain curves for the Region 1 and 2 tested samples (as indicated in Figure 5-23)

Microstructures corresponding to Region 1 sample are shown in Figures 5-25. The low magnification micrograph in Figure 5-25a suggests no pin penetration for Region 1 sample, however a very thin continuous intermetallic layer (with average thickness of approximately ~ 200 nm) can be seen in the SEM micrograph of interfacial region (Figure 5-25b). It should be noted that characterisation of intermetallic layer was not possible in this study due the very thin thickness of interfacial intermetallic layer (Figure 5-25b). However formation of $TiAl_3$ intermetallic compound in Al/Ti FSL welds has been reported in literature [10]. High σ_{Lap} value (732 N/mm) obtained for Region 1 tested sample indicates that this very thin intermetallic layer created a strong continuous metallurgical bond at Al/Ti interface.

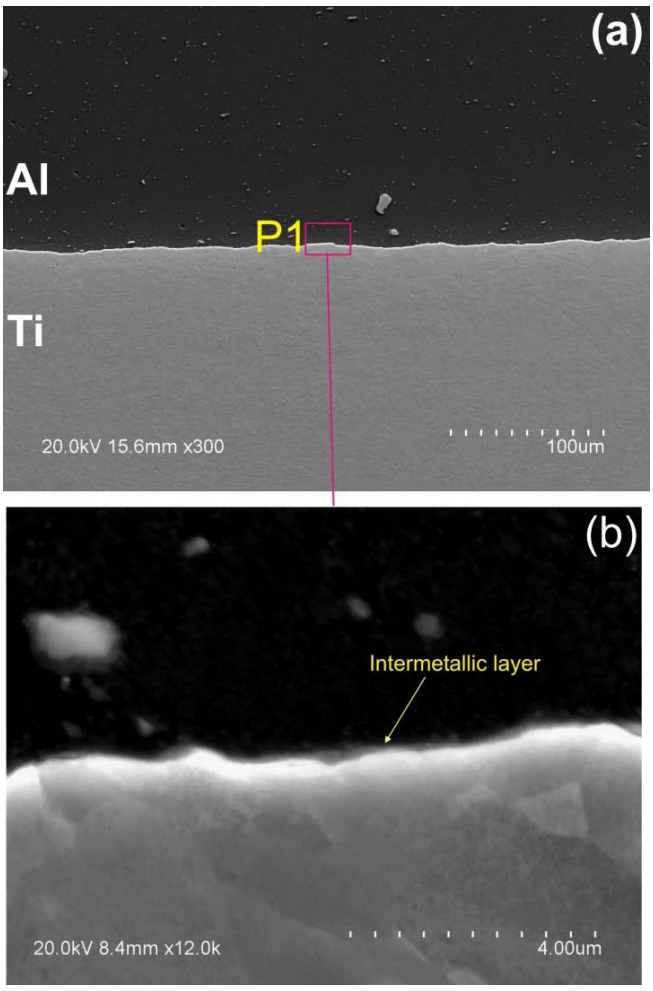

Figure 5-25 Microstructure of Region 1 sample as indicated in Figure 5-23 (a) low magnification SEM micrograph and (b) high magnification SEM micrograph of area P1 showing a very thin interfacial intermetallic layer

For Region 2 sample, significant pin penetration took place as seen in Figure 5-26. Thus an irregular laminate of titanium and Ti-Al intermetallic layers formed in penetrated region (Figures 5-26 b-c), which is similar to the observations made in literature [10]

when the pin penetrating condition used. Also a number of micro-cracks formed in the penetrated region (Figures 5-26 b-c) which is likely due to strain caused by considerable difference in thermal expansion coefficients of titanium and of aluminium. Furthermore the pin penetration and insufficient material flow of titanium alloy during FSLW resulted in formation of many voids in penetrated region (Figure 5-26d). Presence of micro-cracks and void in the weld, resulted in relatively low σ_{Lap} value (340 N/mm) for the Region 2 sample.

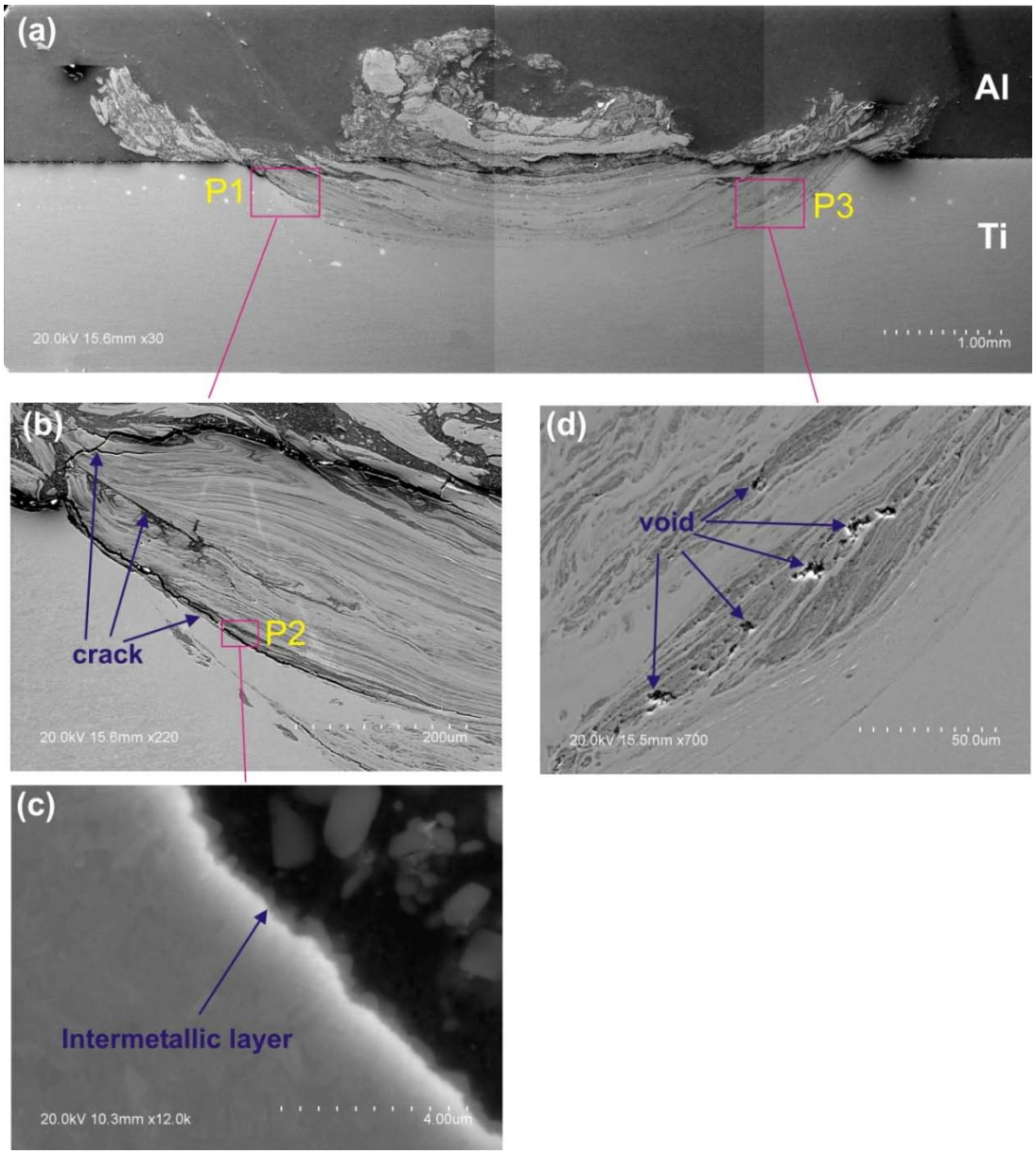

Figure 5-26 Microstructure of Region 2 sample as indicated in Figure 5-23 (a) macrograph, (b) higher magnification micrograph of area P1 in Figure 5-26a showing the cracks formed in the penetrated region, (c) higher magnification micrograph of area P2 in Figure 5-26b showing intermetallic layers in the penetrated region and (d) higher magnification micrograph of area P3 in Figure 5-26a

The photo of the tool pin, after being used in aforementioned FSLW experiment (shown in Figure 5-23) is presented in Figure 5-27. It can be seen that pin tip has severely deformed. This is due to the penetration/contact of pin to hard surface of Ti6Al4V plate, during FSLW.

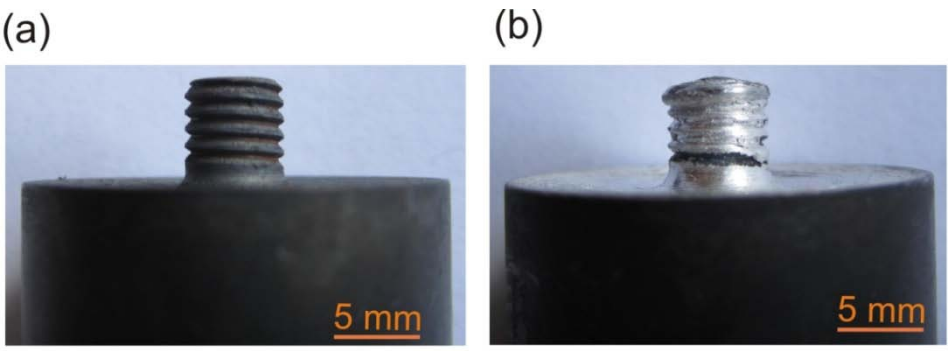

Figure 5-27 Photos of tool pin (a) before FSLW and (b) after FSLW

5.2.2 Effect of Interface Microstructure on Fracture Behaviour

During tensile shear testing, Region 1 sample fractured along the Al/Ti interface (Figure 5-28a) and Al 6060-T5 plate rotated considerably before failure. The bright portion seen on fracture surface of titanium side of tested sample (Figure 5-28b) indicates that fracture surface is covered by the smeared residue of aluminium. Closer view of fracture surface (Figures 5-28 c-e) clearly shows that a ductile fracture is dominant with plastic (shear) deformation preceding failure in aluminium adjacent to and on top of the interfacial intermetallic layer. Also EDS map analysis of fracture surface (Figures 5-28 f-g) clearly reveals the presence of smeared aluminium (heavily deformed) on top of fracture surface. This ductile deformation is consistent with the σ_{lap} –strain curve shown in Figure 5-24, displaying very high σ_{lap} value and fracture energy.

The aluminium macro tear ridge adhered to the fracture surface (Figure 5-28 c-d) indicates the strong cohesion at the interfaces of Ti/intermetallic/Al so that fracture occurred at aluminium side. Moreover, no intermetallic cracking (underneath the smeared aluminium) can be observed on fracture surface, which is in contrast to intermetallic cracking on fracture surface of Al/Steel FSL welds (Figure 5-16). These results suggest that the interface structure for Region 1 sample (with a single continuous intermetallic layer) is highly shear fracture resistant and thus high σ_{Lap} value (732 N/mm) obtained during testing.

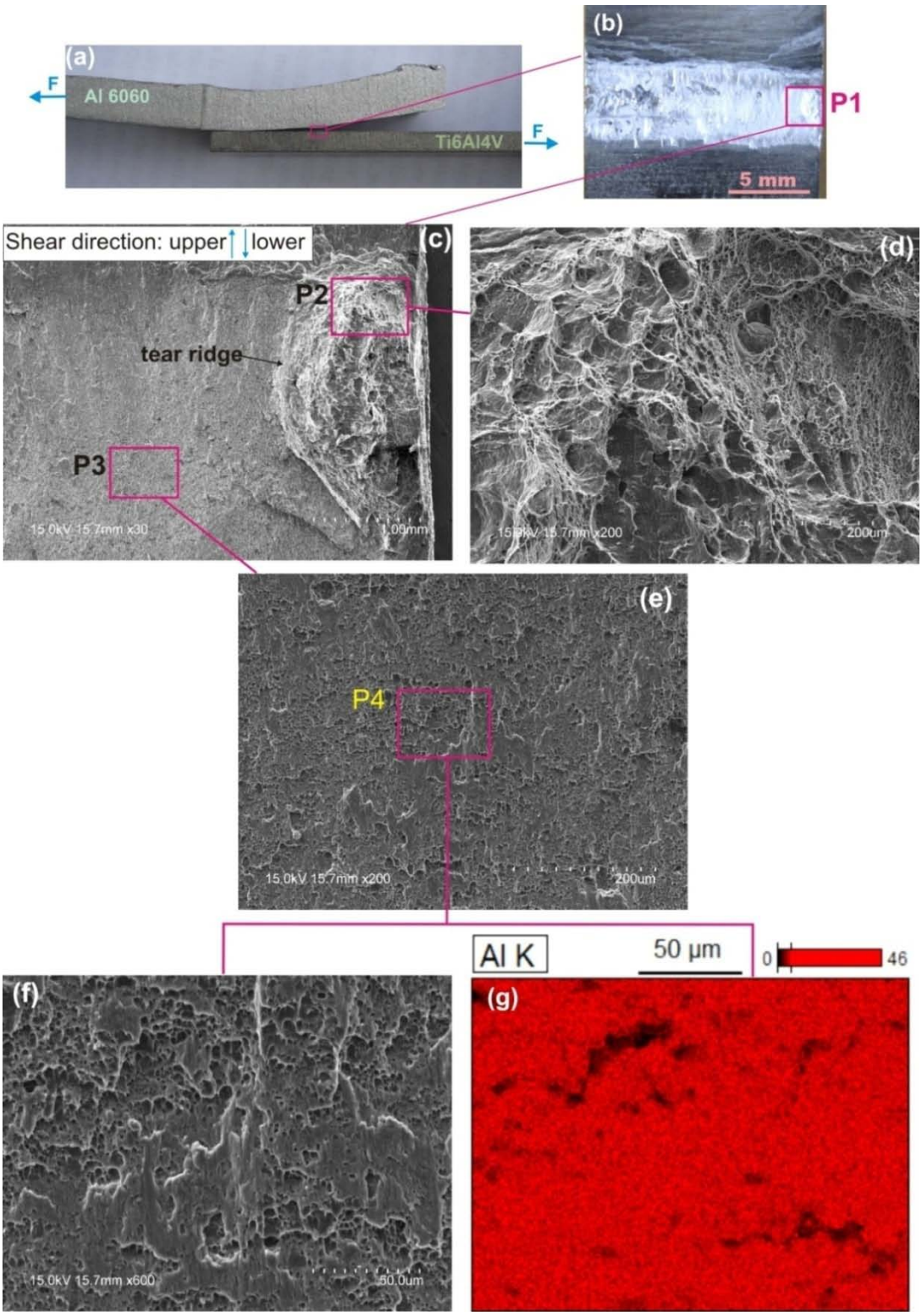

Figure 5-28 Fracture surface of Region 1 tested sample: (a) fractured sample, (b) image of titanium side of tested sample, (c) SEM micrograph of area P1 in Figure 5-28a showing aluminium tear ridges adhering to the titanium surface, (d) SEM micrograph of area P2 in Figure 5-28c showing ductile dimples associated with fracturing in aluminium, (e) SEM micrograph of area P3 in Figure 5-28c showing the heavily deformed aluminium on top of the intermetallic layer, (f) SEM micrograph of area P4 in Figure 5-28e with associated and (g) EDS map of Al

Figure 5-29 shows the Region 2 sample, tensile shear tested to fracture. The fractographs in Figures 5-29 c-d clearly shows that significant portion of the fracture surface is of brittle failure. The flake-like features formed on fracture surface suggest that cracking propagated along (parallel to) the intermetallic layers inside the laminate (penetrated) region. This brittle failure is also consistent with the σ_{lap} –strain curve of Region 2 sample (Figure 5-24) displaying lower σ_{Lap} value (~ 340 N/mm) and fracture energy. Therefore smaller amount of Al 6060-T5 rotation occurred before failure (Figure 5-29a), compared to Region 1 tested sample (Figure 5-28a), indicating smaller plastic deformation during testing.

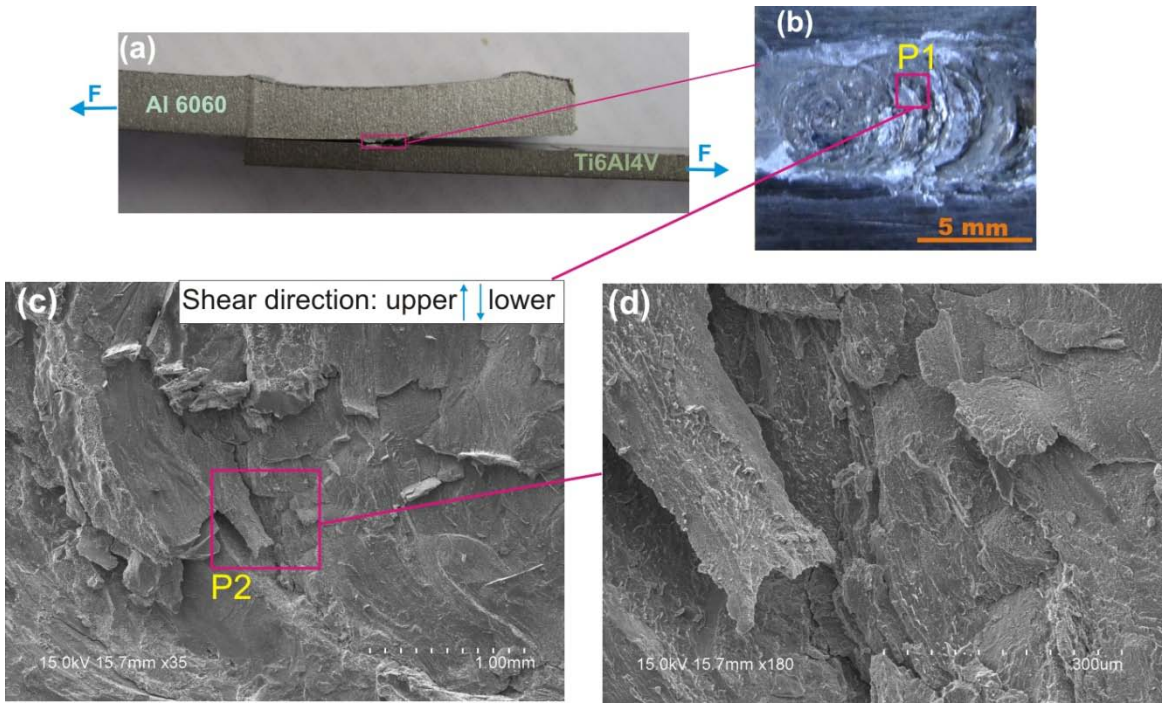

Figure 5-29 Fracture surface of Region 2 tested sample: (a) fractured sample, (b) image of titanium side of tested sample, (c) SEM micrograph of area P1 in Figure 5-29b displaying brittle fracture features and (d) higher magnification micrograph of area P2 in Figure 5-29c

The fracture surface characteristics of Region 2 sample is very similar to those observed on fracture surface of Al/Steel weld, when the pin penetrated to steel (Figure 5-17). These results suggest that the pin penetrating condition in FSLW of either Al/Steel or Al/Ti results in interface microstructures in which cracking tends to propagates along (parallel to) the irregular intermetallic layers inside the penetrated region. Furthermore microcracks formed in the penetrated region, in FSL welds of either Al/Steel or Al/Ti,

can act as favourable cracking initiation source (under loading) and facilitate the fracturing with lower σ_{lap}.

Figure 5-30 shows the fracture surfaces of two tensile shear tested samples, one corresponding to highest strength Al/Steel FSLW sample (σ_{Lap}=435 N/mm) and the other corresponding to highest strength Al/Ti FSLW sample (σ_{Lap}=732 N/mm). It should be pointed out that both tested samples obtained using the condition of $L_{dis} \approx 0$ (during FSLW) with subsequent single continuous intermetallic layer at interface, as shown in Figures 5-13 and 5-25. It can be seen that for Al/Ti sample (Figure 5-30b) large area of fracture surface is covered by the smeared (heavily deformed) aluminium, indicating that continuous metallurgical bonding established at a relatively large area. However for Al/Steel sample (Figure 5-30a) smaller area of fracture surface is covered by the smeared aluminium, indicated by the arrows in Figure 5-30a, meaning that continuous metallurgical bonding established at a smaller region. Therefore these results suggest that the larger bonded area for Al/Ti FSLW sample (due to more contact of bottom of pin with Ti6Al4V plate during FSLW) is likely the main contributor to the higher joint strength of Al/Ti FSL weld.

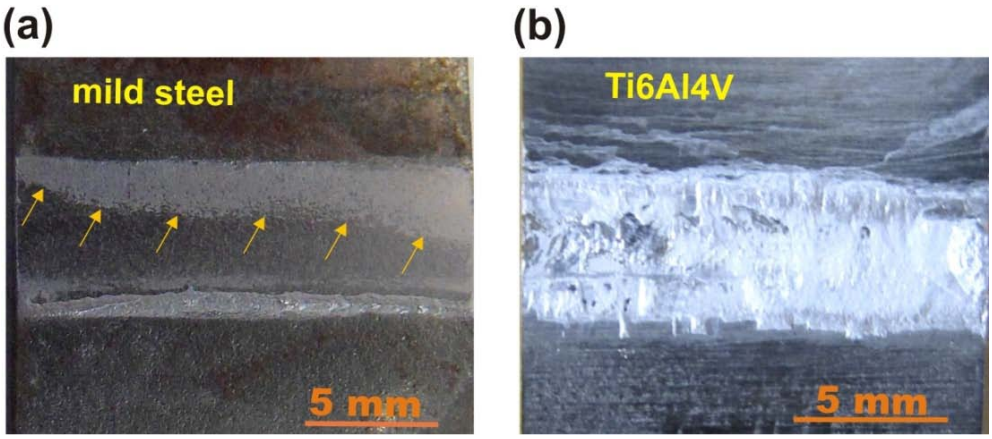

Figure 5-30 Fracture surface of tested samples for: (a) highest strength Al/Steel FSLW sample and (b) highest strength Al/Ti FSLW sample

5.3 Summary

For Al/Steel FSL welds, joint strength was found to be very sensitive to pin positioning during FSLW. The condition of $L_{dis} \geq 0.3$ mm did not insure a continuous intermetallic layer and instead discontinuous intermetallic outbursts formed at the interface, resulting from the early stage of intermetallics growth. The low values of σ_{lap} (~ 70-120 N/mm) for the welds made using $L_{dis} \geq 0.3$ mm is due to the non-continuous metallurgical bond formed at the joint interface.

Once the pin sufficiently penetrates to steel (L_{dis} = -0.1 to -0.3 mm), the interface region was consisted of intermix and irregular layers of intermetallics and recrystallized α-Fe form. The value of σ_{lap} (≈300 N/mm) in pin penetrating condition, although L_{dis} differ for different samples, indicates that σ_{Lap} is not very sensitive to the size of the interface region (with intermix and irregular intermetallic layers), once it forms. Also value of σ_{lap} (≈300 N/mm) for the pin penetrated welds is almost the same as the maximum σ_{lap} value (304 N/mm) reported in literature when pin penetrating condition used. However pin penetrating conditions did not represent a joint condition for optimal σ_{lap} to be obtained, as has been favoured by the current literature.

When the bottom of pin reached the steel surface without penetrating ($L_{dis} \approx 0$ mm) during FSLW, a single continuous intermetallic layer formed along the interface; and thus continuous metallurgical bonding established. The joint produced by this non pin penetrating condition (with a single continuous intermetallic at interface) displayed a high σ_{Lap} value (435 N/mm) which was ~ 42% increase in σ_{Lap} in comparison to the case of pin penetrating condition (with the mixed interface region).

In tensile shear loading of pin penetrated samples (with the mixed interface region) failure occurred through crack propagation along (parallel to) the intermetallics layers embedded inside the penetrated region, resulting in a brittle fracture. However for the sample made using non pin penetrating condition of $L_{dis} \approx 0$ (with a single continuous intermetallic layer at interface), a ductile fracture was dominant with plastic deformation preceding failure mostly in aluminium adjacent to and on top of the interfacial intermetallic layer. Therefore these results indicate that the notion of the

presence of intermetallics embrittling the joint, is scientifically incorrect and a joint interface with single intermetallic layer can be highly shear fracture resistant.

For Al/Ti FSL welds, the pin positioning during FSLW was also found to be the major parameter affecting σ_{Lap} of welds, similar to Al/Steel FSLW. For the sample made using non pin penetrating condition of $L_{dis} \approx 0$ mm, a thin continuous intermetallic layer formed along the joint interface resulting in a strong metallurgical bonding with high σ_{Lap} value (735 N/mm) during testing. However the pin penetrating condition had detrimental effect on joint strength due to formation of voids and micro-cracks in the penetrated region.

Comparison of fracture surfaces for the highest strength Al/Ti FSL weld (σ_{Lap}=732 N/mm) to highest strength Al/Steel FSL weld (σ_{Lap}=435 N/mm), both made using the condition of $L_{dis} \approx 0$ with subsequent single continuous interfacial intermetallic at interface, suggests that the larger bonding area at Al/Ti interface (due to more contact of pin with Ti6Al4V plate) was likely the main contributor to the higher joint strength of Al/Ti FSL weld.

Based on similar observations made in FSLW of Al/Steel and Al/Ti, it is suggested that a force control mechanism of pin positioning can be effective for obtaining the high strength joints of either Al/Steel or Al/Ti welds. Carefully controlling the pin positioning during FSLW make sure that the pin is very close but not penetrating into bottom plate, in order to obtain a single continuous intermetallic layer at the joint interface.

6. Conclusions

The major conclusions of this thesis can be summarized as below:

A. For FSLW of aluminium alloy 6060-T5:

When the pin only slightly penetrates the bottom plate, a sufficiently low ν allows for a sufficient bonding of the lap plates and for the joint strength (σ_{Lap}) to be close to the strength of FS bead-on-plate samples (σ_{BoP}). A more sufficient penetration allows for *v* to increase while maintaining σ_{Lap} to be close to σ_{BoP}.

When pin penetration is sufficient, increasing ω or decreasing ν increases a high stir volume per unit length in the bottom stir zone ($A_{B\text{-}SZ}$). The rate, either $dA_{B\text{-}SZ}/d\omega$ or $dT_{SZ}/d\omega$ (T_{SZ} – stir zone temperature), is high when ω is low and in both cases they diminish as ω increases. This suggests the effect of ω on $A_{B\text{-}SZ}$ more dominantly through the effect of ω on T_{SZ} and thus the plasticity of the stir zone. The initial increase in $A_{B\text{-}SZ}$ above the corresponding area of the rotating pin (which is equal to minimum $A_{B\text{-}SZ}$) rapidly increases the vertical distance of the hook (h) to a maximum value (h_{Max}), which was equal to 40% of the thickness of the top plate (t_{Plate}) in the present study. Evidences have suggested that a hook is depressed by shoulder flow thus limiting the h_{Max} value.

When h tends to zero, despite of the existence of un-welded lap acting as a pre-crack and high stress concentration around it due to the lap geometry (during tensile shear testing), σ_{Lap} is very close to σ_{BoP} (in butt joint geometry). This is due to significant specimen bending (during tensile shear testing), offered by the high ductility of aluminium alloy due to its FCC structure, and thus reorientation of the specimen to a testing geometry close to tensile test geometry; diminishing considerably the stress concentration. The maximum achieved σ_{Lap} (422 N/mm) was about 2/3 of strength of as-received alloy pulled in tensile testing.

It was found that *h* does not necessarily have a strong influence on σ_{Lap} when *h* < ~ 30% t_{Plate}. This is because the end of a hook is not normally located in the lowest strength location of the HAZ, which competes with hooking as the preferred location of fracture. Also a more tortuous and discontinuous hook can reduce the effect of *h* on σ_{Lap}. When *h* > ~ 30% t_{Plate} , σ_{Lap} decreases more sharply when *h* increases, due to the dominant effect of an increasingly larger reduction in load bearing area.

B. For FSLW of magnesium alloy AZ31B-H24:

The rotation speed (ω) was also found to be the major parameter affecting *h*, similar to FSLW of Al 6060-T5. Increasing ω resulted in increase of stir zone temperature and hence stir zone plasticity, affecting the stir flow volumes which cause interface up-lifting. However hooks in AZ31 welds are located much closer to pin compared to hooks in Al 6060 welds, as a result of much smaller stir zone in AZ31 welds. Also the hooks in AZ31 welds are quite continuous while a hook in Al 6060 can be highly discontinuous. The observed difference in hook characteristics (shape, distance to weld center, continuity) of AZ31 and Al 6060 welds is suggested to be related to the difference in plastic properties of these materials at the high temperatures of FSLW, affecting the material flow during welding.

During tensile shear testing, all the AZ31 welds fractured by the same mode in which the crack initiated from the hook location and then propagated through top plate. That is related to the hardness distribution in AZ31 welds in which the hook location had lower hardness (and thus local strength) than HAZ region. Therefore contrary to Al 6060 welds, when *h* is small, HAZ softening could not compete against hooking for deformation and fracturing. Thus failure always occurred at hook location. Consequently σ_{Lap} of AZ31 welds exhibited a stronger dependence on *h*.

The maximum achieved σ_{Lap} (290 N/mm) in AZ31 welds was about 1/3 of strength of original AZ31B-H24 alloy pulled in tensile testing. This ratio is much lower than that for Al 6060-T5 welds with $\sigma_{Lap} \approx$ 2/3 of strength of original Al 6060-T5 alloy. This is due to lack of local ductility and specimen rotation (during tensile shear

testing) of AZ31 welds, owing to low number of slip systems offered by HCP crystal structure, allowing the stress concentration to be maintained during testing and thus resulting in fracturing with lower σ_{Lap}.

It was found that hook orientation is an important parameter affecting fracture location and strength of AZ31 tensile shear samples. In tensile shear testing of the samples with positive hooks, significant stress concentration forms at the hook tip region, facilitating the fracturing with low σ_{Lap}. On the other hand, the samples with negative hooking experience considerably less stress concentration at the hook tip, thus resulting in increase of σ_{Lap}. For the case of negative hook specimens with h >-0.6 mm, the end of hook is almost stress concentration free, but in location where hook start curve downward (from the original lapping interface), significant stress concentration forms and thus fracture occurs.

High ductility of AZ31B-O (with strong basal texture) during uniaxial tensile testing is due to operation of dislocation slip systems as the major deformation mechanisms. Therefore large amount of deformation took place by dislocation slips, prior to formation of contraction twins (to accommodate the strain in thickness direction) which produces a highly localised shear-deformation region, leading to failure. On the other hand, localised high stress concentration caused by tensile shear loading, force the material to locally deform, resulting in activation of deformation twinning at the regions of high stress concentration. The localised plastic deformation by twinning, which was not preceded with substantial deformation by dislocation slip, facilitated the fracturing with lower ductility and fracture strength.

C. For FSLW of Al 6060-T5 to mild steel:

The condition of $L_{dis} \geq 0.3$ mm did not insure a continuous intermetallic layer and instead discontinuous intermetallic outbursts formed at the interface. The low values of σ_{lap} (~70-120 N/mm) for the welds made using $L_{dis} \geq 0.3$ mm is due to the non-continuous metallurgical bond formed at the joint interface.

Once the pin sufficiently penetrates to steel (L_{dis} = -0.1 to -0.3 mm), the interface region was consisted of intermix and irregular layers of intermetallics and recrystallized α-Fe form. The value of σ_{lap} (≈300 N/mm) in pin penetrating condition, although L_{dis} differ for different samples, indicates that σ_{Lap} is not very sensitive to the size of the interface region (with intermix and irregular intermetallic layers), once it forms. Also value of σ_{lap} (≈300 N/mm) for the pin penetrated welds is almost the same as the maximum σ_{lap} value (304 N/mm) reported in literature when pin penetrating condition used. However pin penetrating conditions did not represent a joint condition for optimal σ_{lap} to be obtained, as has been favoured by the current literature.

When the bottom of pin reached the steel surface without penetrating (L_{dis} ≈ 0 mm) during FSLW, a single continuous intermetallic layer formed along the interface; and thus continuous metallurgical bonding established. The joint produced by this non pin penetrating condition (with a single continuous intermetallic at interface) displayed a high σ_{Lap} value (435 N/mm) which was ~ 42% increase in σ_{Lap} in comparison to the case of pin penetrating condition (with the mixed interface region).

In tensile shear loading of pin penetrated samples (with the mixed interface region) failure occurred through crack propagation along (parallel to) the intermetallics layers embedded inside the penetrated region, resulting in a brittle fracture. However for the sample made using non pin penetrating condition of L_{dis} ≈ 0 (with a single continuous intermetallic layer at interface), a ductile fracture was dominant with plastic deformation preceding failure mostly in aluminium adjacent to and on top of the interfacial intermetallic layer. Therefore these results indicate that the notion of the presence of intermetallics embrittling the joint, is scientifically incorrect and a joint interface with single intermetallic layer can be highly shear fracture resistant.

D. For FSLW of Al 6060-T5 to Ti6Al4V:

The pin positioning during FSLW was found to be the major parameter affecting σ_{Lap} of welds, similar to Al/Steel FSLW. For the sample made using non pin penetrating condition of $L_{dis} \approx 0$ mm, a thin continuous intermetallic layer formed along the joint interface resulting in a strong metallurgical bonding with high σ_{Lap} value (735 N/mm) during testing. However the pin penetrating condition had detrimental effect on joint strength due to formation of voids and micro-cracks in the penetrated region.

Comparison of fracture surfaces for the highest strength Al/Ti FSL weld (σ_{Lap}=732 N/mm) to highest strength Al/Steel FSL weld (σ_{Lap}=435 N/mm), both made using the condition of $L_{dis} \approx 0$ with subsequent single continuous interfacial intermetallic at interface, suggests that the larger bonding area at Al/Ti interface (due to more contact of pin with Ti6Al4V plate) was likely the main contributor to the higher joint strength of Al/Ti FSL weld.

Based on similar observations made in FSLW of Al/Steel and Al/Ti, it is suggested that a force control mechanism of pin positioning can be effective for obtaining the high strength joints of either Al/Steel or Al/Ti welds. Carefully controlling the pin positioning during FSLW make sure that the pin is very close but not penetrating into bottom plate, in order to obtain a single continuous intermetallic layer at the joint interface.

7. References

1. W.M. Thomas and E. D. Nicholas, *Friction-stir butt welding*, 1991: UK.

2. P. L. Threadgil , A. J. Leonard, and H. R. Shercliff, *Friction stir welding of aluminium alloys.* International Material Reviews, 2009. **54**(2): p. 49-93

3. R.S. Mishra and Z.Y. Ma, *Friction stir welding and processing.* Materials Science & Engineering R, 2005. **50**(1-2): p. 1-78.

4. R. Nandan, T. DebRoy, and H. K. Bhadeshia, *Recent advances in friction-stir welding -process, weldment structure and properties.* Progress in Materials Science, 2008. **53**: p. 980-1023.

5. D. Fersini and A. Pirondi, *Fatigue behaviour of Al2024-T3 friction stir welded lap joints.* Engineering Fracture Mechanics, 2007. **74**(4): p. 468-480.

6. L. Dubourg, A. Merati, and M. Jahazi, *Process optimisation and mechanical properties of friction stir lap welds of 7075-T6 stringers on 2024-T3 skin.* Materials & Design, 2010. **31**(7): p. 3324–3330.

7. Q. Yang, X. Li, and K. Chen, *Effect of tool geometry and process condition on static strength of magnesium friction stir lap linear weld.* Materials Science & Engineering A, 2011. **528**(6): p. 2463-2478.

8. R. S. Coelho, A. Kostka, and S. Sheiki, *Microstructure and Mechanical Properties of an AA6181-T4 Aluminium Alloy to HC340LA High Strength Steel Friction Stir Overlap Weld.* Advanced Engineering Materials, 2008. **10**(10): p. 961–972.

9. U. Dressler, G. Biallas, and U.A. Mercado, *Friction stir welding of titanium alloy TiAl6V4 to aluminium alloy AA2024-T3.* Materials Science & Engineering A, 2009. **526**(1-2): p. 113-117

10. Y. C. Chen and K. Nakata, *Microstructural characterization and mechanical properties in friction stir welding of aluminium and titanium dissimilar alloys.* Materials & Design, 2009. **30**(3): p. 469-474

11. *ASM Metals Handbook: properties and selection of nonferrous alloys and special purpose materials*. Vol. 2. 1991, ASM International.

12. X. Cao and M. Jahazi, *Effect of tool rotational speed and probe length on lap joint quality of a friction stir welded magnesium alloy.* Materials and Design, 2011. **32**(1): p. 1-11.

13. N. Afrin, D.L. Chen, and X. Cao, *Microstructure and tensile properties of friction stir welded AZ31B magnesium alloy.* Materials Science and Engineering A, 2008. **472**(1-2): p. 179-186.

14. Z. W. Chen and S. Cui, *On the forming mechanism of banded structures in aluminium alloy friction stir welds.* Scripta Materialia, 2008. **58(**5): p. 417-420.

15. M. K. Yavada, R. S. Mishra, and Y. L. Chen, *Study of frictio stir joining of thin aluminium sheets in lap joint configuration.* Science and Technology of Welding & Joining, 2010. **15**(1): p. 70-75.

16. L. Cederqvist and A.P. Reynolds, *Factors Affecting the Properties of Friction Stir Welded Aluminium Lap Joints.* Welding Journal, 2001. **80**(12): p. 281-287.

17. X. Cao and M. Jahazi, *Effect of Welding Speed on Lap Joint Quality of Friction Stir Welded AZ31 Magnesium Alloy*, in *Proceedings of the 8th ASM International Conference, Trends in Welding Research*, 2009: Georgia, USA.

18. G. Cantin, S. A. David, and W. M. Thomas, *Friction skew-stir welding of lap joints in 5083-O aluminium.* Science and Technology of Welding & Joining, 2004. **10**(3): p. 268-280.

19. M. Yadava, R. S. Mishra, and Y. L. Chen, *Friction stir lap welds of AA6611 aluminum alloy*, in *Friction stir welding and Processing IV*2007: Orlando, Florida.

20. G. Buffa, G. Campanile, and L. Fratini, *Friction stir welding of lap joints: Influence of process parameters on the metallurgical and mechanical properties.* Materials Science & Engineering A, 2009. **519**(1-2): p. 19-26

21. V. Soundararajan, E. Yarrapareddy, and R. Kovacevic, *Investigation of the Friction Stir Lap welding of aluminum alloys AA5182 and AA 6022.* Journal of Materials Engineering and Performance 2006. **16**(4): p. 477-484.

22. C. Y. Lee, W. B. Lee, and J. W. Kim, *Lap joint properties of FSWed dissimilar formed 5052 Al and 6061 Al alloys with different thickness.* Journal of Materials Science Letters, 2008. **43(**9): p. 3296-330.

23. W.J. Arbegast and P.J. Hartley, *Friction Stir Weld Technology Development at Lockheed Martin Michoud Space Systems- An Overview*, in *Proceedings of the Fifth international conference of trends in welding research* 1998: Pine Mountaing,GA. p. 541.

24. S. R. Ren, Z. Y. MA, and L. Q. Chen, *Effect of welding parameters on tensile properties and fracture behaviour of friction stir welded Al-Mg-Si alloy.* Scripta Materialia, 2007. **56**: p. 69-72.

25. Z. Y. MA, *Influence of Tool Dimension and Welding Parameters on Microstructure and Mechanical Properties of Friction-Stir-Welded 6061-T651 Aluminum Alloy* Metallurgical and Materials Transactions A, 2008. **39**(10): p. 2378-2389.

26. P. Cavaliere, A. De Santis, and F. Panella, *2198 Al–Li plates joined by Friction Stir Welding: Mechanical and microstructural behavior.* Materials & Design, 2009. **30**(9): p. 3622-3631.

27. A. Elrefaey, M. Gouda, and M. Takahashi, *Characterization of aluminum-steel lap joint by friction stir welding.* Journal of Materials Engineering and Performance 2005. **14**(1): p. 10-17.

28. K. Kimapong and T. Watanabe, *Effect of welding process parameters on mechanical property of FSW lap joint between aluminum alloy and steel.* Materials Transactions, 2005. **46**(10): p. 2211-2217

29. M. K. kulekci, A. Silk, and E. Kaluc, *Effects of tool rotation and pin diameter on fatigue properties of friction stir welded lap joints.* International Journal of Advanced Mnufacturing Technology, 2008. **36**(9-10): p. 877-882.

30. A. P. Reynolds, W. D. Lockwood, and T. U. Seidel, *Processing-property correlation in friction stir welds.* Materials Science Forum, 2000. **331-337**: p. 1719-1724.

31. S. Lim, S. Kim, and C. Lee, *Tensile behavior of friction-stir-welded AZ31-H24 Mg alloy.* Metallurgical and Materials Transactions A, 2005. **36**(6): p. 1609-1612.

32. Y. S. Sato, H. Kokawa, and M. Enomoto, *Microstructural evolution of 6063 aluminum during friction-stir welding.* Metallurgical and Materials Transactions A, 2007. **30**(9): p. 2429-2437

33. F. M. Lucas, P. dasNeves, and R. D. Adams, *Analytical models of adhesively bonded joints—PartI: Literature survey.* International Journal of Adhesion & Adhesives, 2009. **29**: p. 319-330.

34. F. M. Lucas, R. Carbas, and G. Critchlow, *Effect of material, geometry, surface treatment and environment on shear strenght of single lap joints.* International Journal of Adhesion and Adhesives, 2009. **29**(6): p. 621-632.

35. S. Her, *Stress analysis of adhesively bonded lap joints.* Composite structures, 1999. **47**(1): p. 673-678.

36. F. M. Lucas, R. J. C. Carbas, and G. W. Critchlow, *Effect of material, geometry, surface treatment and environment on the shear strength of single lap joints.* International Journal of Adhesion & Adhesives, 2009. **29**: p. 621-632.

37. S. M. R. Khalili, S. Khalili, and M. R. Pirouzhashemi, *Numerical study of lap joints with composite adhesives and composite adherends subjected to in-plane and transverse loads.* International Journal of Adhesion and Adhesives, 2008. **28**(8): p. 411-418.

38. A. Derewonko, J. Godzimirski, and K. Kosiuczenco, *Strenght assesment of adhesive-bonded joints.* Computational Material Science, 2008. **43**(1): p. 157-164.

39. K. Nakata, *Friction stir welding of magnesium alloys.* Welding International, 2009. **23**(5): p. 328-332.

40. L. Commina, M. Dumontb, and J.-E. Massea, *Friction stir welding of AZ31 magnesium alloy rolled sheets: Influence of processing parameters.* Acta Materiala, 2009. **57**(2): p. 326-334.

41. G. Padmanaban and V. Balasubramanian, *An experimental investigation on friction stir welding of AZ31B magnesium alloy.* International Journal of Advanced Manufacturing Technology 2010. **49**(1-4): p. 111-121

42. Q. Miao, L. Hua, and X. Wanga, *Grain growth kinetics of a fine-grained AZ31 magnesium alloy produced by hot rolling, .* Journal of Alloys and Compounds, 2010. **493**(1-2): p. 87-90.

43. D. Ando, J. Koike, and Y. Sutou, *Relationship between deformation twinning and surface step formation in AZ31 magnesium alloys.* Acta Materialia, 2010. **58**(13): p. 4316-4324.

44. Y. Chino, K. Kimura, and M. Hakamada, *Mechanical anisotropy due to twinning in an extruded AZ31 magnesium alloy* Materials Science & Engineering A, 2008. **485**(1-2): p. 311-317.

45. Y. Chino, K. Kimura, and M. Mabuchi, *Twinning behavior and deformation mechanisms of extruded AZ31 Mg alloy.* Materials Science & Engineering A, 2008. **486**(1-2): p. 481-488.

46. J. Koike, *Enhanced deformation mechanisms by anisotropic plasticity in polycrystalline magnesium alloys at room temperature.* Metallurgical and Materials Transactions A, 2005. **36**(7): p. 1689-1696.

47. J. Koike, T. Kobayashi, and T. Mukai, *The activity of non-basal slip systems and dynamic recovery at room temperature in fine-grained AZ31B magnesium alloys.* Acta Materialia, 2003. **51**(7): p. 2055-2065.

48. Y. Chino, K. Kimura, and M. Mabuchi, *Deformation characteristics at room temperature under biaxial tensile stress in textured AZ31 Mg alloy sheets.* Acta Materiala, 2009. **57**(5): p. 1476-1485.

49. J. Koike, Y. Sato, and D. Ando, *Origin of the anomalous {1012} twinning during tensile deformation of mg alloy sheet.* Materials Transactions 2008. **49**(12): p. 2792-2800.

50. M. R. Barnett, *Twinning and the ductility of magnesium alloys: Part I: Tension twins.* Materials Science and Engineering: A, 2007. **464**(25): p. 1-7.

51. M. R. Barnett, *Twinning and the ductility of magnesium alloys: Part II. Contraction twins.* Materials Science and Engineering: A, 2007. **464**(1-2): p. 8-16

52. T. Al-Samman, X. Li, and S. G. Chowdhury, *Orientation dependent slip and twinning during compression and tension of strongly textured magnesium AZ31 alloy.* Materials Science and Engineering A 2010. **527**(15): p. 3450-3463

53. X. Lia, P. Yang, and L.-N. Wanga, *Orientational analysis of static recrystallization at compression twins in a magnesium alloy AZ31* Materials Science and Engineering: A, 2009. **157**(1-2): p. 160-169.

54. Y. Chino, M. Mabuchi, and R. Kishihara, *Mechanical properties and press formability at room temperature of AZ31 Mg alloy processed by single roller drive rolling.* Materials Transactions, 2002. **43**(10): p. 2554-2560.

55. S. R. Agnew and J. F. Nie, *Preface to the viewpoint set on: The current state of magnesium alloy science and technology.* Scripta Materialia, 2010. **63**(7): p. 671-673.

56. J. W. Christian and S. Mahajan, *Deformation twinning*. 1995, Pergamon Press.

57. B. L. Mordike and T. Ebert, *Magnesium Properties - applications - potential.* Materials Science and Engineering A, 2001. **302**(1): p. 37-45.

58. Y. Chino, K. Sassa, and A. Kamiya, *Enhanced formability at elevated temperature of a cross-rolled magnesium alloy sheet.* Materials Science and Engineering A, 2006. **441**(1-2): p. 349-356.

59. B. H. Lee, K. S. Shin, and C. S. Lee, *High temperature deformation behavior of AZ31 Mg alloy.* Materials Science Forum 2005. **475-479**(IV): p. 2927-2930

60. H. Takuda, T. Morishita, and T. Kinoshita, *Modelling of formula for flow stress of a magnesium alloy AZ31 sheet at elevated temperatures.* Journal of Materials Processing Technology, 2005. **164-165**: p. 1258-1262.

61. B.K. Raghunatha, K. Raghukandana, and R. Karthikeyanb, *Flow stress modeling of AZ91 magnesium alloys at elevated temperature.* Journal of Alloys and Compounds, 2011. **509**(15): p. 4992-4998.

62. J. Koike, R. Ohyama, and T. Kobayashi, *Grain-boundary sliding in AZ31 magnesium alloys at room temperature to 523 K* Materials Transactions, 2003. **44**(4): p. 445-451.

63. Y.N. Wanga and J.C. Huanga, *The role of twinning and untwinning in yielding behavior in hot-extruded Mg–Al–Zn alloy.* Acta Materialia, 2007. **55**(3): p. 897-905

64. H. L. Kim, W. K. Bang, and Y. W. Chang, *Deformation behavior of as-rolled and strip-cast AZ31 magnesium alloy sheets,*. Materials Science and Engineering: A, 2011. **528**(16-17): p. 5356-5365.

65. S. Liang, H. Suna, and Z. Liua, *Mechanical properties and texture evolution during rolling process of an AZ31 Mg alloy.* Journal of Alloys and Compounds, 2009. **472**(1-2): p. 127-132

66. Y. C. Chen and K. Nakata, *Effect of surface state of steel on the microstructure and mechanical properties of dissimilar metal lap joints of aluminium and steel by friction stir welding.* Metallurgical and Materials Transactions A, 2008. **39**(8): p. 1985-1992.

67. Y. C. Chen, T. Komazaki, and Y. G. Kim, *Interface microstructure study of friction stir lap joint of AC4C cast aluminium alloy and zinc-coated steel.* Materials Chemistry and Physics 2008. **111**(2-3): p. 375-380

68. K. Kimapong and T. Watanabe, *Lap joint of A5083 aluminum alloy and SS400 steel by friction stir welding.* Materials Transactions, 2005. **46**(4): p. 835-841

69. M. Movahedi, A. H. Kokabi, and S. M. Seyed Reihani, *Mechanical and microstructural characterization of Al-5083/St-12 lap joints made by friction stir welding.* Engineering Procedia, 2011. **10**: p. 3297-3303.

70. W. H. Jiang and R. Kovacevic, *Feasibility study of friction stir welding of 6061-T6 aluminium alloy with AISI 1018 steel*, in *Proceedings of the Institution of Mechanical Engineers, Part B: Journal of Engineering Manufacture* 2004.

71. D. G. Morris, M. Muñoz-Morris, and J. Chao, *Development of high strength, high ductility and high creep resistant iron aluminide* Intermetallics, 2004. **12**: p. 821-826.

72. D.G. Morris and M. A. Morris-Munoz, *The infuence of microstructure on the ductility of iron aluminides.* Intermetallics 1999. **7**: p. 1121-1129.

73. S. Bozzi, A. L. Helbert-Etter, and T. Baudin, *Intermetallic compounds in Al 6016/IF-steel friction stir spot welds.* Materials Science and Engineering A, 2010. **527**(16-17): p. 4505-4509

74. Y. H. Chen, Q. Ni, and L. M. Ke, *Interface characteristic of friction stir welding lap joints of Ti/Al dissimilar alloys.* Transactions of Nonferrous Metals Society of China (English Edition), 2012. **22**(2): p. 299-304.

75. V. Raghavan, *Al-Ti (Aluminium-Titanium).* Journal of Phase Equilibria and Diffusion, 2005. **26**(2): p. 171-172.

76. J. Wilden and J. P. Bergmann, *Manufacturing of titanium/aluminium and titanium/steel joints by means of diffusion welding.* Welding and Cutting, 2004. **3**(5): p. 285-290

77. A. Fuji, K. Ikeuchi, and Y. S. Sato *In-situ observation of interlayer growth during post-weld heat treatment in friction-welded joint of Titanium and Aluminium*. in *Proceeding of the 7th International Symposium Japan Welding Socitey*. 2001. Kobe, Japan.

78. A. Fuji, M. Kimura, and T. H. North, *Mechanical properties of titanium-5083 aluminium alloy friction joints.* Materials Science and Technology 1997. **13**(8): p. 673-678

79. I. M. Robertson and G. B. Schaffer, *Review of densification of titanium based powder systems in press and sinter processing.* Powder Metallurgy 2010. **53**(2): p. 146-162.

80. A. Fuji, K. Ikeuchi, and Y. S. Sato *Interlayer growth at interfaces of Ti/Al-1%Mn, Ti/Al-4.6%Mg and Ti/Pure Al friction weld joints by post-weld heat treatment.* Science and Technology of Welding & Joining, 2004. **9**(6): p. 507-512.

81. W. V. Vaidya, M. Horstmann, and V. Ventzke, *Improving interfacial properties of a laser beam welded Dissimilar joint of aluminium AA6056 and titanium Ti6Al4V for aeronautical applications.* Journal of Materials Science, 2010. **45** (22): p. 6242-6245.

82. S. Chen, L. Li, and Y. Chen, *Improving interfacial reaction nonhomogeneity during laser welding-brazing aluminum to titanium.* Materials & Design, 2011: p. Article in press.

83. Y. V. Milmana, et al., *Mechanical behaviour of Al3Ti intermetallic and L12 phases on its basis.* Intermetallics, 2001. **9**: p. 839-845.

84. Y. C. Kim and A. Fuji, *Factors dominating joint characteristics in Ti - Al friction welds.* Science and Technology of Welding & Joining, 2002. **7** (3): p. 149-154

85. *Oxford Instruments. Basics of EBSD.* Available from: *http://www.ebsd.com/ebsd-explained/basicofebsd1.htm*. 2005.

86. A. J. Schwartz and M. Kumar, *Electron Backscatter Diffraction in Materials Science*. 2009, Springer.

87. *ABAQUS /CAE User's Manual*2008: Habbitt Kalsson & Sorensen Inc.

88. M.R. Stoudt and L.E. Levinea, *The fundamental relationships between grain orientation, deformation-induced surface roughness and strain localization in an aluminum alloy.* Materials Science & Engineering A, 2011. **530**: p. 107–116.

89. Jun-Hyun Han, Dong-Ik Kim, and Kwang-Koo Jee, *Evolution of crystallographic orientations in an aluminum single crystal during tensile deformation.* Materials Science & Engineering A, 2004. **387**: p. 60-63.

90. P. Zhang, S. X. Li, and Z. F. Zhang, *General relationship between strength and hardness.* Materials Science & Engineering A, 2011. **529**: p. 62-73.

91. Y. S. Sato and H. Kokawa, *Distribution of tensile property and microstructure in friction stir weld of 6063 aluminum.* Metallurgical and Material Transaction A 2001. **32**(12): p. 3023-3031.

92. R. Nandan, G. Roy, and T. Lienert, *Numerical modelling of 3D plastic flow and heat transfer during friction stir welding of stainless steel.* Science and Technology of Welding & Joining, 2006. **11**(5): p. 526-537.

93. F.J. MacMaster, K.S. Chan, and S.C. Bergsma, *Aluminum alloy 6069 part II: fracture toughness of 6061-T6 and 6069-T6.* Materials Science & Engineering A, 2000. **289**(1-2): p. 54-59.

94. T. L. Anderson, *Fracture Mechanics: Fundamentals and Applications*1995, Boston: CRC Press.

95. H. Somekawa, K. Nakajima, and A. Singh, *Ductile fracture mechanism in fine-grained magnesium alloy* Philosophical Magazine Letters, 2010. **90**(11): p. 831-839

96. M. Marya, L. G. Hector, and R. Verma, *Microstructural effects of AZ31 magnesium alloy on its tensile deformation and failure behaviours.* Materials Science & Engineering A, 2006. **418**(1-2): p. 341-356.

97. L. Lua, T. Liua, and Y. Chena, *Deformation and fracture behaviour of hot extruded Mg alloy AZ31.* Materials Characterization, 2012. **67**: p. 93-100.

98. Yu.V. Milmana, D.B. Miracle, and S.I. Chugunova, *Mechanical behaviour of Al3Ti intermetallic and L12 phases on its basis.* Intermetallics, 2001. **9**: p. 839-845.

99. Jun-Hyun Han, Kwang-Koo Jee, and Kyu Hwan Oh, *Orientation rotation behavior during in situ tensile deformation of polycrystalline 1050 aluminum alloy.* International Journal of Mechanical Sciences, 2003. **45**(10): p. 1613–1623.

100. R. Nandan, G. G. Roy, and T. J. Lienert, *Three-dimensional heat and material flow during friction stir welding of mild steel.* Acta Materiala, 2007. **55**(3): p. 883-895.

101. H. Wang, P. Colegrove, and H. M. Mayer, *Material constitutive behaviour and microstructure study on aluminium alloys for friction stir welding.* Advanced Materials Research, 2010. **89-91** (615-620).

102. P. A. Colegrove, H. R. Shercliff, and R. zettler, *Model for predicting heat generation and temperature in friction stir welding from the material properties.* Science and Technology of Welding & Joining, 2007. **12**(4): p. 284-297.

103. R. Nandan, *Numerical modelling of 3D plastic flow and heat transfer during friction stir welding of stainless steel.* Science and Technology of Welding and Joining 2006. **11**(5): p. 526-537.

104. P. A. Colegrove, H. R. Shercliff, and R Zettler, *Model for predicting heat generation and temperature in friction stir welding from the material properties.* Science and Technology of Welding and Joining 2007. **12**(4): p. 284-297.

105. *Electron AZ31B sheet plate and coil*. Available from: www.magnesium-elektron.com/data/downloads/DS482.pdf.

106. *Aluminium 6060 alloys*. Available from: http://sales.riotintoaluminium.com/freedom.aspx?pid=522.

107. C. Leitão, R. Louro, and D.M. Rodrigues, *Analysis of high temperature plastic behaviour and its relation with weldability in friction stir welding for aluminium alloys AA5083-H111 and AA6082-T6* Materials & Design, 2012. **37**: p. 402-409.

108. N. Srinivasana, Y. V. R. K. Prasadb, and P. Rama Raoc, *Hot deformation behaviour of Mg–3Al alloy—A study using processing map.* Materials Science & Engineering A, 2008. **476**(1-2): p. 146-156.

109. S.M. Chowdhury, D.L. Chena, and S.D. Bholea, *Tensile properties of a friction stir welded magnesium alloy: Effect of pin tool thread orientation and weld pitch* materials Science & Engineering A, 2010. **527**: p. 6064-6075.

110. F. Erdogan and G. C. Sih, *On the crack extension in plates under plane loading and transverse shear*. Journal of Basic Engineering, 1963. **85**: p. 519-527.

111. R. G. Budynas, *Advanced strenght and applied stres analysis* 1999: McGraw-Hill

112. L. Bian, *Crack growth prediction and non-linear analysis for an elasto-plastic solid.* International journal of engineering science, 2009. **47**: p. 325-341.

113. W. Yuana, R. S. Mishraa, and B. Carlsonb, *Effect of texture on the mechanical behavior of ultrafine grained magnesium alloy* Scripta Materialia, 2011. **64**(6): p. 580-583

114. T. Al-Samman and G. Gottsteina, *Room temperature formability of a magnesium AZ31 alloy: Examining the role of texture on the deformation mechanisms.* Materials Science and Engineering: A, 2008. **488**(1-2): p. 406-414

115. M. R. Barnett, M. D. Nave, and C. J. Bettles, *Deformation microstructures and textures of some cold rolled Mg alloys.* Materials Science and Engineering A 2004. **386**(1-2): p. 205-211.

116. J. Koike, *Enhanced deformation mechanisms by anisotropic plasticity in polycrystalline Mg alloys at room temperature.* Metallurgical and Materials Transactions A, 2005. **36**: p. 1689-1696.

117. H. Somekawa, A. Singh, and T. Mukai, *Fracture mechanism of a coarse-grained magnesium alloy during fracture toughness testing* Philosophical Magazine Letters, 2008. **89**(1): p. 2-10

118. H. Somekawa, T. Inoue, and T. Mukai, *Deformation mechanism near crack-tip by finite element analysis and microstructure observation in magnesium alloys.* Materials Science and Engineering A, 2010. **527**(7-8): p. 1761-1768

119. J. Yang, B. L. Xiao, and D. Wang, *Effects of heat input on tensile properties and fracture behavior of friction stir welded Mg-3Al-1Zn alloy.* Materials Science & Engineering A, 2010. **527**(3): p. 708-714.

120. W. Wooa, H. Chooa, and D.W. Brownc, *Texture variation and its influence on the tensile behavior of a friction-stir processed magnesium alloy* Scripta Materialia, 2006. **54**(11): p. 1859-1864.

121. Z. W. Chen, *Formation and progression of die soldering during high pressure die casting.* Materials Science and Engineering A 2005. **397**(1-2): p. 356-369

122. G. Winkelman, Z. W. Chen, and D. H. StJohn, *Morphological features of interfacial intermetallics and interfacial reaction rate in Al-11Si-2.5Cu-(0.15/0.60)Fe cast alloy/die Steel couples.* Journal of Materials Science 2004. **39**: p. 519-528.

123. Wei-Jen Cheng and Chaur-Jeng Wang, *Study of microstructure and phase evolution of hot-dipped aluminide mild steel during high-temperature diffusion using electron backscatter diffraction.* Applied Surface Science, 2011. **257**(10): p. 4663-4668.

124. Wei-Jen Cheng and C.-J. Wang, *Observation of high-temperature phase transformation in the Si-modified aluminide coating on mild steel using EBSD.* Materials Characterization, 2008. **61**(4): p. 467-473.